Oligonucleotide-based therapies for neuromuscular disease

Andrew G. L. Douglas

Green Templeton College
University of Oxford

A thesis submitted for the degree of
Doctor of Philosophy

Hilary Term 2015

Abbreviations

2’MOE-PS – 2’-O-methoxyethyl phosphorothioate
2’OMePS – 2’-O-methyl phosphorothioate
AAV – adeno-associated virus
ACE – angiotensin converting enzme
AChR – acetylcholine receptor
ALP – alkaline phosphatase
ALS – amyotrophic lateral sclerosis
ALT – alanine aminotransferase
ANOVA – analysis of variance
ApoE – apolipoprotein E
AQP4 – aquaporin-4
ASO – antisense oligonucleotide
AST – aspartate aminotransferase
BBB – blood-brain barrier
BCSFB – blood-cerebrospinal fluid barrier
BMD – Becker muscular dystrophy
bp – base pair
BLASTN – nucleotide basic local alignment search tool
Bpg – bishomopropargylglycine
BSA – bovine serum albumin
c9FTD/ALS – *C9ORF72*-related frontotemporal dementia/amyotrophic lateral sclerosis
CA – California
cDNA – complementary deoxyribonucleic acid
CK – creatine kinase
Cl – clearance
CNS – central nervous system
CPP – cell-penetrating peptide
CSF – cerebrospinal fluid
CT – computed tomography
Ctrl – control
DAGC – dystrophin-associated glycoprotein complex
DAPI – 4’ 6-diamidino-2-phenylindole
ddPCR – digital droplet polymerase chain reaction
DENN – differentially expressed in normal and neoplasia
DIEA – diisopropylethylamine
DIG – digoxigenin
DM1 – myotonic dystrophy type 1
Dmab – dimethylamine borane
DMEM – Dulbecco’s modified eagle medium
DMD – Duchenne muscular dystrophy
DMSO – dimethyl sulfoxide
DNA – deoxyribonucleic acid
dNTP – deoxynucleotide triphosphate
DPAG – Department of Physiology, Anatomy and Genetics

dsRNA – double-stranded ribonucleic acid
dUTP – deoxyuridine triphosphate
EDTA – ethylenediaminetetraacetic acid
FAM – carboxyfluorescein
FBS – fetal bovine serum
FL – full-length
Fmoc – 9-fluorenylmethoxycarbonyl
FTD – frontotemporal dementia
GFAP – glial fibrillary acid protein
G_{T1b} – trisialoganglioside receptor
HBTU – 2-(1H-benzotriazole-1-yl)-1,1,3,3-tetramethyluronium hexafluorophosphate
hnRNP – heterogeneous nuclear ribonucleoprotein
HRP – horseradish peroxidase
IA – Iowa
ICV – intracerebroventricular
IDT – Integrated DNA Technologies
IP – intraperitoneal
iPS – induced pluripotent stem cell
iPS MN – induced pluripotent stem cell-derived motor neuron
IQ – intelligence quotient
IV – intravenous
IVDde – 1-(4,4-Dimethyl-2,6-dioxocyclohex-1-ylidene)- 3-methylbutyl
JAM – junctional adhesion molecule
kb – kilobase
kD –kilodalton
LDL – low density lipoprotein
LDLR – low density lipoprotein receptor
LDS – lithium dodecyl sulphate
LMB – Laboratory of Molecular Biology
LNA – locked nucleic acid
LRP1 – low density lipoprotein receptor-related protein-1
LTD – long-term depression
MA – Massachusetts
MALDI-TOF – matrix assisted laser desorption/ionisation - time of flight
Mb – megabase
MBD2 – methyl-deoxyribonucleic acid-binding domain 2
ME – Maine
miRNA – micro-ribonucleic acid
MN – Minnesota
MND – motor neuron disease
MO – Missouri
MRC – Medical Research Council
MRI – magnetic resonance imaging
mRNA –messenger ribonucleic acid
MSP – muscle-specific peptide
MS-PCR – methylation-specific polymerase chain reaction
MuLV – murine leukaemia virus

Mw – molecular weight
NAT – natural antisense transcript
NBT/BCIP – nitroblue tetrazolium/5-bromo-4-chloro-3-indolyl-phosphate
NC – North Carolina
ncRNA – non-coding ribonucleic acid
NE – Nebraska
NHEJ – non-homologous end-joining
nNOS – neuronal nitric oxide synthase
NO – nitric oxide
nt – nucleotide
OCT – optimal cutting compound
OH – Ohio
OR – Oregon
PBS – phosphate buffered saline
PCR – polymerase chain reaction
PD – Parkinson's disease
PFA – paraformaldehyde
Pip – phosphorodiamidate morpholino oligonucleotide-internalising peptide
PLS – primary lateral sclerosis
PMA – progressive muscular atrophy
PMO – phosphorodiamidate morpholino oligonucleotide
PNA – peptide nucleic acid
PPMO – peptide phosphorodiamidate morpholino oligonucleotide
PS – phosphorothioate
PSD – post-synaptic density
PSI-BLAST – position-specific iterative basic local alignment search tool
Pt – patient
qPCR – quantitative polymerase chain reaction
qRT-PCR – quantitative reverse transcriptase polymerase chain reaction
Rab-GEF – Rab-GTPase GDP/GTP exchange factor
RAN – repeat-associated non-ATG-dependent
RFLP – restriction fragment length polymorphism
RNA – ribonucleic acid
RP-HPLC – reversed-phase high-performance liquid chromatography
RVG – rabies virus glycoprotein
SCR – scrambled
SD – standard deviation
SDS – sodium dodecyl sulphate
siRNA – small interfering ribonucleic acid
SNP – single nucleotide polymorphism
SP – side population
SSC – saline sodium citrate
TA – tibialis anterior
TAE – tris base, acetic acid, ethylenediaminetetraacetic acid
tcDNA – tricyclo-deoxyribonucleic acid
TDP-43 – transactive response DNA-binding protein 43
TEM – transmission electron microscope/microscopy

TfR – transferrin receptor
TGF-β – transforming growth factor beta
TMR – tetramethylrhodamine
TNFα – tumour necrosis factor alpha
tRNA – transfer ribonucleic acid
TRPC – transient receptor potential cation
TSS – transcriptional start site
UK – United Kingdom
UTR – untranslated region
V_d – volume of distribution
VEGF – vascular endothelial growth factor
VLDL – very low density lipoprotein
WA – Washington
ZO – zonula occludens

Acknowledgements

Department of Physiology, Anatomy and Genetics, University of Oxford
Professor Matthew J. A. Wood – for supervision, mentorship and support
Dr Suzan M. Hammond – for support, help and advice relating to animal experiments
Dr Miguel A. Varela – for advice and help in ALS experiments and NAT experiments
Dr Yoshitsugu Aoki – for advice and help with ALS experiments and *in situ* hybridisation
Dr Tom C. Roberts – for advice on qPCR and methyl-DNA pulldown analysis
Dr Caroline Godfrey – for advice on animal experiments
Dr Graham McClorey – for help and advice with animal experiments
Dr Mary McMenamin – for help with BBB qPCR experiments
Dr Corinne Betts – for general help and advice
Dr Samir EL Andaloussi – for advice about PPMOs
Anna Coenen-Stass – for help with ddPCR experiments
Fiona Lee – for help with Western blotting and for helpful discussions about my work
Lee Ann Quek – for help with BBB qPCR experiments
All other members of the Wood laboratory – for general help and support
Dr Rebecca Fairclough – for help with fluorescent imaging of mice
Dr Michele Lufino – for help and advice relating to Southern blotting
Professor John Morris – for advice in interpreting electron microscopy images

Nuffield Department of Clinical Neurosciences, University of Oxford
Professor Kevin Talbot – for supervision, mentorship and support
Dr Ruxandra Mutihac – for supplying iPS motor neuron DNA

William Dunn School of Pathology, University of Oxford
Dr Errin Johnson – for training and supervision in electron microscopy

Molecular Genetics Laboratory, Oxford University Hospitals NHS Trust
Dr Melanie Proven – for training me in Southern blotting

Biomedical Services Building, University of Oxford
Level 2 NACWOs – for care of animals

MRC Laboratory of Molecular Biology, Cambridge
Dr Michael J. Gait – for collaboration in the PPMO project
Dr Fazel Shabanpoor – for helping design, synthesise and test PPMOs *in vitro*
Dr Liz O'Donovan – for synthesising PPMOs

Department of Medical Biochemistry and Biophysics, Karolinska Institute, Stockholm
Professor Christer Betsholtz – for hosting me in his laboratory for a month
Dr Maarja Mäe – for help with BBB tracer and immunofluorescence experiments
Dr Jennifer Hoffman – for help with BBB tracer and immunofluorescence experiments
Dr Guillem Genové – for performing ICV injections of PPMO

Green Templeton College, University of Oxford
Dr Caroline Pond – for general support and advice on thesis writing

This thesis would not have been possible without the support of many different people. I must first thank the Wellcome Trust for their generous support of my clinical DPhil fellowship, along with the Oxford programme directors Professors Rajesh Thakker and Paul Klenerman, who gave me the opportunity to carry out this project. I must also deeply thank my supervisors Professors Matthew Wood and Kevin Talbot, who have provided essential advice, mentorship and support throughout my time in Oxford and without whom none of this work would have been possible. In addition, my very great thanks goes to all the members of the Wood laboratory for their help, guidance and friendship. In particular, I want to thank Suzan Hammond for all her support and advice, particularly with regards to animal experiments. Yoshi Aoki and Miguel Varela also provided much help and advice with regards to the experiments relating to ALS. From the MRC Laboratory of Molecular Biology in Cambridge I would like to thank Mike Gait and the members of his laboratory and in particular Fazel Shabanpoor, who synthesised PPMOs and performed *in vitro* screening experiments of these compounds. From the Karolinska Institute in Stockholm I would like to thank Maarja Mäe, Jennifer Hoffman and Guillem Genové from the laboratory of Professor Christer Betzholz, who made it possible for me to obtain a significant amount of BBB data and also performed ICV injections of PPMO.

Statement

I, Andrew Douglas, hereby declare that the writing of this thesis has been entirely my own work and that, unless otherwise stated, the experiments documented herein were performed by me. The following procedures and experiments were performed by others:

Chapter 3:

- Injections of fluorescent tracer and subsequent perfusion at P1, P7 and P14 (Figure 3.7A-B) were performed by Dr Maarja Mäe and Dr Jennifer Hoffman, Karolinska Institute.

Chapter 4:

- PPMO synthesis and *in vitro* testing was done by Dr Fazel Shabanpoor, MRC Laboratory of Molecular Biology, Cambridge.
- Intravenous injections of selected PPMOs (RVG, Angiopep-2, Tet1, ApoE, BrApoE and BrPepC7) were performed by Dr Suzan Hammond, University of Oxford, and single intravenous injections of Pip6a-PMO were performed by Anna Coenen-Stass, University of Oxford (intraperitoneal injections, repeated intravenous injections of Pip6a-PMO and injections of Cy5-Pip6a-PMO, Cy5-PMO and THR-PMO were performed by me).
- Open field testing was performed by Dr Suzan Hammond, University of Oxford.
- *In situ* hybridisation of Cy5-Pip6a-PMO was performed by Dr Yoshitsugu Aoki and Dr Taeyoung Koo, University of Oxford (tissue sectioning and imaging performed by me).

Chapter 5:

- LNA gapmer design and the NAT knockdown experiment was performed by Dr Miguel Varela, University of Oxford (experimental data analysed by me).

Abstract

Genetic neuromuscular diseases remain essentially untreatable. Duchenne muscular dystrophy (DMD) is one such example and another is *C9ORF72*-related frontotemporal dementia/amyotrophic lateral sclerosis (c9FTD/ALS). Both these conditions may, however, be amenable to treatment with antisense oligonucleotide (ASO) compounds. Therapeutic ASO development for DMD is already in the clinical trial phase, while the applicability of ASO therapies in c9FTD/ALS remains to be clarified. No reliable method has yet been devised in order to target these compounds to the central nervous system following systemic administration. This thesis has investigated the ability to deliver therapeutic ASOs to the brain following systemic administration in the *mdx* mouse model of DMD. It has also investigated the molecular genetics of c9FTD/ALS to see whether ASO treatment may be a beneficial approach.

The integrity of the blood-brain barrier (BBB) was assessed in *mdx* mice. The *mdx* mouse BBB was found to be structurally intact by light and electron microscopy. Brain gene expression of BBB components was similar between *mdx* and wild-type mice. The barrier function of the *mdx* BBB was found to be largely equivalent to that of wild-type mice using systemically administered fluorescent tracers. Peptide-conjugated phosphorodiamidate morpholino oligonucleotides (PPMOs) were tested by intravenous injection in *mdx* mice. Pip6a-PMO was found to be the most active compound for inducing exon skipping in the brain. Fluorescent labelling of Pip6a-PMO showed body-wide distribution after systemic delivery, including increased accumulation in brain compared to unconjugated PMO, particularly in choroid plexus. c9FTD/ALS patient fibroblasts were analysed for *C9ORF72* promoter methylation, expansion size and gene expression. No clear relationship was found between *C9ORF72* expansion size and levels of promoter methylation or gene expression. An unexpected positive correlation was found between the degree of promoter methylation and gene expression. LNA-gapmer knockdown of a putative *C9ORF72* natural antisense transcript resulted in upregulation of gene expression.

These experiments suggest that the BBB is not severely defective in DMD. Furthermore, peptide conjugation of ASOs can be used to induce detectable exon skipping in brain tissue following systemic injection, suggesting that certain PPMOs may cross the BBB. Finally, ASOs may also provide a useful therapeutic approach in c9FTD/ALS, although further work will be needed in future to confirm this and to better characterise the disease.

Contents

Chapter 1:

Introduction

1.1. The burden of neuromuscular disease

Neuromuscular diseases are, for the most part, an unsolved clinical problem. As a group, they can affect any structure of the motor unit. This means that pathology may occur anywhere from the pyramidal neurons of the motor cortex, down through the pyramidal tracts of the internal capsule, brain stem and spinal cord, to the motor neurons of the anterior horn, and beyond into the peripheral nervous system affecting motor axons, the neuromuscular junction and ultimately skeletal muscle itself. With such a wide range of affected targets, neuromuscular disorders are by their very nature a heterogeneous group. A number of these conditions can be acquired through autoimmunity, infection and inflammation or as a consequence of neoplasia. However, the vast majority of neuromuscular diseases are inherited genetic conditions.

This thesis will focus on two specific neuromuscular conditions in particular. Both are genetic in origin but their resulting clinical phenotypes are very different. The first is Duchenne muscular dystrophy (DMD), an intrinsic disease of muscle that begins in childhood. The second is amyotrophic lateral sclerosis (ALS), typically a condition of late adulthood affecting the motor neurons. While the majority of ALS is not strictly genetic in the classical sense, a number of forms are indeed linked to genetic mutations. The particular type of ALS discussed here is one that also causes frontotemporal dementia (FTD) and which is linked to the gene *C9ORF72*.

While our understanding of the molecular basis of many neuromuscular conditions has grown rapidly over recent years, the same cannot be said of our ability to treat these conditions. It is the ineffectualness of current therapy for patients affected by these disorders which is the primary motivation for this thesis. It is hoped that this work might provide some small contribution towards the continued search for effective treatments in this area.

1.2. The blood-brain barrier

1.2.1. Introduction to the BBB

The human brain makes up on average just 2% of total bodyweight. It requires, however, roughly 15% of the body's cardiac output at rest (Segal, 2012). This disproportionate level of consumption reflects the high metabolic demands of neurons and glia within the CNS. Indeed, the brain utilises the equivalent of around 100 g of glucose every day. It is therefore something of a paradox of physiology that whilst the brain requires such a significant and constant supply of nutrition, it has at the same time the most highly selective and tightly regulated endothelial barrier to be found anywhere in the body, which separates its tissue from the blood and restricts the entry of solutes.

1.2.2. Functions of the BBB

The blood-brain barrier (BBB) exists for several reasons (Brady and Tai, 2012):

1. *Maintenance of the CNS electrochemical milieu*

   Its first and primary purpose is to allow the cells of the CNS to operate within a stable and tightly controlled electrochemical environment; one that is isolated from the constituent fluctuations of plasma. The ability of neurons to generate action potentials depends upon maintenance of the correct ionic gradients across their cell membranes. Since much of homeostasis depends upon this ability, it is worth the body investing in a sophisticated BBB.

2. *Barrier to toxins and pathogens*

   Secondly, by limiting which particular solutes may enter the brain, the BBB consequently protects the CNS from various toxins and pathogens that could otherwise gain entry from the plasma. Such toxins not only include exogenous molecules like drugs, poisons and venoms but also may comprise endogenously produced molecules such as neurotransmitters and certain plasma proteins.

3. *Nutrient transport to the CNS*

   Thirdly, the BBB itself may be said to constitute a transport system for nutrient delivery into the brain. Endothelial cells of the BBB express a range of transporters for basic intermediary metabolites as well as a number of receptors for larger molecules.

4. *Regulation of CSF composition*

   A fourth function of the BBB is shared with the other major fluid interface barrier within the brain, the blood-cerebrospinal fluid barrier (BCSFB), which operates at the choroid plexus within the ventricles. Together, the BBB and the BCSFB regulate the composition of CSF, since interstitial or extracellular fluid from the brain parenchyma drains into and thus contributes to the CSF.

1.2.3. Anatomy of the BBB

The arteries that supply the brain run along its exterior surface from whence they send multiple penetrating branches inwards toward the various internal structures. Arteries

have thick, muscular and elasticated walls designed to transport blood at speed and under high pressure. Any fluid exchange that occurs across arterial walls is therefore negligible. However, with continued divisions of arterial branches there is a gradual thinning of the vessel walls so that arteries give rise to arterioles, which themselves eventually give rise to thin-walled brain capillaries. It is capillaries that are particularly specialised for solute exchange and consequently it is at the capillary level that the BBB principally operates.

Mammalian capillaries fall into three broad groups depending on which tissue they supply (Ross and Pawlina, 2011). In liver, spleen and bone marrow, highly permeable sinusoidal (discontinuous) capillaries occur. In the liver, these have multiple open fenestrations and sieve plates in their endothelial cells and the sinusoids lack a surrounding basement membrane, allowing bulk flow of fluid and exchange of plasma constituents with interstitial fluid (Wisse et al., 1996). In the spleen, the endothelial cells of sinusoids are arranged as longitudinal rods separated by narrow slits and connected by junctional complexes at their tapered ends (Ross and Pawlina, 2011; Sarin, 2010; Barnhart and Lusher, 1979). A discontinuous net-like basement membrane surrounds the endothelium. This formation is highly permeable and allows entire blood cells to migrate in and out of splenic sinusoids. Bone marrow endothelium is also specialised for the egress of new blood cells into the circulation (Sarin, 2010).

Fenestrated capillaries occur in various endocrine and exocrine glands, the small intestine, the kidney glomerulus and notably also at the choroid plexus. The fenestrations vary in size in different tissues and some appear to be subtended by a thin electron-dense diaphragm. However, once again they generally allow unimpeded

exchange of material up to a certain size across the endothelium. If no such fenestrations are present then the endothelium is said to be continuous. This is the type present in brain but also in muscle, heart, lungs and skin.

Brain endothelium not only lacks fenestrations but also restricts the paracellular passage of solutes by way of tight junctions that are present at the edges of endothelial cells. These tight junctions link the endothelial cells together to form a continuous barrier that extends throughout the central nervous system save for a few specific regions. These brain areas that lack a fully formed BBB are the circumventricular organs (Benarroch, 2011). They comprise: the posterior pituitary gland which secretes ADH, the median eminence of the hypothalamus which secretes hormones into the hypophyseal portal system of the pituitary, the area postrema of the medulla which among other things senses emetic stimuli in the plasma, the pineal gland which secretes melatonin, the subfornical organ involved in osmotic regulation, the organum vasculosum of the lamina terminalis which is also involved in osmotic regulation and in controlling thirst, and the subcommisural organ whose function is not well understood but which appears to secrete glycoproteins into CSF in a structurally important way during development so as to allow normal CSF circulation (Sisó et al., 2010).

1.2.4. The neurovascular unit

The functional unit of the BBB is the neurovascular unit (Figure 1.1) (Daneman and Prat, 2015). This comprises the continuous brain endothelium surrounded by a basement membrane which itself contains pericytes and enveloping this are the endfoot processes

of astrocytes. Brain endothelial cells have unusually low levels of pinocytotic vesicles and indeed the number of such vesicles has been measured as seven times higher in skeletal muscle endothelium (Reese and Karnovsky, 1967; Coomber and Stewart, 1985). This relative lack of transcytosis further restricts the permeability of the BBB. Brain endothelial tight junctions comprise a number of different proteins including claudins, occludins and junctional adhesion molecules (JAMs) (Furuse, 2010). Claudin-5 in particular is highly expressed in CNS tight junctions and mice deficient for claudin-5 display size-dependent 'loosening' of the BBB (Morita et al., 1999; Nitta et al., 2003). Intracellularly, tight junction components are bound to adaptor proteins such as ZO-1, ZO-2 and ZO-3, which in turn link to the actin cytoskeleton via interactions with proteins such as cingulin (Abbott et al., 2010).

Pericytes are a type of mural cell that are quite hard to reliably distinguish from other types of mural cell such as vascular smooth muscle cells, with which they share some features (Armulik et al., 2011). Embedded within the basement membrane, pericytes send out processes that extend along the capillary wall and an individual pericyte's processes may span several endothelial cells. Direct contact between pericytes and brain endothelial cells is only made at discrete adhesion points known as peg-and-socket junctions, which are mediated by N-cadherin (Gerhardt et al., 2000). Pericytes have been shown to be important regulators of BBB function (Armulik et al., 2010). Pericyte-deficient mice have highly increased levels of transcytosis across brain endothelium and it has also been shown that pericytes not only regulate vesicular trafficking but also regulate tight junction formation in brain endothelial cells (Daneman et al., 2010).

Astrocytes are vital for effective BBB maintenance. They secrete Sonic hedgehog protein to signal to endothelial cells, which express the receptor Patched-1 (Alvarez et al., 2011). They also secrete angiogenic factors such as vascular endothelial growth factor (VEGF), which can disrupt BBB function in inflammatory conditions (Argaw et al., 2012). Other important astrocyte factors include Ang1, ACE-1, TGF-β and retinoic acid (Daneman and Prat, 2015). Aside from secreted factors, astrocytes also play a crucial role in regulating water transport within the CNS through expression of the water channel aquaporin-4 on their endfeet (Tait et al., 2008).

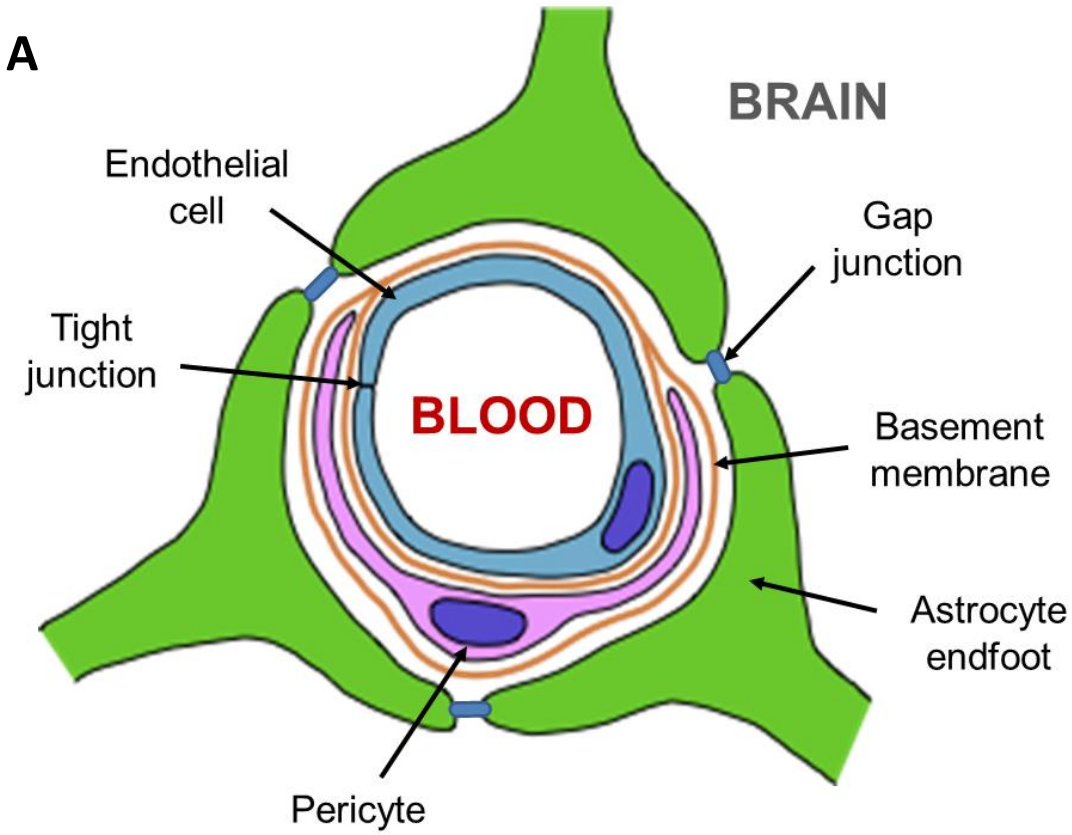

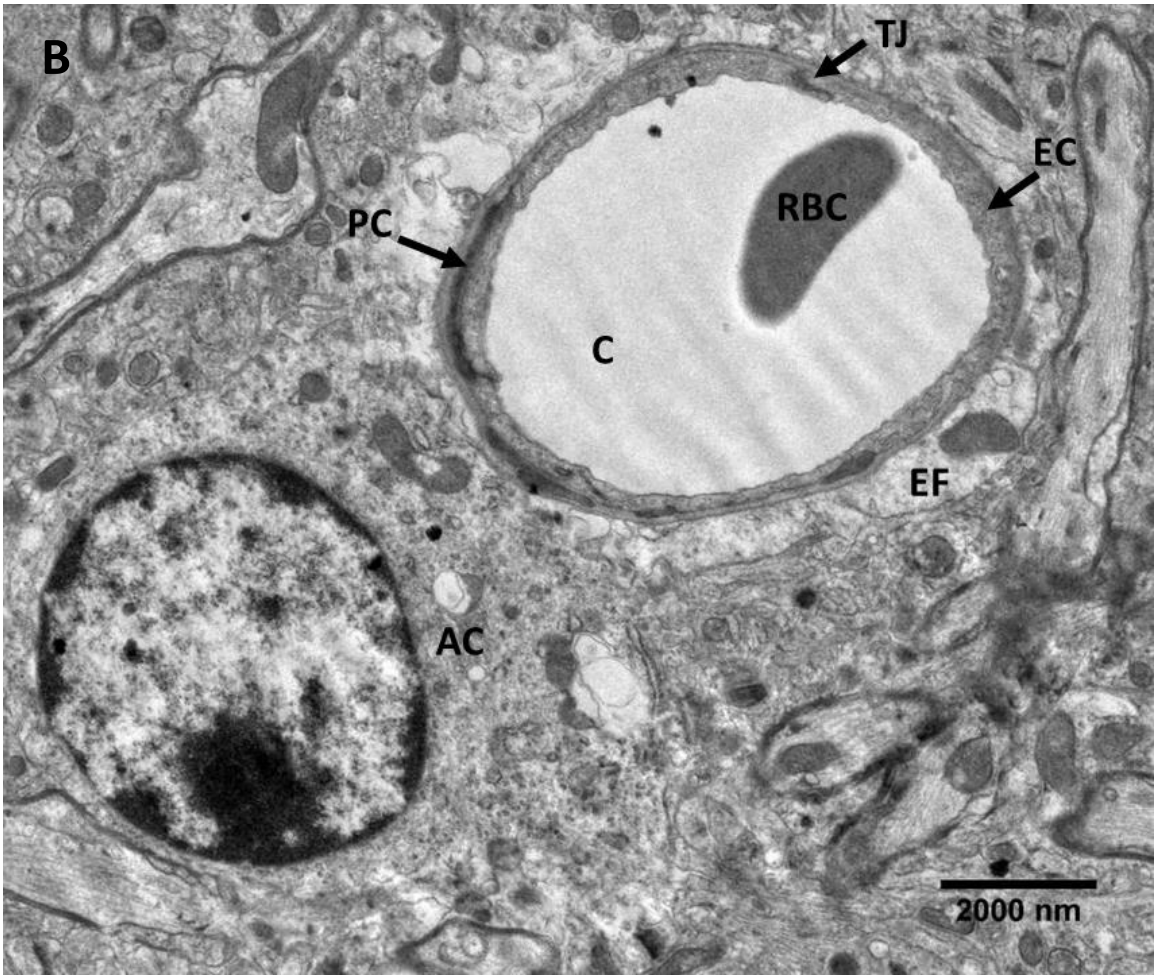

Figure 1.1. The neurovascular unit. **A.** Diagram of the neurovascular unit. Blood is contained within the brain capillary by brain endothelial cells, whose borders are sealed together by tight junctions. A basement membrane surrounds the endothelium and within this lie pericytes. Astrocyte foot processes (endfeet) invest the capillary and their edges are joined together by gap junctions. Neuronal processes (not shown) also make contact with the neurovascular unit. **B.** Transmission electron microscope image of a wild-type (C57BL/10) mouse brain capillary. An astrocyte (**AC**) can be seen in the lower left portion of the image. Its nucleus is clearly defined with an electron-dense rim of heterochromatin and deeply stained nucleolus. The astrocyte cytoplasm is decidedly pale and endfoot (**EF**) processes can be seen extending out from the cell body around the neighbouring capillary (**C**) to the top right. A red blood cell (RBC) lies within the lumen.

The capillary is formed by endothelial cells (**EC**) surrounded by a thin basement membrane just visible at this magnification. A darkly stained tight junction (**TJ**) can be seen towards the top of the capillary where two endothelial cell membrane surfaces meet. The thin dark structures interposed around the capillary lying within the basement membrane and closely apposed to the endothelium are pericyte (**PC**) processes.

1.2.5. Transport across the BBB

Passive diffusion of molecules across the BBB is limited to small lipophilic non-polar molecules (Punitha and Srivastava, 2013). Indeed, the BBB is highly effective and the endothelium therefore needs to express a host of specialised transporters in order to facilitate adequate nutrition and metabolite efflux for the CNS (Abbott et al., 2010). For the most part, such transporters deal with intermediary metabolites such as glucose, amino acids, free fatty acids, organic ions, nucleosides and so forth. There are also a number of transcytotic pathways mediated through caveolin-based endocytosis. Depending on the cargo, this can occur through either an adsorptive or receptor-mediated process. Larger macromolecules tend to be transported in this way, including transferrin, lipoproteins, insulin, leptin, IgG, TNFα and others (Abbott et al., 2010).

Drug delivery to the CNS is similarly hampered by the effectiveness of the BBB. However, a number of possible approaches may be considered (Chen and Liu, 2012). Tight junctions can, for example, be temporarily disrupted using physical means such as ultrasound, or through osmotic or chemical stimulus. However, such forceful approaches may not be best suited to repeated administration of drugs for chronic disease over time.

A particularly attractive option is therefore to utilise the endogenous transport mechanisms of the BBB, such as receptor-mediated transcytosis. A number of promising results have been reported in recent years, including the use of antibody-based monovalent molecular shuttles, and also microvesicles or exosomes expressing CNS-targeting peptides (Niewoehner et al., 2014; Alvarez-Erviti et al., 2011).

1.3. Duchenne muscular dystrophy

1.3.1. DMD the disease

DMD is a genetic muscle disease characterised by progressive muscle wasting and weakness. It is an X-linked condition and affects around 1 in 5000 live male births(Emery et al., 2015). Affected boys typically present to medical attention in early childhood, perhaps around 3-4 years of age, with proximal muscle weakness that impairs their ability to perform gross motor activities such as running and climbing (Emery, 2002). A classic medical sign of such proximal weakness in the lower limbs is Gowers' manoeuvre. This can be elicited by asking an affected child to raise himself off the floor into a standing position. In doing so, because of the weakness of his knee and hip extensor muscles, he must use his arms to climb up his own legs, gripping them to gain purchase in order to achieve a vertical position (Gowers, 1879). The natural history of DMD is one of gradual progression, with increasing weakness leading to loss of ambulation by the age of about 12 years. Patients thereafter remain wheelchair-bound. However, as weakness progresses, further loss of function ensues with increasing compromise of the respiratory muscles (Khirani et al., 2014). Cardiac muscle is also affected and this generally leads to a dilated cardiomyopathy becoming established (van Westering et al., 2015). In addition to this, around one third of affected boys have a variable degree of non-progressive cognitive impairment. Despite significant improvements in supportive care for DMD patients in more recent years, cardiac and respiratory failure remain the most frequent causes of mortality, with death tending to occur in early adulthood (Eagle et al., 2002).

DMD was first described by the English physician Edward Meryon in 1852 (Meryon, 1852). Later work by Guillaume Duchenne, who published a description of the same disease in 1868, led to his name becoming eponymously associated with the condition (Duchenne, 1868). Both Meryon and Duchenne noted in their descriptions that the nervous system of their patients appeared completely intact, while the muscle was abnormally broken down. It was also noted to be a familial condition where only male children were affected. Histologically, skeletal muscle displays a so-called dystrophic appearance, characterised by muscle fibre necrosis, regeneration, inflammation and fibrosis (Amato and Russell, 2008). The continued cycles of degeneration and regeneration lead to a picture of unequal muscle fibre size on muscle biopsy and over time there is also fibrofatty infiltration of muscle tissue. This leads to the characteristic rubbery pseudohypertrophy often seen in the calf muscles of affected patients.

In 1982, the gene responsible for DMD was found to be localised to chromosome locus Xp21 (Murray et al., 1982). Linkage to this region was initially suggested by reports of affected female patients with balanced translocations involving this locus (Lindenbaum et al., 1979; Zatz et al., 1981; Jacobs et al., 1981). Further linkage analysis using restriction fragment length polymorphisms (RFLPs) in a number of affected families confirmed and clarified this location more accurately (Davies et al., 1983). Subsequently, by the use of positional cloning, it was possible to determine candidate cDNA sequences for the gene (Monaco et al., 1986; Burghes et al., 1987; Koenig et al., 1987). Over time, the size and structure of the *DMD* gene was gradually elucidated and its genomic length found to be some 2.3 megabases (Mb) (Den Dunnen et al., 1989). The subsequent finding of a distant upstream brain promoter extended this measurement to around 2.4 Mb (Boyce et al.,

1991). This makes it the largest known gene in the human genome in terms of DNA length. This, however, does not hold true for the length of its coding region, which generates a full-length mRNA of only 14 kilobases (kb) and which codes for a 427 kilodalton (kD) protein of 3,685 amino acids. By comparison, the largest known human protein is titin, which is a 4,200 kD protein comprising 38,138 amino acids and which is translated from an mRNA some 82 kb long (Bang et al., 2001; Labeit and Kolmerer, 1995).

The *DMD* gene comprises 79 exons (Figure 1.2) (Roberts et al., 1993). The full-length mRNA is transcribed from three alternative promoters, named according to their predominant tissue specificities: B in brain, M in muscle and P in Purkinje cells of the cerebellum. Several further promoters, far downstream of the full-length transcriptional start sites, are also present and these generate protein isoforms of different lengths (Muntoni et al., 2003). Full-length dystrophin protein has a molecular weight of 427 kD and is thus designated as Dp427. The next longest isoform is Dp260, which has a promoter in intron 29 and which is principally expressed in retinal neurons (D'Souza et al., 1995). Dp140, whose promoter lies in intron 44, is found in the kidney and central nervous system (CNS) (Lidov et al., 1995). Dp116 is expressed in Schwann cells of the peripheral nervous system and its transcript begins in intron 55 (Byers et al., 1993). Dp71 is a short but ubiquitously expressed isoform, particularly abundant in the CNS, which has a promoter in intron 62 (Bar et al., 1990; Tadayoni et al., 2012). A further isoform, Dp40, has also been described (Tozawa et al., 2012). This appears to share the same promoter as Dp71 but lacks the common C-terminal portion of other isoforms. It has been shown to be present in the brain where it may play a role in presynaptic vesicle function.

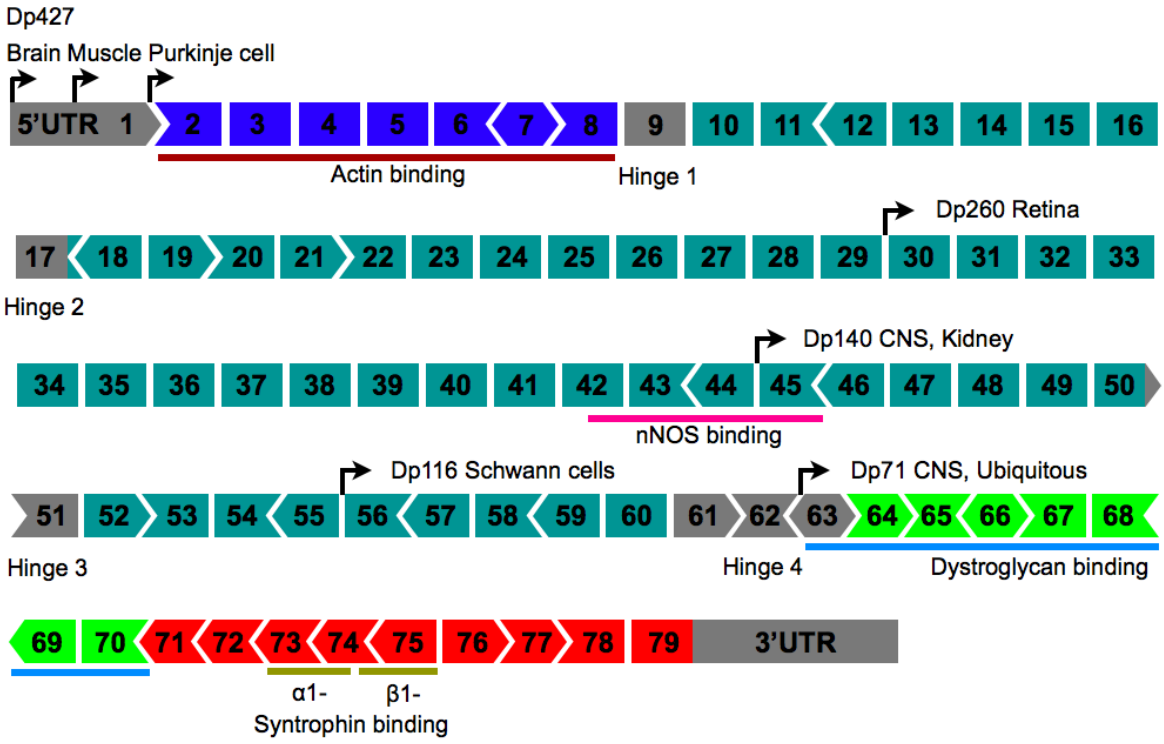

Figure 1.2. Exon structure of the *DMD* gene. A total of 79 exons make up the coding region for dystophin protein. At least seven alternative promoters exist, giving rise to the isoforms designated by their molecular weight: Dp427, Dp260, Dp140, Dp116, Dp71. These isoforms are differentially expressed in different tissues as shown. Another short isoform, Dp40, has also been described (not shown). This shares a promoter with Dp71. The exon-exon junctions of the gene coincide with codon positions 1, 2 or 3 as represented by the shaped ends of the exons in this diagram. The reading frame is maintained in the normal mRNA since the starting codon position of each exon neatly complements that of the preceding exon. Deletions of certain exons can, however, disrupt the reading frame. The colours shown here correspond to the coloured protein domains shown in Figure 1.3. The regions that correspond to various protein-binding domains are also indicated. Reproduced from Douglas and Wood, 2013.

1.3.2. Mutations in DMD

The majority of patients with DMD have deletion mutations that encompass one or more exons of the *DMD* gene. In most cases this results in a frameshift mutation once the remaining exons are spliced together as mRNA. Such mutations invariably generate premature termination codons downstream in the mutant transcript. Cellular recognition of transcripts containing premature STOP codons lead to them being targeted for degradation by nonsense-mediated mRNA decay (Buvoli et al., 2007). Some transcripts may be translated but the resulting truncated protein is dysfunctional. However, deletion of certain DMD exons does not in fact shift the reading frame. In these cases a functional protein can still be produced so long as the domains critical for its function are maintained (see section 1.3.3). Patients with such mutations generally have a much milder phenotype than that typically seen in DMD and they are usually diagnosed as having the allelic condition Becker muscular dystrophy (BMD) (Monaco et al., 1988). In BMD, onset of symptoms does not generally occur until either late childhood, adolescence or even adulthood. Progression of the disease tends not to be so severe and ambulation is normally maintained well into middle age or beyond (Bushby and Gardner-Medwin, 1993).

As an X-linked recessive condition, DMD is most often inherited from an unaffected female carrier. Having said this, carrier females can sometimes be affected by an X-linked cardiomyopathy (Hoogerwaard et al., 1999). In some cases, skewing of X chromosome inactivation can also result in phenotypically affected female DMD patients (Viggiano et

al., 2013). Around one third of DMD cases represent spontaneous *de novo* mutations (Edwards, 1986). Why there should be such a high new mutation rate is not entirely understood, although the sheer size of the gene may predispose it to such alterations. For a woman found to carry a *DMD* mutation, the *a priori* recurrence risk of having a subsequent affected pregnancy is 1 in 4 and the risk to a male pregnancy is 1 in 2. However, in families with an affected child where the mother has not been found to be a carrier, the risk of an affected pregnancy is still quoted as up to 1 in 20 (5%) (Bakker et al., 1989; van Essen et al., 1992). This risk increases to up to 20% recurrence if a male pregnancy is known to have inherited the same X chromosome haplotype as an affected sibling, although more recent studies suggest this may be an overestimate and that a recurrence risk of 8.6% may be more accurate (Helderman-van den Enden et al., 2009). This appreciably significant risk in apparently *de novo* families reflects the occurrence of parental gonadal mosaicism for *DMD* mutations.

Around 65-70% of DMD mutations are intragenic deletions of one or more exons, while about 11% are duplications of one or more exons (Bladen et al., 2015). The remaining 20% or so of mutations comprise point mutations (11% of the total), small deletions and insertions less than a whole exon in size, splice site mutations and, rarely, mid-intronic mutations. Mutations may occur at any point within the *DMD* gene. However, a major deletion hotspot exists between exons 45 and 55 where around 70% of deletions occur (Muntoni et al., 2003). A further hotspot lies between exons 2 and 19. The reason for there being such regional preferences for deletion mutations is not well understood. However, it is perhaps notable that exons 45 to 55 are somewhat clustered together within the *DMD* gene. In all, these 11 exons span a genomic region of around 341 kb

whilst being flanked on either side by the 248 kb of intron 44 and the 120 kb of intron 55. Such exon clustering may predispose the region to genomic disruption or rearrangement following DNA damage. Indeed, processes such as non-homologous end joining (NHEJ) have been suggested as possible mechanisms in the generation of *DMD* deletion mutations (Oshima et al., 2009). More generally, the high prevalence of deletions may be related to the unusually long introns present in *DMD*, which, although they range from just 107 bp (intron 14) up to 319 kb (intron 1 of the transcript for Dp427B), are on average around 30 kb in length.

1.3.3. Dystrophin protein

The *DMD* gene codes for the protein known as dystrophin (Hoffman et al., 1987). In muscle, dystrophin protein localises to the sarcolemmal membrane (Zubrzycka-Gaarn et al., 1988). Its principle role here is to provide a structural link between the internal cytoskeleton and the extracellular matrix. It achieves this through the interactions of its four principle protein domains (Figure 1.3) (Ervasti, 2007). The N-terminal domain of dystrophin contains two calponin homology modules and binds to cytoskeletal filamentous actin (F-actin). The central portion of the protein consists of a long coiled-coil region known as the rod domain that is composed of 24 triple helical spectrin-like repeats. This rod domain is interspersed by four hinge regions that are thought to confer flexibility to the protein. Just proximal to the C-terminal domain is a cysteine-rich domain. This binds to *β*-dystroglycan, a component of the dystrophin-associated glycoprotein complex (DAGC). *B*-dystroglycan lies within the sarcolemmal membrane and is associated with its partner *α*-dystroglyan, which is located at the extracellular face of

the membrane. Here it binds the extracellular matrix protein laminin, which anchors the DAGC in place. Thus, by providing this link to F-actin, dystrophin anchors the contractile cytoskeleton of muscle to the extracellular matrix. This is vital in order to transmit contractile force between fibres and to maintain muscle fibre integrity under the tension and sheer stresses placed upon them by contraction (Davies and Nowak, 2006).

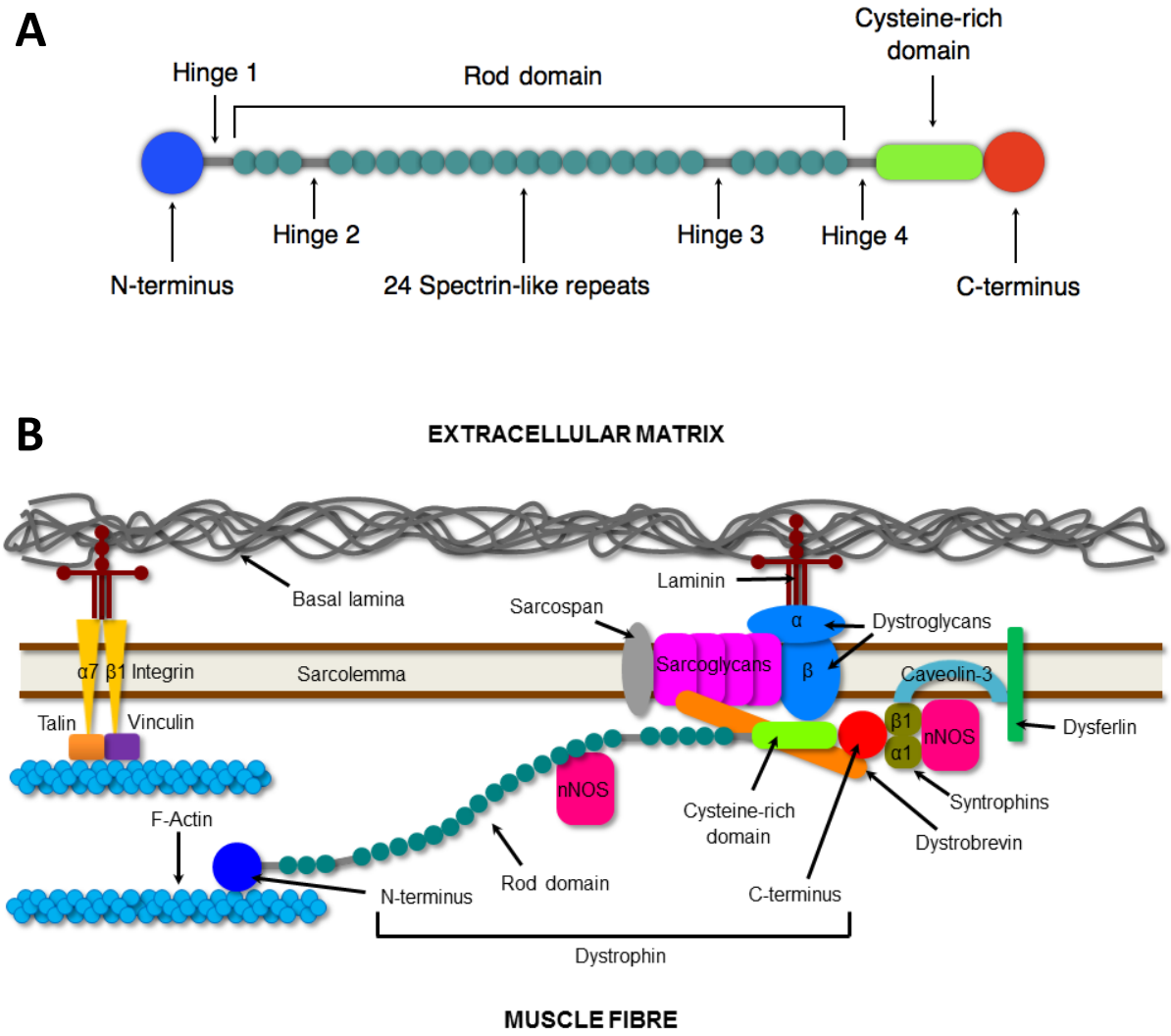

Figure 1.3. Dystrophin protein and the dystrophin-associated glycoprotein complex (DAGC). A. Dystrophin protein comprises four distinct domains which play different functional roles. Proximal to the C-terminus lies a cysteine-rich domain and between this

and the N-terminus lies the rod domain consisting of 24 spectrin-like repeats linked by four hinge regions. **B.** The N-terminus of dystrophin binds F-actin while the cysteine-rich domain near the C-terminus binds to *β*-dystroglycan, part of the DAGC. This provides a physical link between the cytoskeleton, the sarcolemma and the extracellular matrix. Modified from Douglas and Wood, 2013.

1.3.4. Pathogenesis of DMD

In DMD, a lack of dystrophin leads to fragility of muscle fibres. Boys with DMD have significantly elevated levels of muscle enzymes such as creatine kinase (CK) in their blood. This reflects damage to muscle fibres with subsequent release of their contents into the plasma. A number of different contributing factors have been implicated or at least suggested in the pathogenesis of this damage (Deconinck and Dan, 2007).

1. *Mechanical damage*

   The mechanical role of dystrophin between cytoskeleton and sarcolemma is the best studied of its functions. It is known that sustained eccentric contraction ability is greatly reduced in DMD and this is associated with muscle damage (Moens et al., 1993). Furthermore, exercise is known to induce damage in DMD muscle and leads to increased muscle membrane permeability in dystrophin-deficient *mdx* mice (Lim et al., 2004; Sandri et al., 1997). Consequently, high-resistance exercise is not recommended for DMD patients (Bushby et al., 2010b).

2. *Calcium dysregulation*

Dystrophin-deficient muscle appears to demonstrate increased calcium influx through mechanosensitive voltage-independent TRPC calcium channels (Vandebrouck et al., 2002). This can activate proteases such as calpains, leading to increased proteolysis and subsequent cell death (Tidball and Spencer, 2000).

3. *Nitric oxide deficiency*

Nitric oxide (NO) is a potent vasodilator. In muscle it is synthesised by the enzyme neuronal NO-synthase (nNOS), which is part of the DAGC (Figure 1.3). Loss of dystrophin results in mislocalisation of DAGC components including nNOS (Brenman et al., 1995). This reduction in nNOS function could contribute to DMD muscle ischaemia and damage (Sander et al., 2000).

4. *Gene dysregulation*

Loss of dystrophin is likely to have a downstream effect on the expression and regulation of a number of different genes and their products. Dystrophin may, for example, play a role in mechanotransduction signals regulating muscle growth (Goldspink, 1999).

5. *Inflammation*

Inflammatory infiltrates are found within dystrophic muscle in DMD and an overall picture of chronic inflammation is evident (Porter et al., 2002). While such inflammation is thought to be initiated in response to dystrophic muscle fibre damage, activation of inflammatory and immune cells can lead to the perpetuation of cellular damage (De Paepe and De Bleecker, 2013). The beneficial

effect of glucocorticoid therapy, which suppresses the inflammatory response, reflects the importance of inflammation in DMD pathogenesis.

1.3.5. DMD and the brain

Cognitive impairment of DMD patients was noted by Duchenne himself in his original description of the disease (Duchenne, 1868). Around one third of affected boys have significant cognitive deficit and it has been estimated that, as a population, the DMD patient cohort has an IQ distribution one standard deviation below the average (Cotton et al., 2001). Verbal IQ tends to be affected to a greater degree than performance IQ in DMD patients and younger boys in particular appear to have greater deficits in verbal reasoning and processing (Cotton et al., 2005). The reason for this effect has not been fully elucidated and indeed the role of dystrophin within the CNS is not yet well understood.

However, while the main focus of DMD research has necessarily been focussed on skeletal muscle, some CNS-related studies have been performed. Dystrophin is found at the post-synaptic densities (PSDs) of cortical neurons in the CNS as well as in Purkinje cells of the cerebellum (Lidov et al., 1990; Uchino et al., 1994b, 1994a; Kim et al., 1992). The short Dp71 dystrophin isoform has also been found expressed in glia as well as in neurons and in particular it is found to be associated with the perivascular astrocyte endfeet that contribute to the blood-brain barrier (Blake et al., 1999; Haenggi et al., 2004). Of perhaps particular interest is the finding that neurons lacking full-length dystrophin in the hippocampus, cerebellum and amygdala fail to correctly localise γ-

aminobutyric acid ($GABA_A$) receptor subunits, which are usually found in cell membrane clusters (Knuesel et al., 1999; Sekiguchi et al., 2009). Dystrophin may therefore be necessary for the correct clustering and stabilisation of inhibitory $GABA_A$ receptors at postsynaptic membranes. This deficit has also been shown to be associated with functional electrophysiological disturbances, namely a reduction in heterosynaptic long-term depression (LTD) of neurotransmission and an enhancement of homosynaptic LTD (Anderson et al., 2004, 2010). Since these processes relate to synaptic plasticity and are important in information processing, learning and memory, they may partially explain some of the intellectual difficulties experienced by DMD patients.

The degree of cognitive deficit it DMD is not related to the severity of muscle disease. However, it is known that *DMD* mutations toward the 3' end of the gene tend to be associated with more significant cognitive dysfunction (Bushby, 1992; Desguerre et al., 2009). It is thought that this may be related to the increasing number of shorter dystrophin isoforms that are affected the further 3' in the gene a mutation lies. In particular, mutations affecting Dp140, which is expressed in brain, and Dp71, also highly expressed in brain and in other tissues, are associated with greater degrees of cognitive impairment (D'Angelo et al., 2011; Chamova et al., 2013; Daoud et al., 2009).

Some uncertainty exists as to whether dystrophin deficiency leads to structural brain abnormalities and previous studies have yielded inconsistent results (Anderson et al., 2002). A post-mortem examination of the CNS in 21 DMD patients found no gross macroscopic abnormalities of the brain or spinal cord, however some histological changes were noted such as gliosis and evidence of neuronal loss in a small number of cases (Dubowitz and Crome, 1969). All but one of these patients had a normal brain weight. A

Japanese study of 30 clinically diagnosed DMD patients (including two females) reported mild cerebral atrophy on computed tomography (CT) scan in two thirds of patients (Yoshioka et al., 1980). However, another study from the UK found no significant difference in relative ventricular size between 15 DMD boys and controls on magnetic resonance imaging (MRI) (Rae et al., 1998). Then again, a French study of 15 DMD boys found mental impairment in all cases and cortical atrophy on CT scan (Septien et al., 1991). In animals, a study of the cortico-spinal architecture of dystrophin-deficient mice suggested a lower neuronal density and smaller cell size with altered morphology within the CNS (Sbriccoli et al., 1995). However, a detailed anatomical study in dystrophin-deficient *mdx* mice found no gross structural or histological brain abnormalities but reported an increased density of axodendritic inhibitory synapses and increased PSD length within part of the CA1 hippocampal region (Miranda et al., 2009). Recently, a quantitative MRI study of 30 DMD boys and 22 age-matched controls found a significantly reduced total brain volume, smaller grey matter volume and alterations in white matter microstructure in DMD patients (Doorenweerd et al., 2014).

The cognitive impairment in DMD is non-progressive, suggesting either some kind of developmental insufficiency or else a persistent incapacity of function. Whether it is the former or the latter that is the case has potentially profound implications for the would-be treatment of DMD-related mental retardation. If a developmental block is present, leading to incomplete structural or functional pathways within the brain, then corrective treatment is likely to be very hard indeed. However, if the cognitive impairment can be wholly explained by a simple deficit of dystrophin protein in either neurons and/or glia, the therapeutic potential may be considerably greater.

1.3.6. The *mdx* mouse

In 1984 a fortuitous discovery provided the DMD research community with a molecularly robust mouse model of the disease (Bulfield et al., 1984). This spontaneously generated *mdx* mutant line was found to have a C>T transition in exon 23 of the *Dmd* gene (c.3185C>T), which creates a premature termination codon instead of coding for glutamine and thus acts as a nonsense mutation (Sicinski et al., 1989). Since its appearance, the *mdx* mouse has become the most widely used laboratory animal model for studying DMD. However, as with any animal model, it has its limitations owing to interspecies differences between mice and humans. One obvious difference is the apparent severity of the disease, which in mice seems comparatively mild, notwithstanding the confines of laboratory observation.

Mice affected by the Dmd^{mdx} mutation live a lifespan only slightly shorter than normal and their overall muscle function does not appear to be significantly impaired until older age, although dystrophic pathology does increase with age (Pastoret and Sebille, 1995). Notably, *mdx* mice undergo a period of extensive and widespread muscle fibre necrosis from 20 days of age, which is not outwardly detrimental to their development or health and which is compensated for by a highly active and apparently almost inexhaustible propensity for muscle fibre regeneration inherent in mice (Tanabe et al., 1986). Why the disease should run such a different course in mice compared to boys has not been fully elucidated. However, a number of theories have been suggested, aside from the obvious differences in stress placed on muscle tissue in such differently sized organisms (Partridge, 2013). One such theory relates to the different pattern of muscle growth in

mice. Mouse satellite cells contribute to muscle growth in the first three weeks of life through a *Pax7*-dependent programme of serial asymmetrical cell divisions that raises the number of myonuclei in myofibres to adult levels over the course of 21 days (White et al., 2010). Thereafter, muscle growth occurs through a regenerative programme of satellite cell proliferative expansion, for example in response to injury. In mice, these two patterns of growth are temporally separated. In humans, however, myofibre myonuclear addition continues throughout childhood up until adulthood and this process therefore occurs in parallel and contemporaneously to the regenerative patterns associated with muscle injury, as in DMD (Partridge, 2013).

While the muscular phenotype of the *mdx* mouse is not severe, it has been shown to have an altered neurocognitive behavioural profile. The phenotype includes impaired passive avoidance learning, whereby *mdx* mice are less good than controls at learning to avoid a behaviour that results in an unpleasant stimulus (Muntoni et al., 1991). There is also impaired long-term recognition of objects (though not short-term recognition) and impairment of long-term spatial memory using a shortened water maze training protocol (Vaillend et al., 2004). However, when a more extended training protocol was used, no abnormalities were seen in *mdx* mice evaluated by Morris water maze, which tests hippocampus-dependent spatial learning (Sesay et al., 1996). In addition, *mdx* mice demonstrate an exaggerated defensive freeze response to danger, suggesting enhanced anxiety perhaps relating to dystrophin deficiency in the amygdala (Sekiguchi et al., 2009). However, free exploration of surroundings and choice of light/dark area is no different to controls in unthreatened *mdx* mice (Vaillend et al., 1995).

1.3.7. Therapeutic approaches for DMD

Current therapies available to DMD patients are generally limited to supportive care, improvements in which have led to significant improvement in survival, particularly when implemented through a multidisciplinary setting (Eagle et al., 2002; Bushby et al., 2010a). Systemic glucocorticoid therapy is as yet the only available pharmacological treatment able to slow disease progression and indeed such treatment prolongs ambulation by 2 to 5 years, as well as improving cardiorespiratory function and reducing the need for scoliosis surgery (Moxley et al., 2010). However, whilst steroids are able to achieve some degree of temporary benefit, this is somewhat tempered by the numerous side effects of long-term corticosteroid use such as weight gain, osteoporosis, propensity to diabetes, thinning of the skin, hypertension and behavioural disturbance (Angelini, 2007). Indeed, the mechanism of therapeutic action of corticosteroids in DMD is not fully understood. Part of this may be explained by the anti-inflammatory actions of steroids, which would be predicted to decrease the inflammatory response to muscle fibre necrosis in DMD, leading to a reduction in endomysial fibrosis. However, it may also be mediated through an anabolic effect or by inhibition of proteolysis and reduced muscle breakdown (Rifai et al., 1995; Sklar and Brown, 1991). Recently, a novel steroid-mimicking compound known as VBP15 has been developed in order to try to retain the therapeutic anti-inflammatory effects of glucocorticoids while reducing the unwanted side-effect profile of such drugs (Heier et al., 2013).

Gene therapy approaches for DMD have previously suffered from a number of technical constraints. Skeletal muscle presents a significant challenge in terms of gene

replacement therapy because of the sheer bulk of tissue involved. Indeed, skeletal muscle accounts for some 30-40% of total body mass (Janssen et al., 2000). Furthermore, the multinucleate nature of individual muscle fibres demands a highly efficient gene delivery vector if complete coverage of all muscle nuclei is to be achieved. The second major hurdle to overcome is the vast size of the *DMD* gene itself. No *in vivo* delivery vector currently in common use can hope to package a 2.4 Mb insert and even a 14 kb cDNA is beyond the capacity of most. In order to circumvent this problem, attempts have been made to reduce the size of insert required, taking advantage of the maintained functionality of mutant dystrophin proteins with internally deleted portions of their rod-domains. The products of such internally truncated *DMD* constructs have been termed mini- and microdystrophins and promising results have been obtained with this approach using adeno-associated virus (AAV) vectors in both *mdx* mice and also the dystrophic dog model of DMD (Foster et al., 2008; Koo et al., 2011). Effective systemic delivery remains an issue, however recent ongoing trials of systemic therapy in DMD dogs look promising. Another important limitation of viral vector gene delivery is the issue of immune response. AAV vectors tend to stimulate the generation of neutralising antibodies as well as a T cell response to capsid epitopes (Ploquin et al., 2014). This limits the ability to perform more than one treatment with a given vector serotype. In addition, many individuals already possess immunity to certain AAV serotypes through having encountered these previously in the environment.

Another therapeutic strategy under investigation is muscle stem cell therapy (Konieczny et al., 2013). The resident stem cells of muscle are satellite cells. These are able to divide and differentiate into myoblasts in response to muscle injury, repairing damaged and

torn muscle fibres. In DMD, however, the requirement for chronic ongoing fibre regeneration leads to satellite cell exhaustion. Being able to reseed a patient's muscles with a healthy satellite or myoblast cell pool could therefore help repair damaged DMD muscle. However, trials of myoblast transfer in DMD patients failed to achieve significant levels of dystrophin restoration (Mendell et al., 1995; Miller et al., 1997). More recently, transfer of highly proliferative satellite cells has been tested in *mdx* mice with some success (Cerletti et al., 2008). However, a relative limitation of such approaches lies in the poor migratory capabilities of satellite cells and myoblasts following injection. For this reason, other cell types able to contribute to muscle tissue following systemic delivery have been investigated. These include bone marrow-derived side population (SP) cells, mesenchymal cells and CD133+ cells (Bachrach et al., 2004; Dezawa et al., 2005; Benchaouir et al., 2007). Pericyte-derived mesangioblasts have also been found to achieve muscle engraftment and dystrophin production after intra-arterial delivery (Tedesco et al., 2011). As with gene therapy strategies, cell-based therapies for muscle disease must also contend with the issue of achieving an adequate dosage to effect significant change in such an abundant target tissue.

Aside from gene and cell replacement strategies, another approach known as STOP codon read-through has been employed specifically for point mutation base substitutions in the *DMD* gene that generate premature termination codons. In these cases, since the reading frame of the gene is maintained, inducing the patient's ribosomes to continue translation through the premature STOP codon is enough to restore protein production. Early studies found that aminoglycoside drugs such as gentamicin were able to induce STOP codon read-through (Singh et al., 1979; Palmer et al., 1979). This effect was also

demonstrated in *mdx* mice, however it did not translate into highly positive trials in patients (Barton-Davis et al., 1999; Wagner et al., 2001; Politano et al., 2003). More recently, a novel drug that binds to the ribosomal 60S subunit, known as PTC124 (ataluren), was developed and shown to work in *mdx* mice (Welch et al., 2007). However, phase II trials in DMD boys (ClinicalTrials.gov identifier NCT00847379) did not demonstrate an improvement in primary outcome measure (30 m increase in 6-minute walk test over placebo-treated controls). Despite this, the compound (now known as translarna) has been given conditional approval by the European Medicines Agency (Haas et al., 2015).

Before discussing exon skipping, one further therapeutic strategy for DMD is important to note. This involves the upregulation of an autosomal homologue of dystrophin known as utrophin, which is encoded by the *UTRN* gene. Its structure is highly similar to dystrophin and in mature muscle it is found principally at the neuromuscular and myotendinous junctions (Tinsley et al., 1992; Khurana et al., 1991). Furthermore, in developing and regenerating muscle it appears to be expressed at the sarcolemma in place of dystrophin and to substitute for its function (Takemitsu et al., 1991; Helliwell et al., 1992). Overexpression of utrophin in muscle, to levels still significantly less than endogenous levels seen in lung and kidney, has been shown to rescue the dystrophic phenotype in *mdx* mice (Tinsley et al., 1998). A small molecule compound (SMT C1100) has been identified which is able to transcriptionally activate the *UTRN* promoter and increase utrophin protein production in muscle (Tinsley et al., 2011). This compound has been taken forward into clinical trials. As a treatment strategy, utrophin upregulation has the

benefit of being potentially applicable to all patients with DMD and SMT C1100 is in addition an orally administered drug.

1.3.8. Exon skipping for DMD

The furthest advanced of the genetic therapies currently in progress for DMD is exon skipping (Koo and Wood, 2013). The goal of exon skipping in DMD is to convert an out-of-frame mRNA into an in-frame mRNA by means of splicing out a specifically targeted exon from the pre-mRNA transcript. In effect, at the RNA level, this converts what is a DMD mutation into a BMD one. This can be achieved through use of specifically designed oligonucleotide sequences that hybridise to and mask either a splice site or a splicing enhancer sequence from a selected exon. By preventing the access of splicing factors to these key sequence elements, the spliceosome machinery is encouraged to ignore the targeted exon's splice sites and instead uses the next available sites on the transcript, which tend to be those of the following exon. The targeted exon is thus spliced out of the mature transcript. Such RNA-targeted therapy has the effect of turning a frame-shifted transcript incapable of producing functional protein into an in-frame one that can once again be translated into a functional, though internally shortened, dystrophin protein. So long as both the *DMD* mutation and the exon being skipped do not interfere with the critical functional regions of the gene (i.e. both lie within the rod domain) then the internally truncated dystrophin protein should retain useful function.

The exon reading frame structure of *DMD* is conserved between humans and mice. In reference to Figure 1.1 it can be seen that skipping of certain exons (such as exon 23) will

not alter the overall reading frame. This means that should exon 23 harbour a nonsense mutation, as is the case in the *mdx* mouse, it may safely be skipped without disrupting the frame, thereby restoring dystrophin production. Conversely, skipping of other exons (such as exon 51) does alter the reading frame. Therefore, should a patient have a deletion of exon 50, for example, skipping exon 51 will restore the correct reading frame and allow dystrophin to be made (Figure 1.4).

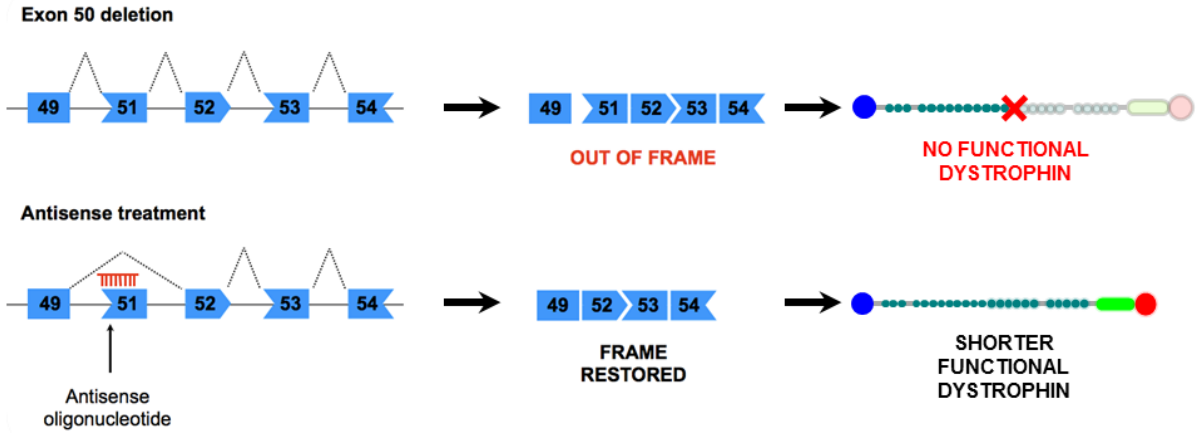

Figure 1.4. Exon skipping for DMD. A deletion of *DMD* exon 50 will lead to a frameshift in the spliced transcript, which is unable to code for functional dystrophin. Hybridisation of an antisense oligonucleotide complementary to an exonic splice enhancer sequence in exon 51 of the pre-mRNA causes the exon to be spliced out. In the presence of the exon 50 deletion, skipping of exon 51 restores the reading frame and allows production of an internally truncated but functional dystrophin.

It has been estimated that up to some 55% of DMD patient mutations could be amenable to treatment by exon skipping (Bladen et al., 2015). This figure includes 80% of deletions. Indeed, antisense oligonucleotides have been designed and tested *in vitro* for skipping of

every *DMD* exon apart from the first and last (Wilton et al., 2007). However, clinical development has so far concentrated on those exons likely to provide treatment for the greatest proportion of patients. Skipping of exon 51 can potentially treat around 13% of DMD patients, while skipping of exon 45 applies to 8.1%, exon 53 to 7.7% and exon 44 to 6.2% (Aartsma-Rus et al., 2009). The applicability of skipping of other individual exons beyond this continues to fall. This has spurred research into ways of increasing the applicability of exon skipping to larger groups of patients. In particular, the idea of multiple exon skipping encompassing the entire DMD mutation hotspot from exons 45 to 55 has been proposed (Béroud et al., 2007). This approach could treat up to 63% of deletion patients and is highly attractive, since BMD patients with such exon 45-55 deletions have an especially mild phenotype. Using a cocktail of 10 oligonucleotides, skipping of these exons has been demonstrated in mice following intravenous injection (Aoki et al., 2012).

1.4. Antisense oligonucleotide therapies

1.4.1. Introduction to antisense oligonucleotides

Antisense oligonucleotides (ASOs) are short lengths of nucleotides (nt) or nucleotide analogues up to around 30 nt in length that are designed to be complementary in sequence to their target. They can be constructed from a wide range of different chemistries depending on their intended purpose, since different cellular pathways can be activated or inhibited by different kinds of oligonucleotide molecule. One of the great advantages of ASOs as therapeutic agents is their sequence specificity. By utilising the unique sequence properties inherent in the genome, ASOs have the potential to provide an unparalleled degree of targeting with minimal off-target effects. This high-precision specificity of ASOs also opens the door to the possibility of truly personalised genetic medicine, since the technology lends itself to being able to discriminate between individual mutations. As a form of gene therapy, ASOs have some further advantages. One common concern about conventional gene therapy approaches involving gene replacement, particularly with transgene integration, is that the process cannot be 'undone'. ASOs target RNA rather than DNA and do not alter the genomic sequence. This means therapy can be titrated to need, modified and completely stopped if necessary, providing a high degree of control. Furthermore, ASOs do not suffer from the risks of insertional mutagenesis seen with integrative gene therapies.

1.4.2. Chemistry and design of ASOs

Therapeutic ASOs must satisfy several requirements in their design in order to be effective. Among these are the following:

1. *Target specificity*

   As previously mentioned, sequence specificity is key to ensuring minimal off-target effects while maximising an ASO's effect on the RNA target of interest.

2. *Localisation to the correct cellular compartment*

   An ASO designed to affect splicing (such as a phosphorodiamidate morpholino) must traffic to the nucleus, where splicing occurs. Similarly, an ASO designed to induce RNase H cleavage of RNA:DNA hybrids (such as a locked nucleic acid gapmer) can only act once transported to the nucleus. Conversely, an ASO seeking to utilise the RNA interference pathway of Dicer cleavage (such as an siRNA or miRNA mimic) needs to remain in the cytoplasm.

3. *Nuclease resistance*

   Although many ASOs are designed to activate specific nucleases such as RNase H, they must still be resistant to other exo- and endonucleases that could otherwise degrade them before they reach their site of action.

4. *Favourable pharmacokinetics and pharmacodynamics*

   As with other drugs, an ASO that is cleared rapidly from the circulation is unlikely to achieve a prolonged period of therapeutic activity. It would therefore be

desirable to deliver ASOs in a form that ensures an adequate plasma half-life and allows good biodistribution.

5. *Non-toxicity*

   Clearly any clinically usable ASO must have an acceptable toxicity profile. Unwanted effects must not outweigh the potential therapeutic benefits of the compound.

6. *Effective target tissue delivery*

   An ideal ASO would distribute solely to the tissue of interest, maximising the effect of a given dose and reducing the possible side effects on other tissues. While such tropism may be possible in some cases, a well-designed ASO should at least distribute well through the body and include the desired target tissue.

A growing number of different ASO chemistries are available (Deleavey and Damha, 2012; Dias and Stein, 2002; Saleh et al., 2012). Importantly, these chemistries all maintain the correct structural conformation required for complementary Watson-Crick base-pairing to take place. However, their backbone structures can be significantly different from normal RNA or DNA (Figure 1.5). One of the earliest designs was the phosphorothioate (PS) modification. This involves a substitution of sulphur for oxygen in the phosphate group of the standard sugar-phosphate backbone. Replacing the non-bridging oxygen with sulphur creates chirality around the phosphorus atom, generating two possible stereoisomers, Rp and Sp. The Sp isomer is nuclease-resistant, while the Rp isomer remains sensitive (Eckstein, 2002). Furthermore, the PS linkage remains sensitive to RNase H and induces cleavage when bound to RNA. This is thought to be because a

PS/RNA heteroduplex adopts a conformation in-between that of B-form and A-form DNA, which approximates to the conformation of a DNA/RNA heteroduplex, the substrate of RNase H (Noy et al., 2008).

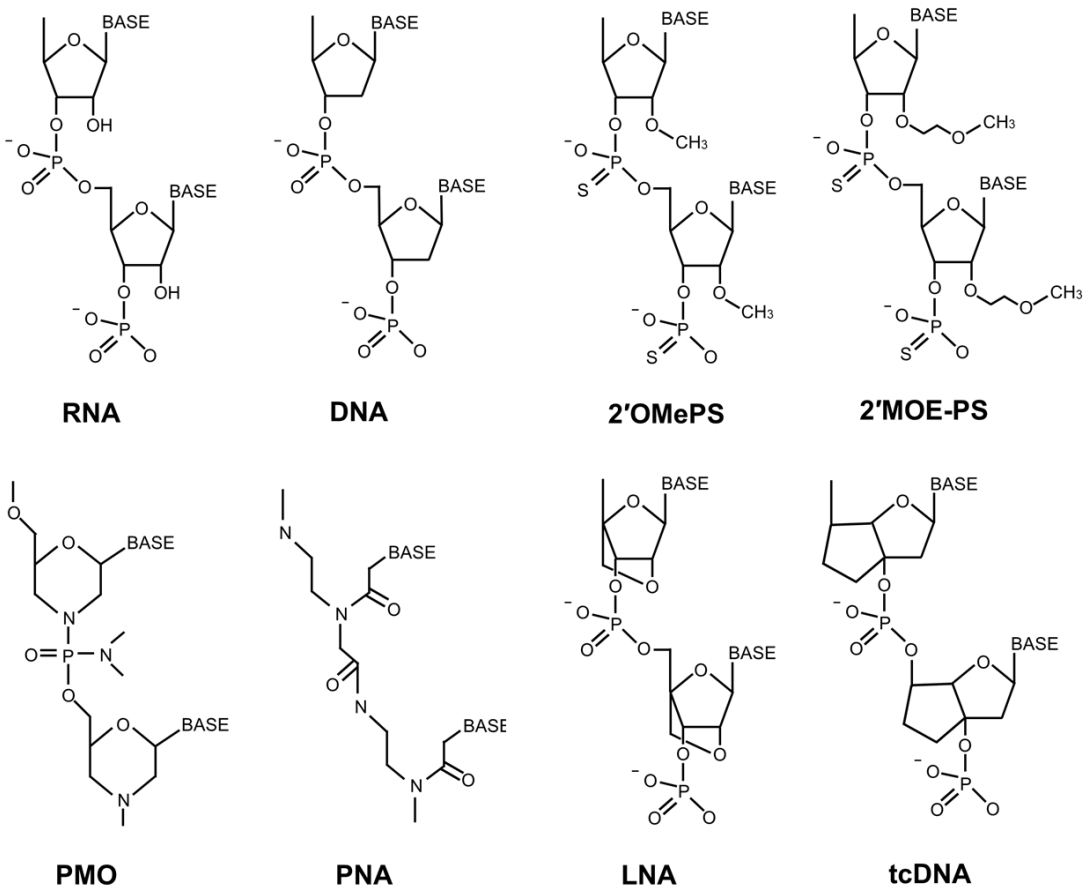

Figure 1.5. Examples of several different oligonucleotide chemistries. RNA and DNA are shown for comparison. 2'-O-methyl phosphorothioate (2'OMePS) resembles RNA but adds a methyl group at the 2'-hydroxyl position and substitutes sulphur for oxygen to form a phosphorothioate rather than a phosphate backbone linker. 2'-O-methoxyethyl phosphorothioate (2'MOE-PS) is similar to 2'OMePS but has a methoxyethyl rather than a methyl modification. Phosphorodiamidate morpholino (PMO) uses a morpholine ring rather than a sugar and it has phosphorodiamidate rather than phosphodiester bond

linkers. Peptide nucleic acid (PNA) replaces the sugar-phosphate backbone with one made of repeating aminoethylglycines with acetyl linkers to the nucleobases. Locked nucleic acid (LNA) uses an extra carbon linker between the 2'-O and the 4' carbon of RNA. Tricyclo-DNA (tcDNA) has an additional ring in its structure.

Locked nucleic acid (LNA) is an RNA analogue that employs a methylene bridge to join the 2'-OH group to the 4' carbon of ribose. This physically restricts the conformation of the molecule in a way that approximates the A-form structure and promotes RNA binding (Braasch and Corey, 2001). This increased binding affinity, together with nuclease resistance, makes LNA especially useful in combination with other nucleotide chemistries such as in LNA gapmers or mixmers, where a single ASO is made from a combination of both nuclease resistant LNA nucleotides and other nuclease sensitive nucleotides (Wahlestedt et al., 2000). Tricyclo-DNA (tcDNA) is another sugar-modified chemistry where the deoxyribose ring of DNA has been augmented by a further carbonyl ring. As with LNA, the conformational restriction in tcDNA structure introduced by the additional ring helps to raise its binding affinity and affords it nuclease resistance (Renneberg et al., 2002; Ittig et al., 2010). tcDNA ASOs have been shown to achieve widespread *in vivo* efficacy in preclinical exon-skipping studies in *mdx* mice (Goyenvalle et al., 2015).

Target cleavage is not the aim of exon skipping and therefore applicable oligonucleotide chemistries need to resist cleavage. For PS oligonucleotides this can be achieved by modifications to the 2'-hydroxyl group that encourage a more dsRNA-like A-form structural conformation when bound to RNA (Deleavey and Damha, 2012). One of the major chemistries in current clinical trials for DMD exon skipping utilises an added methyl

group at this position, forming 2'-O-methyl phosphorothiate (2'OMePS) (Flanigan et al., 2014; Voit et al., 2014). An extension of this resistance is achieved by addition of a methoxyethyl group to form 2'-O-methoxyethyl phosphorothioate (2'MOE-PS), which has been successfully tested as a splicing modulatory agent in mouse models of spinal muscular atrophy (Hua et al., 2010, 2011). An important feature of PS ASOs is that they retain the negative charge of their backbone, which greatly aids their solubility, allows for complexation with cationic lipids or proteins, and facilitates an extended plasma half-life through binding to plasma proteins (Bennett and Swayze, 2010).

Phosphorodiamidate morphlino (PMO) is another chemistry resistant to nuclease cleavage that is in clinical trials for DMD (Mendell et al., 2013). It uses a six-membered morpholine ring moiety in place of ribose and has phosphorodiamidate instead of phosphodiester linkers. An important difference from PS is that PMO molecules are uncharged. Peptide nucleic acid (PNA) is another uncharged chemistry. It substitutes the entire backbone with repeating N-(2-aminoethyl)glycine units with carbonyl linkages holding the nucleobases (Nielsen, 2010).

1.4.3. Delivery of ASOs

A major challenge to the clinical use of ASOs as therapies is the issue of drug delivery. For DMD and other muscle diseases this is especially true as the compound needs to effectively reach all skeletal muscles throughout the body. There is therefore a requirement for effective systemic ASO delivery. Current clinical trials of 2'OMePS and PMO for DMD exon skipping have utilised subcutaneous and intravenous administration

respectively (Flanigan et al., 2014; Voit et al., 2014; Mendell et al., 2013). For 2'OMePS, studies in mice have shown that subcutaneous injection achieved better pharmacokinetic and pharmacodynamic properties than intravenous injection (Heemskerk et al., 2010). PMO, on the other hand, has been reported to demonstrate similar pharmacokinetic profiles whether given orally, intravenously, intraperitoneally, subcutaneously or by other routes (Amantana and Iversen, 2005). However, in terms of efficiency of exon skipping in muscle, best systemic results for PMO have been obtained with intravenous injection (Lu and Wu, 2012).

For both chemistries, significant accumulation has been observed in liver and kidneys after systemic delivery (Heemskerk et al., 2010; Amantana and Iversen, 2005; Amantana et al., 2007). PMO does not appear to be toxic, even when tested at extremely large intravenous doses such as 3 g/kg in mice (Wu et al., 2010). The majority of compound is excreted essentially unchanged in the urine (Amantana and Iversen, 2005). 2'OMePS has been associated with some mild side effects during clinical trials, such as subcutaneous injection site reactions and non-progressive, reversible proteinuria (Flanigan et al., 2014). Both chemistries appear, however, to be generally well tolerated.

The mechanism of uptake of ASOs remains a matter of ongoing research. The negative charge of certain ASOs such as 2'OMePS should prevent them from directly interacting with the cell's negatively charged phospholipid membrane. However, charged ASOs can be taken up via a process called gymnosis (Stein et al., 2010). This process has subsequently been shown to occur for 2'OMePS and in fact also for PNA, even though these molecules are uncharged (Torres et al., 2011). Gymnotic mechanisms are themselves a matter of some study and the process may in fact represent a form of

receptor-mediated endocytosis, since nucleic acids are known to be internalised by surface glycoproteins known as scavenger receptors (Pearson et al., 1993; Saleh et al., 2006). Scavenger receptors have many ligands including low density lipoprotein (LDL), phospholipid and bacterial lipopolysaccharide, all of which are polyanionic, a feature shared with nucleic acids.

At least two other theories exist about ASO uptake into muscle. It is known that dystrophic muscle appears to have increased membrane permeability (Allen and Whitehead, 2011). One view is that dystrophic muscle fibres in fact have a 'leaky' membrane because of physical damage or tears accumulated in the absence of dystrophin. This could facilitate both release of cytoplasmic enzymes like creatine kinase into the plasma as well as the entry of ASOs into myofibres. However, an alternative view is that elevations in calcium influx in dystrophic muscle activate phospholipase A2 and increase reactive oxygen species abundance. These in turn lead to sarcolemmal damage. Interestingly, a recent study has shown that PMO is preferentially taken up by regenerating muscle fibres rather than by mature fibres (Aoki et al., 2013). This supports the idea that it is the property of regeneration rather than the absence of dystrophin that may be facilitating PMO entry.

1.4.4. Peptide conjugation of PMO

An important part of ongoing ASO research has been to investigate improved ways of delivering these therapeutics to the cells and tissues of interest. One option to improve uptake is to complex or conjugate ASOs with carrier compounds. These may take the

form of proteins, cationic lipids, nanoparticles and cationic polymers (Malik and Roy, 2011). Much work has focussed on so-called cell-penetrating peptides (CPPs), which are short cationic or amphipathic peptides able to facilitate delivery of various cargoes across the cell membrane (Margus et al., 2012). Two of the earliest examples of CPP were the Tat protein domain from human immunodeficiency virus type 1 (HIV-1) and the penetratin domain of the *Drosophila melanogaster* protein antennapaedia (Dupont et al., 2011). The mechanisms of CPP uptake are not fully understood but are likely to involve endocytosis, although direct translocation across the cell membrane has also been suggested (Lundin et al., 2008; Rydström et al., 2011). Scavenger receptors have also been implicated in this process (Ezzat et al., 2012).

PMO is comparatively straightforward to chemically conjugate to peptides because of its lack of charge. Arginine-rich peptides in particular have been found to significantly increase uptake efficiency (Moulton et al., 2004). An early form of peptide-PMO (PPMO) conjugate known as B-PMO was able to restore up to 30% of dystrophin protein expression in heart muscle following repeated intravenous injections in *mdx* mice (Jearawiriyapaisarn et al., 2008). The same compound was also able to improve muscle pathology and strength and reduce cardiac failure in mice (Wu et al., 2008). Further refinement of these arginine-rich CPPs led to the development of a range of PMO-internalising peptide (Pip) compounds (Ivanova et al., 2008). These peptides comprise a hydrophobic core flanked by two arginine-rich cationic hydrophilic domains. One of the most effective iterations of this design has been the Pip5 and Pip6 series of peptides (Yin et al., 2011; Betts et al., 2012). Notably these PPMOs have shown particularly effective dystrophin restoration in cardiac muscle, even after a single intravenous injection.

Pip CPPs have not been designed with a specifically targeted receptor in mind. However, it is possible to use peptides to select for tissue specificity to some extent using techniques such as peptide phage display. This has been tried for muscle and a 7-amino-acid-long peptide called muscle-specific peptide (MSP) was found to augment the muscle efficacy of low-dose B-PMO when combined as a B-MSP-PMO fusion peptide (Yin et al., 2009). Such results support the feasibility of utilising similar tissue-specific peptides for other organs, including the brain.

1.5. Amyotrophic lateral sclerosis

1.5.1. An introduction to ALS

Amyotrophic lateral sclerosis (ALS), also known as motor neuron disease (MND), is a term used to describe a pattern of neurodegenerative disease that primarily affects the motor neurons (Swinnen and Robberecht, 2014). Like the term 'muscular dystrophy', ALS is not a single disease but rather comprises a group of distinct motor neuron disorders of differing though likely interlinked aetiologies, which ultimately lead to a similar and overlapping neurodegenerative pathway. Onset is typically in late adulthood with increasing weakness and muscle wasting. There are usually signs of lower motor neuron involvement such as muscle fasciculation but upper motor neurons are also typically involved, which can lead to a mixed clinical picture of both spastic and flaccid paralysis in different muscle groups, increased or diminished tendon reflexes and upward or downward going plantar responses. Progression of the disease tends to be relentless and survival is usually around 3-5 years after diagnosis, with respiratory failure again accounting for the majority of deaths. European incidence of ALS is 2.16 per 100,000 per year and the lifetime risk is around 1 in 350 for men and 1 in 400 for women (Logroscino et al., 2010; Johnston et al., 2006).

The phenotype of ALS is highly variable with multiple patterns of onset depending on which motor neuron group is predominantly affected (Swinnen and Robberecht, 2014). Among the main types of presentation are: classic limb-onset ALS, bulbar-onset ALS, primary lateral sclerosis (PLS) with pure upper motor neuron signs, and progressive muscular atrophy (PMA) with pure lower motor neuron involvement (Kiernan et al.,

2011). While a classic spinal onset of signs and symptoms is the most common presentation, 25% of patients (a greater proportion of whom tend to be women) have bulbar onset with dysarthria, dysphagia and tongue fasciculation (Turner et al., 2010; Kiernan et al., 2011). The rarest phenotype (more commonly affecting men) is that of respiratory muscle onset (Chiò et al., 2011).

Our molecular understanding of ALS is not as far advanced as it is for the muscular dystrophies, which of course are themselves far from being completely understood. Nevertheless, significant advances have been made in recent years and a growing number of genes are now known to contribute to this condition. The majority of ALS remains apparently sporadic in nature. However, around 10% of cases are familial (Renton et al., 2014). The first gene identified as being linked to ALS was *SOD1*, coding for Cu/Zn superoxide dismutase (Rosen et al., 1993). This is a ubiquitous enzyme involved in the scavenging of free radicals. Mutant SOD1 protein becomes misfolded, ubiquitinated and tends to aggregate (Basso et al., 2006). Mutations in *SOD1* account for only between 10-20% of familial ALS. Further genes were subsequently identified such as *FUS*, *TARDBP*, *ALS2* (alsin), *SETX* (senataxin), *VAPB*, *OPTN* (optineurin) and others (Robberecht and Philips, 2013). How mutations in these diverse genes all lead to a similar spectrum of disease remains uncertain. However, some common themes can be discerned in these genes' functions, such as RNA binding and processing, protein turnover and degradation, and cytoskeletal or cytoplasmic transport.

1.5.2. *C9ORF72*-related ALS and FTD

In late 2011, two back-to-back papers published in Neuron reported that a hexanucleotide GGGGCC repeat expansion in the *C9ORF72* gene at chromosome locus 9p21 was associated with a large proportion of familial amyotrophic lateral sclerosis (ALS) and frontotemporal dementia (FTD) (Renton et al., 2011; DeJesus-Hernandez et al., 2011). Subsequent studies have shown that this expansion, located at the 5' end of the *C9ORF72* gene between two alternative first exons, is responsible for up to 40% of familial ALS and up to 25% of familial FTD (Majounie et al., 2012). Since the discovery of this association, it has become common to refer to this spectrum of disease related to *C9ORF72* as a single entity: c9FTD/ALS.

Patients with c9FTD/ALS tend to exhibit a characteristic disease phenotype that differs somewhat from other forms of ALS. Such features include a younger age of onset, a shorter survival time and a tendency towards behavioural disturbance (Turner et al., 2013). A more frequent bulbar onset has also been reported (Millecamps et al., 2012). There is also likely to be a clear family history of neurodegenerative disease, since the disease is inherited in an autosomal dominant fashion, though with some reduced penetrance. Brain imaging of c9FTD/ALS patients often shows predominant temporal lobe atrophy and pathological findings are also highly distinctive (Simón-Sánchez et al., 2012). As with most other forms of ALS, TDP-43 inclusions are seen in the brain but they are distributed in a very different and pathognomonic pattern in *C9ORF72* expansion carriers. This is especially true in hippocampus and cerebellum, where instead of finding

TDP-43 inclusions colocalised with p62 and ubiquitin, TDP-negative inclusions are found that stain positive for p62 (Al-Sarraj et al., 2011).

The function of *C9ORF72* is as yet unknown; hence its provisional name defining it as 'chromosome 9 open reading frame 72'. It did not at first sight appear to have homology to any other known gene. However, further bioinformatic analysis of its sequence has revealed similarity to the "differentially expressed in normal and neoplasia" (DENN) protein family (Zhang et al., 2012; Levine et al., 2013). These are Rab-GTPase GDP/GTP exchange factors (GEFs) that play an important role in membrane trafficking. Rab-GEFs activate Rab proteins, several of which have been implicated in the autophagy pathway (Nishida et al., 2009; Longatti et al., 2012; Zoppino et al., 2010). Indeed, one study has implicated *C9ORF72* in endosomal regulation and has linked its function to normal autophagosome formation (Farg et al., 2014).

The gene itself encompasses a region some 23 kb long at 9p21.2. It is comprised of 11 exons with two alternative non-coding first exons. Three alternative mRNA transcripts have been described (Figure 1.6). The nomenclature for these transcripts is somewhat inconsistent within the literature and so they are referred to here in the following manner. '1a' refers to the longest transcript, beginning at exon 1a and with a mature mRNA 3339 nucleotides (nt) long (NM_001256054). 'Δ1a' refers to the short transcript (mRNA 1901 nt) which begins with a truncated version of exon 1a (80 rather than 158 nt) and ends with a shortened exon 5 (NM_145005). '1b' refers to a transcript that starts at exon 1b just downstream of the hexanucleotide repeat and which has an mRNA of 3244 nt (NM_018325). Both transcripts 1a and 1b code for identical proteins of 481 amino

acids since their first exons are non-coding. Δ1a codes for a shorter protein of 222 amino acids.

Analysis of the protein sequence by PSI-BLAST has identified that C9ORF72 is a highly conserved protein present not only across vertebrate phyla but also in diverse organisms such as *Entamoeba histolytica*, *Rhizopus delemar* (a fungus), *Metaseiulus occidentalis* (a predatory mite) and *Caenorhabditis elegans* (Levine et al., 2013). This analysis did not, however, find any C9ORF72 homologues in plants, insects or in most fungi. The gene appears to have been conserved as a single block with highly conserved residues distributed throughout its length. This suggests that the entire protein as a single unit is required for its functional role. Tissue-specific expression analysis has been undertaken in mice, looking at the mouse *C9ORF72*-orthologue *311004O21Rik* tagged with a *LacZ* reporter gene (Suzuki et al., 2013). This study identified expression in multiple brain regions including hippocampus, dentate gyrus, striatum, thalamus, brainstem nuclei, cerebellum and cortex. White matter regions did not show any expression and in the spinal cord expression was highest in the ventral horn. Interestingly, expression was specifically seen in neurons but not in astrocytes or microglia. Expression was also noted in germinal centres of the spleen and in the testes but was not seen in heart, lung, liver, kidney or skeletal muscle (*tibialis anterior*).

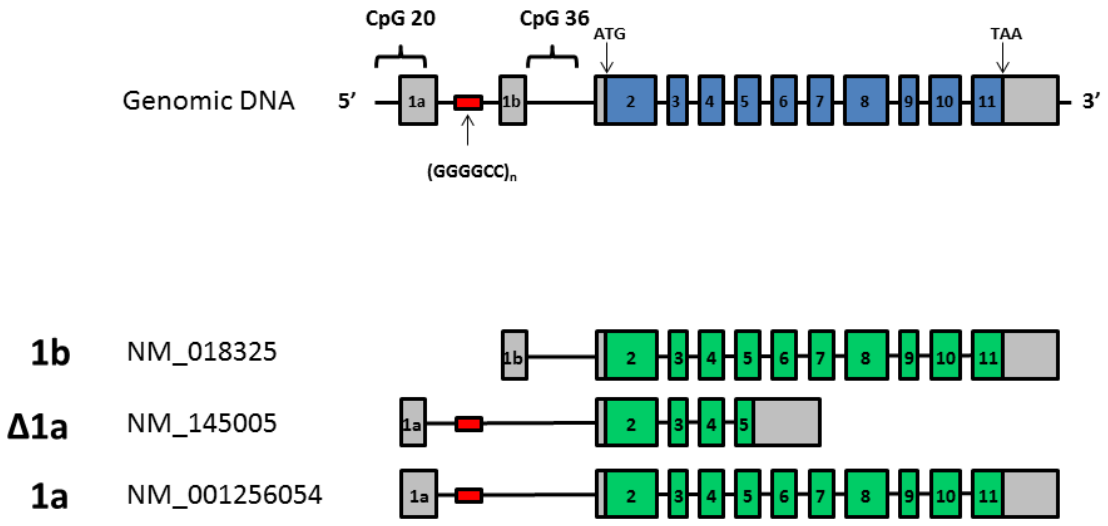

Figure 1.6. Diagram illustrating the layout of the *C9ORF72* gene and its three annotated alternative transcripts (introns not shown to scale). The gene comprises 11 exons but has two alternative first exons, which lie either side of the GGGGCC repeat (shown in red) and which all form part of the 5' untranslated region (UTR) of their respective transcripts (5' and 3' UTRs denoted in grey). The first exon of the shorter transcript (Δ1a) is attenuated, being 78 nucleotides shorter than in transcript 1a. Two CpG islands lie either side of the repeat region, the 5' one has 20 CpG dinucleotides while the 3' one has 36.

1.5.3. c9FTD/ALS pathogenesis

The mechanism by which the GGGGCC microsatellite expansion leads to disease remains to be determined. However, a number of theories have been put forward as plausible explanations (Figure 1.7). Three of these have received particular attention: toxicity through the accumulation of RNA foci, toxicity through repeat-associated non-ATG-dependent (RAN) translation of dipeptide repeats, and gene loss-of-function.

1. *RNA toxicity*

   Several groups have reported the existence of RNA foci in cells derived from *C9ORF72* expansion patients (DeJesus-Hernandez et al., 2011; Gendron et al., 2013; Donnelly et al., 2013; Almeida et al., 2013; Sareen et al., 2013). Using RNA-FISH it has been possible to demonstrate such foci within the nuclei of cells carrying the expansion. Furthermore, both sense and antisense foci appear to form (Gendron et al., 2013). It is postulated that these repeat-containing foci can bind to and thereby sequester important cellular proteins, thus disrupting vital cellular processes and ultimately leading to motor neuron degeneration.

2. *RAN-translation*

   An alternative mechanism involves translation of the repeat-containing RNA into a variety of dipeptide repeats. This appears to occur through so-called RAN translation and interestingly, both sense and antisense-encoded dipeptide sequences have been identified in central nervous tissue from affected patients (Ash et al., 2013; Mori et al., 2013b; Gendron et al., 2013). RAN-translation has also been reported to occur in other repeat expansion disorders such as fragile X tremor-ataxia syndrome (FXTAS) and myotonic dystrophy type 1 (Todd et al., 2013; Zu et al., 2011).

3. *Loss of function*

   A further possibility is that the *C9ORF72* gene becomes silenced in the presence of the repeat, leading to haploinsufficiency. A number of studies have reported a reduction in gene expression in expansion carriers. DeJesus-Hernandez et al.

(2011) found a 50% reduction in transcript 1b expression in frontal cortex and also in derived lymphoblasts, while a milder reduction (38% in frontal cortex and 34% in lymphoblasts) was seen for transcripts 1a and Δ1a combined. However, no difference in protein expression was seen. A Flanders-Belgian cohort study similarly found a 50% reduction in frontal cortex expression of two of the alternative *C9ORF72* transcripts tested (1b and Δ1a) (Gijselinck et al., 2012). This study also performed cDNA sequencing of an exon 8 region spanning a silent coding SNP and showed that it was specifically transcripts from the expanded allele that were reduced. However, no differences in protein expression level in the brain could be detected. Interestingly this same study reported highly variable and thus inconclusive *C9ORF72* expression in patient-derived lymphoblast lines.

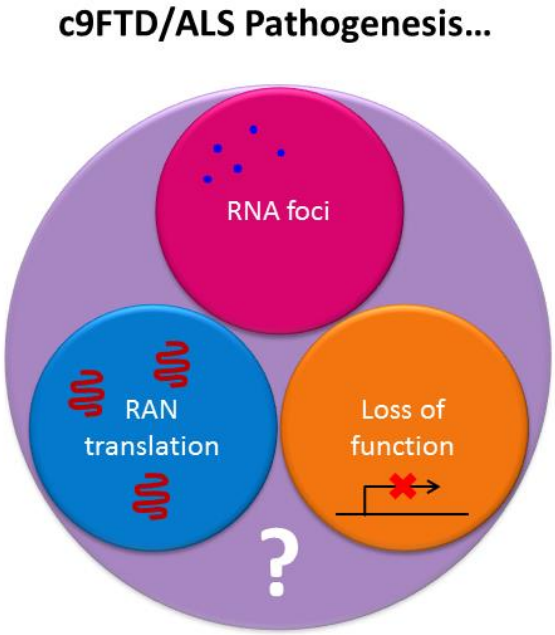

Figure 1.7. Possible mechanisms of c9FTD/ALS pathogenesis. The GGGGCC repeat has been found to form RNA foci within the nuclei of neurons from affected patients. These may bind and sequester important cellular factors. Repeat-associated Non-ATG (RAN) translation into aggregating dipeptide repeats has also been reported in tissue from affected patients. The build-up of such peptides may cause toxicity. Haploinsufficiency through epigenetic gene silencing is another possible cause of disease. Alternatively, some as-yet unidentified mechanism may be responsible.

It has been reported that a CpG island just upstream of the *C9ORF72* repeat is methylated in expansion carriers (Xi et al., 2013). This DNA methylation anlaysis was mainly carried out on blood DNA but similar findings were also seen in frontal cortex and cervical spinal cord from 7 expansion carrier patients. In this study, expansion carriers also showed decreased *C9ORF72* expression, except for one individual who only had a short 48-repeat-long expansion. However, although the upstream CpG island was methylated, the other CpG island lying 3' of the repeat and which is in fact longer than the upstream CpG island, was not found to be methylated in either patients or controls. Neither was it determined whether or not the repeat itself was methylated. Another study looked at histone methylation in the *C9ORF72* promoter region (Belzil et al., 2013). Expansion-carrying c9FTD/ALS patients were found to have histone trimethylation at the *C9ORF72* promoter in frontal cortex and cerebellum, with trimethylation of H3K9, H3K27, H3K79 and H4K20 in particular. This study also noted globally reduced *C9ORF72* transcript expression in these c9FTD/ALS patient tissues.

It has been suggested that antisense oligonucleotide (ASO) therapies could be used to treat this disease, for example by knocking down the expanded mutant transcript (Fernandes et al., 2013). However, the applicability of this approach will depend upon understanding the predominant mechanism by which the expansion causes disease. If a pure loss-of-function mechanism is to blame, then simply knocking down the mutant transcript is unlikely to prove therapeutically beneficial. On the other hand, if a toxic RNA gain-of-function effect predominates, then allele-specific ASO knockdown could be the ideal solution. A third possibility exists. This concerns knocking down not the usual sense transcript of *C9ORF72* but instead the antisense transcript that has been reported at this locus by several studies (Gendron et al., 2013; Mori et al., 2013b). Natural antisense transcripts (NATs), while so far only studied in a minority of genes, are an increasingly recognised phenomenon (Varela et al., 2012). They act as regulatory non-coding RNAs that can downregulate their sense transcript partners through epigenetic transcriptional gene silencing. Such an RNA-based gene regulatory system lends itself ideally to oligonucleotide-based intervention and indeed it has been shown that oligonucleotide-induced knockdown of a NAT can lead to corresponding transcriptional upregulation of a specific gene (Modarresi et al., 2012). The fact that antisense transcription has been reported for *C9ORF72* raises the intriguing possibility that knockdown of this NAT will allow selective upregulation of the gene, potentially ameliorating any loss-of-function deficit.

The questions this thesis hopes to answer

This has been a lengthy introduction as the scope of topics covered in the following chapters is quite diverse. Nevertheless, it is hoped that a unifying theme can be discerned in this work and that the different chapters seek to complement each other. The following overarching questions will be addressed in this thesis:

The blood-brain barrier in *mdx* mice

Is there a defect in the BBB in Duchenne muscular dystrophy and if so, of what nature?

Treating *mdx* mice with peptide-conjugated antisense oligonucleotides

Can systemic oligonucleotides successfully cross the BBB using peptide conjugation?

Investigation of *C9ORF72* molecular genetics and the applicability of ASO therapies

Are C9ORF72 expression, methylation and expansion size related and could the disease be treatable with antisense oligonucleotides?

Chapter 2:

Materials and methods

2.1. Chapter 3 methods

2.1.1. Animals

C57BL/10ScSnOlaHsd (BL/10) mice were obtained from Harlan Laboratories, Bicester, UK, and *mdx* mice (C57BL/10ScSn-*Dmd*^{mdx}/J) from Jackson Laboratories, Bar Harbor, ME. Both strains were maintained as breeding colonies both at the Biomedical Services Building, University of Oxford, and also at the Department of Medical Biochemistry and Biophysics, Karolinska Institute, Stockholm. Animals had access to food and water *ad libitum* at all times. All procedures in the UK were performed in accordance with the Animals (Scientific Procedures) Act 1986 and procedures in Sweden were carried out in accordance with the Stockholm North Ethical Committee for Animal Research.

2.1.2. Fluorescent tracer accumulation assay

Mice aged from P14 to 3-4 months (Figure 3.7 C-F) were assayed in Oxford as follows ($n \geq 3$ per group and both males and females were used). Lysine-fixable Alexa Fluor 555 cadaverine (cat. no. A-30677, Life Technologies, Paisely, UK) tracer was made up in 0.9% NaCl at a concentration of 5 µg/µl and administered by intraperitoneal injection at a dose of 20 µg/g. Lysine-fixable tetramethylrhodamine (TMR) 10 kD dextran (cat. no. D-1868, Life Technologies) was also used at a concentration of 25 µg/µl in 0.9% NaCl and injected

intraperitoneally at 100 µg/g in P14 mice and intravenously in 8-week-old mice. Cadaverine tracer was left to circulate for 2 hours (3 hours for TMR 10 kD dextran), after which time the mice were terminally anaesthetised by pentobarbitol overdose followed by intracardiac perfusion with ice-cold phosphate-buffered saline (PBS). Successful systemic circulation of tracer was confirmed by examination of internal organs and by observing discolouration of the urine. Brain tissue was removed, weighed and homogenised in 600 µl PBS 1% Triton-X100 using a Precellys tissue lyser (Bertin Technologies, Montigny le Bretonneux, France). Homogenised samples were centrifuged at 4°C for 15 minutes at full speed in a benchtop centrifuge and 150 µl of supernatant loaded in duplicate onto a black 96-well calorimetric plate for analysis of fluorescent signal using a Wallac plate reader (Perkin Elmer, MA). Fluorescent signal was normalised to the weight of brain tissue and also for background using age-matched, control brain samples.

For mice ($n \geq 3$, a mixture of males and females were used) aged P1, P7 and P14 (Figure 3.7 A and B) assayed in Sweden, tracer injections, perfusions and raw quantification data collection was performed with help from Dr Maarja Mäe and Dr Jennifer Hofmann, Department of Medical Biochemistry and Biophysics, Karolinska Institute, Stockholm. Tracer administration was identical to the method described above. Mice were terminally anaesthetised with Hypnorm/midazolam and perfused intracardially with cold PBS, after which brains were harvested and weighed. Homogenisation of brains was achieved using a hand-held tissue homogeniser in 400 µl PBS 1% Triton-X100. After 15 minutes full-speed centrifugation at 4°C, 150 µl of homogenate supernatant was assayed in duplicate on a POLARstar Omega fluorescent plate reader (BMG Labtech GmbH,

Ortenberg, Germany). Fluorescence values were again normalised to weight of brain tissue and to background value of age-matched controls. If being prepared for vibratome sectioning, PBS perfusion was followed by perfusion with 4% paraformaldehyde (PFA). Please note that Alexa Fluor 555 cadaverine administration to adult 5-month-old female *mdx* and wild-type mice (*n* = 1) for Figure 3.8 E and F was by intravenous rather than intraperitoneal injection. Brains were removed and post-fixed for at least 2 hours in 4% PFA. 75 µm vibratome sections were made of PFA-fixed brains using a Microm HM650V vibratome (Cellab Nordia AB, Stockholm, Sweden). Sections were mounted directly onto slides in Prolong Gold mounting medium (cat. no. P36930, Life Technologies) for fluorescent microscopy. Fluorescent images of unstained tracer-exposed sections were obtained using a Zeiss Axio Observer.Z1 microscope (Carl Zeiss Microscopy GmbH, Jena, Germany). Only one wild-type and one *mdx* mouse per age group (P1, P14, 5 months) had sections imaged in this way.

2.1.3. Immunofluorescent staining

PFA-fixed vibratome sections were prepared as above. Sections were blocked overnight at 4°C in blocking solution (1X PBS, 1% BSA, 0.5% Triton-X100). Primary anti-mouse antibodies were applied to coronal 75 µm thick vibratome sections in 150 µl blocking solution in 24-well plates and incubated overnight at 4°C with rocking. The following primary antibodies were used, diluted as listed:

Rat anti-CD13 (AbD Serotec, Kidlington, UK)	1 in 100
Goat anti-podocalyxin (R&D Systems, Minneapolis, MN)	1 in 200

Chicken anti-GFAP (cat. no. AB5541, Millipore, Billerica, MA)	1 in 100
Rabbit anti-dystrophin (cat. no. ab15277, Abcam, Cambridge, UK)	1 in 100

Sections were washed three times in blocking solution diluted 1:1 with 1X PBS, rocking at room temperature for 30 minutes with each wash. Tubes of secondary fluorescent antibodies were centrifuged at ≥18,000 g for 5 minutes at 4°C in order to reduce aggregates of antibody/dye. Secondary antibody from the surface of the supernatants was used to apply to washed sections in 200 µl blocking solution. The following secondary antibodies were used (all from Jackson ImmuoResearch, West Grove, PA), diluted as listed:

Donkey anti-rat AlexaFluor 488	1 in 400
Donkey anti-goat DyLight 405	1 in 200
Donkey anti-rabbit DyLight 488	1 in 200
Donkey anti-chicken DyLight 488	1 in 200

Sections were washed three times in 1X PBS, again rocking at room temperature for 30 minutes with each wash. Sections were then mounted on microscope slides using ProLong Gold mounting medium without DAPI. Images were captured with an Olympus VS120-S5 fluorescent microscope and viewed with OlyVIA software (Olympus, Tokyo, Japan).

2.1.4. Transmission electron microscopy

Electron microscopy sample preparation and imaging was carried out at the William Dunn School of Pathology electron microscopy facility with the help of Dr Errin Johnson. Adult wild-type and *mdx* mice aged 4-6 months (*n* = 4 per group, 2 females and 2 males of each) were perfused under terminal anaesthesia with 0.1M sodium cacodylate buffer followed by 2.5% glutaraldehyde. Brains were extracted and the superficial cortical layer dissected into 1 mm^3 cubes. These were post-fixed in 2.5% glutaraldehyde overnight at 4°C. Samples were rinsed three times in 0.1M sodium cacodylate buffer and then underwent secondary fixation with 1% osmium tetroxide in 0.1M buffer at room temperature for 2 hours. After rinsing four times with 18.2 MΩ.cm water (5 minutes each wash), tertiary fixation was performed with 2% uranyl acetate for 2 hours at 4°C in the dark. Samples were dehydrated in increasing concentrations of ethanol: 30% and 50% ethanol each for 20-30 minutes at room temperature, 70% ethanol overnight, 90% and 95% ethanol at room temperature for 20-30 minutes and then 100% ethanol for 90 minutes with 3 solution changes. Following this, brain samples were infiltrated with low viscosity epoxy resin by sequential incubation with rotation at room temperature in the following mixtures of ethanol/resin:

2:1	100% dry ethanol:Agar 100 resin	1 hour
1:1	100% dry ethanol:Agar 100 resin	2-4 hours
1:2	100% dry ethanol:Agar 100 resin	1 hour

Samples were further incubated in pure Agar 100 resin overnight and then for 2 more days with several changes of resin. Single cubes of infiltrated tissue were transferred to

BEEM capsules filled with fresh resin and embedded blocks made by polymerisation at 60°C overnight. Tissue blocks were trimmed and faced up using a Leica UC7 ultramicrotome. 500 nm semi-thin sections were cut and stained with toluidine blue and examined by light microscopy. Ultrathin sections of 70 nm were cut and placed on copper grids. Post-staining was carried out using 2% uranyl acetate followed by Reynolds' lead citrate (Reynolds, 1963). A Phillips/FEI Tecnai 12 transmission electron microscope (TEM) was used to visualise images.

2.1.5. Gene expression by qRT-PCR

C57BL/10 and *mdx* mice of the following ages were sacrificed: P1, P7, P14, P21, 4 weeks, 8 weeks, 13-16 weeks (3-4 months) and 12-13 months (1 year). For each age group $n = 3$ and a mixture of males and females was used at each age. Brains were removed and frozen at -80°C. Tissue from one hemisphere of cerebrum was homogenised in TRIzol reagent (cat. no. 15596-018, Life Technologies) using a Precellys tissue lyser. RNA was extracted using chloroform as follows. 1 ml TRIzol reagent was used to homogenise each tissue sample. After 10 minutes incubation at room temperature, 200 µl chloroform was added and incubated for 5 minutes. Samples were centrifuged at 12,000 g for 15 minutes at 4°C. The clear aqueous phase was removed and 500 µl isopropanol was added for 5 minutes at room temperature in order to precipitate RNA. RNA pellets were formed by centrifugation of the precipitated samples at 12,000 g for 10 minutes. Pellets were washed with 1 ml 75% ethanol, air-dried and resuspended in nuclease-free water. RNA concentrations were determined using a Nanodrop spectrophotometer.

cDNA was made by reverse transcription using the High Capacity Reverse Transcription cDNA Kit (cat. no. 4368814, Life Technologies) with random primers. 800 ng RNA was used as a template. The following reagents and conditions were used per 20 µl reaction:

Reagent	Volume
10X RT Buffer	2 µl
25X dNTP Mix (100 mM)	0.8 µl
10X Random Primers	2 µl
MultiScribe Reverse Transcriptase (50 U/µl)	1 µl
H_2O	4.2 µl
RNA + H_2O	10 µl

Temperature	Time
25°C	10 minutes
37°C	2 hours
85°C	5 minutes
4°C	Hold

cDNA was diluted 1 in 5 in water prior to qPCR analysis. Hydrolysis probe-primer PCR assays for the following mouse genes were either predesigned and purchased from Integrated DNA Technologies (IDT), Coralville, IA, or else designed using the online IDT RealTime PCR Tool (http://eu.idtdna.com/scitools/Applications/RealTimePCR/):

Cldn5

Primer 1 5'-CATCCTACCAGACACAGCAC-3'

Primer 2 5'-AGAGGCACCAGAATCAATTC-3'

Probe 5'-/56-FAM/AGACCCCAT/ZEN/GGCTAAAGACTGAATGC/3IABkFQ/-3'

Tjp1: IDT assay Mm.PT.56a.33451248.g

Primer 1 5'-ACATACCCTCCTTACTCACCA-3'

Primer 2 5'-CTTCAGAATACGGCTCCTTCC-3'

Probe 5'-/56-FAM/AGCGCAGCC/ZEN/ACAAGCTATTCATAGA/3IABkFQ/-3'

Aqp4: IDT assay Mm.PT.56a.9080805

Primer 1 5'-GGAAGGCATGAGTGACAGAG-3'

Primer 2 5'-TCCAGACTCCTTTGAAAGCC-3'

Probe 5'-/56-FAM/AATGTCCAC/ZEN/ACTTACCCCACCGC/3IABkFQ/-3'

Pdgfrb: IDT assay Mm.PT.56a.5869521

Primer 1 5'-CAGCCCAATGAGAGTGACAA-3'

Primer 2 5'-GAGATGGTGGAGGAAGTGTTG-3'

Probe 5'-/56-FAM/CATTCAAGG/ZEN/TGGAACTGGCAAGGC/3IABkFQ/-3'

Gfap: IDT assay Mm.PT.58.6609337

Primer 1 5'-TGCAGGAGTACCAGGATCTAC-3'

Primer 2 5'-GATCTGGAGGTTGGAGAAAGTC-3'

Probe 5'-/56-FAM/CAGGAATGG/ZEN/TGATGCGGTTTTCTTCG/3IABkFQ/-3'

Mfsd2a: IDT assay Mm.PT.58.32675283

Primer 1 5'-GCTCCTATCATCCTCATCTTGC-3'

Primer 2 5'-GAGTCTGTATCCGAGCAACC-3'

Probe 5'-/56-FAM/ATTCTGTCG/ZEN/CCGCTTCTCCTCATC/3IABkFQ/-3'

Csnk2a2: IDT assay Mm.PT.58.10226157

Primer 1 5'-CCACATAGACCTAGATCCACAC-3'

Primer 2 5'-GTGCCTGTTCTCACTATGGAT-3'

Probe 5'-/56-FAM/CGCTTCCGT/ZEN/GAATGTTGTCCCAG/3IABkFQ/-3'

Fbxw2: IDT assay Mm.PT.58.12526684

Primer 1 5'-TGAGGATGAAGCAACTGGAG-3'

Primer 2 5'-CAGCTTTGCAGACAAGTCATC-3'

Probe 5'-/56-FAM/CCATGAAGC/ZEN/CTTTGAGACCTCTTCGT/3IABkFQ/-3'

In addition, custom hydrolysis probe assays for *Dmd* (Dp71 transcript and full-length *Dmd* Dp427 transcript) were designed using the online IDT qPCR design tool.

Dmd (Dp427): exon 20-21

Primer 1 5'-CAGATGACAACTACTGCCGAA-3'

Primer 2 5'-TGACAATCTGTTGACTTCATCCT-3'

Probe 5'-/56-FAM/CCAGTCTAC/ZEN/CACCCTATCAGAGCCA/3IABkFQ/-3'

Dmd (Dp71)

Primer 1 5'-TCCTATACGCGGAGAACCTG-3'

Primer 2 5'-ACTGCCTGTGAAACCCTTAC-3'

Probe 5'-/56-FAM/AAAGGCCAC/ZEN/GAGACCCAAACCA/3IABkFQ/-3'

Two reference genes (*Csnk2a2* and *Fbxw2*) were selected using geNorm analysis (qbase+ software, Biogazelle, Ghent, Belgium) with a panel of 12 reference gene assays from the geNorm+ kit (PrimerDesign, Southampton, UK) (Vandesompele et al., 2002). Reference

gene stability was assayed across cDNA samples obtained from one brain from each age-group, both *mdx* and wild-type (Figure 3.1).

A.

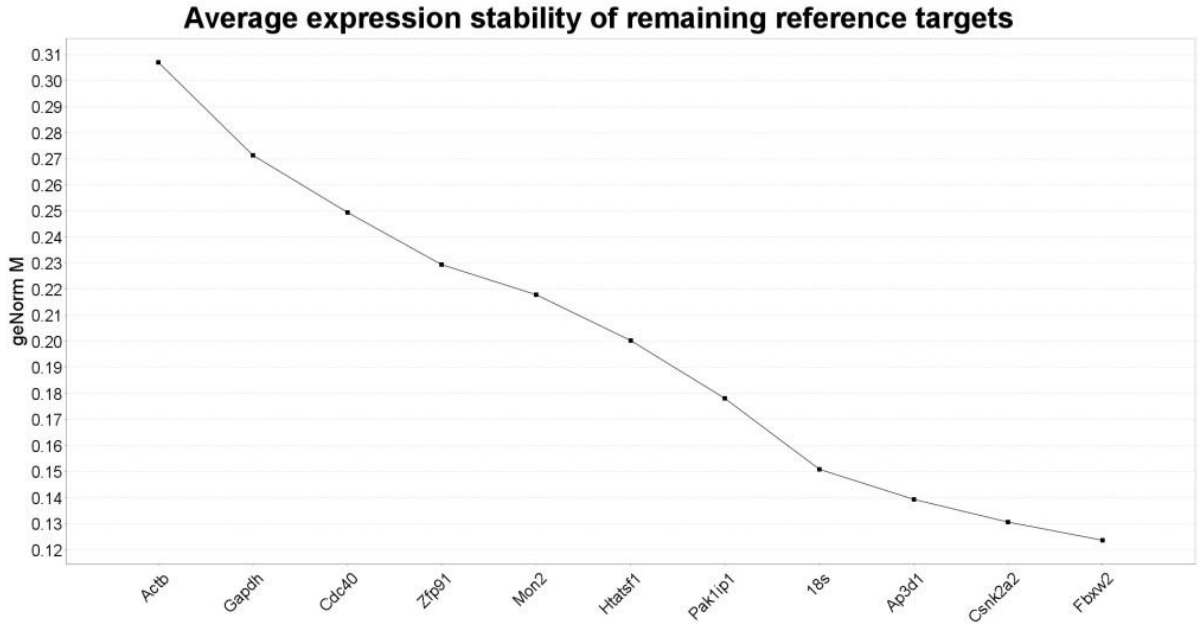

B.

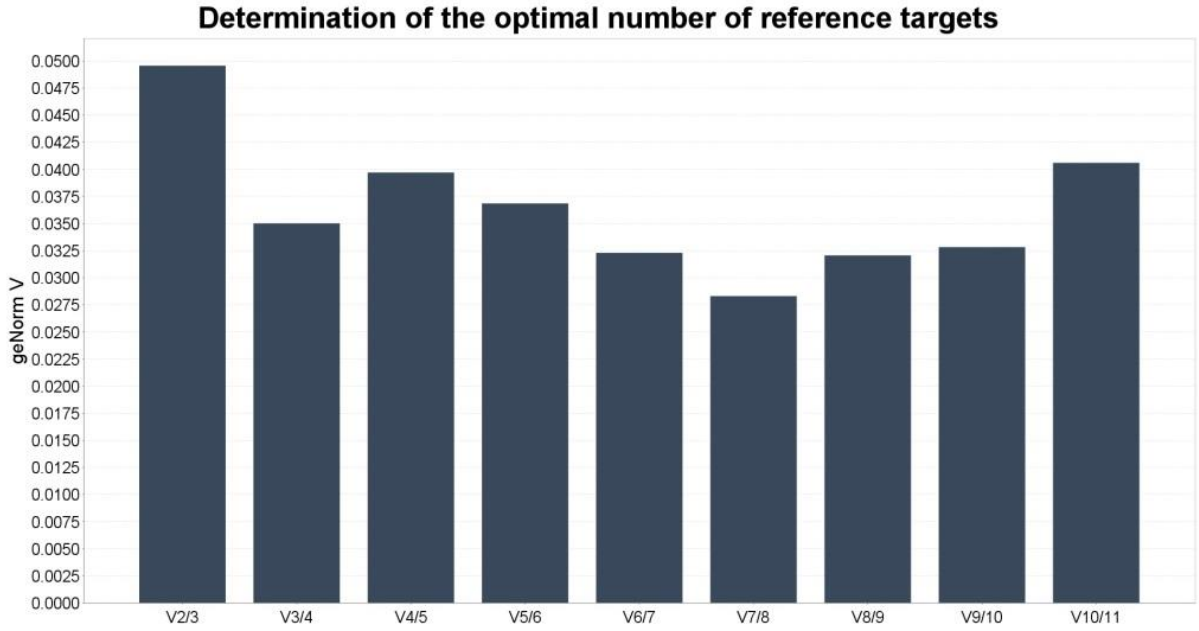

Figure 3.1. Brain geNorm analysis. Analysis of 11 reference genes from the geNorm+ kit assayed in cDNA made from RNA from wild-type and *mdx* brains at different ages (note that the kit assays 12 genes but only 11 genes are displayed as the assay for Fbxo38

failed). **A**. geNorm M analysis shows that the two most stable genes in this set are *Fbxw2* and *Csnk2a2*. The 11 reference genes tested are listed from left to right ranked in increasing expression stability based on the M (average expression stability) value. **B**. geNorm V analysis shows that the use of two reference genes is sufficient for this sample set. This analysis measures pairwise variation ($V_{(n/n+1)}$) between using *n* and *n*+1 reference genes for qPCR normalisation. The optimal n number of reference genes is found when V falls below 0.15, thus in this case *n* = 2 suffices since V is already beneath this threshold.

2.2. Chapter 4 methods

2.2.1. Identification of putative brain-targeting peptides

Extensive literature searching was performed to identify candidate peptides that might have the ability to traverse the BBB. This was done in collaboration with the laboratory of Dr Michael J. Gait, MRC Laboratory of Molecular Biology, Cambridge, whose members (and in particular Dr Fazel Shabanpoor) synthesised the peptides and chemically conjugated them to PMO.

2.2.2. Synthesis of PPMOs

PMO was obtained commercially from Gene Tools LLC (Philomath, OR) as a 25-mer antisense sequence targeting the 5' splice site of *Dmd* intron 23. The sequence was as follows:

5’–GGCCAAACCTCGGCTTACCTGAAAT–3’

Peptides were synthesised by standard 9-fluorenylmethoxycarbonyl (Fmoc) chemistry. A full technical description of PPMO chemical synthesis is likely somewhat beyond the scope of this work. For reference, however, there follows an explanatory description of the main principles involved. Further details of the click chemistry labelling of PPMOs used here has previously been published (Shabanpoor and Gait, 2013).

2.2.2.1. Peptide synthesis

In order to synthesise peptides with specific amino acid sequences, commercially available resin beads were used that had functional chemical linkers on their surface. The peptide chains were synthesised one amino acid at a time on the beads’ surface using a Liberty Peptide Synthesizer (CEM Corporation, Matthews, NC). The beads with growing peptide chains were exposed to one amino acid solution at a time. Fmoc peptide synthesis utilises amino acids that have their amino group protected by an Fmoc group. This Fmoc protection prevents polymerisation of all the free amino acids in solution during the reaction.

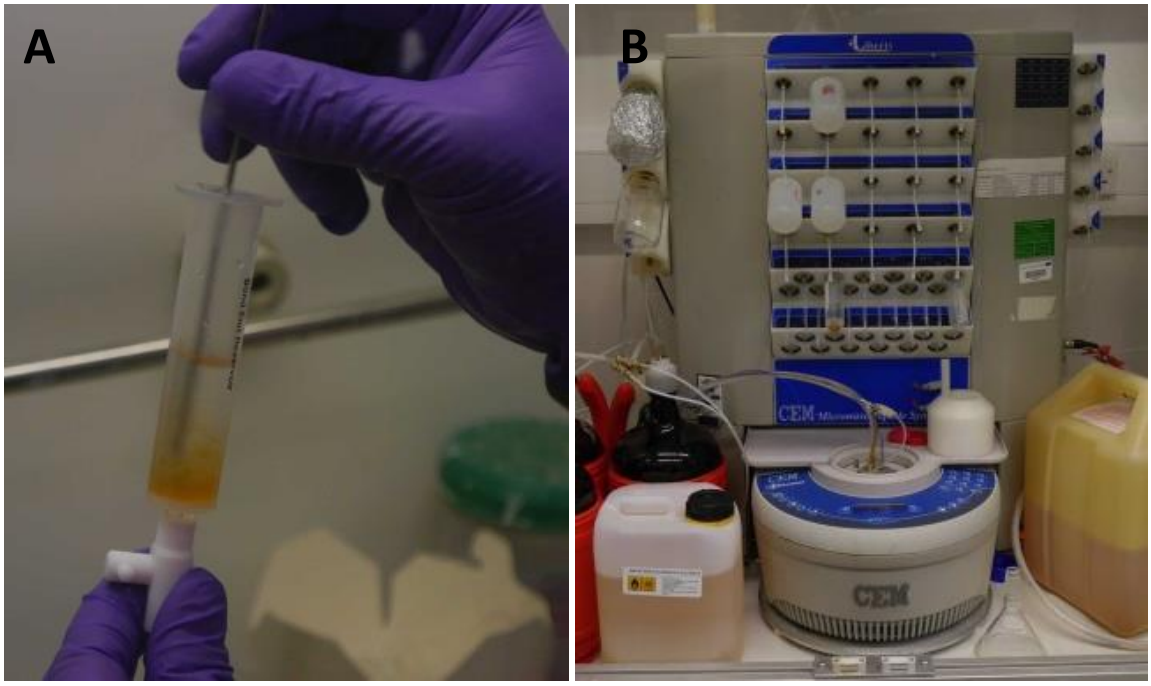

Figure 4.1. Solid-state peptide synthesis equipment. **A**. Resin beads in suspension. These beads are covered by chemical linkers on which to build sequential chains of amino acid residues. **B**. Peptide synthesis is automated through use of a synthesiser.

For each amino acid addition, the activator 2-(1H-benzotriazole-1-yl)-1,1,3,3-tetramethyluronium hexafluorophosphate (HBTU) was added as well as the base diisopropylethylamine (DIEA) and piperidine. The activator reacts with the carboxyl group of the free amino acid to form an ester. The base is required for the coupling reaction since it deprotonates the amino group, leaving a lone electron pair on the nitrogen that can then perform a nucleophilic reaction with the HBTU-ester of the amino acid to be added. Piperidine is required for a 'deprotection' step to remove the protective Fmoc group from the end of the growing peptide chain. Fmoc prevents amino acid polymerisation during the activator esterification step. By adding the base, the Fmoc is reduced back to an amino group. This step prepares the growing peptide chain for the next amino acid addition. The resin was washed clean in-between each step.

Once the peptide chains were completed, the N-terminus of the peptides were modified by acetylation. This was necessary since as a primary amine, the peptide N-terminus would react with the carboxyl group of other peptide chains during PMO conjugation resulting in polymerisation of the peptide. Acetyl anhydride was added, which reacted with the N-terminal amine leaving an acetyl group attached to the nitrogen, essentially making another amide link.

Trifluoroacetic acid (a strong acid) was added to liberate the synthesised peptide from the resin. Different types of starting resin coated with different chemical linkers produce different cleavage groups on the end of the peptide, depending on what is required. For PMO conjugation, resins that yield a carboxyl group were used.

2.2.2.2. Peptide purification

The peptides were purified by reversed-phase high-performance liquid chromatography (RP-HPLC). This was done by passing the peptide solutions through a column of silicon beads coated with C18 hydrocarbons. Peptides bind to the hydrocarbons with different affinity depending on their length and charge. Over about 30 minutes, H_2O in the column is substituted for an increasing concentration of acetonitrile. Acetonitrile is an organic solvent and it gradually elutes peptides from the C18 depending on their binding affinity. Different fragments are thus impeded to different degrees and can be collected as fractions. For positively charged peptides like Pips, a different approach was needed using a cation exchanger column. This type of column is filled with negatively charged beads that bind the cationic peptide. NaCl is then added in increasing concentration so

that Na^+ gradually displaces the peptide, which is then eluted and collected. This is an example of cation exchange.

As the HPLC fractions were collected, a UV detector at the bottom of the column was use to read absorption at 214 nm (wavelength of the N-terminal ester bond) and 280 nm, plotting these values as peaks over time. These fractions were then analysed by mass spectrometry (MALDI-TOF – matrix assisted laser desorption/ionisation - time of flight) to look at the mass/charge ratio. This allowed identification of the compound in each fraction based on the predicted molecular weight. Essentially the peptide or PPMO molecules are coated by a matrix (like battering fish) which allows them to be easily ionised by a laser, making them fly down the spectrometer tube at rates dependent on their mass and charge.

2.2.2.3. Conjugating peptide to PMO

The 3' end of the PMO molecule is formed by a secondary amine group. The 5' end of PMO is capped by an amide group and so there is no free functional group there to take part in the conjugation reaction. For each synthesised compound, the carboxyl group of the peptide was reacted with the amine group of the PMO to make an amide link, thus creating a PPMO conjugate.

2.2.2.4. Difficult amino acids

Some amino acids have carboxyl groups or amino groups on their side chains that could potentially take part in the PMO conjugation reaction. These must therefore be modified first before being added to the growing peptide chain. Such modified amino acids are

commercially available so that those with carboxyl side chains (e.g. aspartate and glutamate) have a Dmab modification and those with amino group side chains (e.g. lysine and histidine) have an IVDde modification. These modifications can be removed at the end of the synthesis process.

2.2.2.5. Branched peptides

The ability to make branched peptides made use of the fact that the amino acid lysine has a terminal amino group on its side chain. This meant that a lysine residue could be used as a branch point from which two chains of identical amino acid residues could be synthesised in parallel. For branched PepC7, which required cyclisation of each peptide branch, disulphide bonds were formed between cysteine residues by the addition of iodine with acetic acid.

2.2.2.6. Click chemistry

Peptides were functionalised for click chemistry during synthesis by incorporating a commercially available bishomopropargylglycine (Bpg) derivative containing a functional alkyne group at the end of its side chain (Figure 4.2 B). Following PPMO conjugation, the alkyne group could be reacted with an azide-functionalised dye such as Cy5 in the presence of copper sulphate to produce a covalent attachment between dye and PPMO via a triazole bond.

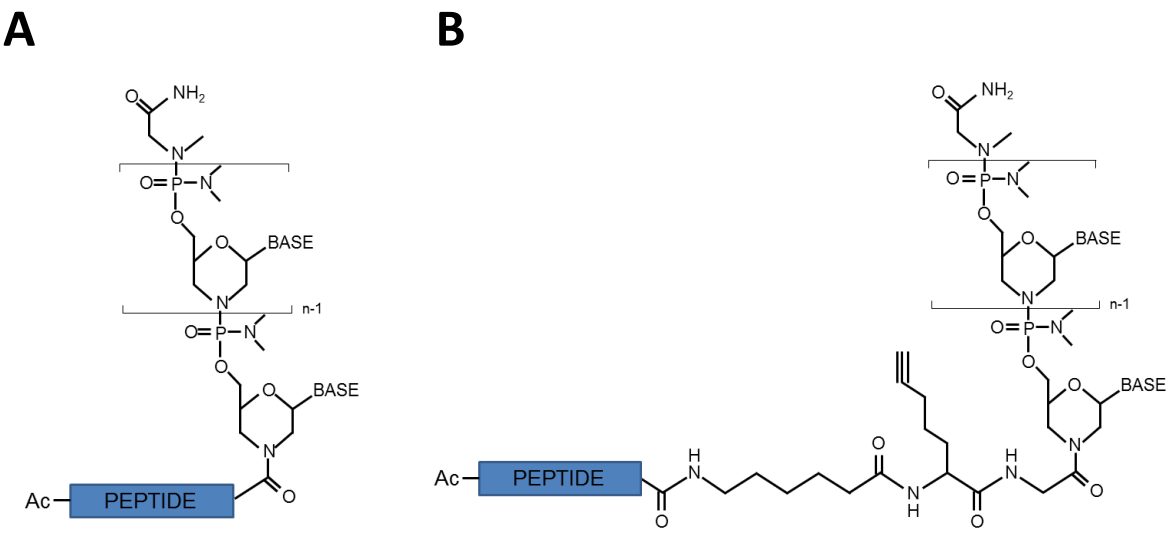

Figure 4.2. Structure of PPMO. **A**. PPMO without Bpg alkyne-functionalised linker. **B**. PPMO with Bpg alkyne-functionalised linker, which allows click chemistry covalent addition of azide dyes.

2.2.3. *In vitro* screening of PPMOs

In vitro screening was performed by Dr Fazel Shabanpoor, MRC LMB, Cambridge. Mouse H2K/*mdx* myoblasts were cultured in 24-well plates pre-coated with 0.01% gelatin at a seeding density of around 5000 cells per well. Cultures were maintained in DMEM, 20% fetal bovine serum, 2% chick embryo extract, 0.002% interferon-γ at 33°C in a 10% CO_2 atmosphere. In order to differentiate myoblasts into myotubes, culture medium was changed to DMEM containing 5% horse serum and cells were incubated at 37°C for 3-4 days with daily replacement of medium.

For transfection, PPMOs were made up to appropriate concentrations in serum-free Opti-MEM and 350 µl of this was added to duplicate wells. Transfections were incubated for 4

hours at 37°C, after which time the medium was replaced with DMEM, 5% horse serum, for a further 20 hours at 37°C. In order to collect RNA, cells were washed once with PBS and 0.5 ml of TRIzol reagent (Life Technologies, Carlsbad, CA) was added to each well. Cells mixed with TRIzol were frozen at -80°C for 1 hour, after which RNA was extracted as per the manufacturer's instructions.

RT-PCR was performed using the Transcriptor One-Step RT-PCR Kit (Roche, Basel, Switzerland) with 500 ng of template RNA in 50 µl reactions in 1X reaction buffer with 1 µl Transcriptor Enzyme Mix and with primers at a final concentration of 0.4 µM. The following cycling conditions were used:

Temperature	Time
50 °C	30 minutes
94°C	7 minutes
30 cycles:	
94°C	20 seconds
55°C	40 seconds
68°C	80 seconds
End of cycle	

Gene-specific RT-PCR for *Dmd* was performed using the following primers:

Dmd exon 20 forward outer: 5'-CAGAATTCTGCCAATTGCTGAG-3'

Dmd exon 26 reverse outer: 5'-TTCTTCAGCTTGTGTCATCC-3'

Nested PCR was performed using 1 µl of the RT-PCR reaction as template and using SuperTaq polymerase (H T Bioscience, Cambridge, UK) as per manufacturer's instructions

with 25 cycles of amplification as follows: 94°C for 30 seconds, 55°C for 1 minute, 72°C for 1 minute. The primers for nested PCR were as follows and these lie nested within the amplicon formed by the outer primers:

Dmd exon 20 forward inner: 5′-CCCAGTCTACCACCCTATCAGAGC-3′

Dmd exon 26 reverse inner: 5′-CCTGCCTTTAAGGCTTCCTT-3′

PCR products were separated by electrophoresis on 1.5% agarose gels. Efficiency of exon skipping was measured by gel band densitometry using ImageJ software (National Institutes of Health, Bethesda, MD).

2.2.4. *In vivo* administration of PPMOs

2.2.4.1. Intravenous injection

Solutions of PMO and PPMO were thawed and warmed to 37°C and briefly sonicated in a waterbath sonicator. PPMOs were injected intravenously into the tail vein of *mdx* mice if aged 4 weeks or older. Intravenous injections of selected PPMOs (RVG, Angiopep-2, Tet1, ApoE, BrApoE and BrPepC7) were performed by Dr Suzan Hammond, University of Oxford, and single intravenous injections of Pip6a-PMO were performed by Anna Coenen-Stass, University of Oxford. All other injections and subsequent analyses following all injections were performed by Andrew Douglas, University of Oxford. The sex of the mice used for these experiments can be found in the relevant results sections relating to each experiment. In pups aged P0 up to P5, intravenous administration was achieved by injection into the lateral facial vein using a Hamilton syringe. Injection

volumes were between 5-10 µl per gram weight of mouse and all compounds were made up in 0.9% NaCl.

2.2.4.2. Intracerebroventricular injection

Intracerebroventricular (ICV) injections were carried out by Dr Guillem Genové at the Department of Medical Biochemistry and Biophysics, Karolinska Institute, Stockholm, Sweden. 5-month-old *mdx* mice (2 females and 1 male in each group) were anaesthetised and positioned in a stereotaxic frame. Hair was removed from the scalp and the skin incised and retracted to reveal the skull. The bregma was visualised and the following coordinates used for injection into the right lateral ventricle: X -0.1, Y 0, Z -0.2. The skull was breached using a small drill and 5 µl total volume of PMO or Pip6a-PMO dissolved in 0.9% sodium chloride was injected into the ventricle using a Hamilton syringe. The burr-hole in the skull was plugged with sterile wax and the overlying skin sutured closed. Tissues were harvested one week after the procedure.

2.2.5. Open field testing

Mice were immobilised for 30 seconds by scruffing. They were then immediately placed into new clean cages that were placed within an open field testing system of infrared beams (Columbus Instruments, Columbus, OH). Activity was monitored for 5 minutes across 10-second intervals, counting both horizontal and vertical beam breaks. Activity measurements over the 5-minute period were summed for each mouse. This testing was kindly performed by Dr Suzan Hammond, DPAG, University of Oxford.

2.2.6. Grip strength

Mice were weighed and held by the tail in front of a metal bar attached to a force meter (Columbus Instruments). Each mouse was allowed to grip the bar with its forelimbs only after which increasing traction was gently applied via the tail in a horizontal direction away from the bar until the mouse released its grip. The force generated was noted and the test repeated five times in succession before returning each mouse to its cage.

2.2.7. Haematology and clinical chemistry

Blood was collected from mice by severing the jugular vessels immediately following schedule 1 asphyxiation by CO_2. Microvette 100/200 EDTA-treated tubes (SARSTEDT AG & Co., Nümbrecht, Germany) were used to collect blood for haematology testing and Microvette CB 300 tubes (SARSTEDT AG & Co.) were used to collect blood for serum clinical chemistry. Serum samples were allowed to clot and centrifuged at 10,000 g for 5 minutes and the serum supernatant collected. Laboratory analysis was carried out by MRC Harwell Mary Lyon Centre.

2.2.8. Nested RT-PCR analysis of *Dmd* exon 23 skipping

Animals from P14 upwards were euthanised by exposure to an increasing concentration of CO_2. Younger animals up to P4 were killed by decapitation. Tissues were harvested post-mortem and either immediately processed for RNA extraction or else frozen at -80°C until processing. Where tissue sectioning was required, tissues were mounted on cork

discs in optimal cutting compound (OCT) embedding matrix (Thermo Fisher Scientific, Waltham, MA) and plunge frozen in isopentane pre-cooled in dry ice.

Tissue harvested from mice was homogenised either manually by pipette or by cutting frozen shavings with a cryostat or by using a tissue lyser. RNA was extracted using TRIzol reagent (Life Technologies) as per manufacturer's instructions. Gene-specific dystrophin RT-PCR was carried out on 400 ng RNA using the GeneAmp RNA PCR Core Kit (Applied Biosystems Inc., Foster City, CA) followed by nested PCR using AmpliTaq Gold DNA polymerase (Life Technologies). The primers used were identical to those used for *in vitro* samples. Although both primer sets are sited across exons 20 and 26, the inner pair lie within the amplicon formed from the outer pair, thereby creating a nested PCR. An optimised PCR protocol was applied as follows:

Step 1	Volume
25 mM $MgCl_2$	2 µl
10X PCR Buffer	1.5 µl
2.5 mM dNTPs	4 µl
RNase inhibitor	0.5 µl
10 µM Exon 26 outer reverse primer	0.75 µl
MuLV reverse transcriptase	0.5 µl
400 ng RNA + H_2O	5.75 µl
	15 µl reaction

Temperature	Time
42°C	30 minutes
99°C	5 minutes

5°C	5 minutes

Step 2	Volume
25 mM $MgCl_2$	2 µl
10X PCR Buffer	3.5 µl
10 µM Exon 20 outer forward primer	0.75 µl
AmpliTaq DNA polymerase	0.25 µl
H_2O	28.5 µl
	35 µl added to Step 1 to make 50 µl reaction

Temperature	Time
95°C	2 minutes
30 cycles:	
95°C	30 seconds
58°C	60 seconds
72°C	2 minutes
End of cycle	
72°C	10 minutes

Nested PCR reagents	Volume
25 mM $MgCl_2$	4 µl
10X PCR Gold buffer	5 µl
10 mM dNTPs	1 µl
10 µM Exon 26 inner reverse primer	2.5 µl
10 µM Exon 20 inner forward primer	2.5 µl
AmpliTaq Gold DNA polymerase	0.25 µl

RT-PCR template	2 µl
H_2O	32.75 µl
	50 µl reaction

Temperature	Time
95°C	10 minutes
22 cycles:	
95°C	30 seconds
58°C	60 seconds
72°C	2 minutes
End of cycle	
72°C	10 minutes

PCR products were run on 2% agarose gels containing 0.000001% ethidium bromide in 1X TAE buffer.

2.2.9. Skipped product-specific RT-PCR and qRT-PCR

cDNA was synthesised from 800 ng of tissue-extracted RNA using the High Capacity cDNA Reverse Transcription Kit (Applied Biosystems) with random primers as per the manufacturer's instructions. The following reagents and cycling conditions were used:

Reagent	Volume
10X RT Buffer	2 µl
25X dNTP Mix (100 mM)	0.8 µl

10X Random Primers	2 µl
MultiScribe Reverse Transcriptase (50 U/µl)	1 µl
H_2O	4.2 µl
RNA + H_2O	10 µl

Temperature	Time
25°C	10 minutes
37°C	2 hours
85°C	5 minutes
4°C	Hold

For specific PCR amplification of skipped product, the following primer set was used:

Dmd exon 22-24 forward: 5'-GAGAGACTCGGGAAATTACAGAA-3'

Dmd exon 26 reverse inner: 5'-CCTGCCTTTAAGGCTTCCTT-3'

The final two nucleotides of the forward primer bind to the first two nucleotides of exon 24, while the rest of the primer binds to the 3' end of exon 22. The following reagents and cycling conditions were used:

Reagent	Volume
25 mM $MgCl_2$	4 µl
10X PCR Gold buffer	5 µl
10 mM dNTPs	1 µl
10 µM Exon 26 reverse primer (inner)	2.5 µl
10 µM Exon 22-24 forward primer	2.5 µl

AmpliTaq Gold DNA polymerase	0.25 µl
RT-PCR template	2 µl
H_2O	32.75 µl

Temperature	Time
95°C	10 minutes
35 cycles:	
95°C	30 seconds
58°C	60 seconds
72°C	2 minutes
End of cycle	
72°C	10 minutes

For qPCR, a hydrolysis probe-primer PCR assay specific for the exon 23 skipped product was obtained from Integrated DNA Technologies (IDT), Coralville, IA, with sequences having been designed partly by eye and partly by using the online IDT RealTime PCR Tool (http://eu.idtdna.com/scitools/Applications/RealTimePCR/). Similar assays (designed by Dr Graham McClorey, DPAG, University of Oxford) were obtained to detect only the unskipped transcript as well as total *Dmd* transcript.

Dmd exon 22-24F 25-24R (Δ23 skipped transcript)

Forward	5'-GAGAGACTCGGGAAATTACAGAA-3'
Reverse	5'-CTAAAAGTCTGCATTGTTTGAGCT-3'
Probe	5'-/56-FAM/CCTGGGGGA/ZEN/TGCTGAAATCCTGAA/3IABkFQ/-3'

Dmd exon 20-21 (total transcript)

Forward 5'-CAGATGACAACTACTGCCGAA-3'

Reverse 5'-TGACAATCTGTTGACTTCATCCT-3'

Probe 5'-/56-FAM/CCAGTCTAC/ZEN/CACCCTATCAGAGCCA/3IABkFQ/-3'

Dmd exon 23-24 (unskipped transcript)

Forward 5'-GAAACTTTCCTCCCAGTTGGT-3'

Reverse 5'-AACATCAACTTCAGCCATCCA-3'

Probe

5'-/56-FAM/AGTTTATTC/ZEN/ATATGTTCTTCTAGCTTTTGGCAGC/3IABkFQ/-3'

qRT-PCR analysis of cDNA was carried out using a StepOnePlus Real-Time PCR system with TaqMan gene expression master mix (Applied Biosystems). Duplicate 20 µl reactions using a 2 µl cDNA template were prepared in 96-well optical microplates from the following reagent mixture and with the following cycling conditions:

Reagent	Volume
2X TaqMan Gene Expression Master Mix	22 µl
20X Probe Primer	2.2 µl
H_2O	15.4 µl
cDNA	4.4 µl

Temperature	Time
50°C	2 min
95°C	10 min

40 cycles:

95°C	15 sec
60°C	60 sec

Relative quantities of transcripts were obtained using a standard curve method based on cDNA taken from a mouse injected ICV with Pip6a-PMO. The values of exon 23-skipped product obtained were normalised to values of total *Dmd* transcript and these values were further normalised to the proportion of skipped transcript found in the same ICV-injected standard curve sample obtained by digital droplet PCR.

2.2.10. Digital droplet PCR analysis of skipped versus unskipped product

Digital droplet PCR (ddPCR) was performed using 2 µl of random primer cDNA made from 800 ng RNA as above. The same hydrolysis probe qPCR assays could be directly employed in the ddPCR system. The following reagents were used to generate 20 µl reactions:

Reagent	Volume
Bio-Rad ddPCR Supermix for Probes (no dUTP)	1 µl
20X Probe Primer	1.1 µl
H_2O	7.7 µl
cDNA	2.2 µl

20 µl of reaction mix was combined with 70 µl droplet generation oil for probes (Bio-Rad Laboratories, Inc., Hercules, CA) in DG8 cartridges and droplets made using a Bio-Rad QX200 droplet generator. 40 µl of each resulting droplet mixture was added to one well of a twin.tec semi-skirted 96-well plate (Eppendorf, Hamburg, Germany). Each plate was

heat-sealed with a foil lid using a Bio-Rad PX1 PCR Plate Sealer and subjected to the following conditions in a thermal cycler:

Temperature	Time
95°C	10 minutes
40 cycles:	
94°C	30 seconds
60°C	60 seconds
End of cycle	
95°C	10 minutes

The resulting droplets were analysed using a Bio-Rad QX200 Droplet Reader and QuantaSoft Version 1.5.38.1118 software.

2.2.11. Western blotting

Hemi-cerebrum samples of mouse brain were homogenised in 200 µl lysis buffer containing Tris-HCl 75 mM (pH 6.8), 10% SDS, 5% β-mercaptoethanol, 1X protease inhibitors (Roche, Basel, Switzerland). Samples were heated to 100°C for 3 minutes, centrifuged at 13000 rpm for 10 minutes and the supernatant removed and stored at -80°C before analysis. Protein concentration was quantified using a Bradford reagent colorimetric assay, measuring samples diluted 1 in 100 against a BSA serial dilution standard curve. 30-60 µg of protein was made up to 10 µl with 2.5 µl NuPAGE 4X LDS buffer (Life Technologies), 1 µl NuPAGE 10X sample reducing agent (Life Technologies) and water. Samples were loaded in precast NuPAGE 3-8% Tris-acetate gels (Life

Technologies) and run at 150V for 2-2½ hours in NuPAGE running buffer. 8 µl HiMark pre-stained protein standard (Life Technologies) was used as a marker ladder. Separated proteins were transferred to a methanol-activated PVDF membrane at 30V for 100 minutes in transfer buffer (1X NuPAGE transfer buffer, 10% methanol, 0.01% SDS).

PVDF membrane was blocked in Odyssey blocking buffer (LI-COR Biosciences, Lincoln, NE) overnight at 4°C and at room temperature for 1 hour with rocking. Primary antibodies for dystrophin (NCL-DYS1, 1 in 100, Leica Microsystems, Wetzlar, Germany) and vinculin (hVIN-1, 1 in 100,000, Sigma-Aldrich, St Louis, MO) were applied to the membrane diluted in Odyssey blocking buffer with 0.1% Tween for 1-4 hours at room temperature with rocking. Membrane was washed 4 times for 5 minutes with wash buffer (1X PBST, 0.25 M NaCl) before incubation with secondary antibody (800 FL goat anti-mouse, 1 in 20,000, LI-COR Biosciences) diluted in Odyssey blocking buffer with 0.1% Tween for 1 hour at room temperature with rocking. Membrane was again washed 4 times for 5 minutes in wash buffer before imaging at 700 nm and 800 nm using an Odyssey Fc imager (LI-COR Biosciences).

2.2.12. Fluorescent imaging of Cy5-labelled ASOs

An IVIS Lumina imaging system (Perkin Elmer, Waltham, MA) was used to image mice injected with Cy5-labelled ASOs. 8-week-old female *mdx* mice were injected intravenously with either Cy5-Pip6a-PMO at 12.5 mg/kg or Cy5-PMO at 9.4 mg/kg (molar equivalent doses both 1 nmol/g, Cy5-Pip6a-PMO Mw 12209, Cy5-PMO Mw 9217). 24 hours later the mice were transcardially perfused with PBS and imaged with an excitation

wavelength of 640 nm and with a Cy5.5 emission filter. Even though this emission filter was not ideal for Cy5 fluorescence, adequate signal was obtained with a 0.5 second exposure time. The colour scale of fluorescence intensity (radiant efficiency) was manually adjusted to be equal across comparable groups of images.

2.2.13. Microscopy and *in situ* hybridisation of Cy5-Pip6a-PMO

Coronal cryosections of brain 10 µm thick were made using an OTF 5000 cryostat microtome (Bright Instrument Co Ltd, Huntingdon, UK). Sections dried at room temperature for 30 minutes and then fixed with 4% paraformaldehyde (PFA) in PBS for 30 minutes. These sections were then subjected to an *in situ* hybridisation procedure (performed by Dr Yoshitsugu Aoki and Dr Taeyoung Koo, DPAG, University of Oxford). Sections were washed three times for 5 minutes with PBS and then again with distilled water and dried at room temperature for 30 minutes and for 2-16 hours at 42°C. Sections were then rewashed in PBS (3 x 3 minutes) and incubated in 0.2 M HCl for 20 minutes, washed for 10 seconds with distilled water and 2 minutes with PBS and incubated in 0.2% Triton X-100 in PBS for 10 minutes. After a further 5-minute PBS wash, sections were incubated for 15 minutes in PBS supplemented with 1 µg/ml proteinase K (Roche) at 37°C, after which they were washed for 10 seconds in distilled water and three times for 5 minutes in PBS and then refixed in 4% PFA for 5 minutes. Following a further 3 x 5 minute PBS wash, 10 mg/ml glycine in PBS was applied for 15 minutes twice. After washing with distilled water for 3 minutes, sections were incubated at room temperature for 2 hours in 40% deionised formamide in 4X SSC. A digoxigenin-labelled probe complementary (i.e. antisense) to the PMO sequence (or a sense sequence as a control)

was prepared at 3 µg/ml and heated for 5 minutes at 95°C before snap cooling on ice and adding to hybridisation solution. Sections were incubated at 30°C in hybridisation solution overnight, which had the following composition.

Reagent	Volume per 100 µl
1M Tris-HCl (pH 7.5)	1 µl
5M NaCl	12 µl
0.2M EDTA (pH 7.5)	0.5 µl
Deionized formamide	40 µl
50X Denhardt solution	2 µl
Yeast tRNA (10 mg/ml)	2.5 µl
Salmon sperm DNA (10 mg/ml)	1.3 µl
Dextran sulfate	20 µl
DIG-labelled probe (3 µg/ml)	2 µl
H_2O	18.7 µl

Antisense probe: 5'-ATTTCAGGTAAGCCGAGGTTTGGCC-3'

Sense probe: 5'-GGCCAAACCTCGGCTTACCTGAAAT-3'

Next, sections were incubated at room temperature in 40% deionised formamide in 4X SSC for 5 minutes, followed by two 1-hour washes with 2X SSC, two 1-hour washes with 1X SSC, one 40-minute wash with 0.5X SSC, one 40-minute wash with 0.1X SSC and one 5-minute wash with PBS. Sections were then incubated with blocking solution for 40 minutes at room temperature before being incubated with anti-digoxigenin-alkaline phosphatase antibody for 60 minutes at room temperature (or overnight at 4°C). This

was followed by two washes of 30 minutes in 0.1 M Tris-HCl (pH 9.5) / 0.1 M NaCl, after which sections were incubated in NBT/BCIP solution (1X NBT/BCIP in 0.1 M Tris-HCl / 0.1 M NaCl) for at least 5 minutes and until staining became visible. Sections were then washed in distilled water to stop the reaction. After drying at room temperature for 10 minutes, sections were mounted with Vectashield mounting medium containing DAPI (Vector Laboratories, Inc., Burlingame, CA). Microscope images were taken using a Leitz DMRBE microscope (Leica, Wetzlar, Germany) fitted with an AxioCam MRm camera using AxioVision software (Carl Zeiss, Jena, Germany).

2.2.14. Serum elimination analysis

Serum was collected from 6-week-old female *mdx* mice that had been intravenously injected 5, 15, 30, 60 and 360 minutes previously with 10 mg/kg Cy5-Pip6a-PMO. 50 µl of serum was loaded into a colourless 96-well colorimetric plate and fluorescence read using an Odyssey Classic imaging system (LI-COR Biosciences, Lincoln, NE). Graphs of serum fluorescence were plotted using Microsoft Excel (Microsoft Corporation, Redmond, WA).

2.3. Chapter 5 methods

2.3.1. Fibroblast culture

Primary fibroblast cultures from c9FTD/ALS patients were obtained as gifts from the laboratories of Professor John Hardy, University College London (T2 and 7245 – Pt 1 and 2) and Dr Sally Cowley, University of Oxford (OXC901 and OXC902 – Pt 3 and 4). Three control fibroblast lines were commercially sourced (CC2511 from Lonza, AG05839 and

AG02261 from Coriell Cell Repositories – Pt 6, 7 and 8 respectively). A further fibroblast line from a *C9ORF72* expansion-positive patient with Parkinson's disease was purchased from Coriell (ND40069 – Pt 5). Fibroblasts were cultured in Dulbecco's modified eagle medium (DMEM) supplemented with 20% fetal bovine serum (FBS) and 1X antibiotic/antimycotic (A5955 Sigma-Aldrich, final concentration 100 units penicillin, 100 µg streptomycin, 250 ng amphotericin B per ml). 20% FBS allowed for better growth of cultures. However, when setting up cultures for RNA extraction and for transfection with oligonucleotides, DMEM with only 10% FBS was used. All cultures were incubated at 37°C in a humidified 5% CO_2 atmosphere.

2.3.2. Nucleic acid extraction

Fibroblasts were trypsinised and pelleted before undergoing DNA extraction using the DNeasy Blood & Tissue Kit from QIAGEN. DNA was stored at -20°C. RNA was extracted using the RNeasy Mini Kit from QIAGEN after direct lysis of cells within tissue-culture wells. RNA was stored at -80°C. DNA and RNA concentrations were measured using a NanoDrop spectrophotometer.

2.3.3. Southern blotting

5 µg of DNA was digested with 2 µl each of FastDigest DdeI and FastDigest AluI (#FD1884 and #FD0014 respectively from Thermo Scientific) for 2 hours at 37°C in a volume of 100 µl. 10µl was run in a 0.8% agarose TAE gel in order to confirm digestion. The rest of the digest was run in a large 0.8% agarose TAE gel without addition of ethidium bromide.

This gel was run at 55 V for about 16 hours. Roche DIG-labelled DNA molecular weight marker II was also loaded as a ladder. Prior to blotting, the gel was subjected to the following conditions in an orbital shaker at 30 rpm: depurination in 0.25 M HCl for 10 minutes, wash with 18.2 MΩ.cm water for 1 minute, denaturation in 0.5 M NaOH / 1.5 M NaCl twice for 30 minutes, wash with 18.2MΩ.cm water for 1 minute, neutralisation in 0.5 M Tris-HCl / 1.5 M NaCl twice for 20 minutes, incubate in 20X SSC (3 M NaCl, 0.3 M $Na_3C_6H_5O_7$ for 30 minutes. The blot was set up as shown in the diagram below (Figure 5.3) and left overnight at room temperature.

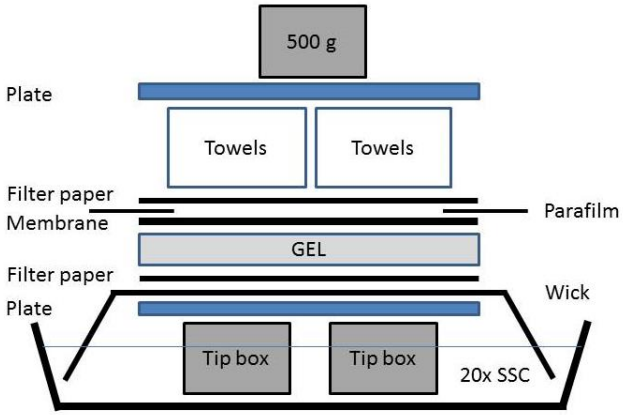

Figure 5.3. Diagram illustrating how to set up Southern blotting. A clean plastic tray is used to hold the 20X SSC solution (about 500 ml). Pipette tip boxes are used to support and elevate the blot above the level of the liquid. Two firm plastic or glass plates are used to provide a rigid compressible surface between which the blot can take place. The wick is formed from two sheets of filter paper. Strips of parafilm placed between the edges of the membrane and overlying filter paper prevent contact of blotting materials with the lower part of the set-up beneath the gel, which could otherwise allow flow of liquid around the gel and membrane rather than through it. The entire apparatus can be covered with clingfilm overnight to reduce evaporation.

After blotting onto a positively-charged nylon membrane (Roche 11 417 240 001), the membrane was prepared for DNA fixation by incubating in 2X SSC twice for 15 minutes on an orbital shaker. DNA was cross-linked to the membrane by exposure to UV light for 2½ minutes. The membrane was placed in a hybridisation bottle with DIG Easy Hyb solution (Roche 11 796 895 001, 10 ml per 100 cm^2 membrane) and incubated in a hybridisation oven at 53°C for 2 hours as a prehybridisation step. DIG-labelled $(GGGGCC)_5$ probe (custom synthesised by Integrated DNA Technologies, Inc) was prepared by diluting 10 µl of 1 ng/µl probe to 50 µl in water, heating to 95°C for 5 minutes, snap cooling on ice for 30 seconds and then immediately adding this to prewarmed DIG Easy Hyb solution (3.5 ml per 100 cm^2 membrane). The membrane was incubated in the probe hybridisation mixture overnight at 53°C in a hybridisation oven. Stringency washes were performed at 64°C as follows: 2X SSC 0.1% SDS 5 minutes, 2X SSC 0.1% SDS 10 minutes, 1X SSC 0.1% SDS 15 minutes, 1X SSC 0.1% SDS 15 minutes, 1X SSC 0.1% SDS 15 minutes, 0.5X SSC 0.1% SDS 15 minutes, 0.5X SSC 0.1% SDS 15 minutes.

Using the DIG Wash and Block buffer set (Roche 11 585 762 001), the membrane was washed with wash buffer for 2 minutes then placed in a polythene wallet and incubated with block buffer for 1-2 hours on a shaker. Anti-digoxigenin-AP Fab fragments (Roche 11 093 274 910) at 1 in 10,000 dilution in block buffer were incubated with the membrane for 20-25 minutes. Three wash buffer steps were carried out for 5, 15 and 15 minutes followed by a 5 minute equilibration step using supplied detection buffer. CDP-Star (Roche 12 041 677 001) was added to the membrane for 5 minutes and signal was detected by exposure to X-ray film.

2.3.4. Repeat-primed PCR

Amplification of the repeat-containing allele by repeat-primed PCR was achieved following the protocol of Renton et al., 2011 (Figure 5.4). 100 ng of DNA was used as a template in a total volume of 28 µl using 14 µl of FastStart PCR Master Mix (Roche) with the following reagents at final concentration: 0.9 mM $MgCl_2$, 0.18 mM 7-deaza-dGTP, 7% DMSO (Sigma-Aldrich), 1X Q-solution (QIAGEN), 1.4 µM forward primer, 0.7 µM reverse primer, 1.4 µM anchor primer. Primers had the following sequences:

Forward: 5′-TACGCATCCCAGTTTGAGACGGGGGCCGGGGCCGGGGCCGGGG-3′

Reverse: 5′-6-FAM-AGTCGCTAGAGGCGAAAGC-3′

Anchor: 5′-TACGCATCCCAGTTTGAGACG-3′

A touchdown PCR cycling protocol was used whereby annealing temperature was gradually reduced by 2°C per cycle from 70°C to 58°C over 7 cycles. Each annealing step lasted 1 minute, was preceded by 30 seconds' denaturation at 95°C and was followed by 3 minutes' extension time. This was followed by 40 cycles of PCR with denaturation at 95°C for 30 seconds, annealing at 58°C for 1 minute and extension at 72°C for 3 minutes. A final prolonged extension step was carried out at 72°C for 10 minutes. Capillary electrophoresis fragment analysis was carried out through Source BioScience using an ABI3730XL genetic analyser. Data analysis was performed using Peak Scanner Software 2 (Applied Biosystems).

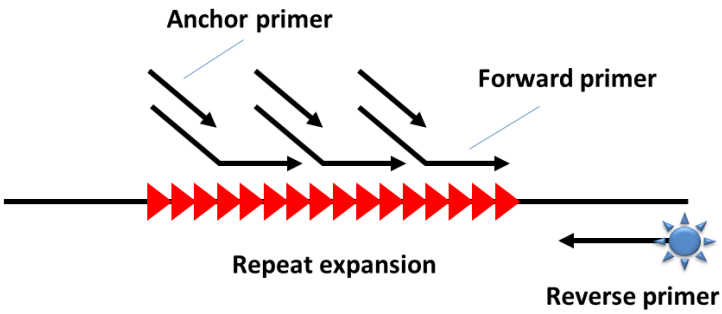

Figure 5.4. Principle of repeat-primed PCR. The GGGGCC repeat expansion in *C9ORF72* is too GC-rich to allow amplification via a standard PCR approach with flanking primers. Instead, a forward primer is designed so that its 3' end binds directly to the repeat while its 5' end acts as a unique anchor sequence. This primer will tend to bind to the expanded region at any and every point along the expansion at 6-nucleotide intervals. Together with a standard reverse primer (which can be fluorescently labelled) located in the downstream flanking sequence, a touchdown PCR approach can be used to generate copies of template separated in size by multiples of 6 nucleotides. A third primer, the anchor primer, has the same sequence as the free end of the repeat-binding forward primer. This allows further amplification of all the differently-sized amplicons generated by the forward and reverse primers. The upper limit of the amplicon length is dependent upon the ability of the polymerase to progress through the GC-rich DNA region. This means the quantity of product reduces the longer the amplicon, leading to a typical saw-tooth appearance on capillary electrophoresis.

2.3.5. Methylation-specific PCR

1000 ng DNA was treated with sodium bisulphite using the EpiTect Bisulfite Kit (QIAGEN). Around 100 ng of bisulphite-treated DNA was used for methylation-specific PCR (MS-

PCR). Primers were designed for the upstream CpG island region taking into account conversion of unmethylated cytosine to uracil (Figure 5.5). A common reverse primer did not contain any CpG dinucleotides while two alternative forward primers ended at a CpG site and covered at least two CpG dinucleotides. One of the forward primers was specific for methylated CpGs and its design assumed no conversion of cytosine at these dinucleotides. The other forward primer was specific for unmethylated CpGs and assumed conversion of CpG to UpG. In addition, the forward primers, while overlapping, generated products of slightly different length, allowing separation on size by electrophoresis. By using a FAM-label on the common reverse primer, methylated and unmethylated product peaks could be visualised using an ABI3730XL bioanalyser (samples were processed by Source BioScience) and Peak Scanner Software 2 (Applied Biosystems).

The following primer sequences were used:

Methylated forward: 5'-ACGCTATTACGCCAACG-3'

Unmethylated forward: 5'-CCAACACTCCTCCAAAACA-3'

Common reverse: 5'-/56FAM/TTGAGTTTTAGAGTTTGTTATAGGTTG-3'

The following reagents and cycling conditions were used for each 50 µl reaction (AmpliTaq Gold DNA Polymerase, LD, Applied Biosystems):

AmpliTaq Gold buffer (10X)	5 µl
$MgCl_2$ (25 mM)	4 µl
dNTPs (10 mM)	1 µl
Methylated forward primer (10 µM)	1.25 µl

Unmethylated forward primer (10 µM)	1.25 µl
Common reverse primer (10 µM)	2.5 µl
AmpliTaq Gold DNA polymerase (5 units/µl)	0.25 µl
Nuclease-free water	32.75 µl
Bisulphite-treated DNA	2 µl

Temperature	Time
95°C	10 minutes
Start cycle	
95°C	30 seconds
60°C	30 seconds
72°C	30 seconds
Repeat cycle 22X	
72°C	10 minutes

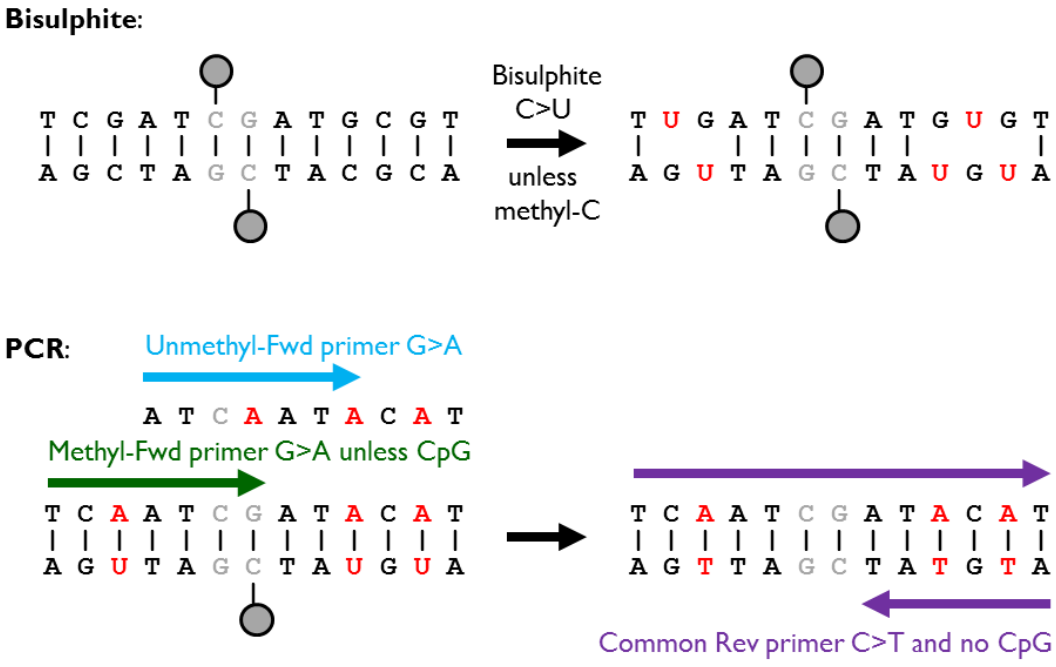

Figure 5.5. Illustration of the principle of methylation-specific PCR. Treatment of genomic DNA with sodium bisulphite first converts unmethylated cytidine bases to uracil. Alternative forward primers are designed so as to overlap CpG dinucleotides and take into account a C to U conversion (unmethylated) or no conversion (methylated). A common reverse primer, which can be fluorescently labelled, does not overlap any CpG dinucleotides and thus assumes full conversion of C to U. However, it must also be designed to amplify only the forward-synthesised strand, rather than the original bisulphite-treated DNA template, which will have guanine bases where the forward primer product has adenine if the original template was unmethylated.

2.3.6. Gene expression by qRT-PCR

cDNA was synthesised from 100 ng fibroblast RNA in a reaction volume of 50 µl using the High Capacity cDNA Reverse Transcription Kit (Applied Biosystems) with random primers. Quantitative PCR was carried out using a StepOne Plus Real-Time PCR system (Applied Biosystems). Samples of 2 µl cDNA were set up in duplicate 20 µl reaction volumes using TaqMan Gene Expression Master Mix (Applied Biosystems) and premixed probe/primer hydrolysis probe assays ordered from Integrated DNA Technologies, Inc (IDT). Relative quantities were calculated by use of a standard curve method using five-fold serial dilutions of cDNA pooled from control fibroblasts. Reference gene assays for *ACTB* and *GAPDH* were used for normalisation by taking the geometric mean of the relative quantities calculated for each gene. The stability of both reference genes across all fibroblast lines was confirmed by use of a geNorm Kit (PrimerDesign) using a panel of 12

reference gene assays and analysis using qbase+ software (Biogazelle). Hydrolysis probe qPCR assays were either purchased as predesigned inventoried assays from IDT or else were designed using the online IDT RealTime PCR Tool (http://eu.idtdna.com/scitools/Applications/RealTimePCR/) with some manual modifications. Assay sequences are as follows:

C9ORF72 all transcripts (exons 3-5): IDT assay Hs.PT.58.38350554

Forward 5'-CGGAAAGGAAGAATATGGATGC-3'

Reverse 5'-CCATTACAGGAATCACTTCTCCA-3'

Probe

5'-/56-FAM/AGCATTGGA/ZEN/ATAATACTCTGACCCTGATCTTC/3IABkFQ/-3'

C9ORF72 transcript 1b (exons 1b-2)

Forward 5'-GCGGTGGCGAGTGGATA-3'

Reverse 5'-CTTAAAGCAATCTCTGTCTTGGC-3'

Probe 5'-/56-FAM/AGATGGCGG/ZEN/TGGGCAAAGAGT/3IABkFQ/-3'

ACTB: IDT assay Hs.PT.39a.22214847

Forward 5'-ACAGAGCCTCGCCTTTG-3'

Reverse 5'-CCTTGCACATGCCGGAG-3'

Probe 5'-/56-FAM/TCATCCATG/ZEN/GTGAGCTGGCGG/3IABkFQ/-3'

GAPDH: IDT assay Hs.PT.39a.22214836

Forward 5'-ACATCGCTCAGACACCATG-3'

Reverse 5'-TGTAGTTGAGGTCAATGAAGGG-3'

Probe 5'-/56-FAM/AAGGTCGGA/ZEN/GTCAACGGATTTGGTC/3IABkFQ/-3'

The following reagents were used to make duplicate 20 µl reactions for qPCR:

2X TaqMan Gene Expression Master Mix	22 µl
20X Probe Primer	2.2 µl
H_2O	15.4 µl
cDNA	4.4 µl

Reaction mixtures were arranged in 96-well optical microplates and qPCR was performed with the following conditions:

Temperature	Time
50°C	2 min
95°C	10 min
40 cycles:	
95°C	15 sec
60°C	60 sec

2.3.7. Digital droplet PCR analysis of *C9ORF72* expression

Fibroblast cDNA was prepared from 100 ng RNA as described above for qRT-PCR. The same hydrolysis probe assays were used as mentioned above for *ACTB*, *GAPDH* and total *C9ORF72* expression. In addition, the following assays were designed manually and obtained from IDT:

C9ORF72 transcript Δ1a (exons Δ1a-2)

Forward 5'-CACGTAAAAGATGACGCTTGATAT-3'

Reverse 5'-GCCACTTAAAGCAATCTCTGTC-3'

Probe 5'-/56-FAM/TGATGTCGA/ZEN/CTCTTTGCCCACCG/3IABkFQ/-3'

C9ORF72 transcript 1a (exons 1a-2)

Forward 5'-TCCGCCCACGTAAAAGATG-3'

Reverse 5'-CACTGCATTCCAACTGTCAC-3'

Probe 5'-/56-FAM/TCCTAAACC/ZEN/CACACCTGCTCTTGC/3IABkFQ/-3'

Owing to small amounts of starting material, cDNA was diluted 1 in 2 for *C9ORF72* transcript analysis to provide sufficient volume. For reference gene analysis, cDNA was diluted 1 in 20 to take into account the high copy number of reference gene transcripts and to lower this to a level that fell within the dynamic range of the ddPCR system. The following reagents were used to make 20 µl reactions for ddPCR:

Bio-Rad ddPCR Supermix for Probes (no dUTP)	1 µl
20X Probe Primer	1.1 µl
H_2O	7.7 µl
cDNA	2.2 µl

20 µl reactions were each combined with 70 µl droplet generation oil for probes (Bio-Rad) in DG8 cartridges and droplets made using a Bio-Rad QX200 droplet generator. 40 µl of each resulting droplet mixture was added to one well of a twin.tec semi-skirted 96-well plate (Eppendorf). Each plate was heat-sealed with a foil lid using a Bio-Rad PX1 PCR Plate Sealer and subjected to the following conditions in a thermal cycler:

Temperature	Time
95°C	10 min
40 cycles:	
94°C	30 sec
60°C	60 sec
End of cycle	
95°C	10 min

The resulting droplets were analysed using a Bio-Rad QX200 Droplet Reader and QuantaSoft Version 1.5.38.1118 software.

2.3.8. Expression of mouse *C9ORF72*-orthologue *3110043O21Rik*

Brains were harvested from C57BL/10 mice of different ages ranging from P1 to 1 year old (*n* = 3 with a mixture of both males and females used in each age group). Tissue was taken from the right cerebrum to make RNA using TRIzol reagent (Life Technologies) as per the manufacturer's instructions. 800 ng of RNA was used to make cDNA using random primers and the High Capacity cDNA Reverse Transcription kit (Applied Biosystems) as above. Inventoried TaqMan assays were purchased from IDT for *3110043O21Rik*, *Csnk2a2* and *Fbwx2.* qRT-PCR was carried out as described above. Reference genes were chosen based on geNorm analysis for the most stable genes across these age ranges (see Materials and Methods, Chapter 3). Relative quantities were determined by standard curve using a mixed cDNA sample (a combined additive mixture of one cDNA sample from each age group) as a standard from which 5-fold serial dilutions

were made. Normalisation of values was carried out using the geometric means of the relative values obtained for the two reference genes.

The following probe-primer sets were used:

3110043O21Rik: IDT assay Mm.PT.58.13127725

Primer 1 5'-GCTTCTACCTCCCACTTCAC-3'

Primer 2 5'-TGACCCTGATCTTCCATCCT-3'

Probe

5'-/56-FAM/TTCTTGTCT/ZEN/TTCCTTATGCATCCATATTCTTCCT/3IABkFQ/-3'

Csnk2a2: IDT assay Mm.PT.58.10226157

Primer 1 5'-CCACATAGACCTAGATCCACAC-3'

Primer 2 5'-GTGCCTGTTCTCACTATGGAT-3'

Probe 5'-/56-FAM/CGCTTCCGT/ZEN/GAATGTTGTCCCAG/3IABkFQ/-3'

Fbxw2: IDT assay Mm.PT.58.12526684

Primer 1 5'-TGAGGATGAAGCAACTGGAG-3'

Primer 2 5'-CAGCTTTGCAGACAAGTCATC-3'

Probe 5'-/56-FAM/CCATGAAGC/ZEN/CTTTGAGACCTCTTCGT/3IABkFQ/-3'

2.3.9. Methyl-DNA immunoprecipitation assay

1 µg of genomic DNA was digested with EcoRI-HF and ScaI-HF with CutSmart buffer (all New England Biolabs) in a final volume of 100 µl at 37°C overnight. 10 µl of digest was run on a 2% agarose gel with ethidium bromide to confirm digestion. Restriction

enzymes were inactivated at 85°C for 20 minutes and fragments purified using the QIAquick PCR Purification Kit (QIAGEN), eluting in 50 µl of water. The EpiMark Methylated DNA Enrichment Kit (New England Biolabs) was used to pull down methylated DNA fragments (Figure 5.6). Briefly, the methyl-CpG binding domain of the human MBD2 protein is fused to the Fc tail of human IgG1 (MBD2-Fc). This is coupled to paramagnetic hydrophilic protein A beads. These are incubated with the digested DNA using a rotating mixer and the fraction adhering to MBD2-Fc is then pulled down with the protein A beads using a magnetic rack. The pulled down fraction can be eluted by heating the beads to 65°C.

The methyl-CpG-enriched DNA fractions were assayed by qPCR using the following TaqMan assay for the 5' end of the *C9ORF72* gene:

5' *C9ORF72* gDNA

Forward	5'-GGGTTTGCAGTGGAGTTTTG-3'
Reverse	5'-GGATCTGGAGAAAGTGAAGACG-3'
Probe	5'-/56-FAM/TTTGTGCTT/ZEN/GGTAGGCAGTGGG/3IABkFQ/-3'

This assay was applied to the pulled down fractions and also to the original DNA fragment mixtures that had been digested but not pulled down. A relative 'methylation index' was calculated from the ratio of DNA quantified in the pulled down fraction compared to the amount quantified in the digested DNA fragment mixture.

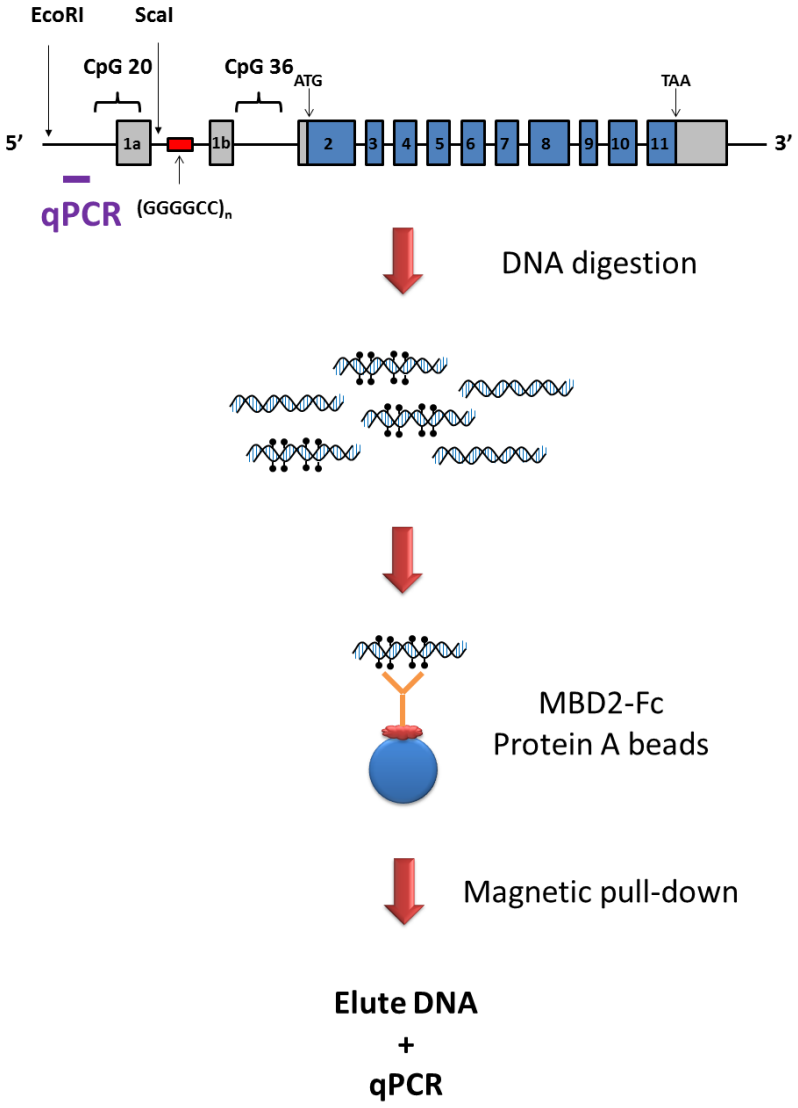

Figure 5.6. Methyl-DNA immunoprecipitation assay. Digestion of genomic DNA with the restriction enzymes EcoRI and ScaI results in a mixture of methylated and unmethylated fragments. These are incubated with an antibody-like fusion protein that recognises methyl-CpG DNA and is attached to paramagnetic protein A beads. This recognises methylated CpG DNA via a methyl-DNA-binding domain 2 (MBD2) region, which is fused to the Fc portion of human IgG1. After capturing methylated CpG DNA fragments, the beads are pulled down magnetically and washed. The pulled down fraction can then be eluted through heat. qPCR can then be performed to identify the fragment of interest

(assay position shown in purple) and to relatively quantify it in comparison to the original mixture of DNA fragments.

2.3.10. Knockdown of *C9ORF72* natural antisense transcript

This experiment was performed by Dr Miguel A. Varela, University of Oxford, while the data was analysed by Andrew Douglas, University of Oxford. Oligonucleotides targeting the *C9ORF72* antisense transcript (NAT) were designed manually so as to have an LNA-phosphorothioate gapmer chemistry. Synthesis was carried out by IDT. The following sequences were used:

NAT5 5′-CAAGCTCTGGAACTC-3′

NAT3 5′-CTCTCCTCAGAGCTC-3′

SCR 5′-CAGTGTGCTAGTCA-3′

Underlined sequence denotes LNA chemistry. Note that all nucleotides in these sequences have phosphorothioate linkages. The gapmers were applied to patient fibroblasts by reverse transfection. Oligonucleotides were diluted in 20 µl Opti-MEM. 1 µl Lipofectamine RNAiMAX reagent (Life Technologies) was diluted in 85 µl Opti-MEM. Diluted oligonucleotide was then added to diluted Lipofectamine RNAiMAX reagent in 12-well tissue culture plates and incubated at room temperature for 5 minutes to allow the formation of lipid/gapmer complexes. Around 20,000 cells were seeded into the 12-well plates in 700 µl DMEM 10% FBS without antibiotics to achieve a final concentration of 100 nM LNA gapmer. Cultures were incubated for 24 hours, after which time a further 2 ml DMEM 10% FBS including antibiotics was added. Cells were harvested after another

24 hours and RNA was extracted using the RNAeasy Kit (QIAGEN) with on-column DNase treatment. 100 ng RNA was used to make cDNA using the High Capacity cDNA Reverse Transcription kit (Applied Biosystems) and *C9ORF72* expression was analysed by qRT-PCR using an inventoried TaqMan assay (Hs00376619_m1, sequences not publicly available) that spans exons 2-3, normalised to *ACTB* using the IDT assay mentioned previously.

Chapter 3:

The blood-brain barrier in *mdx* mice

3.1. Introduction

The blood-brain barrier (BBB) describes the physiological separation of blood from the parenchymal tissue of the central nervous system (CNS). Its presence allows a relatively constant electrochemical environment to be maintained for normal neuronal function, as well as protecting the CNS against the free entry of toxins and pathogens from the blood (see section 1.5).

Two previous studies, both from the same research group, reported significant BBB abnormalities in the *mdx* mouse model of Duchenne muscular dystrophy (DMD) (Nico et al., 2003, 2004). In the first study comparing *mdx* to control mice, 18-20-month-old *mdx* mice were found to have severe injury to their brain endothelial cells, which were irregular, contained vacuolated cytoplasm and were surrounded by a discontinuous basement membrane (Nico et al., 2003). Detachments were observed within endothelial tight junctions, large perivascular spaces were seen and astrocyte endfeet appeared swollen. In *mdx* mice there was a 60% reduction in zonula occludens-1 (ZO-1) protein and a 70% reduction in aquaporin-4 (AQP4) protein by Western blot densitometry, however it should be noted that no staining for a loading control was reported in this analysis. Intracardiac injections of horseradish peroxidase (HRP) tracer demonstrated areas of increased capillary permeability within the brains of *mdx* mice after 5 minutes.

The second study assessed the BBB at a range of ages of *mdx* mice across both pre- and postnatal development (Nico et al., 2004). This reported decreased expression of the short dystrophin isoform Dp71 in *mdx* mouse brain from early on in embryonic development, with a visible difference in immunostaining apparent from E16 onwards using an antibody detecting the C-terminal of dystrophin (MANDRA1). Immunostaining also suggested visibly decreased ZO-1 and AQP4 expression at all *mdx* ages tested and glial fibrillary acidic protein (GFAP) staining was also reported to be weak across all time points. Western blot analysis of brain protein suggested significant decreases in both AQP4 and GFAP at E16, E19, P2 and P30 as well as a reduction in ZO-1 at P30. Brain endothelial tight junctions appeared abnormal in *mdx* mice at every age assessed, with irregular endothelial cell cytoplasm containing vacuoles and vesicles, discontinuous basement membranes and widespread perivascular spaces. HRP assays in P2 mice suggested increased capillary permeability in *mdx* brain with numerous areas of perivascular HRP escape 5 minutes after intracardiac injection.

Further work using 2-month-old *mdx* mice has also previously reported a deficiency in the short Dp71 isoform of dystrophin within astrocyte endfeet, an associated decrease in α- and β-dystroglycans, α-syntrophin, AQP4 and potassium channel Kir 4.1 as well as reductions in basement membrane proteins laminin and agrin within the brain (Nico et al., 2010). Once again, similar ultrastructural abnormalities as described previously were reported in the *mdx* brains. The reductions in brain gene expression were demonstrated not only by Western blotting but also by real-time PCR analysis of mRNA. More recently, a study investigating the effects of prednisolone treatment on the *mdx* BBB found that the integrity of the BBB in 2-3-month old *mdx* mice was improved by chronic high-dose

glucocorticoid therapy with 1 mg/kg prednisolone 6 days a week over a 4-8 week period (Tamma et al., 2013). Integrity was assessed by HRP leakage from brain capillaries 5 minutes after intracardiac injection. Prednisolone-treated *mdx* mice also appeared to have some normalisation of expression of several BBB markers including Dp71, AQP4, α- and β-dystroglycans, occludin, ZO-1, GFAP, pericyte desmin and basement membrane laminin.

The reported BBB defect in *mdx* mice has been suggested as a possible contributory factor to the cognitive impairment seen in DMD. However, increased BBB permeability could also potentially lend itself to improved drug delivery to the CNS. The treatment of DMD using antisense oligonucleotides (ASOs) is currently the focus of much research and the subject of several ongoing clinical trials (Douglas and Wood, 2013). The experiments detailed in this chapter have sought to better characterise the structure and permeability of the BBB in *mdx* mice with a view to possible CNS-directed therapy using ASOs. To do this, the following three approaches have been used to compare the BBB components within the brains of control wild-type and *mdx* mice:

1. Histological and ultrastructural analyses of brain capillaries.
2. Expression analysis of several important BBB components assayed by qRT-PCR.
3. Studies of fluorescent tracer accumulation within the brain.

3.2. Results

3.2.1. Neurovascular unit morphology

Immunofluorescent microscopy was used to visualise neurovascular unit components in both wild-type C57BL/10 and *mdx* mouse brains (Figure 3.2). Astrocytes were stained for GFAP and cellular processes were seen to emanate from cell bodies towards neighbouring capillaries where they could be seen to form endfeet surrounding the endothelium. Such structures could be seen both in wild-type and *mdx* cortex. Furthermore, astrocyte endfeet themselves could be seen by staining for dystrophin protein using an antibody binding the C-terminus, thus detecting not only full-length dystrophin isoform Dp427 but also shorter isoforms such as Dp71. This antibody was used because it gave the best data in terms of staining. No obvious difference in astrocyte endfoot dystrophin staining could be discerned between *mdx* and wild-type brain. Similarly, pericyte morphology using CD13 staining appeared similar in both *mdx* and wild-type brain, with long fibrillary processes extending along the length of capillaries.

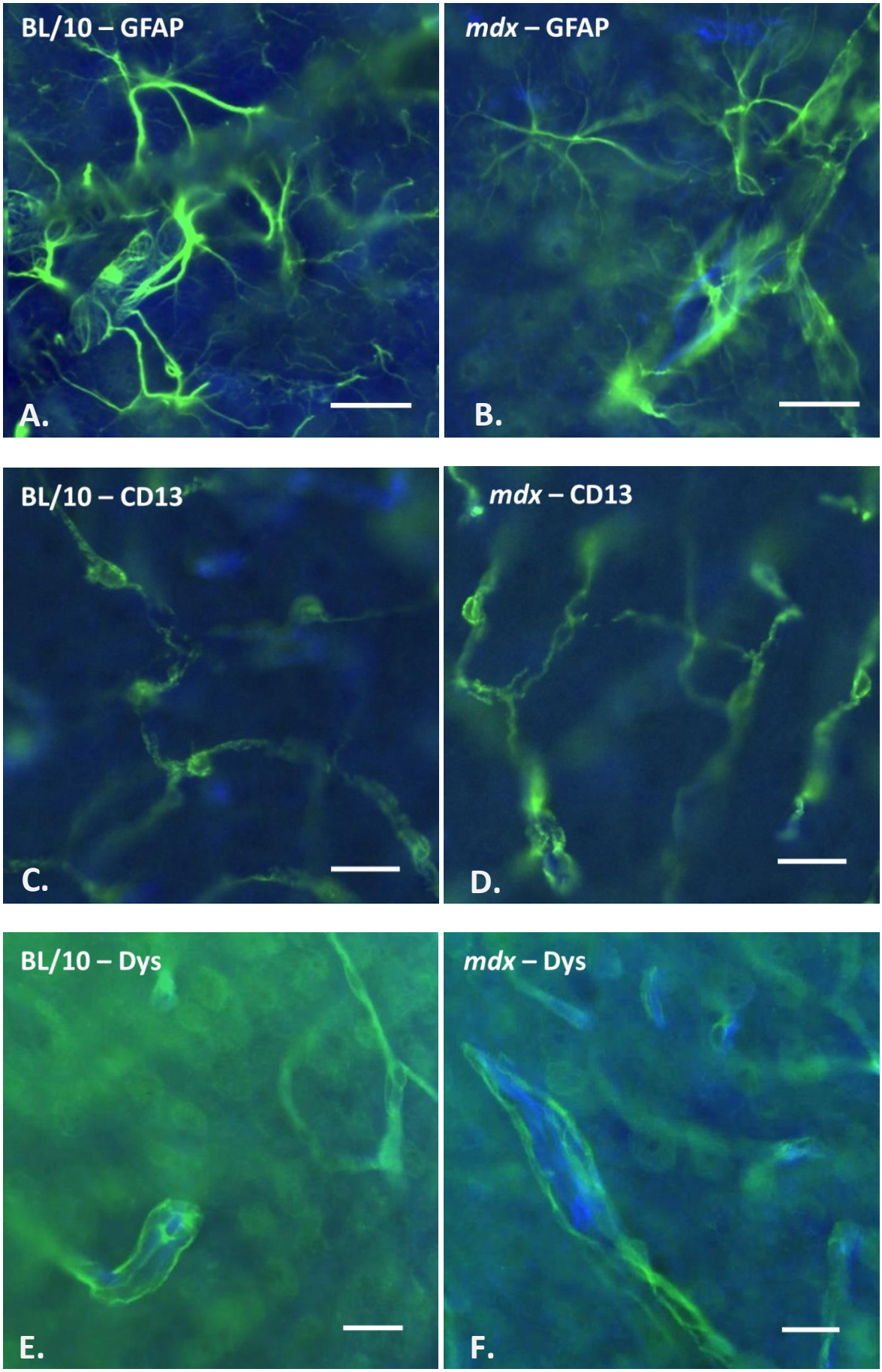
BL/10 – GFAP
A.
mdx – GFAP
B.
BL/10 – CD13
C.
mdx – CD13
D.
BL/10 – Dys
E.
mdx – Dys
F.

Figure 3.2. Fluorescent immunostaining of adult (5-month-old female) mouse cerebral cortex. **A**. In wild-type brain stained for GFAP, astrocytes can be seen to send out processes towards nearby blood-vessels. **B**. Similar processes are also seen in *mdx* brain. **C**. Pericytes can be seen to extend along the length of brain capillaries in wild-type brain. **D**. The pattern of pericyte staining is not appreciably different in *mdx* brain. **E**. Dystophin is present at astrocyte endfeet surrounding capillaries in wild-type brain. **F**. Dystrophin staining is still seen in astrocyte endfeet in *mdx* brain since this antibody stains the C-terminus and detects shorter protein isoforms such as Dp71. Green = GFAP (**A**, **B**), CD13 (pericyte, **C**, **D**), Dys (dystrophin, **E**, **F**). Blue = podocalyxin (endothelial). Scale bars = 20 µm.

Transmission electron microscopy (TEM) was used to assess the ultrastructure of capillaries within mouse cerebral cortex (Figures 3.3, 3.4 and 3.5). In both wild-type and *mdx* samples, endothelial cells had an intact structure with no visible vacuolation of the cytoplasm. The basement membrane surrounding the capillaries appeared continuous in all cases and the tight junctions present between endothelial cells had a similar appearance in both groups of mice, comprising electron-dense regions situated along closely apposed cell membranes. Depending on the plane of orientation of the cut section, several 'kissing points' could be discerned along the length of the tight junction complexes. Very little active endocytosis or exocytosis could be seen within the brain endothelial cells.

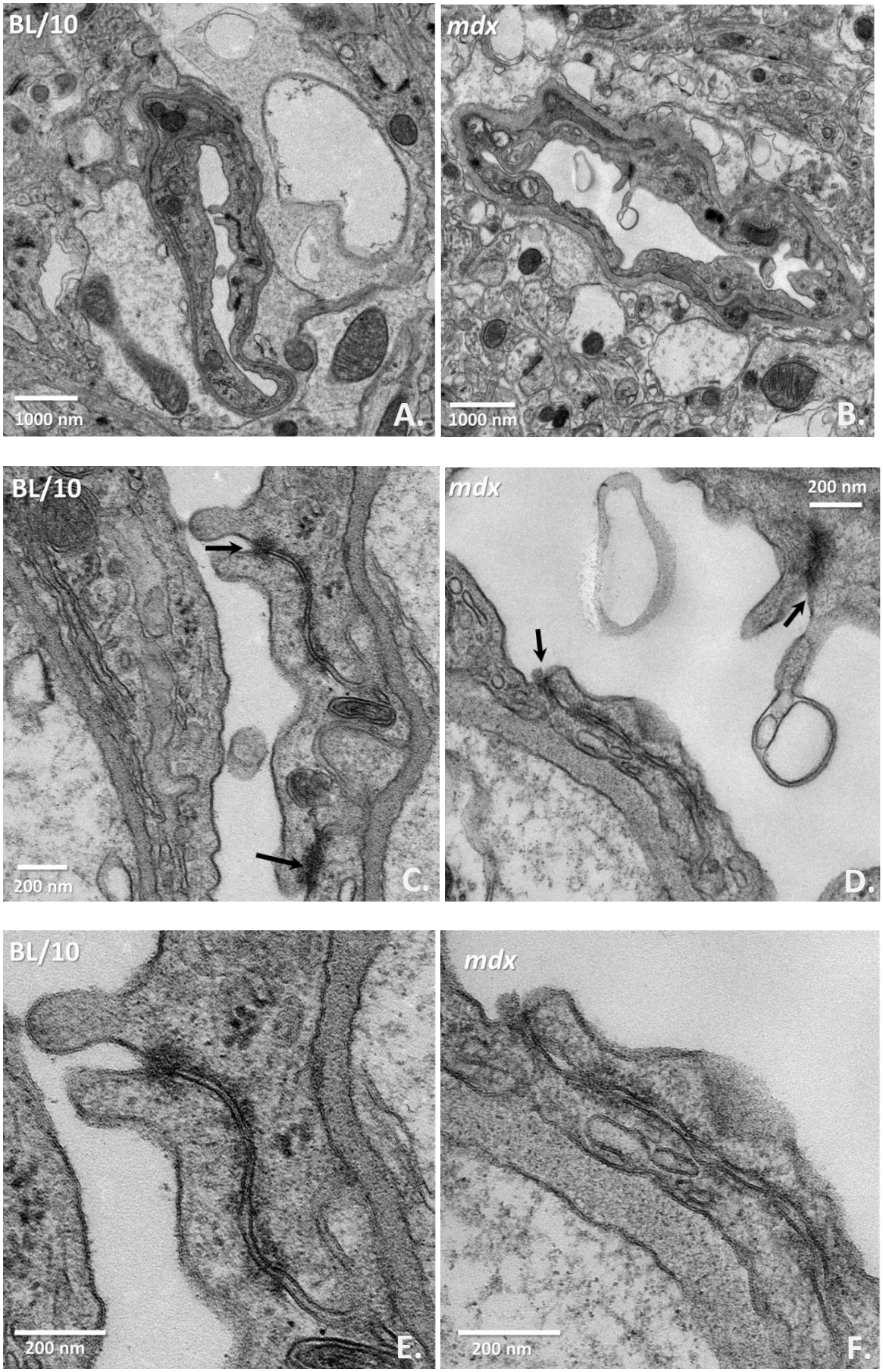
BL/10
1000 nm
A.
mdx
1000 nm
B.
BL/10
200 nm
C.
mdx
200 nm
D.
BL/10
200 nm
E.
mdx
200 nm
F.

Figure 3.3. Ultrastructure of brain capillaries from cerebral cortex of adult wild-type and *mdx* mice. **A**, **C** and **E**. Transverse section of a wild-type brain capillary seen at increasing magnification. The lumen of the capillary has collapsed with specimen preparation. However, two electron-dense tight junctions are visible at the interfaces between the apposing endothelial cell membranes (arrows in **C**). **B**, **D** and **F**. Increasingly magnified views of a brain capillary in transverse section from an *mdx* mouse. Two tight junctions can also be seen in the endothelial wall of this vessel (arrows in **D**). In both sets of images, note the relative sparsity of intracellular vesicles.

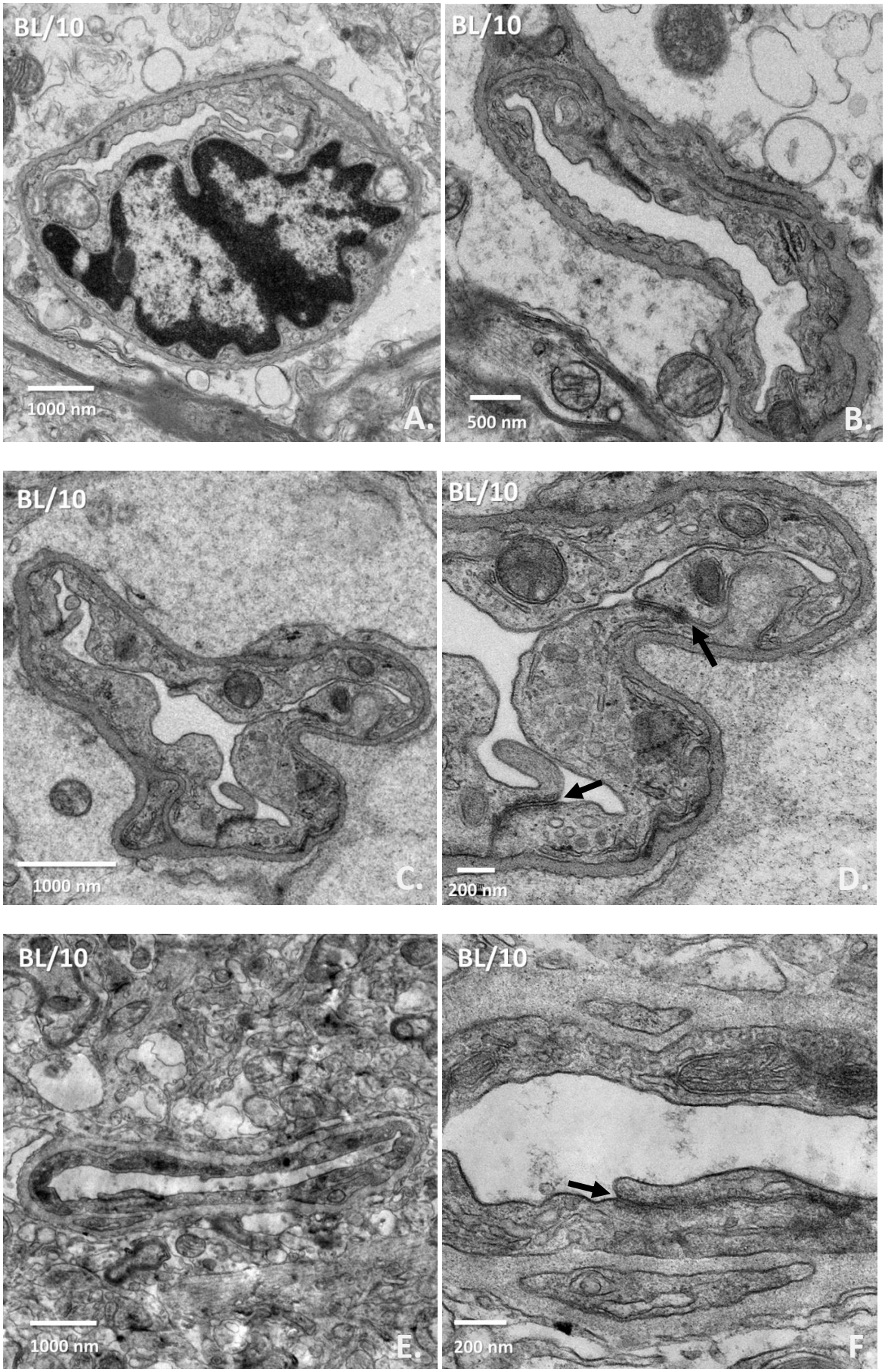
BL/10
1000 nm
A.
BL/10
500 nm
B.
BL/10
1000 nm
C.
BL/10
200 nm
D.
BL/10
1000 nm
E.
BL/10
200 nm
F

Figure 3.4. Further examples of wild-type (BL/10) mouse cerebral cortex capillary ultrastructure. **A**. An endothelial cell nucleus is clearly visible. **B**. A dark electron-dense tight junction can be seen in the upper border of this capillary. **C**. Here the capillary is surrounded by pale granular material, which is the cytoplasm of astrocyte endfoot processes. **D**. This view of the capillary in **C** at higher magnification shows two endothelial tight junctions (arrows). **E**. A capillary can be seen among surrounding neuropil structures. **F**. This magnified view of **E** shows a tight junction present between two interdigitating endothelial cell leaflets (arrow). This capillary appears to have a number of vesicular structures undergoing endo- and/or exocytosis.

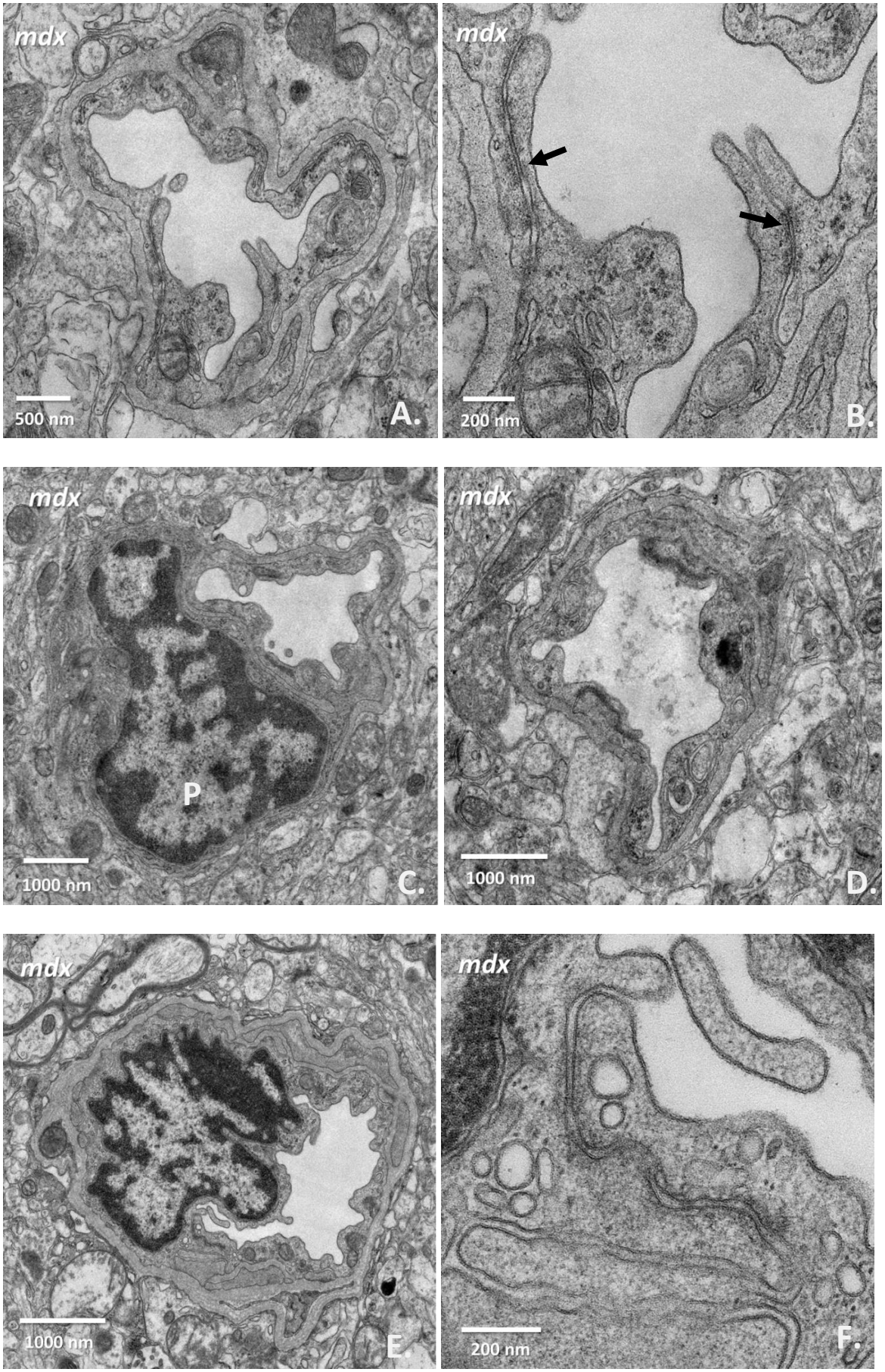
mdx
500 nm
A.
mdx
200 nm
B.
mdx
P
1000 nm
C.
mdx
1000 nm
D.
mdx
1000 nm
E.
mdx
200 nm
F.

Figure 3.5. Further examples of *mdx* mouse capillary ultrastructure in cerebral cortex. **A**. This capillary has two tight junctions visible. Higher magnification (**B**) reveals several electron-dense regions at several points along each junction (arrows). **C**. Here the nucleus of a pericyte (**P**) is clearly visible. The pericyte is enclosed within the same basement membrane as the endothelium. Note that the basement membrane is continuous in all these cases. **D**. Another capillary with two well-formed tight junctions. **E**. The nucleus of an endothelial cell is visible here. Part of a pericyte process is visible within the basement membrane to the bottom right of the image. **F**. This higher magnification view of **E** shows a tight junction between endothelial cell membranes.

3.2.2. BBB gene expression by qRT-PCR

In order to examine possible differences in the expression of genes associated with the BBB in *mdx* mice, qRT-PCR was used to analyse RNA collected from the brains of mice aged from P1 up to 1 year (Figure 3.6). *Cldn5* encodes claudin-5, an important tight junction protein known to be present in brain endothelium (Morita et al., 1999). Expression in brain was similar between wild-type and *mdx* mice except at P7 where expression in *mdx* was slightly reduced (89% of wild-type) and at 4 weeks where it was slightly increased (29% increase over wild-type). *Tjp1* encodes ZO-1, an adaptor protein linking tight junction occludin to the endothelial cytoskeleton (Fanning et al., 1998). The only difference in *Tjp1* expression was found at P14 where it was decreased in *mdx* (80% of wild-type). *Mfsd2a* is a gene recently found to regulate BBB permeability via control of endothelial vesicular trafficking (Ben-Zvi et al., 2014). Interestingly, there appeared to be

some decrease in this gene's expression in *mdx* brain at P1 and P14 and also at 1 year of age. The pericyte marker *Pdgfrb* had slightly increased expression at P1 in *mdx* (18% more) and slightly decreased expression in P14 *mdx* (75% of wild-type). Expression of *Aqp4*, a marker for astrocyte endfeet (Nielsen et al., 1997), was low at P1 but increased to a peak of expression at P14, reducing somewhat at subsequent ages. At P14 and P21 there was decreased *Aqp4* expression in *mdx* brain (78% and 60% of wild-type respectively). *Gfap* expression was not significantly different between either group at any time point, however expression was considerably lower at P1 than at other ages.

The brain expression of two important *Dmd* isoforms was also analysed. Dp71 is a dystrophin protein isoform known to be highly expressed in brain. Its RNA transcript has a transcriptional start site located between exons 62 and 63, far downstream of the exon 23 STOP mutation present in *mdx* mice. Expression of this isoform was fairly uniform across all ages and no statistically significant difference was detected between *mdx* and wild-type expression except at 8 weeks where *mdx* expression was 93% of wild-type. The full-length *Dmd* transcript encodes the Dp427 dystrophin isoform and this therefore contains the *mdx* mutation. Interestingly, mRNA expression of full-length *Dmd* at P1 is much lower than the adult level in both *mdx* and wild-type mice, being 30% and 23% of 3-4 month adult values respectively. From P7 to 1 year old, full-length *Dmd* expression in *mdx* is reduced, being between 55% and 71% that of wild-type.

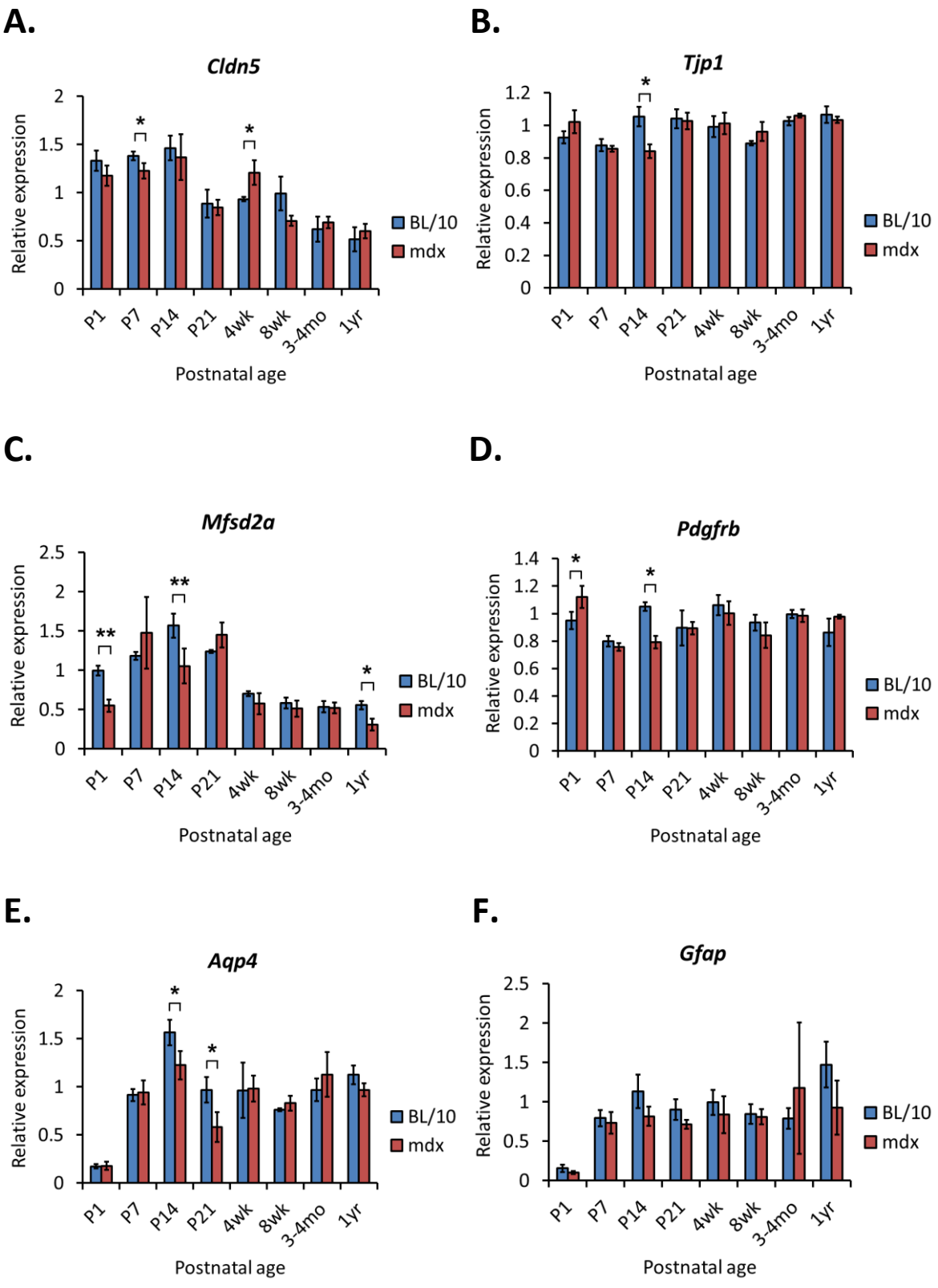
A.
Cldn5
Relative expression
Postnatal age
BL/10
mdx
P1
P7
P14
P21
4wk
8wk
3-4mo
1yr
B.
Tjp1
C.
Mfsd2a
D.
Pdgfrb
E.
Aqp4
F.
Gfap

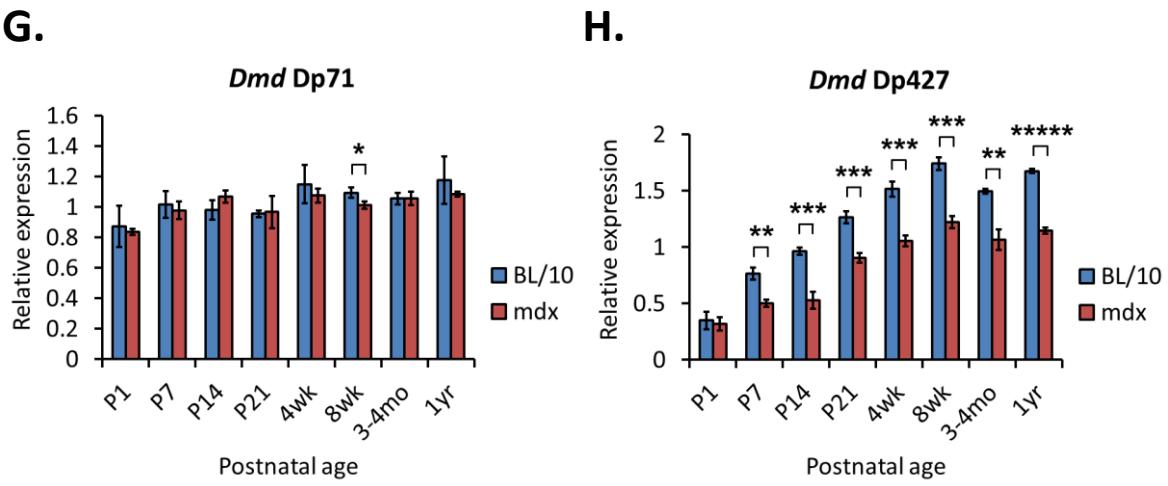

Figure 3.6. qRT-PCR analysis of BBB component gene expression in mouse cerebrum. Both wild-type (BL/10) and *mdx* mice generally exhibit similar levels of BBB-related gene expression at different ages. Values have been normalised to those obtained from pooled wild-type cDNA across all ages. **A**. *Cldn5* expression is slightly reduced in P7 *mdx* (1.23) versus wild-type (1.38) but conversely expression is increased in 4-week-old *mdx* (0.98) versus wild-type (0.93). **B**. *Tjp1* (ZO-1) expression is stable across all ages and similar between groups except at P14 where *mdx* (0.84) has decreased expression to wild-type (1.05). **C**. *Mfsd2a* expression is decreased in *mdx* versus wild-type at P1 (0.55 vs. 1.00), P14 (1.05 vs. 1.57) and at 1 year (0.31 vs. 0.56). **D**. *Pdgfrb* expression is increased in *mdx* compared to wild-type at P1 (1.12 vs. 0.95) but decreased in *mdx* at P14 (0.79 vs. 1.05). **E**. *Aqp4* expression is low at birth but increases rapidly in the first week or so of life. There is some decreased expression in *mdx* versus wild-type at P14 (1.22 vs. 1.56) and at P21 (0.58 vs. 0.97). **F**. *Gfap* expression is similarly low at birth but increases in the first week or so. There are no significant differences in expression between wild-type and *mdx* mice. **G**. *Dmd* isoform Dp71 is expressed quite stably over time with only a slight difference in expression at 8 weeks between *mdx* (1.01) and wild-type (1.09). **H**. In

comparison, the full-length *Dmd* isoform Dp427 has marked and consistently decreased expression in *mdx* brain from P7 onwards. * $p < 0.05$, ** $p < 0.01$, *** $p < 0.001$, ***** $p < 0.00001$ by unpaired, two-tailed t-test assuming equal variance.

3.2.3. Fluorescent tracer accumulation in brain

A functional assessment of BBB integrity was carried out by analysing the accumulation of fluorescent tracer within the brain following systemic administration in *mdx* and wild-type mice (a mixture of males and females) at different ages. AlexaFluor 555 cadaverine (Mw ~950) was used as a tracer and was administered by intraperitoneal injection at a dose of 20 μg/g. Mice were perfused 2 hours after injection, after which the fluorescence of homogenised cerebrum was quantified and normalised to tissue weight. Although this experiment was conducted at two different centres using differing equipment and instruments (P1 – P14 at Karolinska Institute, Sweden, P14 – 4 months at University of Oxford), clear trends could still be discerned (Figure 3.7). In terms of overall fluorescence per gram of tissue, brain accumulation of tracer in both *mdx* and wild-type mice decreased with age, suggesting a reduction in BBB permeability. Across the range of age groups tested, the only significant differences detected between *mdx* and wild-type brain fluorescence were at P14 where *mdx* showed higher brain fluorescence (between 1.9- and 2.2-fold), at 4 weeks old where *mdx* showed decrease in brain fluorescence (0.70-fold) compared to wild-type, and at 4 months where mdx again appeared to show only 0.42-fold the fluorescence of wild-type.

A higher molecular weight tracer (TMR 10 kD dextran) was also used in P14 and 8 week mice to investigate the possibility that larger molecules of a similar size to therapeutic oligonucleotides might demonstrate a different pattern of BBB penetration (Figure 3.7 E and F). While a decrease in brain fluorescence was observed between P14 and 8 weeks, no significant difference in permeability was seen between *mdx* and wild-type mice.

A.

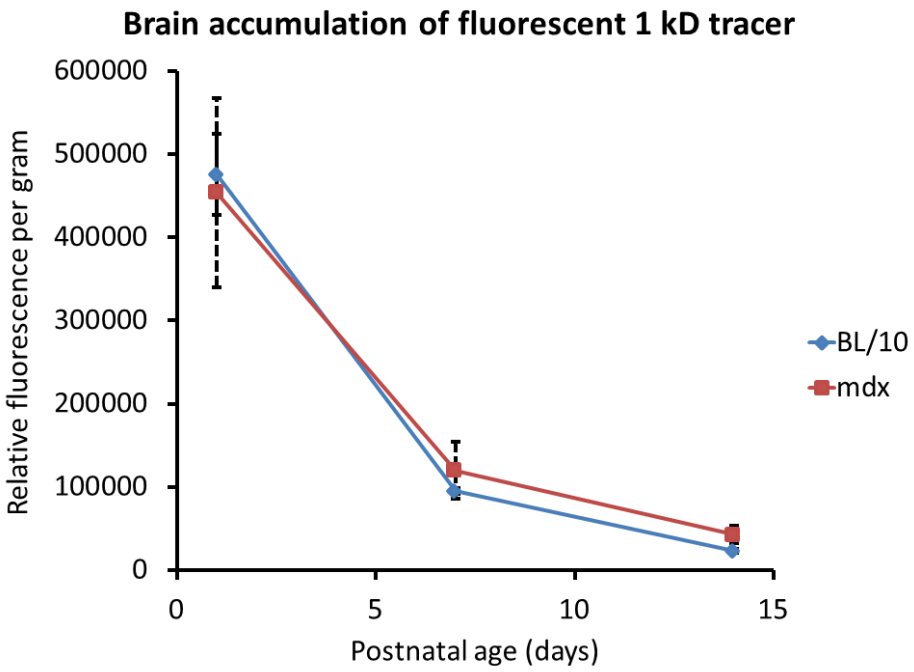
Brain accumulation of fluorescent 1 kD tracer
Relative fluorescence per gram
600000
500000
400000
300000
200000
100000
0
0
5
10
15
Postnatal age (days)
BL/10
mdx

B.

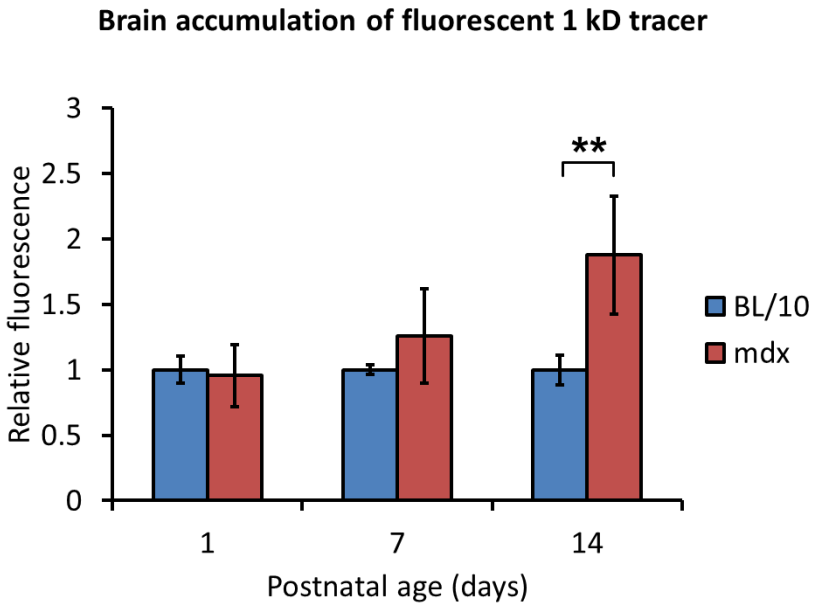
Brain accumulation of fluorescent 1 kD tracer
Relative fluorescence
3
2.5
2
1.5
1
0.5
0
**
1
7
14
Postnatal age (days)
BL/10
mdx

C.

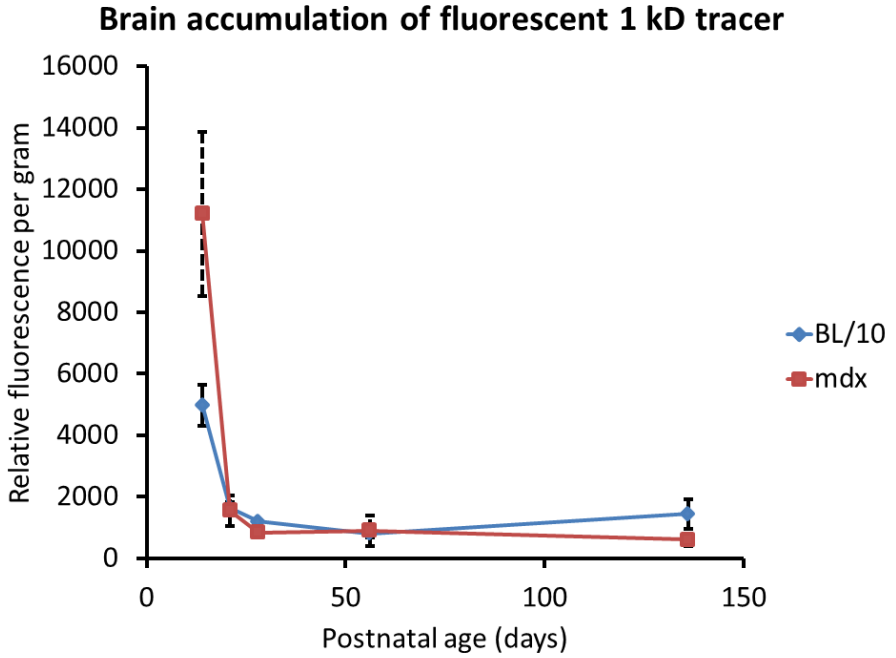
Brain accumulation of fluorescent 1 kD tracer
Relative fluorescence per gram
16000
14000
12000
10000
8000
6000
4000
2000
0
0
50
100
150
Postnatal age (days)
BL/10
mdx

D.

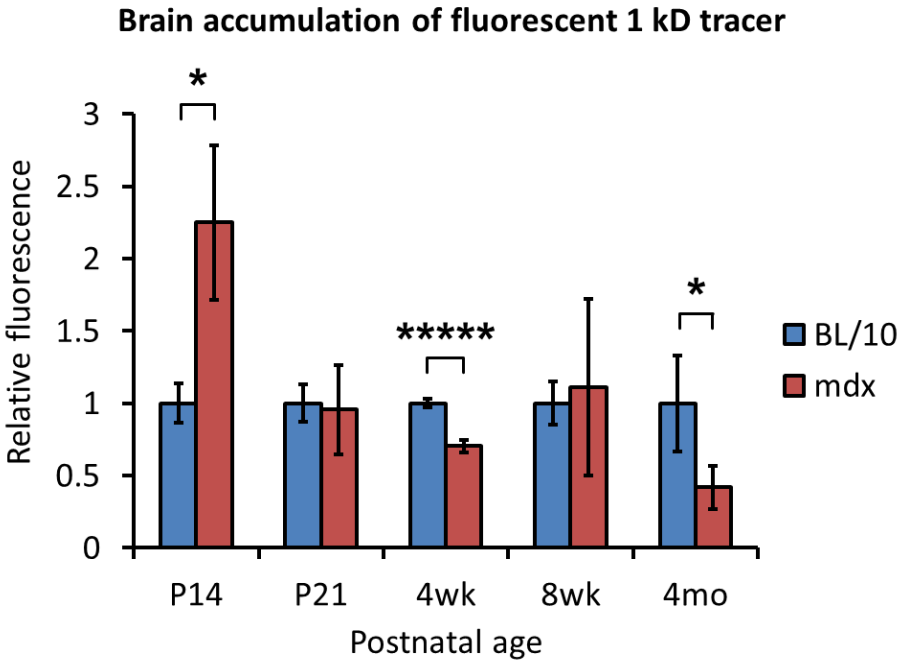
Brain accumulation of fluorescent 1 kD tracer
Relative fluorescence
3
2.5
2
1.5
1
0.5
0
*
*****
*
P14
P21
4wk
8wk
4mo
Postnatal age
BL/10
mdx

E.

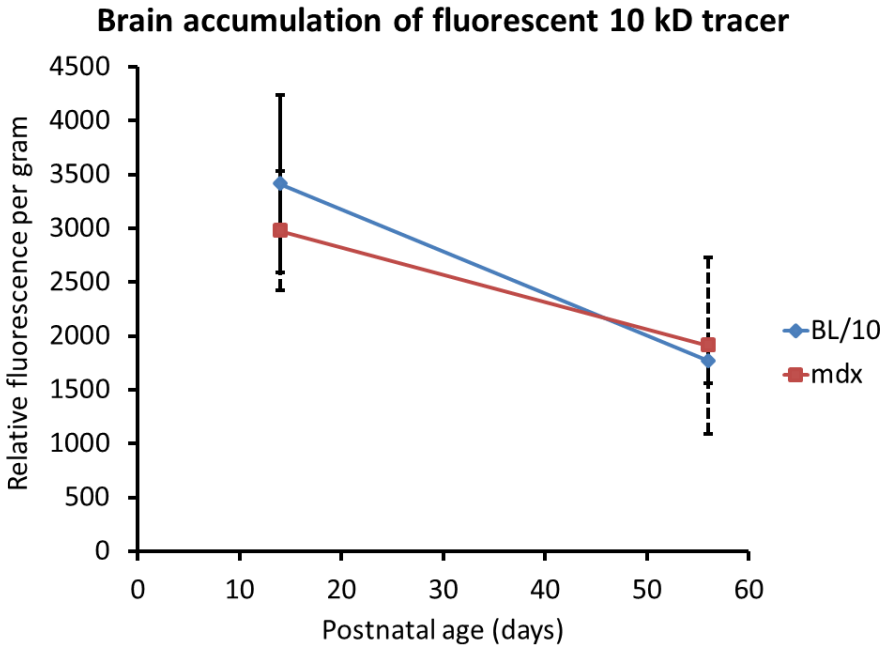

F.

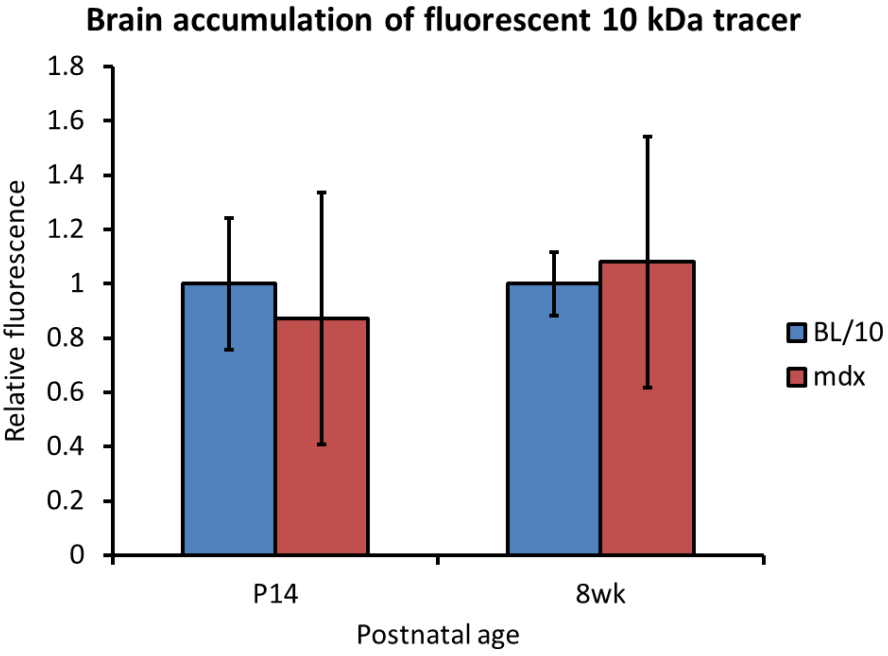

Figure 3.7. Accumulation of fluorescent tracer in *mdx* and wild-type (BL/10) mouse brain at different ages (mixture of males and females). AlexaFluor 555 cadaverine (1 kD)

was injected intraperitoneally and allowed to circulate for 2 hours, after which mice were perfused transcardially with PBS. Cerebral tissue was weighed, homogenised and assayed for fluorescence, generating a relative figure for fluorescence by weight of tissue. Note that the fluorescence data for **A** and **B** were collected in Sweden using a slightly different protocol and with different instruments to those in **C** and **D** and so the figures cannot be directly compared. **A.** Relative fluorescence per gram of cerebrum for ages P1, P7 and P14. There is a downward trend in fluorescence in brain tissue from P1 to P14 for both *mdx* (90% reduction) and wild-type (95% reduction). **B.** Data for P1, P7 and P14 normalised to wild-type levels of fluorescence. **C.** Relative fluorescence per gram of cerebrum for ages P14 to 4 months. There is a continued downward trend of fluorescence per gram in both *mdx* and wild-type brain. **D.** Data for for P14 to 4 months normalised to wild-type fluorescence. The data appear to demonstrate significant differences in fluorescence in *mdx* brain versus wild-type at P14 (2.2-fold increase), at 4 weeks (a decrease to 0.70-fold wild-type) and at 4 months (a decrease to 0.42-fold wild-type). **E** and **F**. The same analysis was performed at P14 and 8 weeks with a larger molecular weight tracer (TMR 10 kD dextran), which was also injected intraperitoneally and left to circulate for 3 hours before perfusion. No significant differences in fluorescence can be observed. $n \geq 3$ in each age group. 4wk = 4 weeks, 8wk = 8 weeks, 4mo = 4 months. Error bars represent standard deviation (in **A** and **C**, solid line error bars are BL/10, dashed error bars are *mdx*). * $p < 0.05$, ** $p < 0.01$, ***** $p < 0.00001$ based on unpaired, two-way t-test assuming equal variance.

In order to evaluate the pattern of tracer accumulation within the brain, coronal sections of PFA-fixed brains were imaged by fluorescent microscopy (Figure 3.8). At P1 there was

abundant tracer uptake seen in the choroid plexus as well as scattered uptake in inferolateral regions of the brain. At P14 there was still choroid plexus uptake visible in *mdx* brain but not in wild-type. Portions of the brain that had been damaged in the course of extracting the tissue from the skull also appeared to show tracer uptake. In adult brain, little to no discrete tracer uptake was seen, except for some mild uptake in *mdx* choroid plexus. Notably, portions of adult brain damaged during harvesting did not demonstrate any tracer uptake.

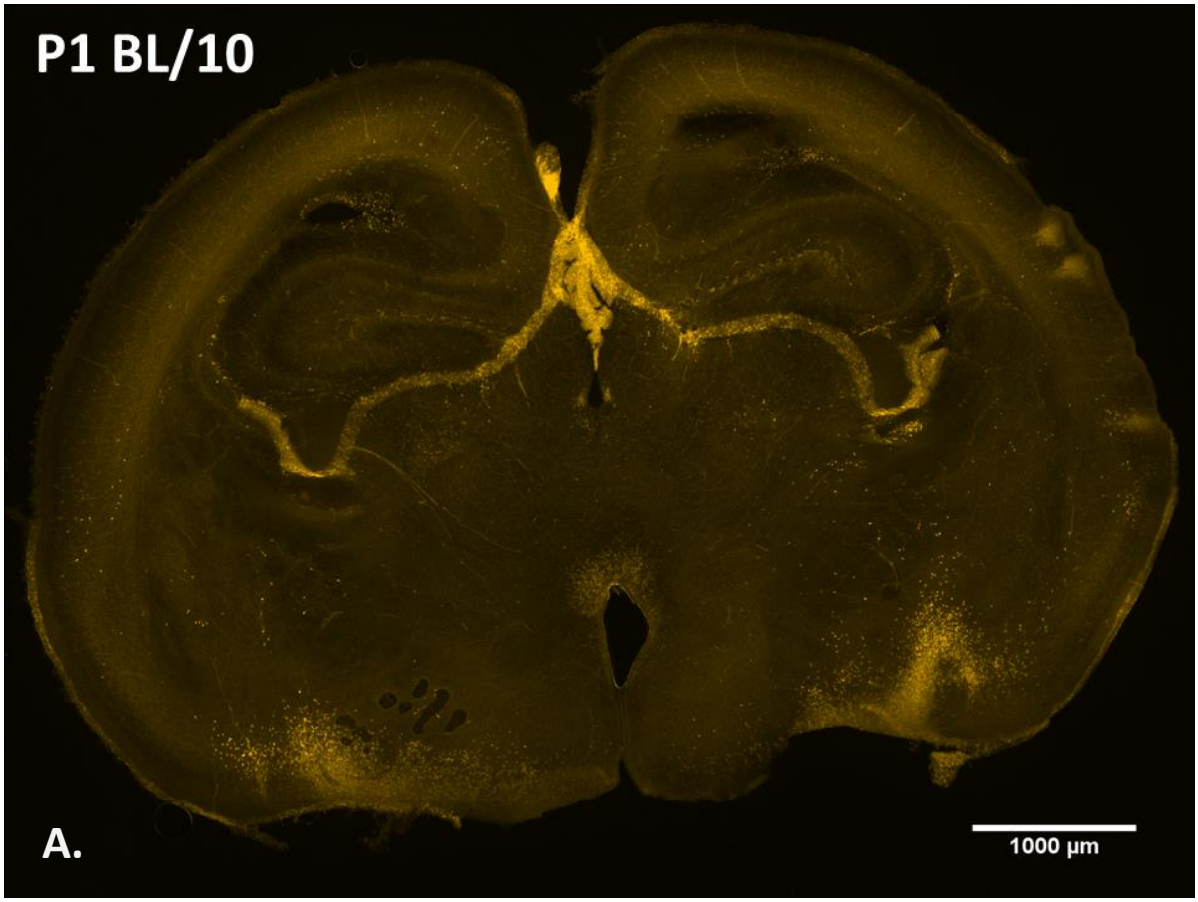
P1 BL/10
A.
1000 µm

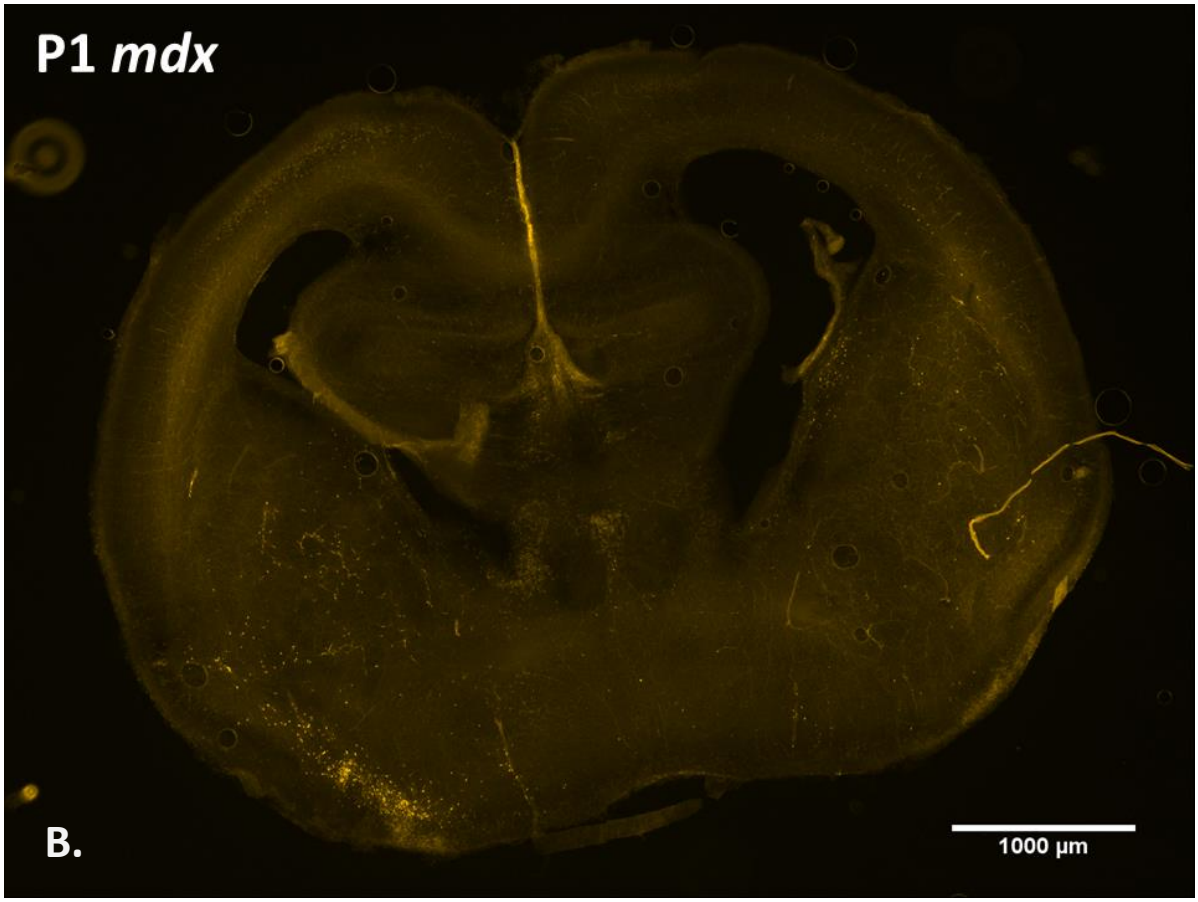
P1 *mdx*
B.
1000 µm

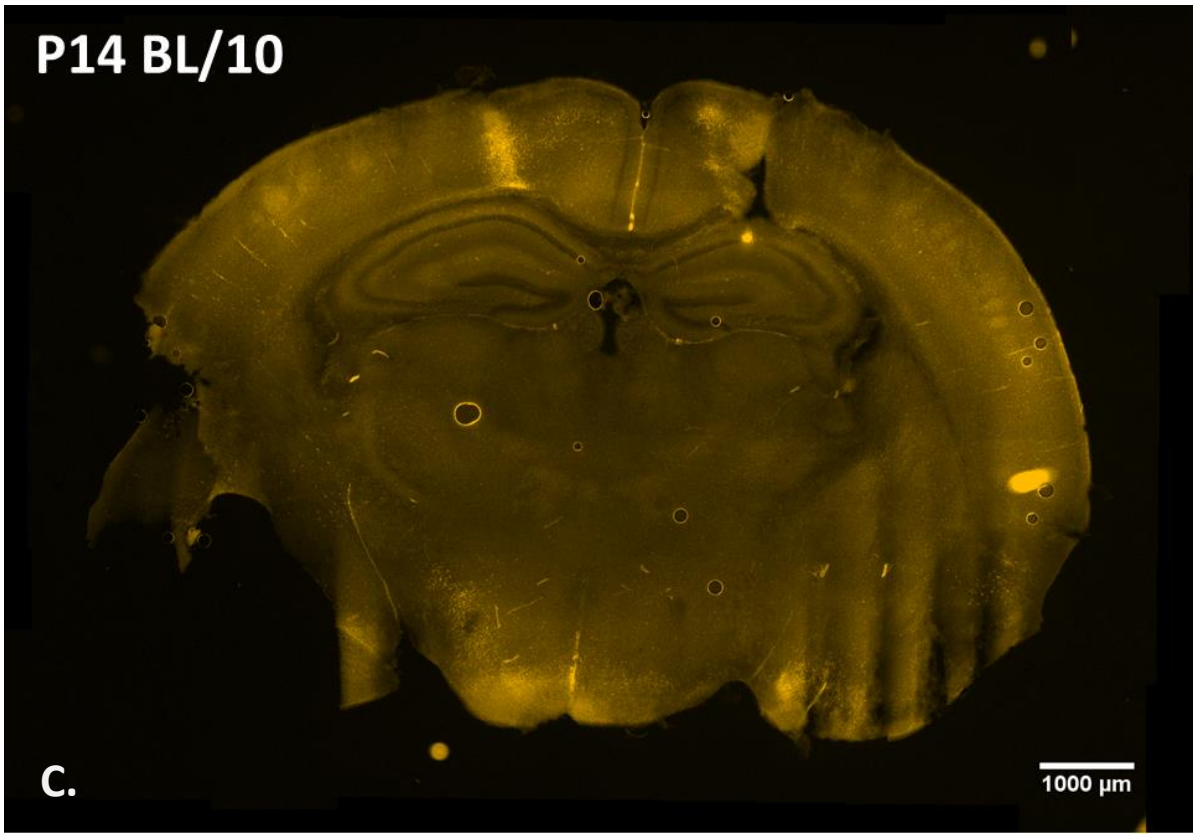
P14 BL/10
C.
1000 µm

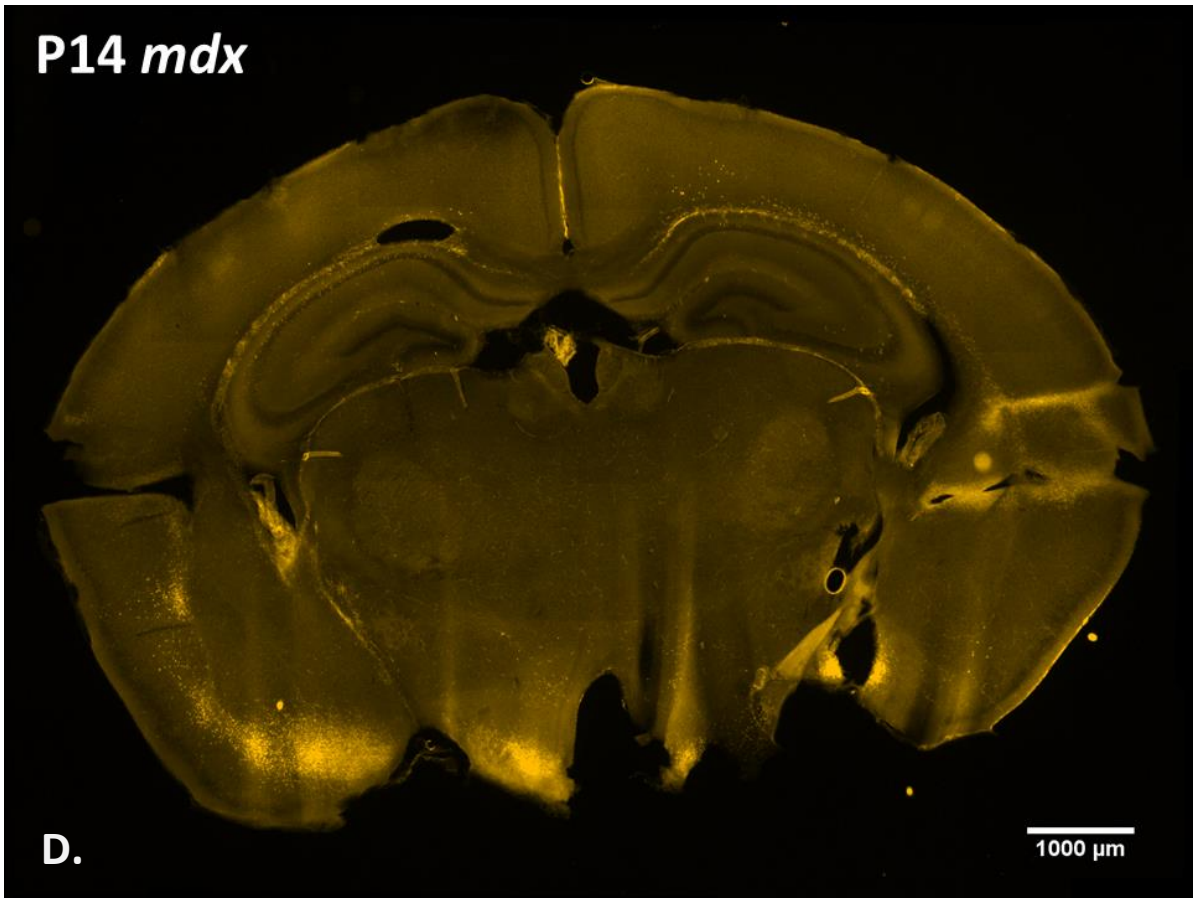
P14 mdx
D.
1000 µm


Adult BL/10
E.
1000 µm

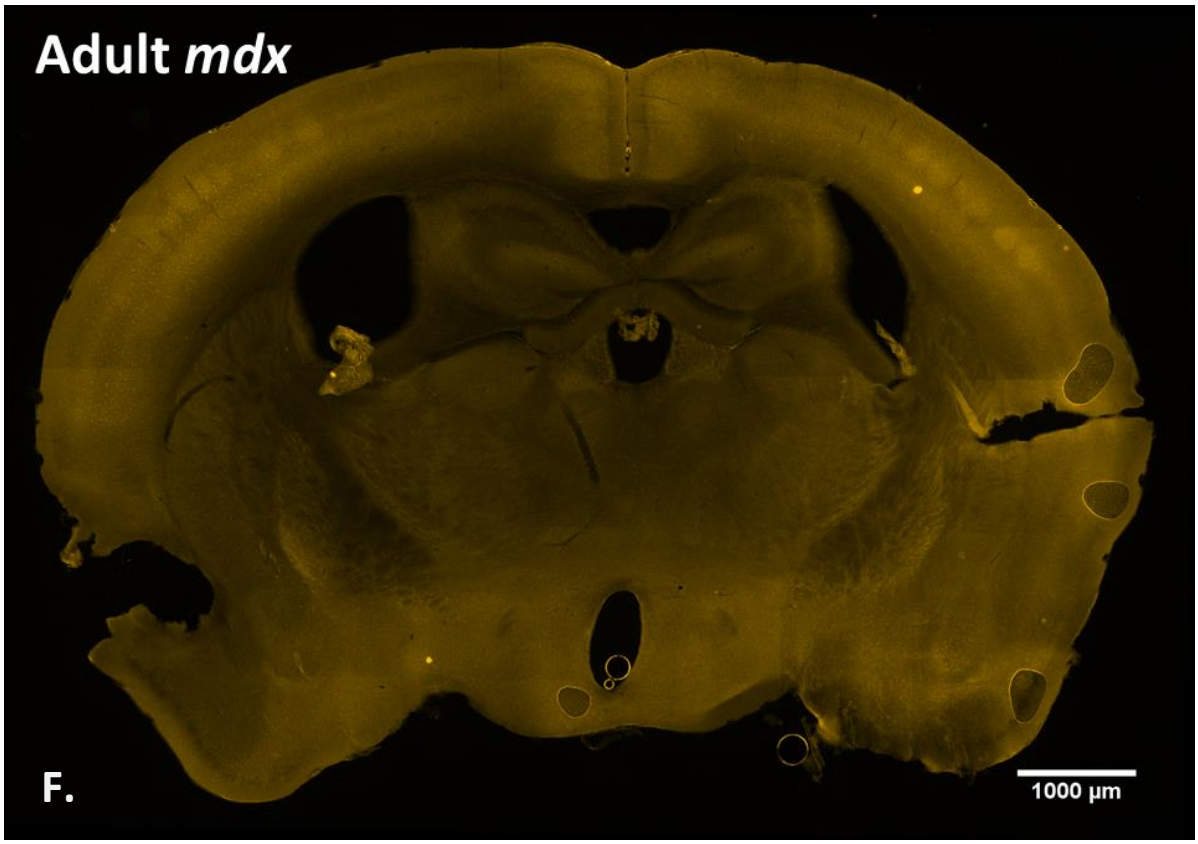
Adult *mdx*
F.
1000 µm

Figure 3.8. Coronal sections of mouse brain following systemic AlexaFluor 555 cadaverine administration. **A**. Wild-type P1 brain. Choroid plexus lying within the dorsal third ventricle is highlighted by tracer, as is the inferior border of the hippocampal fimbriae bilaterally. There is also some scattered uptake of tracer superior to the ventral portion of third ventricle in the region of the hypothalamus, as well as within the inferolateral portions of the section. **B**. *mdx* P1 brain. Although this section is slightly more rostral than **A**, it is still possible to discern some tracer uptake in the choroid plexus in the lateral ventricles. There is also some inferolateral tracer uptake as well as bright tracer signal in-between the cerebral hemispheres. **C**. Wild-type P14 brain. Note this section is incomplete at the lower left and has some knife chatter marks at the bottom right. In this case, choroid plexus within the dorsal third ventricle and in the lateral ventricles does not appear to be highlighted by tracer. There is, however, faint tracer signal at the inferior border of the hippocampal formation extending towards the fimbriae and some diffuse uptake in the inferior portion of the section. Notably, there is also tracer uptake at two points in the dorsal cerebral cortex where the brain has been injured during removal of the brain from the skull. **D**. *mdx* P14 brain. Here, choroid plexus in lateral and dorsal third ventricles is clearly stained by tracer. Tracer also appears to outline both superior and inferior borders of the hippocampus. Once again there is uptake in the cerebral cortex where the brain has been injured during harvesting, as well as diffuse uptake inferiorly. **E**. Wild-type adult brain (5 months). In contrast to sections from earlier ages, there is no focal tracer uptake seen in adult sections. There is neither any choroid plexus uptake nor uptake here the cortex has been damaged. **F**. *mdx* adult brain (5 months). Once again there is no clear focal tracer uptake. However, in this

section the choroid plexus appears more brightly stained than in **E**. Please note that for **E** and **F**, tracer injections were performed intravenously rather than intraperitoneally.

3.3. Discussion

3.3.1. Summary of results

In this study, a number of structural and functional analyses have been performed in order to investigate the integrity of the BBB in *mdx* mice. In terms of structure, immunofluorescent staining of adult brain sections was able to successfully demonstrate intact components of the neurovascular unit (namely endothelium, pericytes, astrocytes and astrocyte endfeet) in both wild-type and *mdx* mice. Similarly, using TEM it was possible to show that capillaries within the cerebral cortex of adult *mdx* mice appeared to have an intact ultrastructure with no obvious tight junction abnormalities, endothelial vacuolations or discontinuities in basement membranes. Expression analysis of genes contributing to BBB structure and function showed generally similar expression patterns between wild-type and *mdx* mice. Full-length *Dmd* expression was reduced in *mdx* mice but this is to be expected and is likely a reflection of nonsense-mediated decay. However, a number of apparently significant, though generally quite modest, differences were found in nearly all genes tested at certain ages. The limits of the statistical methods used are likely to be a factor here and so such significance should be interpreted with caution, especially as only three mice were assayed per age group and each set of three consisted of a mixture of both males and females. Nevertheless, most of these observable differences were seen in the first two weeks of life.

In terms of BBB function, brain accumulation of systemically administered fluorescent 1 kD tracer decreased with age. There were apparent differences in accumulation between wild-type and *mdx* mice at P14 and at 4 weeks of age. Although these differences

between groups appeared to achieve statistical significance (particularly at 4 weeks where $p < 0.00001$), their overall effects were small in terms of fluorescence per gram of tissue when compared to the effect of age. Use of a larger 10 kD tracer did not result in different brain accumulation at P14 or at 8 weeks of age. Imaging of fixed brain sections following fluorescent tracer administration revealed unusually discrete patterns of accumulation in certain areas of the brain in P1 and P14 mice. Interestingly, the choroid plexus exhibited tracer signal at P1 (both in wild-type and *mdx*) and also at P14 in *mdx* mice. Tracer uptake was greatly diminished in the adult brain of both wild-type and *mdx* mice, although some tracer was still seen in adult *mdx* choroid plexus.

3.3.2. Does the *mdx* mouse have a defective BBB?

The BBB is of fundamental importance to the function of the CNS. Indeed, the consequences of its anatomical disruption or physiological dysfunction are generally dire, leading to significant neurological compromise. Brief consideration of disorders known to involve BBB damage will serve to make this fact abundantly clear: CNS infection, brain tumour, brain trauma, ischaemic stroke, multiple sclerosis, Alzheimer's disease, Parkinson's disease, epilepsy, motor neuron disease (Ballabh et al., 2004; Rosenberg, 2012; Zlokovic, 2008). While such disorders are of course more complex than just being a matter of BBB disturbance, it is nevertheless instructive to note that all of them involve an acquired BBB defect, which in many of these cases affects only a portion of the cerebral vasculature. This being so, any disorder causing a global congenital deficit in BBB function across both developmental and adult life would be expected to result in proportionately greater neurological dysfunction. Clearly this is not the case in patients

with DMD, even though there may be some cognitive impairment to a varying degree. Similarly, the *mdx* mouse is able to function relatively well in the laboratory environment and its neurocognitive phenotype is suitably subtle as to require specific behavioural testing to elicit it (Sekiguchi et al., 2009). *A priori* then, any BBB defect that might occur in human DMD and be present in the *mdx* mouse would be at worst expected to be of a mild and limited nature.

The endothelial tight junctions of the BBB are integral to its barrier function (Wolburg and Lippoldt, 2002). The apparent integrity of these structures as seen in the electron micrographs shown above thus supports the idea that the *mdx* BBB is structurally intact. Similarly, the results of immunofluorescent staining of the neurovascular unit in adult wild-type and *mdx* mice looked noticeably similar and do not support the idea of a severely disrupted BBB in *mdx* mice. In terms of gene expression, the overall trends in up- and downregulation of individual genes over time appeared generally similar between both *mdx* and wild-type mice. Given that these genes are all involved in functions relating to the neurovascular unit, this would again suggest an overall similarity in BBB functionality between the two groups. Interestingly, a number of expression differences were in fact detected, mainly during the developmental period. However, the anatomical and physiological significance of these differences remains unclear. Whilst further information regarding this may be obtainable through protein-based analyses such as Western blotting and immunohistochemical staining, the relevance of performing such studies must be weighed against the functional data from the fluorescent tracer results.

Two different fluorescent tracers have been used in this study, dextran and cadaverine. Dextran amines are synthetic hydrophilic polysaccharides that are generally biologically inert and resistant to glycosidic cleavage. They have been widely used as tracers to study neuronal axonal transport (Reiner et al., 2000). Cadaverine (pentane-1, 5-diamine) is a naturally occurring metabolite of lysine that is excreted in the urine along with other diamine compounds (Andersson et al., 1978). It is formed through the decarboxylation of lysine either by bacterial lysine decarboxylase within the gut or by ornithine decarboxylase within mammalian cells and it has been found to occur naturally within the brain (Alhonen-Hongisto and Jänne, 1980; Hawel et al., 1994; Stepita-Klauco and Dolezalova, 1974). Fluorescently-labelled cadaverine has been used previously to measure BBB permeability using a protocol very similar to the one described here (Armulik et al., 2010). The use of these two tracers in the present study has demonstrated that their uptake in brain following systemic administration was broadly similar between *mdx* and wild-type mice over a range of ages. This suggests an overall similarity in BBB permeability between the two groups. However, as with the results of gene expression, there were some apparent differences detected, specifically at P14, 4 weeks and 1 year. While statistically significant, the inter-group differences at 4 weeks and 1 year were of overall small amplitude and it may be a technical limitation of this experiment (e.g. insufficient n number or variable quality of perfusion) that accounts for these discrepancies. The increase in *mdx* brain fluorescence at P14, on the other hand, was somewhat larger and remained consistent across two separately performed experiments, one in Sweden and the other in Oxford. This is thus more suggestive of a real difference in brain tracer accumulation. Whilst this increased accumulation may relate to the variations in BBB gene expression mentioned previously and may possibly

represent some kind of delay in BBB maturation in *mdx* mice, it may also be that the true explanation for such a difference does not strictly relate to the BBB at all.

3.3.3. What about the BCSFB?

In considering the images of fluorescent tracer accumulation in the brain, several notable observations become apparent. First of all, the uptake of tracer in P1 and P14 brain was not uniform across the sections but instead was limited to discrete regions. This is not what one would expect if tracer accumulation were the result of a generalised increase in BBB permeability, since the ubiquitous distribution of brain capillaries would tend to lead to uptake throughout the parenchyma. An alternative explanation must therefore be sought. Given that tracer uptake was prominent in the choroid plexus, it is possible that tracer uptake into the cerebrospinal fluid (CSF) is in fact responsible for the pattern of uptake observed in the brain sections. This might explain the tracer signal seen to outline the hippocampal formations as well as the midline bright tracer signal seen to lie in the longitudinal fissure (Figure 3.8 B, C and D) since these structures coincide with regions of CSF circulation. Furthermore, tracer residing within the CSF compartment would not be cleared by transcardial perfusion. It would therefore be predicted to persist *in situ* during harvesting of the brain. In this way, damage to the brain tissue during extraction from the skull could lead to tracer accumulation at the sites of injury, as well as causing a certain amount of tracking of tracer from the injured site to dependent tissue regions. Indeed, cadaverine has previously been shown to cross from the ventricular space into the brain. A study of intracerebroventricular injection of radiolabeled cadaverine into the rat brain demonstrated uptake in telencephalon, striatum, hypothalamus, midbrain,

medulla-pons and cerebellum (Salzman and Stepita-Klauco, 1981). Interestingly, however, this study found that maximal uptake of cadaverine into brain tissue from the ventricular space was relatively slow, reaching a peak 24 hours after injection, although cadaverine metabolites appeared to be taken up more quickly and peaked at 4 hours.

If this model is correct, it raises the question of whether there may be differences in the blood-CSF barrier (BCSFB) between wild-type and *mdx* mice. While the experiments performed here were not designed to specifically answer this question, there is some suggestion of this since the *mdx* choroid plexus is more prominently stained by tracer at P14 and also in adult brain. Whether such staining bears any relation to BCSFB permeability, however, remains a matter of speculation. Indeed, even in the absence of such staining, wild-type P14 brain (Figure 3.8 C) shows evidence of injury-associated tracer uptake within the cortex. Clearly further replicates would be needed to help investigate the existence of this phenomenon, as would fluorescence analysis of directly collected CSF samples. Furthermore, regardless of whether or not a difference in BCSFB permeability exists, the overall fluorescence quantification data for brain still stand and these indicate generally similar levels of fluorescent accumulation between *mdx* and wild-type mice.

3.3.4. Conclusion

From the experiments described in this chapter, it can be concluded that the BBB of *mdx* mice is not as severely damaged as previously reported in the literature. It also follows from this that the role of full-length dystrophin within the brain is not one that is central

to the development or maintenance of the BBB. Having said this, the present study is by no means comprehensive and the experiments performed are necessarily limited in their scope. The major caveats would include the small n numbers tested (particularly relating to the imaged sections of cadaverine accumulation where $n = 1$), the technical limitations of transcardial perfusion which will have affected the efficiency of tracer clearance from the cerebral microvasculature, and the lack of direct analysis of choroid plexus functionality and of CSF composition. Nevertheless, the integrity of the *mdx* BBB as demonstrated here provides a sufficient basis on which to use this mouse model to investigate the delivery of therapeutic oligonucleotide drugs to the CNS. Prior to this study, it might have been expected that delivery of oligonucleotides to the brain would have been easier to achieve in *mdx* mice owing to their reported BBB defects. However, to date the only ASO chemistry that has been reported to cross the BBB in *mdx* mice is tcDNA, whereby a study using repeat high-dose intravenous tcDNA has demonstrated an ability to reach the brain (Goyenvalle et al., 2015). This study would tend to refute this notion of a defective BBB and would instead support the applicability of the *mdx* mouse as a model for CNS drug delivery that is relevant to the potential treatment of other diseases. The investigation of such CNS-directed therapies is therefore the subject of the next chapter.

Chapter 4:

Treating *mdx* mice with peptide-conjugated antisense oligonucleotides

4.1. Introduction

In recent years, antisense oligonucleotide (ASO) therapy in the form of exon skipping has become a leading potential therapeutic prospect for the treatment of Duchenne muscular dystrophy (DMD). Two particular chemistries of oligonucleotide, 2'O-methyl phosphorothioate (2'OMePS) and phosphorodiamidate morpholino (PMO), have been taken into clinical trials for the skipping of exon 51 in DMD patients with amenable mutations (Koo and Wood, 2013). While skipping of exon 51 only has therapeutic relevance for about 13% of patients, similar trials are also planned targeting different exons, which would widen the proportion of potentially treatable patients (Aartsma-Rus et al., 2009).

A significant limitation to the use of ASO-based exon skipping has been the relatively low efficiency with which the compounds can distribute to the skeletal musculature, enter muscle fibres and have their effect. Furthermore, plain ASO chemistries such as 2'OMePS and PMO have shown negligible uptake into heart muscle and virtually no uptake into the central nervous system (CNS). Since both heart and brain are involved in DMD, it is important that novel ASO therapeutics seek to have at least some effect in these tissues.

It has previously been shown that the conjugation of short peptide sequences to PMO can facilitate improved cell penetration and enhanced effect on splicing (Moulton et al., 2004). A particular class of peptide, so-called PMO-internalising peptide (Pip), has been developed in collaboration between the Wood laboratory at the University of Oxford and the Gait laboratory, MRC Laboratory of Molecular Biology, Cambridge (Yin et al., 2011). These peptides are arginine-rich but have a short central portion of hydrophobic residues. The Pip6 series of such peptides have proven to be particularly successful in terms of delivery of PMO to skeletal muscle and heart (Betts et al., 2012). However, the efficacy of Pip6 peptides for CNS delivery has not been previously tested.

In order to facilitate the possibility of PPMO passage across the blood-brain barrier (BBB) it is necessary to design peptides able to utilise one of the potentially available BBB transport mechanisms. For large molecules, these would include receptor-mediated endocytosis and adsorptive endocytosis (Chen and Liu, 2012). In this chapter, several peptides have been designed and synthesised to try to take advantage of these mechanisms. By chemically conjugating these peptides to a 25-mer PMO known to induce skipping of *Dmd* exon 23 in *mdx* mice, it has been possible to assay these PPMOs *in vivo* for their CNS delivery capabilities. In addition, the Pip6a peptide has been investigated in some detail in terms of its biodistribution as a PPMO and as to whether it has the ability to induce exon skipping within the brains of both adult and neonatal mice.

4.2. Results

4.2.1. Identification of putative brain-targeting peptides

A total of eight different PPMOs with different peptide sequences were designed and tested *in vitro* and *in vivo* (Table 4.1).

Peptide	Amino acid sequence	Mw	Receptor
RVG	Ac-YTIWMPENPRPGTP**S**DIFTNSRGKRASNG**G**-**PMO**	11757	AChR
Angiopep-2	Ac-TFFYGGSRGKRNNFKTEEY**GG**-**PMO**	10856.6	LRP1
Tet1	Ac-HLNILSTLWKYR**GG**-**PMO**	10112	G_{T1b}
$ApoE_{(141-150)}$	Ac-LRKLRKRLLR**GG**-**PMO**	9904	LDLR
Branched $ApoE_{(141-150)}$	Ac-LRKLRKRLLR**GG**┐ **K-X-Bpg-G-PMO** Ac-LRKLRKRLLR**GG**┘	10958.7	LDLR
Branched PepC7	┌S———S┐ Ac-CTSTSAPYC**GG**┐ **K-X-Bpg-G-PMO** Ac-CTSTSAPYC**GG**┘ └S———S┘	11806	Unknown
THR	Ac-THRPPMWSPVWP**X**-**Bpg-G-PMO**	10220	TfR
Pip6a	Ac-RXRRBRRXRYQFLIRXRBRXRB-**PMO**	11348	Unknown

Table 4.1. Details of PPMOs. Alterations and additions to the originally published amino-acid sequences of these peptides are shown in bold. In the sequences above, B stands for *β*-alanine, X for aminohexanoic acid and Ac for an acetyl group at the N-terminus. Bpg is a commercially available bishomopropargylglycine derivative containing a functionalised alkyne group allowing for click chemistry. The PepC7 peptide has a disulphide bond between its two cysteine residues as shown. The PMO for *Dmd* exon 23

skipping (also shown in bold) has a molecular weight of 8413. AChR, acetylcholine receptor; LRP1, low density lipoprotein receptor-related protein 1; G_{T1b}, trisialoganglioside receptor; LDLR, low density lipoprotein receptor; TfR, transferrin receptor.

RVG is a peptide fragment derived from rabies virus glycoprotein that has previously been shown to target the CNS (Kumar et al., 2007; Alvarez-Erviti et al., 2011). It shares sequence similarity to several snake venoms, has previously been shown to bind to the nicotinic acetylcholine receptor (AChR) and is able to competitively inhibit the binding of both α-bungarotoxin and labelled rabies virus to this receptor (Lentz et al., 1987; Lentz, 1990). The original 29 amino acid RVG peptide has a cysteine residue at position 15 (YTIWMPENPRPGTPCDIFTNSRGKRASNG). In this synthesis, however, the cysteine residue was substituted for a serine. This was to prevent the formation of disulphide bonds between the peptides. An additional glycine residue was also added at the C-terminus as a spacer to allow greater flexibility between the peptide and PMO. Examples of such glycine linkers can be seen in most of the other synthesised PPMOs in Table 4.1.

Angiopep-2 is a synthetic peptide whose sequence (TFFYGGCRGKRNNFKTEEY) was derived by comparison of human protein Kunitz domains with the sequence of aprotinin (Demeule et al., 2008b). In an *in vitro* model of the BBB, Angiopep-2 was shown to be transported across brain endothelial cells by means of the LRP1 receptor (Demeule et al., 2008a).

Tet1 is a 12-amino acid peptide (HLNILSTLWKYR) identified by phage display as binding to the trisialoganglioside receptor G_{T1b} (Liu et al., 2005). This mimics the binding of tetanus

toxin C fragment to neuronal axon terminals., which similarly requires ganglioside binding (Williamson et al., 1999). ICV injection of a Tet1-PEG-PEI complex in mice resulted in increased activity of a plasmid construct in brain tissue with specific targeting of adult neural progenitor cells (Kwon et al., 2010).

$ApoE_{(141-150)}$ is a fragment of the apolipoprotein E protein comprising amino acid residues 141-150 (LRKLRKRLLR) of the native protein. Apolipoprotein E is a 34 kD protein that is an important component of serum lipoproteins, particularly very low density lipoprotein (VLDL) from which it was first isolated as an arginine-rich polypeptide (Shore and Shore, 1973). It contains 299 amino acids separated into two domains by a flexible loop (Hauser et al., 2011). The C-terminal domain allows lipid binding while the N-terminal domain contains four amphipathic α-helices. Nanoliposomes covalently coupled to $ApoE_{(141-150)}$ have been shown to facilitate uptake into rat brain endothelial cells (Re et al., 2011). From here on in the conjugated PPMO made with $ApoE_{(141-150)}$ is referred to simply as ApoE-PMO.

PepC7 is a 9-mer cyclic peptide sequence (CTSTSAPYC) that was identified by M13 phage display (Li et al., 2012). Using an intravenously injected library of 1.2×10^9 genotypes encoding random 7-mer cyclic peptides fused to the pIII coat protein of M13 filamentous phage, it was possible to perform four rounds of biopanning of adult mouse brain homogenate in *Escherichia coli* to obtain phages displaying the PepC7 consensus sequence. The circulation time of phage prior to brain harvesting was 1 hour and the PepC7 sequence achieved a 41-fold enrichment in brain compared to the original library. This peptide adopts a cyclic structure due to the formation of a disulphide bond between the two cysteine residues.

THR is a 12-amino acid peptide (THRPPMWSPVWP) that was found by phage display and which binds to the transferrin receptor. It has been used to deliver gold nanoparticle conjugates across an *in vitro* BBB model (Prades et al., 2012). This study also suggested some *in vivo* BBB-crossing activity in rats after intraperitoneal injection of THR gold nanoparticles as measured by radioactive gold quantification in neutron-irradiated brains. Some isolated gold particles could also be seen by electron microscopy within brain parenchyma.

Pip6a is a 22-residue synthetic anionic peptide (RXRRBRRXRYQFLIRXRBRXRB) that has previously been shown to enable excellent delivery of PMO to skeletal muscle and heart (Betts et al., 2012). It is arginine-rich with a number of interspersed aminohexanoic acid spacers and *β*-alanine residues which improve stability by being resistant to protease digestion. While the flanking arginine-rich regions of the peptide are positively charged and hydrophilic, the central five residues are hydrophobic (apart from glutamine) and together they form a hydrophobic core. This structure imparts an amphipathic property to the peptide, which appears to be vital for its cell-penetrating activity.

4.2.2. *In vitro* screening of PPMOs

Early-stage *in vitro* screening of PPMOs was undertaken by Dr Fazel Shabanpoor at MRC LMB, Cambridge. All synthesised PPMOs showed a degree of dose-responsive efficacy in terms of exon 23 skipping in the *Dmd* mRNA of *mdx* H2K cells (Figure 4.2). Pip6a-PMO appeared to be the most effective PPMO *in vitro* with the majority of transcript showing exon 23 skipping as measured by densitometry. Indeed, virtually no full-length unskipped

transcript was visible by agarose gel electrophoresis at 0.5 µM or 1 µM concentrations. Branched ApoE-PMO (BrApoE-PMO) also showed a similarly high level of efficacy to Pip6a-PMO at 1 µM concentration. The least effective PPMO appeared to be THR-PMO, which even at 5 µM concentration resulted in a lower percentage of exon 23 skipping than any other tested PPMO produced at 1 µM.

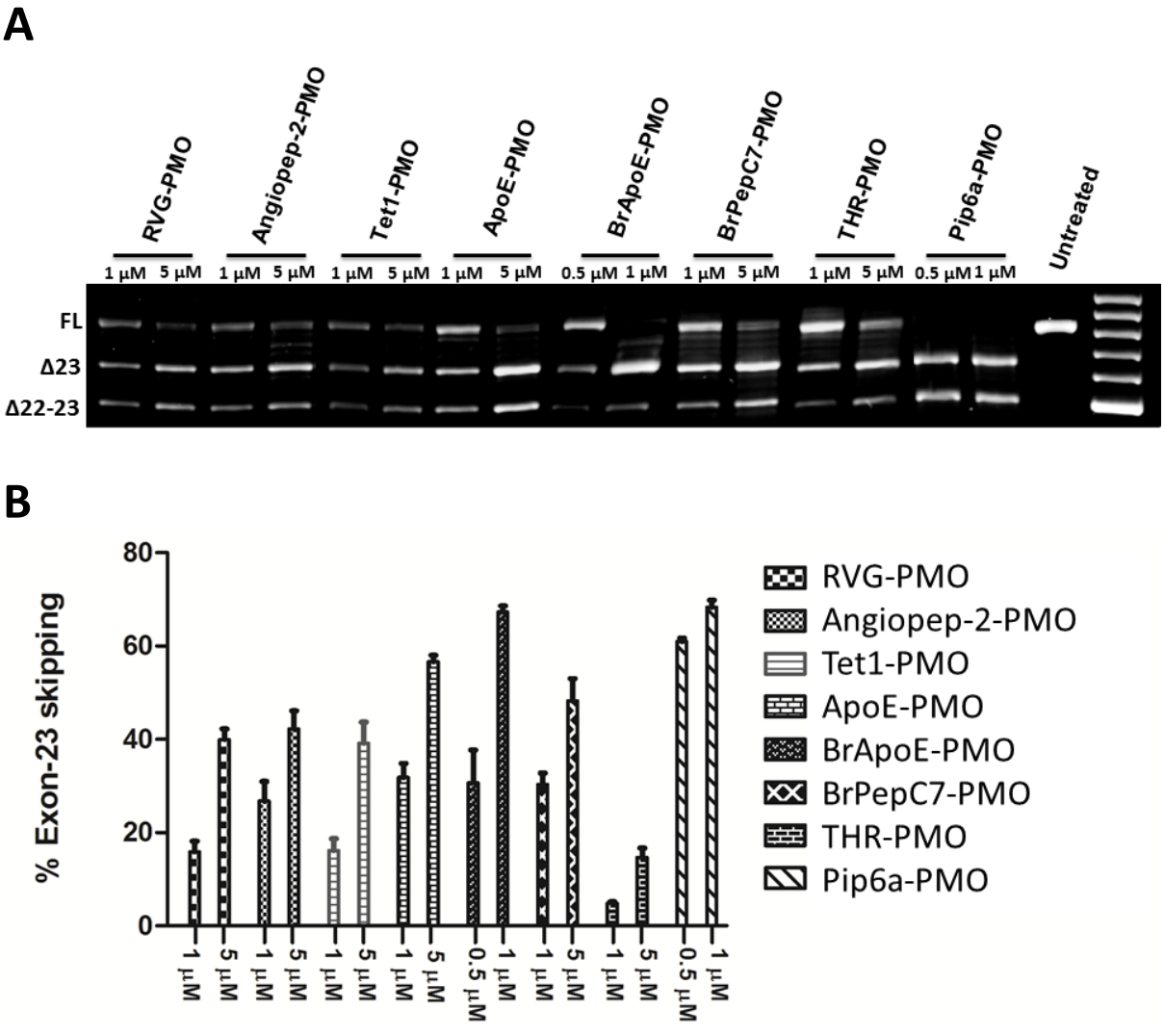

Figure 4.2. ***In vitro*** **activity of PPMOs.** Please note that this data was obtained by Dr Fazel Shabanpoor, MRC LMB, Cambridge. **A.** Representative composite agarose gel image of nested RT-PCR analysis showing *Dmd* exon 23 skipping in H2K *mdx* cells

incubated with PPMOs as indicated. Aside from the full-length (FL) unskipped band, note that not only is a skipped Δ23 band seen but also a double-skipped Δ22-23 band. **B.** Densitometry analysis of collected gel images for each PPMO (*n* = 3) provides a measure of the percentage of exon 23 skipping seen with each PPMO. BrApoE, branched ApoE; BrPepC7, branched PepC7.

4.2.3. *In vivo* testing of PPMOs

The compounds tested *in vitro* were taken forward to *in vivo* testing by intravenous injection of PPMOs. Testing was performed in several stages or batches and for practical reasons, mice of varying age and sex were utilised for this analysis (details of age and sex of animals can be found in the relevant paragraphs relating to each experiment). For the experiments reported in this section (4.2.3), tissues were harvested two weeks after injection and RNA was analysed for skipping of *Dmd* exon 23 by nested RT-PCR.

RVG, Angiopep-2, Tet1 and ApoE were initially chosen to be taken forward for testing *in vivo*. Single 13-week-old female *mdx* mice were injected intravenously with one of these four compounds at a dose of 1 nmol/g (*n* = 1). Since this dose was well-tolerated, a further four mice received 2 nmol/g and subsequently another four received 4 nmol/g (*n* = 1 for each compound at each dose), all of which were well tolerated with no discernible side-effects. However, by nested RT-PCR, none of these four compounds resulted in detectable exon skipping in the brain even at high dose, although some skipping activity was seen in other tissues (Figure 4.3). ApoE-PMO induced the greatest degree of exon skipping in skeletal muscles.

In light of these results, a branched form of ApoE-PMO (BrApoE-PMO) was tested *in vivo* to see whether this would achieve better efficacy, since its structure incorporated two copies of the peptide instead of one. Two 5-month-old female *mdx* mice were injected intravenously with BrApoE-PMO at 2 nmol/g. Unfortunately one of these mice died as a result of compound toxicity following the injection, while the other survived until harvesting two weeks later. No exon skipping was seen in the brain of this mouse after two weeks by nested RT-PCR, although significant skipping was seen in other tissues (Figure 4.3). Another branched PPMO, BrPepC7-PMO, was also tested in two *mdx* mice (again 5-month-old females) and these mice tolerated the compound well. However, once again nested RT-PCR failed to show any exon skipping activity in the brains of these mice and detected very little in other tissues.

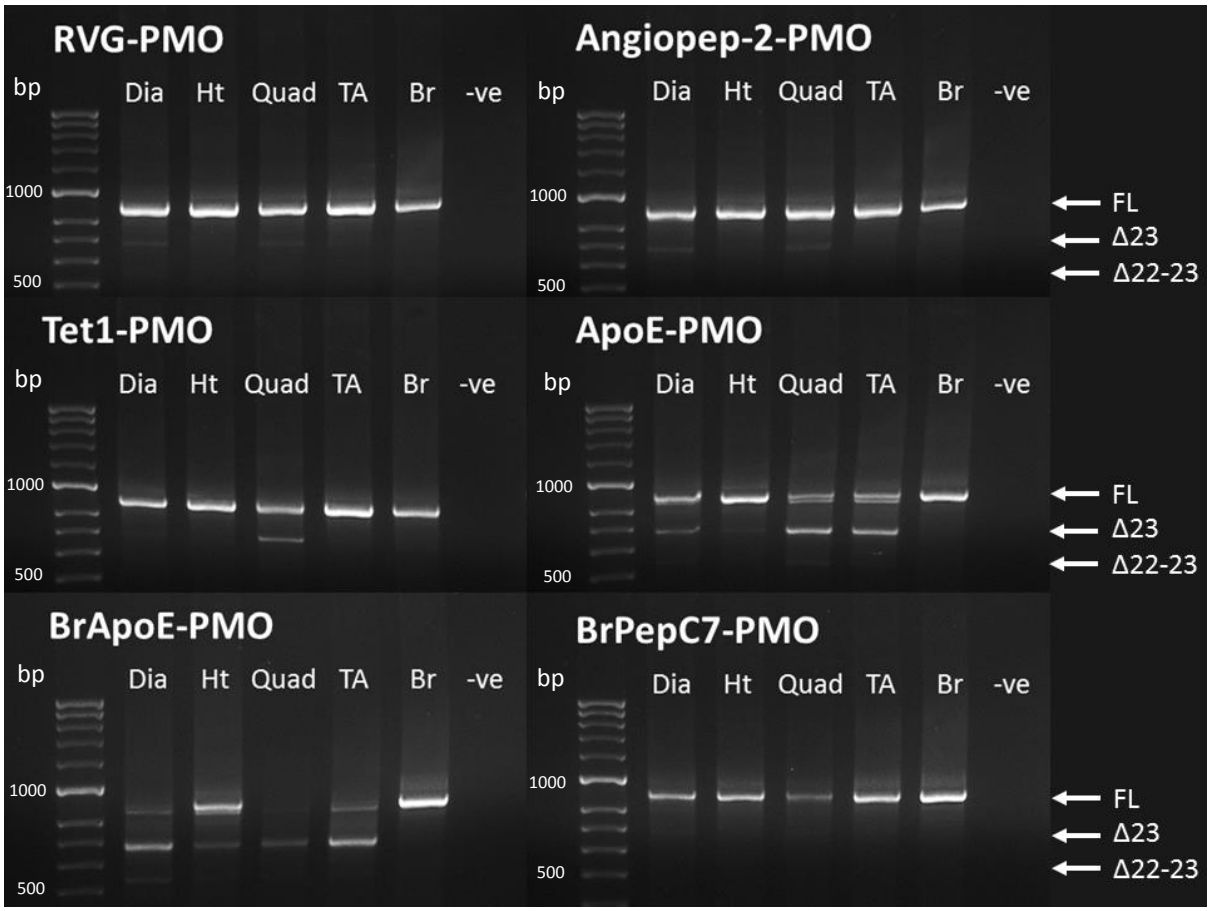

Figure 4.3. Intravenous testing of PPMOs. For RVG-PMO, Angiopep-2-PMO, Tet1-PMO and ApoE-PMO, PPMOs were injected IV at 4 nmol/g into 13-week-old female *mdx* mice (*n* = 1). For BrApoE-PMO and BrPepC7-PMO, 2 nmol/g was injected IV in 5-month-old female *mdx* mice (*n* = 2). Tissues were harvested 2 weeks after injection. Nested RT-PCR demonstrates variable degrees of exon 23 skipping depending on the PPMO used. Dia, diaphragm; Ht, heart; Quad, quadriceps; TA, tibialis anterior; Br, brain (i.e. cerebrum); -ve, non-template control. Note that no exon skipping is seen in brain samples following treatment with any of the PPMOs.

Pip6a-PMO had previously been tested *in vivo* for its ability to induce exon skipping in skeletal muscle and heart. However, its ability to deliver to brain had not been investigated. In order to test this, 12-week-old male *mdx* mice received intravenous Pip6a-PMO at a dose of 1 nmol/g (*n* = 4). Brains were harvested two weeks later and RNA analysed by nested RT-PCR. However, despite good levels of skipping in peripheral tissues, no skipping was detectable in brain (Figure 4.4).

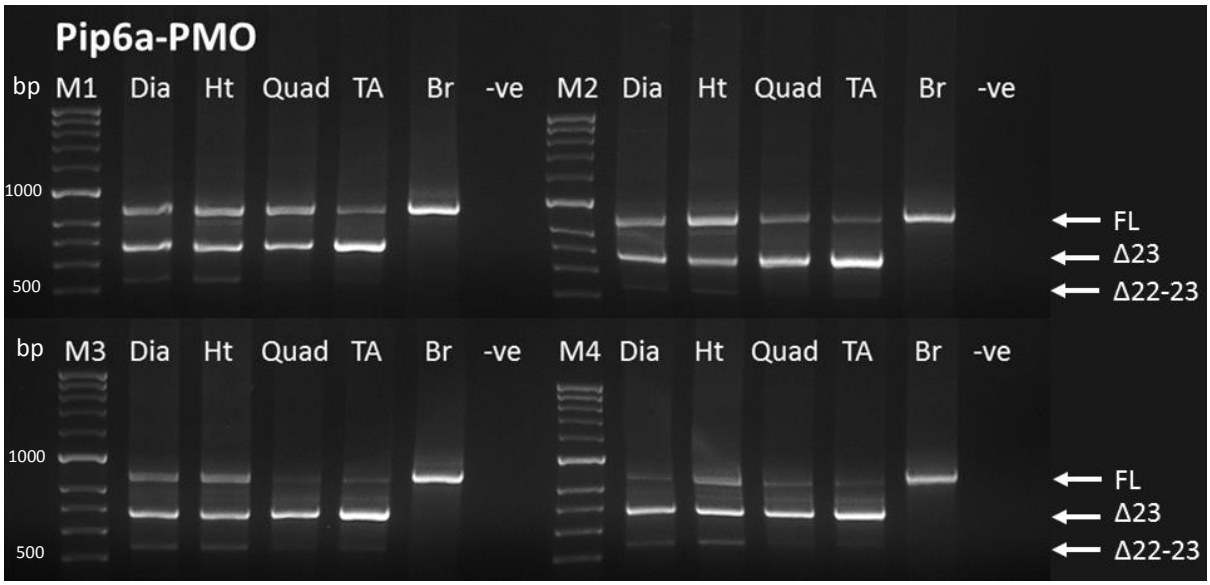

Figure 4.4. Pip6a-PMO 1 nmol/g IV injection at 12 weeks in male *mdx* mice (*n* = 4, results shown for each animal M1-4). Tissues were harvested 2 weeks later and nested RT-PCR performed. Exon 23 skipping (Δ23) can be seen in all peripheral tissues but not in brain. Dia, diaphragm; Ht, heart; Quad, quadriceps; TA, tibialis anterior; Br, brain (i.e. cerebrum); -ve, non-template control.

4.2.4. ICV Pip6a-PMO injections

In order to demonstrate that activity of PPMOs in the brain was possible, intracerebroventricular (ICV) injections of Pip6a-PMO (6.25 µg / 0.55 nmol) and of PMO (37 µg / 4.4 nmol, eight times the molar equivalent Pip6a-PMO dose) were carried out in 5-month-old *mdx* mice (*n* = 3 per group, animals 1 and 2 in each group were female, animal 3 in each group was male). Injections were performed by Guillem Genové, Department of Medical Biochemistry and Biophysics, Karolinska Institute, Stockholm, Sweden. Brains were harvested one week after injection. Nested RT-PCR confirmed exon

skipping in the majority of brain samples, though the degree of skipping was variable (Figure 4.5A). However, protein extracted from the same brains did not demonstrate any detectable dystrophin staining on Western blot (Figure 4.5B). This may be because no protein was restored. However, it may also be that the amount of dystrophin restored after 1 week was beyond the limit of detection of this technique, since the control dystrophin band itself shows relatively weak staining.

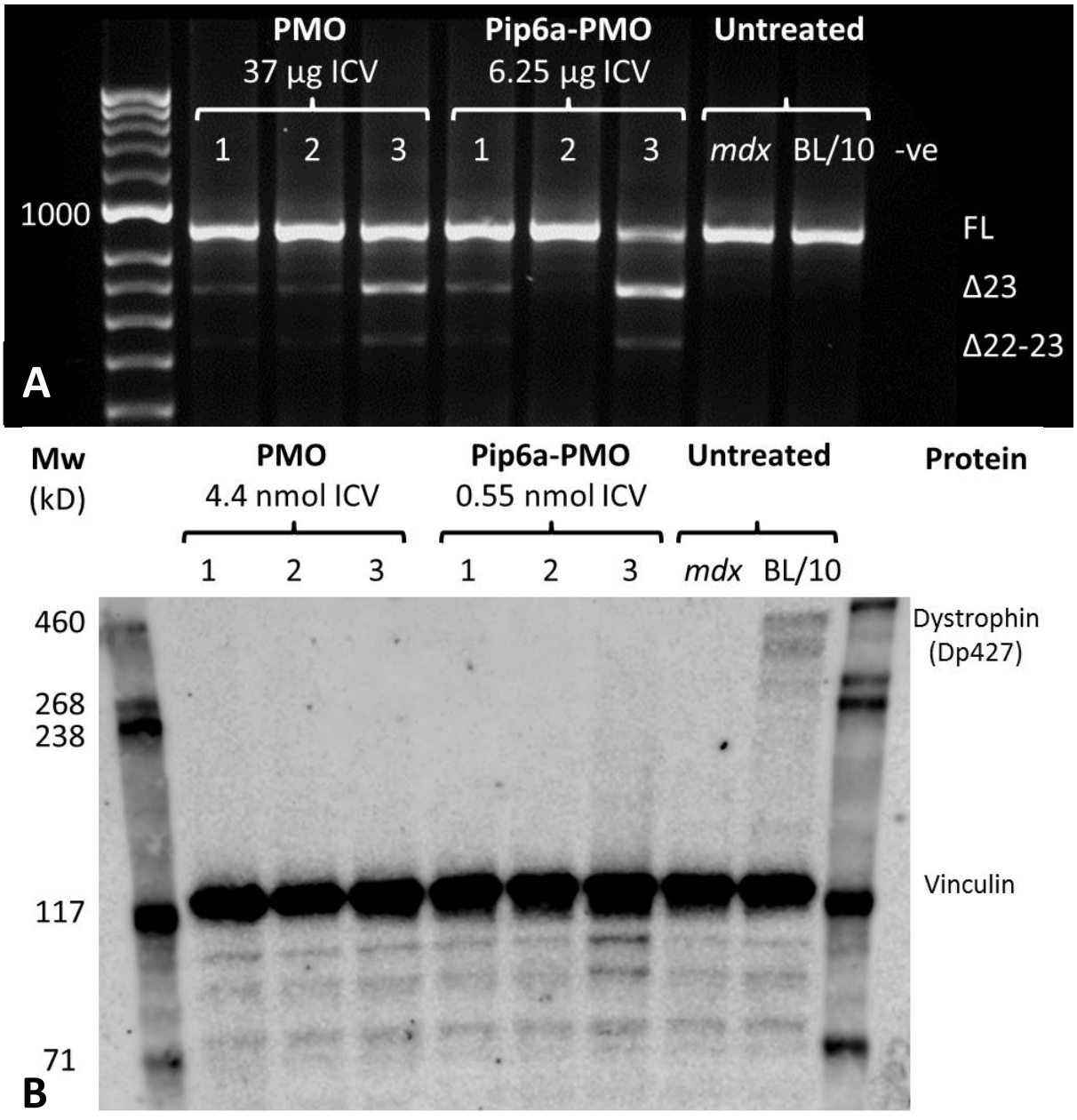

Figure 4.5. ICV injection of PMO and Pip6a-PMO in 5-month-old *mdx* mice. Animals 1 and 2 in each group were female, animal 3 in each group were male. The ICV dose of PMO used (37 μg, 4.4 nmol) was 8 times the molar dose of Pip6a-PMO (6.25 μg, 0.55 nmol). Tissues were harvested one week after injection. **A.** Nested RT-PCR from brain (cerebrum) RNA. Skipping of exon 23 (Δ23) and of exons 22 and 23 (Δ22-23) can be seen in all three PMO-injected brains and in at least 2/3 Pip6a-PMO-injected brains. The degree of skipping appears quite variable. **B.** Western blot of brain protein. The membrane has been probed with the anti-dystrophin antibody DYS1, which detects the rod domain of the full-length Dp427 isoform. An antibody to vinculin (Mw 117 kD) has also been used as a loading control. No evidence of dystophin restoration is seen in the treated samples.

4.2.5. High-dose repeat PPMO injection

One further novel PPMO was tried, namely THR-PMO. Since the previously tried PPMOs had not resulted in brain exon skipping and given the apparently low *in vitro* efficacy of THR-PMO, this time a large dose of 5 nmol/g was given intravenously to two 9-week-old female *mdx* mice on day 1 and the dose repeated on day 3. Brains from these mice were harvested 7 days after the initial injection and assayed for exon skipping. However, nested RT-PCR once again showed no evidence of skipping in brain (Figure 4.6). In parallel, in order to see whether a higher dose protocol of Pip6a-PMO would succeed, two further *mdx* mice (7-week-old females) were given a near maximal tolerable dose of 1.6 nmol/g Pip6a-PMO on day 1 and again on day 3, with harvesting of brain 7 days after

initial injection. Even with this high dose, nested RT-PCR was negative for brain exon skipping (Figure 4.6).

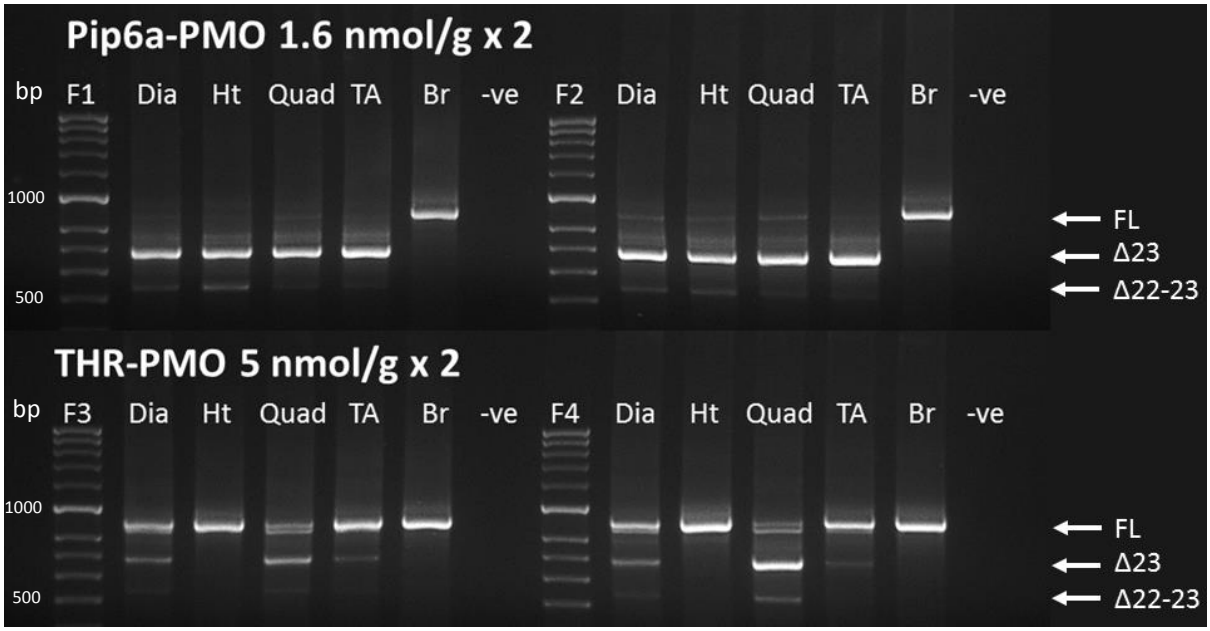

Figure 4.6. High-dose repeat injection of Pip6a-PMO and THR-PMO. For Pip6a-PMO, 7-week-old female *mdx* mice (F1 and F2) were injected IV with 1.6 nmol/g on day 1 and day 3. For THR-PMO, 9-week old female *mdx* mice (F3 and F4) received 5 nmol/g IV injections on days 1 and 3. Tissues were harvested 1 week after first injection. Nested RT-PCR shows a preponderance of exon 23 skipped products in Pip6a-PMO-treated mice in skeletal muscles and heart but not in brain. THR-PMO-treated mice exhibit some exon skipping in skeletal muscle but not in heart or brain. Dia, diaphragm; Ht, heart; Quad, quadriceps; TA, tibialis anterior; Br, brain (i.e. cerebrum); -ve, non-template control.

4.2.6. Neonatal Pip6a-PMO

Attempts were made to utilise the increased permeability of the BBB in neonatal mice to facilitate brain exon skipping. P1 *mdx* mice (*n* = 6, not sexed at birth but subsequently found to be 5 females and 1 male) received Pip6a-PMO 1 nmol/g intravenously via the lateral facial vein. None of these mice demonstrated brain exon skipping two weeks later using nested RT-PCR (Figure 4.7). Furthermore, the amount of skipping in peripheral tissues in neonatal mice varied considerably and was less than that seen in adult mice.

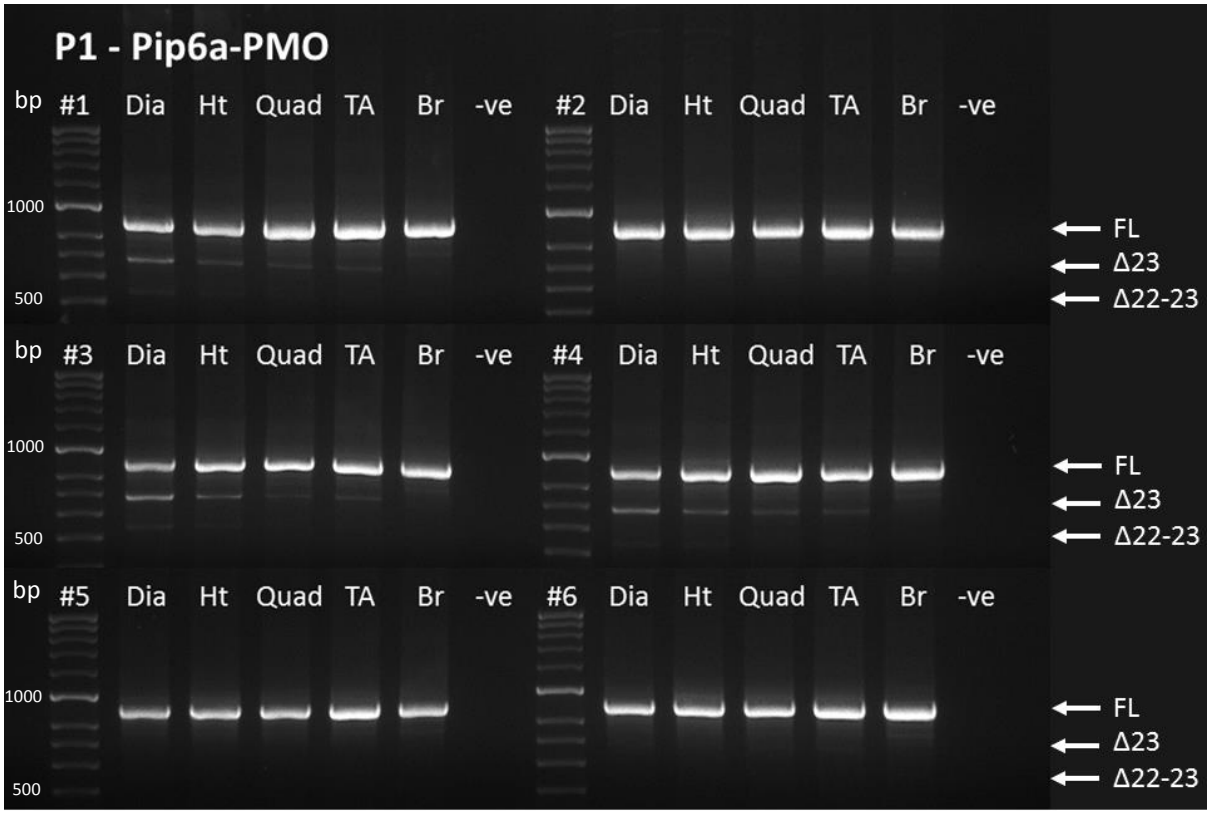

Figure 4.7. P1 neonatal *mdx* mice injected IV with Pip6a-PMO. A single IV injection was administered at P1 and tissues were harvested at 2 weeks. Nested RT-PCR shows only a small degree of skipping of *Dmd* exon 23 in skeletal muscle and heart and not in brain.

Dia, diaphragm; Ht, heart; Quad, quadriceps; TA, tibialis anterior; Br, brain (i.e. cerebrum); -ve, non-template control.

4.2.7. A skipped product-specific assay for *Dmd* Δ23

During the course of this study, data presented by Aurélie Goyenvalle from the group of Luis Garcia, Institute of Myology, Paris, France, showed that repeated weekly administration of tricyclo-DNA (tcDNA) oligonucleotides in *mdx* mice over 12 weeks could in fact induce exon skipping in the brain (Goyenvalle et al., 2015). In this study, exon skipping was detected by performing RT-PCR with a primer set specific for the skipped product only, since it had been found that nested RT-PCR could not detect the low levels of exon skipping present in brain (personal communication). Based on this finding, a new forward primer was designed that overlapped the exon 22-24 junction. Using this together with the reverse primer used previously for nested PCR, it was found that Δ23 skipped product could indeed be detected in brain samples from PPMO-treated mice (Figure 4.9).

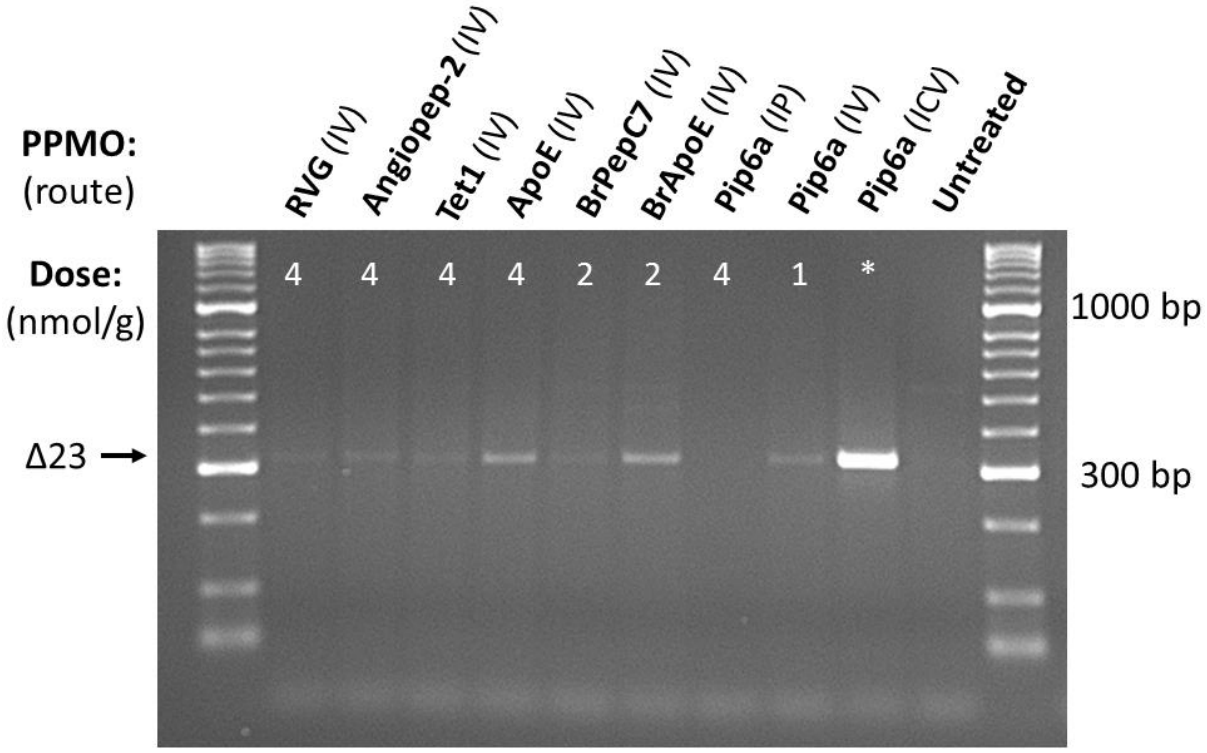

Figure 4.9. Reanalysis of PPMO activity in brain using *Dmd* Δ23-specific primers. These samples underwent cDNA synthesis from 800 ng RNA using random primer reverse transcription prior to PCR. The PCR primers used are predicted to generate a 318 bp product. The dose of each PPMO is shows in nmol/g. Tissues were harvested 2 weeks after injection, except for ICV Pip6a where tissue was harvested at 1 week. In the case of ICV-injected Pip6a-PMO (*), a total dose of 0.55 nmol was used. Of the IV PPMOs, the most prominent skipping is seen with ApoE, branched ApoE (BrApoE) and Pip6a. No skipped product is seen with intraperitoneal (IP) Pip6a-PMO. The range of intensities seen across the gel suggests that this form of analysis may have a quantitative utility. THR-PMO was tested separately and was also found to display low levels of skipped product (data not shown). An untreated *mdx* brain sample was used for a negative control.

4.2.8. Detection of exon skipping in brain by ddPCR

In light of these apparently positive results, a hydrolysis probe qRT-PCR assay was designed to specifically detect *Dmd* Δ23 skipped product. The same forward primer was used and a new reverse primer designed to make the amplicon under 150 bp in length. Using further assays (designed by Dr Graham McClorey, DPAG, University of Oxford) for *Dmd* exon 20-21 (total full-length transcript) and *Dmd* exon 23-24 (unskipped transcript only), it was possible to employ digital droplet PCR (ddPCR) to measure the proportion of skipped product (Figure 4.10). IV PPMO treatment resulted in very low levels of exon 23 skipping in brain. The highest degree of brain exon skipping with IV treatment was seen after two doses of Pip6a-PMO at 1.6 nmol/g, where at day 7 there was 0.054% skipped transcript. The most successful brain exon skipping following single IV injection was seen with BrApoE-PMO at a dose of 1 nmol/g, which achieved 0.050% skipped transcript two weeks after injection. ICV injections achieved much higher levels of skipping, with 4.4 nmol of plain PMO achieving an average of 5.1% skipped transcript and 0.55 nmol Pip6a-PMO achieving an average of 12.7% one week after ICV injection, although these levels were highly variable between replicates.

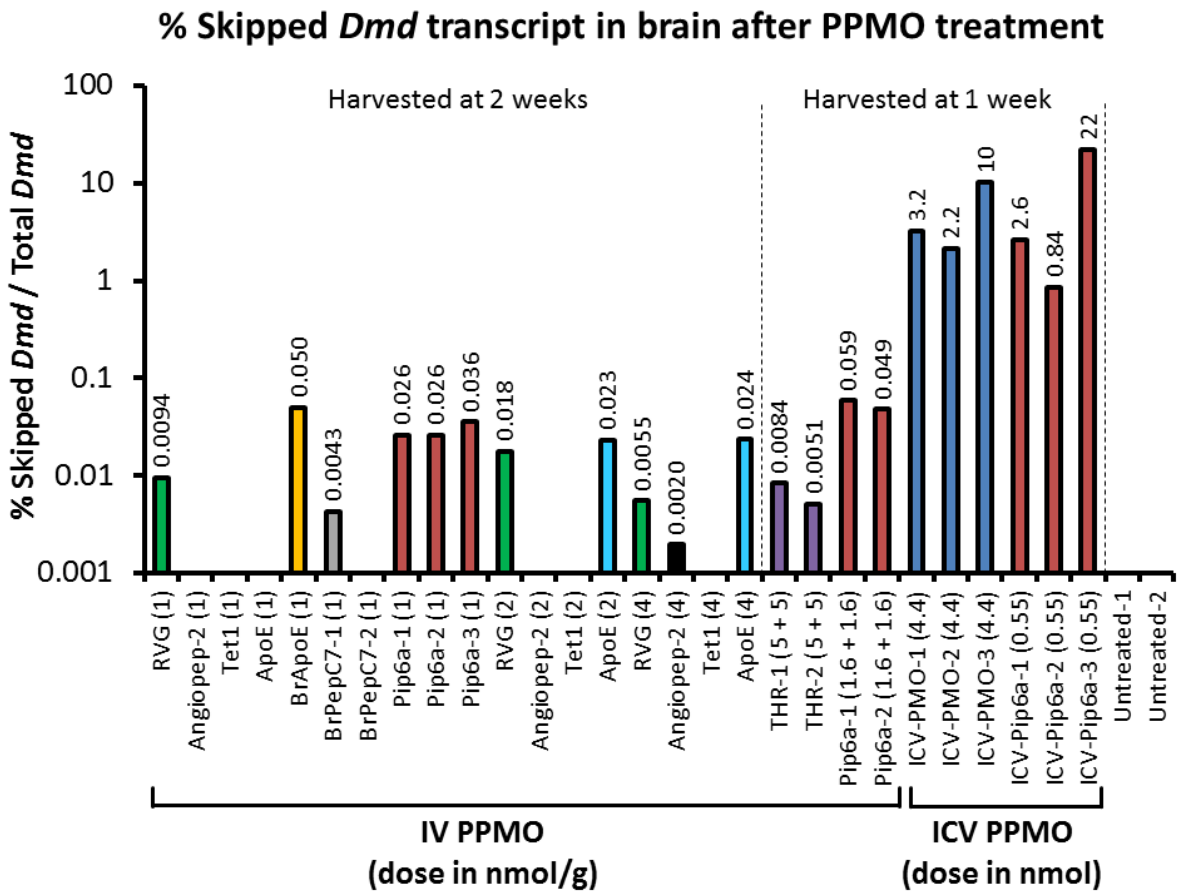

Figure 4.10. Measurement of *Dmd* exon 23 skipping in *mdx* mouse brain by digital droplet PCR (ddPCR). Note that the y-axis is displayed as a logarithmic scale. The graph shows ddPCR quantification of *Dmd* Δ23 skipped transcript as a percentage of total *Dmd* transcript detected in brain for each PPMO tested at the doses indicated. Brain tissue (cerebrum) was harvested 1 or 2 weeks after injection of compound as shown. In certain cases, replicate samples were available, denoted by sequential numbering. Samples from mice treated with ICV PMO and ICV Pip6a-PMO are shown alongside IV-treated samples.

4.2.9. Repeated Pip6a-PMO dosing from P1 to 10 weeks old

Since Pip6a-PMO appeared to have the best activity in terms of exon skipping (at least in non-brain tissues) of all the PPMOs tested, a longer-term dosing study was performed. A

litter of *mdx* mice were injected IV with 1 nmol/g Pip6a-PMO at P1 and again at P3. From the age of 4 weeks these mice (two females, F1 and F2, and four males, M3-M6) were then commenced on weekly IV injections at the same dose, receiving a ninth and final dose at 10 weeks of age. Tissues were harvested at 12 weeks. By nested RT-PCR, skeletal muscles showed almost complete skipping of exon 23 and a majority of skipped product was also seen in heart. No skipping could be detected in brain and no protein restoration could be detected by Western blotting (Figure 4.8). However, using qRT-PCR it was possible to detect a low level of skipping in brain (0.044%). This was compared against the levels of skipping observed in mice treated with Pip6a-PMO as single 1 nmol/g or double 1.6 nmol/g doses (Figure 4.9). 9 doses of Pip6a-PMO did not achieve significantly increased levels of skipping in brain.

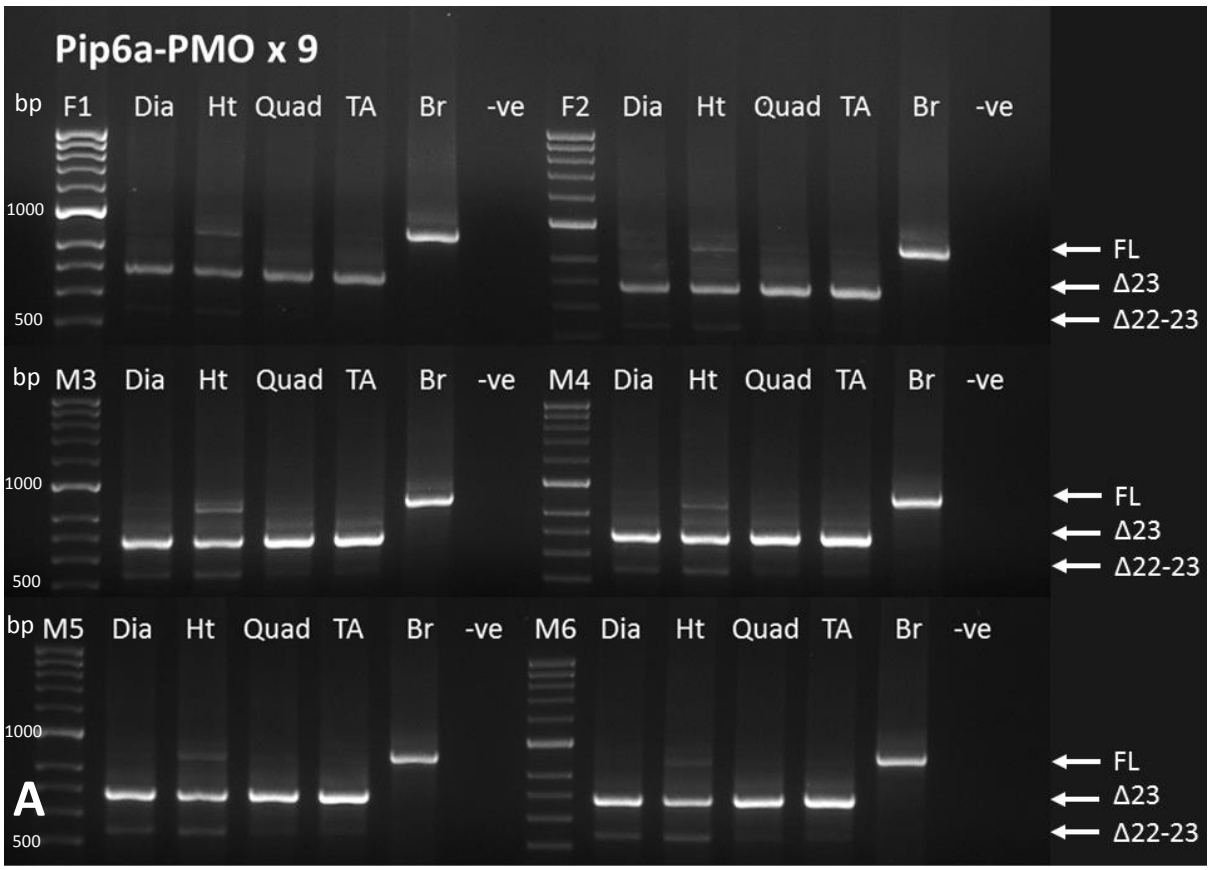

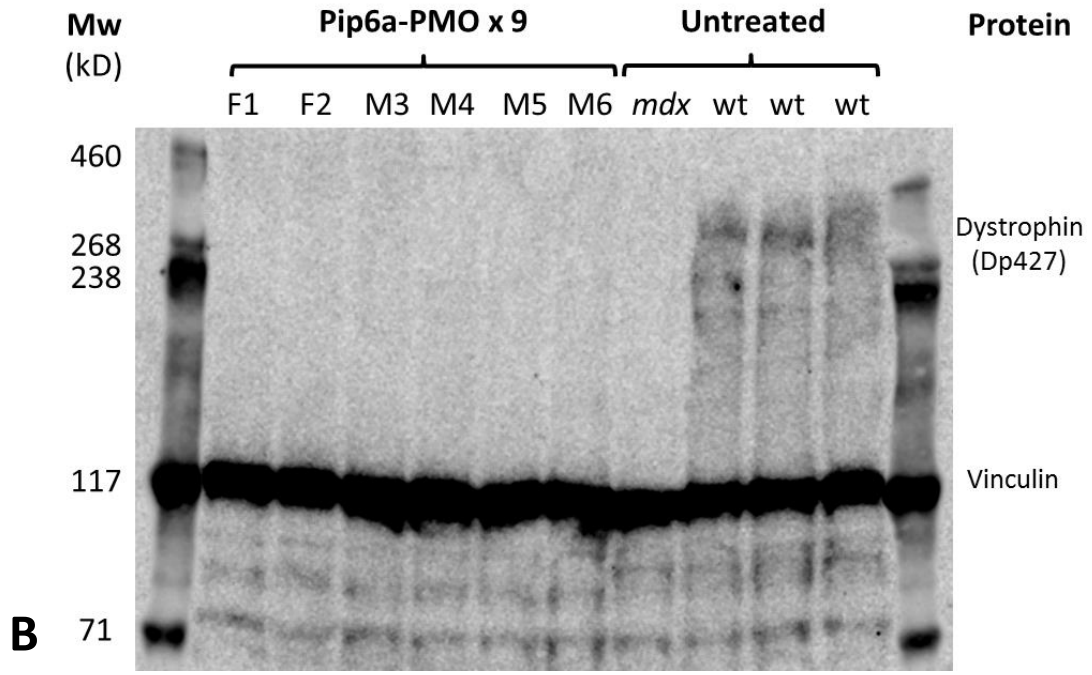

Figure 4.8. Pip6a-PMO intravenous injections over 10 weeks. Neonatal *mdx* mice received IV Pip6a-PMO at 1 nmol/g with repeated dosing at P3. Further IV doses were given at weekly intervals from 4-10 weeks of age and tissues were harvested at 12 weeks. **A**. Nested RT-PCR shows almost complete skipping of *Dmd* exon 23 in skeletal muscles and also brighter skipped than unskipped bands in heart. No exon skipping can be seen in brain. Dia, diaphragm; Ht, heart; Quad, quadriceps; TA, tibialis anterior; Br, brain (i.e. cerebrum); -ve, non-template control. F1 and F2, females; M3-M6, males. **B.** Western blot of brain protein for dystrophin with vinculin loading control. Although dystrophin staining in wild-type (wt) controls is weak, no restoration can be seen in Pip6a-PMO-treated brains.

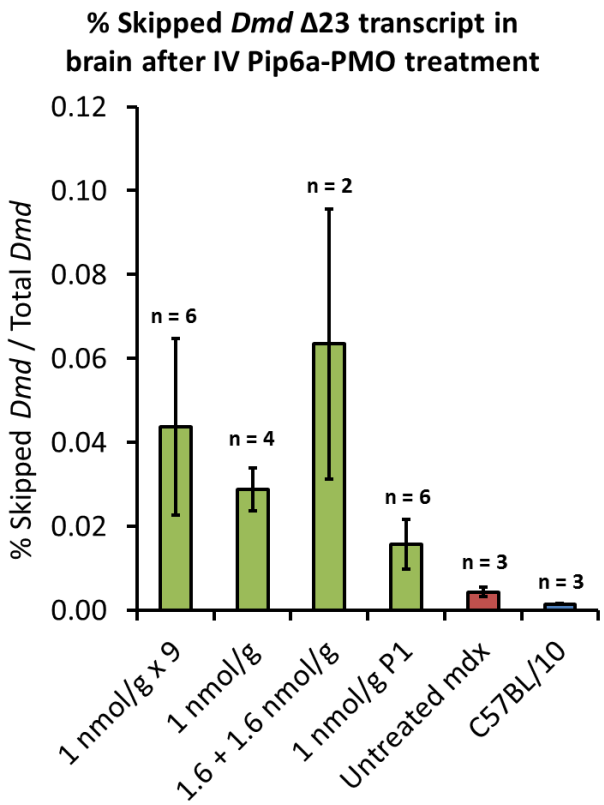

Figure 4.9. Comparison of *Dmd* exon 23 skipping in brain following different regimens of IV Pip6a-PMO administration. Samples were assayed for total *Dmd* transcript and Δ23 transcript. Since ddPCR was not available for this analysis, relative quantification of transcripts was obtained by qRT-PCR against a standard curve prepared from an ICV Pip6a-PMO-injected brain sample. Using this standard curve, percentages of skipped transcript were normalised to the percentage value of skipped transcript previously obtained for the ICV sample through ddPCR. Error bars represent standard deviation.

4.2.10. Functional effects of repeated Pip6a-PMO dosing

Two simple functional measures were tested on 12-week-old *mdx* mice that received repeated Pip6a-PMO dosing over 10 weeks (*n* = 6, comprising 2 females and 4 males). The first assay was open field testing. This test measures the activity of an animal over time in a defined caged area by use of a grid of infrared beams passing through the cage to detectors on the opposite sides. The frequency and speed with which the beams are cut by the animal's movement provides a measure of activity. Open field testing of mice treated with repeat-dose Pip6a-PMO appeared to show significant correction of behaviour towards wild-type values compared to untreated *mdx* mice (Figure 4.10).

The second test was forelimb grip-strength. This measures the force with which a mouse can hold onto a horizontal metal bar or grid with its forelimbs while gradually being pulled away from it in a horizontal direction by the tail. Male *mdx* mice treated with Pip6a-PMO over 10 weeks appeared to have significantly increased best and average grip-strength compared to both untreated *mdx* and wild-type mice (Figure 4.11). Female Pip6a-PMO-treated mice appeared to have significantly increased average grip-strength compared to untreated *mdx* mice.

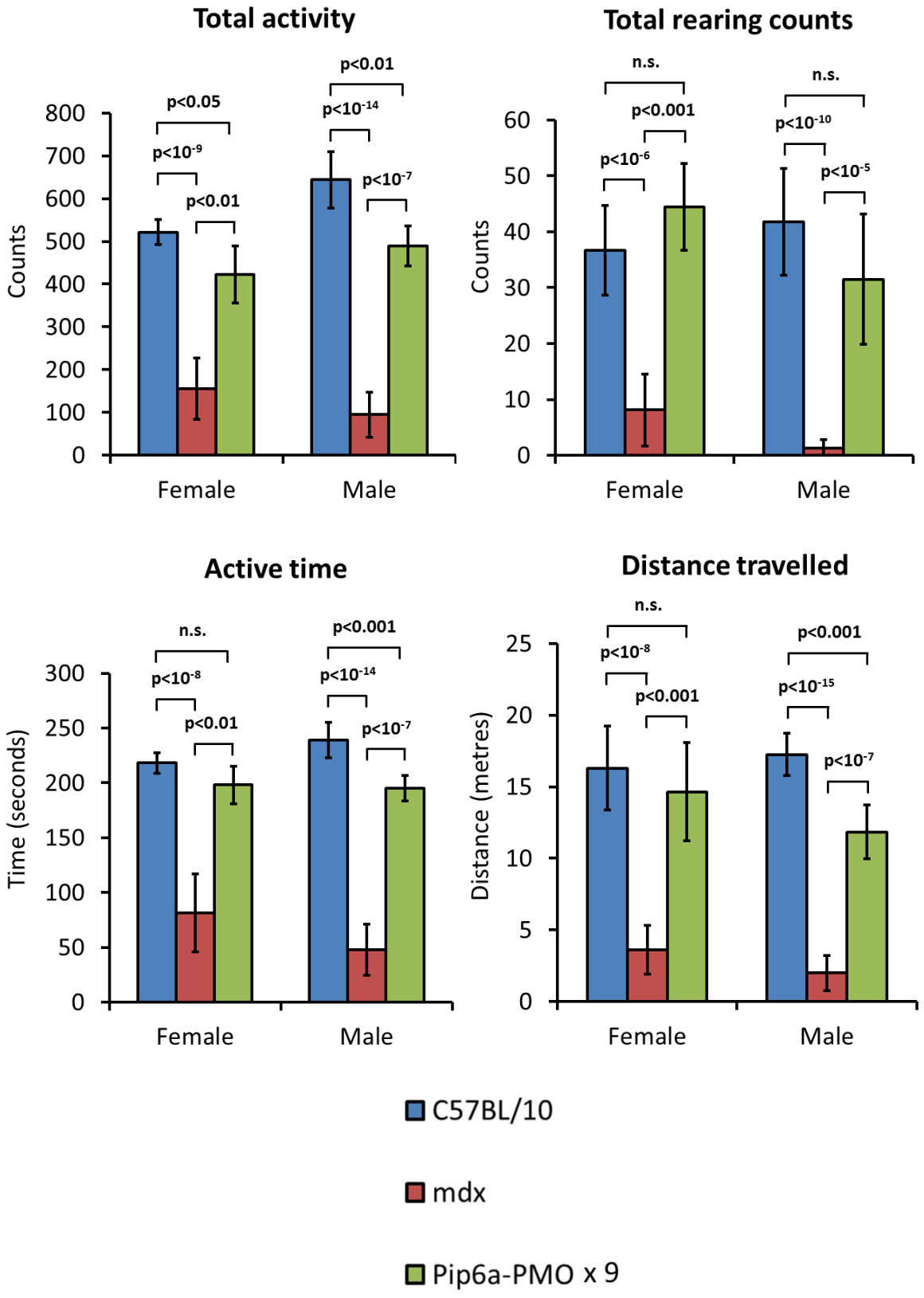
Total activity
Counts
800
700
600
500
400
300
200
100
0
p<0.05
p<10-9
p<0.01
p<0.01
p<10-14
p<10-7
Female
Male
Total rearing counts
Counts
60
50
40
30
20
10
0
n.s.
p<0.001
p<10-6
n.s.
p<10-10
p<10-5
Female
Male
Active time
Time (seconds)
300
250
200
150
100
50
0
n.s.
p<10-8
p<0.01
p<0.001
p<10-14
p<10-7
Female
Male
Distance travelled
Distance (metres)
25
20
15
10
5
0
n.s.
p<10-8
p<0.001
p<0.001
p<10-15
p<10-7
Female
Male
C57BL/10
mdx
Pip6a-PMO x 9

Figure 4.10. Open field testing of 12-week-old mice after 30-second restraint by scruffing. Untreated *mdx* mice show markedly reduced activity compared to wild-type C57BL/10 mice. In all four measures of activity, *mdx* mice treated with 9 doses of Pip6a-PMO at 12.5 mg/kg (1 nmol/g) show significant increase in activity compared to untreated *mdx* mice. The active time and distance travelled in female mice is not significantly different between C57BL/10 and Pip6a-PMO-treated *mdx* mice. Similarly, rearing activity is not significantly different between wild-type and treated mice in either females or males. Error bars represent standard deviation. Statistical p values calculated by post-hoc t-test with Bonferroni correction following single-factor ANOVA. Numbers of animals were as follows: C57BL/10 female n = 10, male n = 11; untreated *mdx* female n = 9, male n = 11; Pip6a-PMO-treated *mdx* female n = 2, male n = 4.

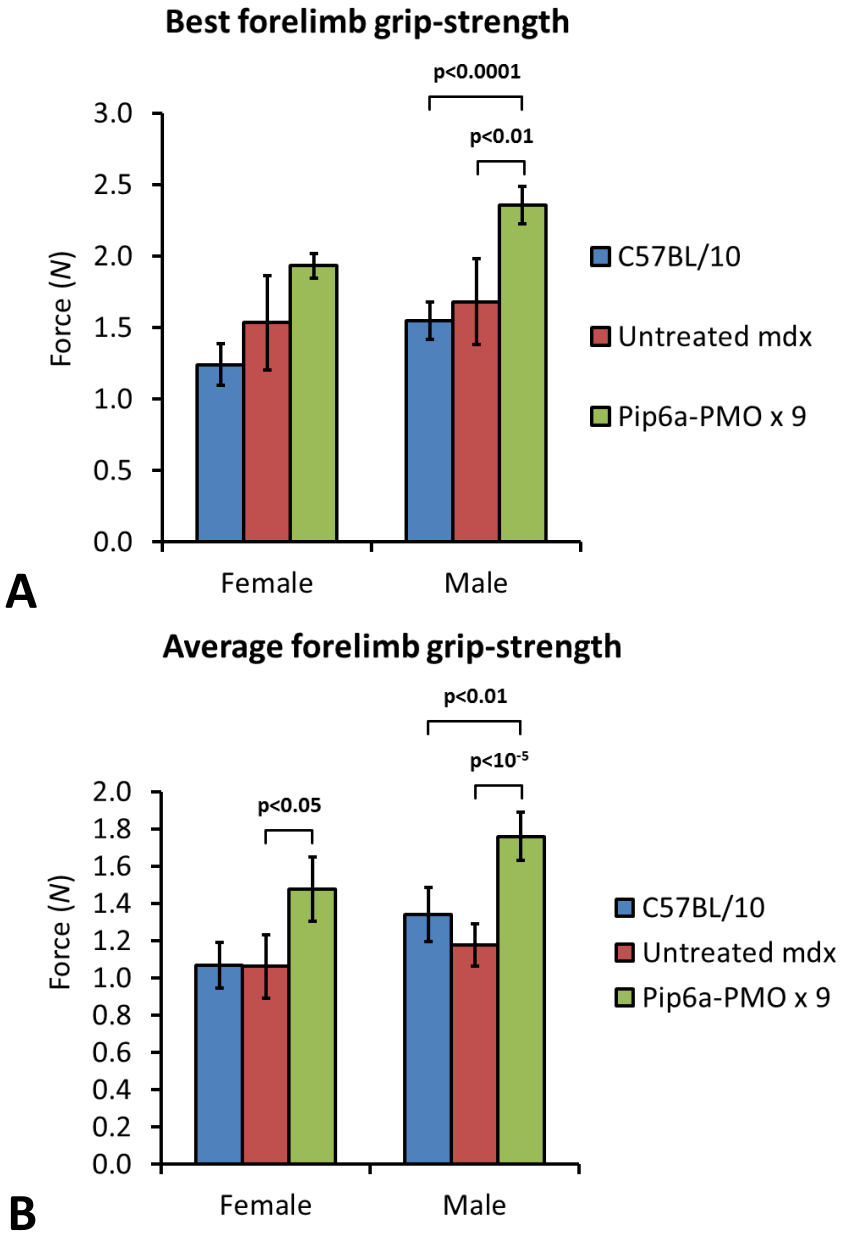

Figure 4.11. Forelimb grip-strength testing. **A**. Best forelimb grip-strength over five attempts. **B**. Average grip-strength across five attempts. After treating *mdx* mice with 9 doses of Pip6a-PMO at 1 nmol/g, forelimb grip-strength appears to be increased both over untreated *mdx* and wild-type controls. Number of animals were as follows: C57BL/10 female *n* = 3, male *n* = 6; untreated *mdx* female *n* = 12, male *n* = 10; Pip6a-

PMO-treated *mdx* female *n* = 2, male *n* = 4. All mice were aged between 11-15 weeks old.

4.2.11. Haematology and clinical chemistry profile of Pip6a-PMO-treated mice

Blood was collected at the point of tissue harvesting from the group of *mdx* mice treated with 9 doses of 1 nmol/g Pip6a-PMO from P1 to 10 weeks, as well as from control *mdx* and C57BL/10 wild-type mice. Analysis of haematological and clinical chemistry values is summarised in Figures 4.12 and in Tables 4.2 and 4.3. For most analytes, values were equivalent across the three groups in both males and females. The most marked differences between groups was seen in alanine aminotransferase (ALT), aspartate aminotransferase (AST) and creatine kinase (CK), all of which were highly elevated in untreated *mdx* mice but were substantially normalised towards wild-type values in Pip6a-PMO-treated *mdx* mice.

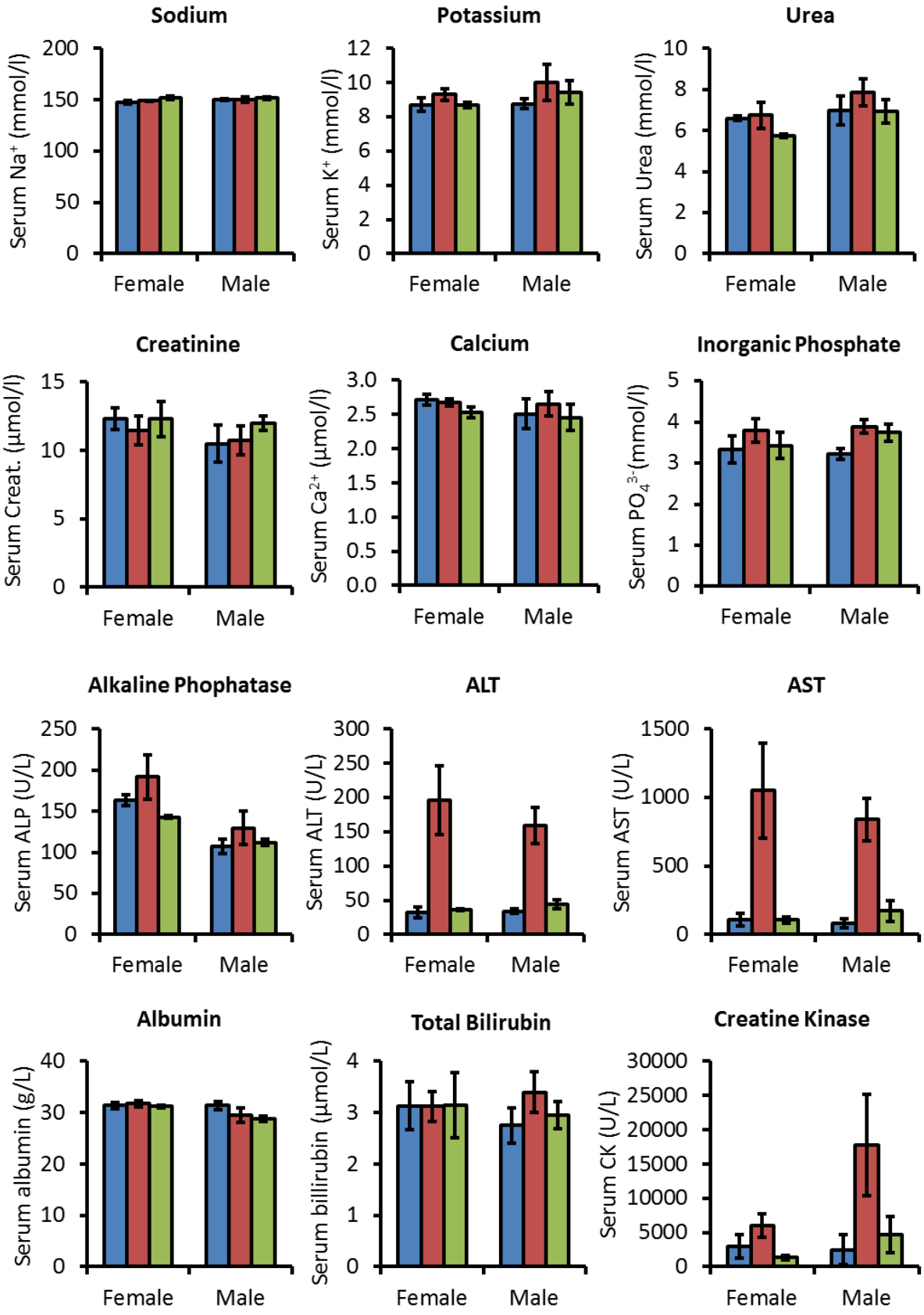
Sodium
Serum Na+ (mmol/l)
200
150
100
50
0
Female
Male
Potassium
Serum K+ (mmol/l)
12
10
8
6
4
2
0
Female
Male
Urea
Serum Urea (mmol/l)
10
8
6
4
2
0
Female
Male
Creatinine
Serum Creat. (µmol/l)
15
10
5
0
Female
Male
Calcium
Serum Ca2+ (µmol/l)
3.0
2.5
2.0
1.5
1.0
0.5
0.0
Female
Male
Inorganic Phosphate
Serum PO4 3-(mmol/l)
5
4
3
2
1
0
Female
Male
Alkaline Phophatase
Serum ALP (U/L)
250
200
150
100
50
0
Female
Male
ALT
Serum ALT (U/L)
300
250
200
150
100
50
0
Female
Male
AST
Serum AST (U/L)
1500
1000
500
0
Female
Male
Albumin
Serum albumin (g/L)
40
30
20
10
0
Female
Male
Total Bilirubin
Serum billirubin (µmol/L)
4
3
2
1
0
Female
Male
Creatine Kinase
Serum CK (U/L)
30000
25000
20000
15000
10000
5000
0
Female
Male

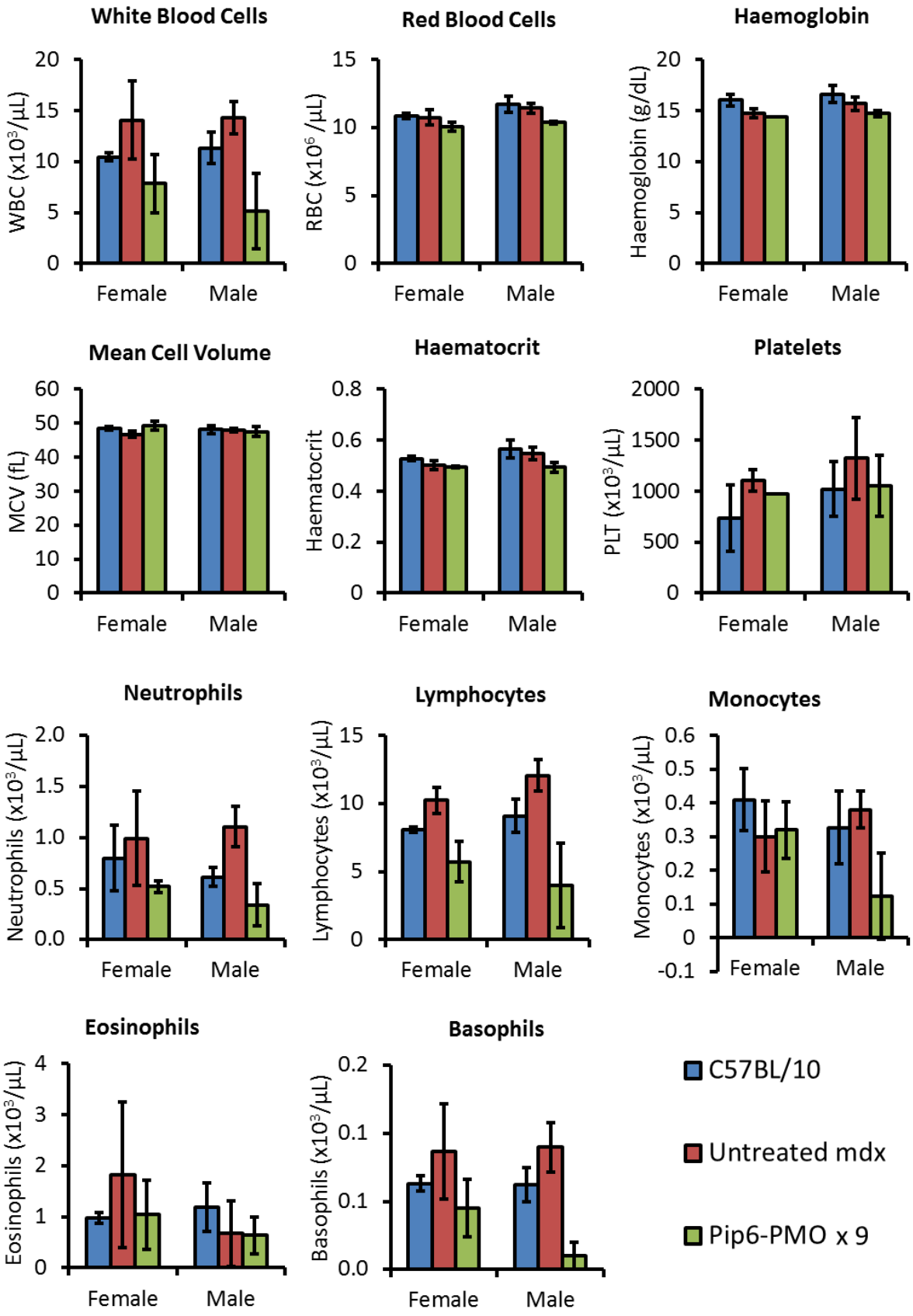
White Blood Cells
WBC (x10³/µL)
20
15
10
5
0
Female
Male
Red Blood Cells
RBC (x10⁶ /µL)
15
10
5
0
Female
Male
Haemoglobin
Haemoglobin (g/dL)
20
15
10
5
0
Female
Male
Mean Cell Volume
MCV (fL)
60
50
40
30
20
10
0
Female
Male
Haematocrit
Haematocrit
0.8
0.6
0.4
0.2
0
Female
Male
Platelets
PLT (x10³/µL)
2000
1500
1000
500
0
Female
Male
Neutrophils
Neutrophils (x10³/µL)
2.0
1.5
1.0
0.5
0.0
Female
Male
Lymphocytes
Lymphocytes (x10³/µL)
15
10
5
0
Female
Male
Monocytes
Monocytes (x10³/µL)
0.6
0.5
0.4
0.3
0.2
0.1
0
-0.1
Female
Male
Eosinophils
Eosinophils (x10³/µL)
4
3
2
1
0
Female
Male
Basophils
Basophils (x10³/µL)
0.2
0.1
0.1
0.0
Female
Male
C57BL/10
Untreated mdx
Pip6-PMO x 9

Figure 4.12. Clinical chemistry analysis of serum and haematological analysis of whole blood. Error bars represent standard deviation. For clinical chemistry the following number of animals apply: C57BL/10 female *n* = 3, male *n* = 4; untreated *mdx* female *n* = 5, male *n* = 5; Pip6a-PMO-treated *mdx* female *n* = 2, male *n* = 4. For haematology, the following sample numbers apply: C57BL/10 female *n* = 3, male *n* = 4; untreated *mdx* female *n* = 3, male *n* = 4; Pip6a-PMO-treated *mdx* female *n* = 2, male *n* = 3.

Serum analyte	Female			Male		
	C57BL/10 (±SD)	*mdx* (±SD)	Pip6a-PMO (±SD)	C57/BL10 (±SD)	*mdx* (±SD)	Pipa-PMO (±SD)
Na^+ (mmol/l)	148 (±1.53)	149 (±0.71)	152 (±1.41)	150 (±1.26)	150 (±2.45)	152 (±1.50)
K^+ (mmol/l)	8.72 (±0.40)	9.31 (±0.35)	8.70 (±0.16)	8.75 (±0.29)	10.01 (±1.05)	9.44 (±0.68)
Cl^- (mmol/l)	109 (±1.53)	108 (±1.52)	113 (±0.71)	109 (±2.22)	107 (±2.92)	112 (±0.96)
Urea (mmol/l)	6.60 (±0.10)	6.74 (±0.66)	5.75 (±0.07)	6.98 (±0.69)	7.86 (±0.64)	6.93 (±0.58)
Creat. (µmol/l)	12.3 (±0.80)	11.4 (±1.05)	12.3 (±1.27)	10.5 (±1.36)	10.7 (±1.07)	12.0 (±0.52)
Ca^{2+} (mmol/l)	2.71 (±0.08)	2.67 (±0.06)	2.54 (±0.08)	2.51 (±0.22)	2.66 (±0.18)	2.46 (±0.19)
PO_4^{3-} (mmol/l)	3.33 (±0.33)	3.80 (±0.29)	3.43 (±0.33)	3.23 (±0.13)	3.89 (±0.17)	3.75 (±0.20)
ALP (U/l)	163 (±6.43)	192 (±26.9)	143 (±1.41)	108 (±8.89)	130 (±20.05)	112 (±3.92)
ALT (U/l)	32.7 (±8.02)	196.2 (±50.80)	36.0 (±1.41)	34.0 (±3.16)	159 (±26.38)	44.5 (±6.76)
AST (U/l)	109 (±49.0)	1052 (±346.7)	108 (±24.0)	82.5 (±30.8)	841 (±155.7)	172 (±76.1)
Tot. Prot. (g/l)	50.1 (±0.78)	54.3 (±0.97)	52.6 (±0.00)	55.4 (±1.65)	55.3 (±1.52)	53.4 (±1.03)
Albumin (g/l)	31.4 (±0.60)	31.7 (±0.66)	31.2 (±0.28)	31.4 (±0.74)	29.5 (±1.40)	28.8 (±0.50)
Gluc. (mmol/l)	12.82 (±1.74)	15.88 (±2.20)	14.87 (±1.04)	14.40 (±0.55)	17.79 (±4.89)	15.80 (±3.48)
Bili. (µmol/l)	3.13 (±0.46)	3.12 (±0.29)	3.15 (±0.64)	2.75 (±0.34)	3.40 (±0.40)	2.95 (±0.26)
CK (U/l)	2925 (±1704)	6029 (±1730)	1357 (±317)	2503 (±2162)	17740 (±7410)	4687 (±2665)

Table 4.3. Clinical chemistry. Serum values for wild-type (C57BL/10), control *mdx* and *mdx* mice treated with 9 doses of 1 nmol/g Pip6a-PMO over 10 weeks. Creat., creatinine; ALP, alkaline phosphatase; ALT, alanine aminotransferase; AST, aspartate aminotransferase; Tot. Prot., total protein; Gluc., glucose; Bili., total bilirubin; CK, creatine kinase.

Blood analyte	Female			Male		
	C57BL/10 (±SD)	*mdx* (±SD)	Pip6a-PMO (±SD)	C57BL/10 (±SD)	*mdx* (±SD)	Pip6a-PMO (±SD)
WBC ($x10^3/\mu L$)	10.46 (±0.39)	14.08 (±3.85)	7.85 (±2.86)	11.33 (±1.54)	14.30 (±1.58)	5.18 (±3.70)
RBC ($x10^6/\mu L$)	10.87 (±0.22)	10.77 (±0.58)	10.05 (±0.33)	11.74 (±0.60)	11.44 (±0.38)	10.38 (±0.12)
Hb (g/dL)	16.07 (±0.57)	14.73 (±0.45)	14.40	16.63 (±0.84)	15.70 (±0.64)	14.73 (±0.31)
HCT	0.53 (±0.01)	0.50 (±0.02)	0.50 (±0.00)	0.57 (±0.04)	0.55 (±0.02)	0.49 (±0.02)
MCV (fL)	48.5 (±0.66)	46.7 (±0.95)	49.4 (±1.34)	48.2 (±1.14)	47.9 (±0.47)	47.6 (±1.46)
PLT ($x10^3/\mu L$)	737 (±325)	1104 (±104)	971	1020 (±269)	1322 (±399)	1055 (±298)
Neut ($x10^3/\mu L$)	0.80 (±0.32)	0.99 (±0.46)	0.52 (±0.06)	0.62 (±0.09)	1.11 (±0.20)	0.34 (±0.21)
Lymph ($x10^3/\mu L$)	8.10 (±0.22)	10.24 (±0.93)	5.75 (±1.48)	9.11 (±1.21)	12.09 (±1.15)	3.98 (±3.09)
Mono ($x10^3/\mu L$)	0.41 (±0.09)	0.30 (±0.11)	0.32 (±0.08)	0.33 (±0.11)	0.38 (±0.05)	0.12 (±0.13)
Eos ($x10^3/\mu L$)	0.98 (±0.11)	1.82 (±1.43)	1.04 (±0.68)	1.18 (±0.47)	0.68 (±0.64)	0.64 (±0.36)
Baso ($x10^3/\mu L$)	0.06 (±0.01)	0.09 (±0.04)	0.05 (±0.02)	0.06 (±0.01)	0.09 (±0.02)	0.01 (±0.01)

Table 4.3. Haematological analysis. Values for wild-type (C57BL/10), control *mdx* and *mdx* mice treated with 9 doses of 1 nmol/g Pip6a-PMO over 10 weeks. WBC, white blood cells; RBC, red blood cells; Hb, haemoglobin; HCT, haematocrit; MCV, mean cell volume; PLT, platelets; Neut, neutrophils; Lymph, lymphocytes; Mono, monocytes; Eos, eosinophils; Baso, basophils. Where no standard deviation (SD) is shown, this is because only 2 samples were analysed and both returned the same value.

4.2.12. Biodistribution of Cy5-Pip6a-PMO

In order to better understand the distribution pattern of ASOs *in vivo*, a fluorescent label was added to both PMO and Pip6a-PMO so as to be able to directly visualise these compounds in tissues. Fluorescent labelling was achieved using click chemistry to covalently attach Cy5 dye to an alkyne-functionalised linker between the peptide and the PMO. This process results in a chemically stable fluorescent label that should remain attached to the PMO (and to the peptide so long as this part is not enzymatically degraded). 8-week-old *mdx* mice were injected with the labelled compound and imaged 24 hours later. Mice were perfused and the skin and tail removed before imaging. Cy5-PMO demonstrated to the majority of organs including kidney and liver, spleen, lungs, skeletal muscles, thymus and lymph nodes (Figure 4.13). Fluorescent signal was not readily detected in brain, spinal cord, heart or TA muscle. In comparison, Cy5-Pip6a-PMO demonstrated increased distribution (as seen by increased fluorescent signal) in nearly all organs observed, notably including heart and brain, but not including spinal cord. Note that in the Cy5-Pip6a-PMO-treated mouse the lymph nodes were not noted to be of increased fluorescence compared to surrounding tissue and so could not be reliably extracted.

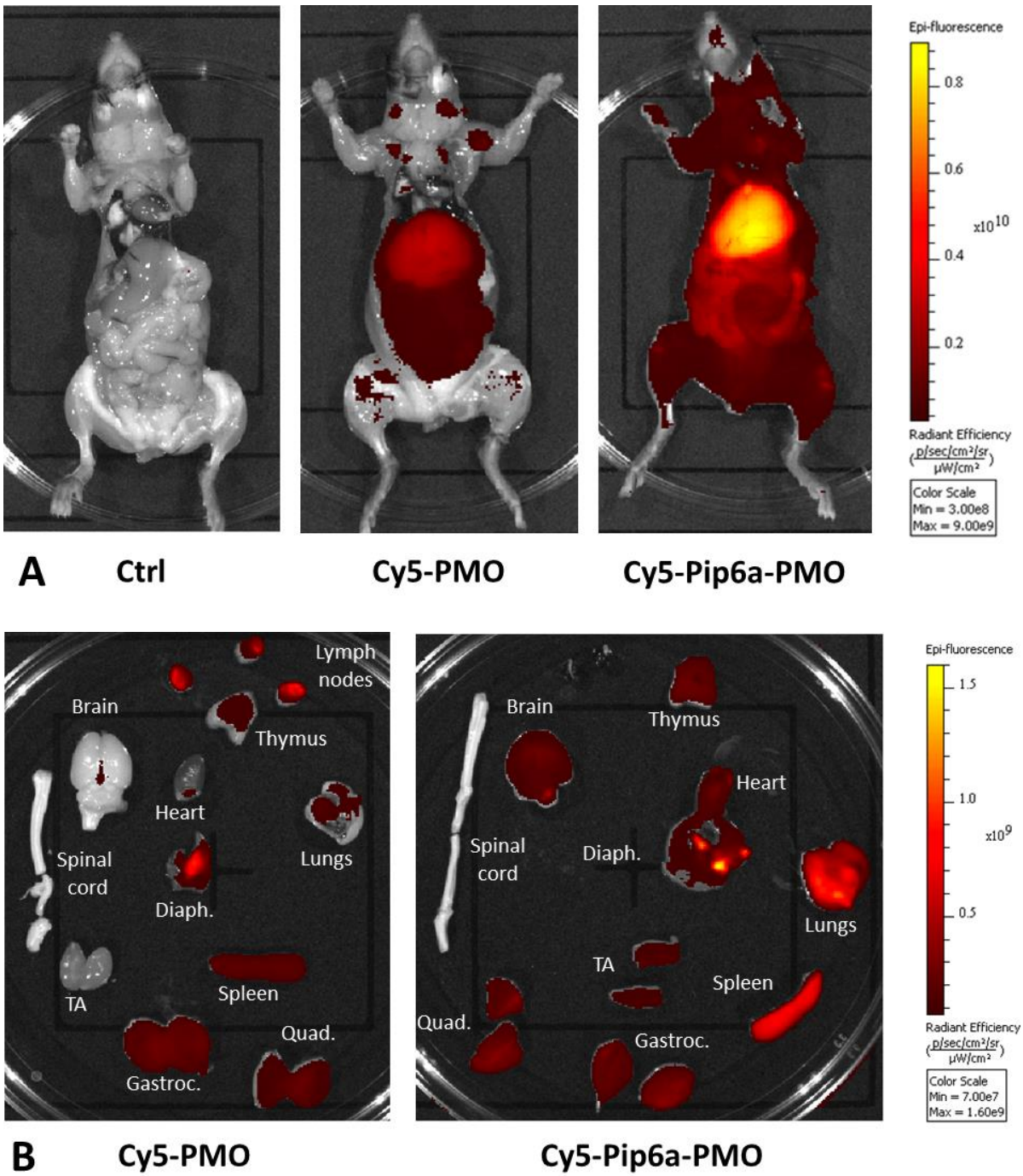

Figure 4.13. Distribution of Cy5-Pip6a-PMO and Cy5-PMO in *mdx* mice 24 hours after IV injection at 1 nmol/g. A. Fluorescent imaging of PBS-perfused mice with skin removed. **B.** Fluorescent imaging of extracted organs. Note that kidney and liver have been removed as these were too bright to image alongside the other organs. Ctrl, uninjected

control; Diaph, diaphragm; Quad, quadriceps; Gastroc, gastrocnemius; TA, tibialis anterior.

In order to further investigate the apparent distribution of Pip6a-PMO to the brain, coronal brain sections were examined from an *mdx* mouse injected with IV Cy5-Pip6a-PMO. Fluorescent microscopy showed Cy5 signal within the choroid plexus but this was not detectable in any other brain region (Figure 4.14). The presence of PMO in the choroid plexus was confirmed by *in situ* hybridisation using a probe with sequence antisense to the PMO.

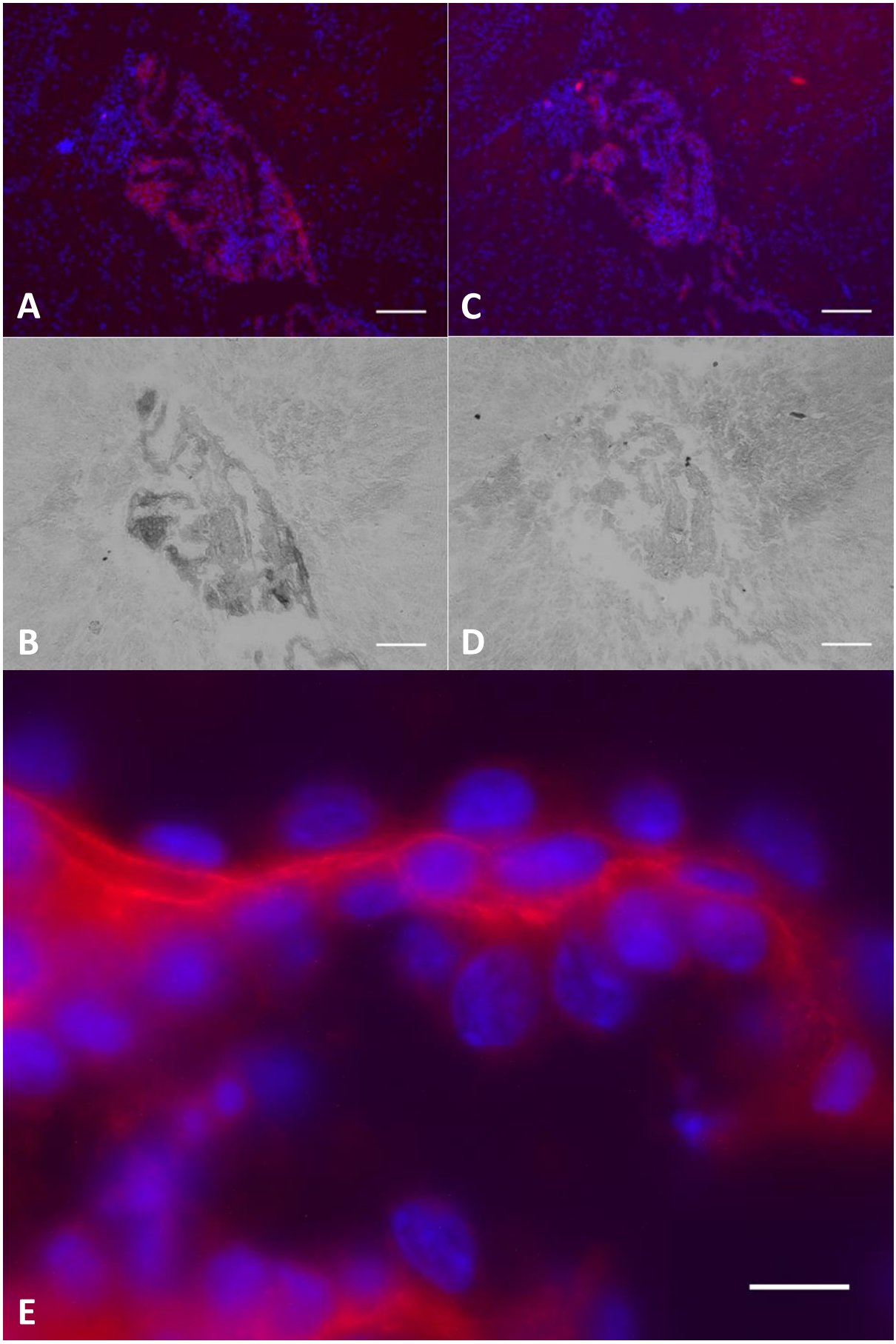
A
C
B
D
E

Figure 4.14. Fluorescent microscopy of choroid plexus and PMO *in situ* hybridisation detection. An 8-week-old female *mdx* mouse was injected intravenously with 1 nmol/g Cy5-Pip6a-PMO and transcardially perfused with PBS after 90 minutes. Frozen brain coronal sections were fixed with PFA and subjected to *in situ* hybridisation with a probe that had either the antisense sequence to PMO (**A** and **B**) or sense sequence (**C** and **D**). Cy5 fluorescence (red) can be seen within the choroid plexus (blue = DAPI counterstaining) in both **A** and **C** and this colocalises with PMO *in situ* detection in **B**, which clearly delineates the choroid plexus of the third ventricle. The control sense *in situ* probe fails to stain choroid plexus structures in **D**. Scale bars in **A**-**D** 100 µm. **E** is a close-up image of **A** (scale bar 10 µm) showing Cy5 signal within the choroid plexus. Choroid plexus epithelial cells with prominent nuclei appear to encapsulate the high-signal regions.

4.2.13. Pharmacokinetics of Cy5-Pip6a-PMO

Fluorescence of the Cy5 label was used to analyse the elimination of Pip6a-PMO from serum over a period of 6 hours. Serum was collected from 6-week-old female *mdx* mice that had been intravenously injected with 10 mg/kg Cy5-Pip6a-PMO. Serum was obtained immediately prior to transcardial perfusion at 5, 15, 30, 60 and 360 minutes post injection. By quantifying the fluorescence in the serum and assuming a first-order exponential decay function, it was possible to plot clearance of compound from the serum across these time points (Figure 5). By plotting the natural logarithm of serum fluorescence values against time it was possible to discern a linear relationship,

confirming that Cy5-Pip6a-PMO appears to obey first-order kinetics. By determining a line of best fit it was possible to interpolate these data to obtain an estimate of serum (and by inference plasma) half-life of the compound equal to 68 minutes. The plasma concentration at time *t* (C_t) of a drug obeying first-order elimination kinetics in a single-compartment model is given by the equation $C_t = C_0.e^{-kt}$ where C_0 is the initial plasma concentration ($t = 0$) and *k* is the elimination rate constant. Thus, for this experiment it can be seen from Figure 4.15. D that the following values were obtained for Cy5-Pip6a-PMO:

C_0 = 6.742 µg/ml

k = 0.612 per hour

Furthermore, by assaying in parallel the fluorescence of known quantities of Cy5-Pip6a-PMO that were serially diluted in mouse serum, it was possible to determine the actual quantities of compound detected in the timed samples (Figure 5. C, D). On the basis of these results, it was possible to estimate the compound's apparent volume of distribution (V_d) using the equation $V_d = Q/C_0$ where *Q* is the amount of drug in the body and C_0 is the concentration of drug in plasma immediately after administration, as estimated by interpolation of the concentration-time graph (in this case 6.742 µg/ml). Since five different mice were used, each with a dose (*Q*) of 10 mg/kg, an average V_d was calculated:

V_d = 26.43 ml

Knowing the apparent volume of distribution V_d allows calculation of drug clearance *Cl* using the equation $Cl = V_d.k$. In this experiment the following value for clearance of Cy5-Pip6a-PMO was therefore obtained:

Cl = 16.2 ml/hr = 269 µl/min

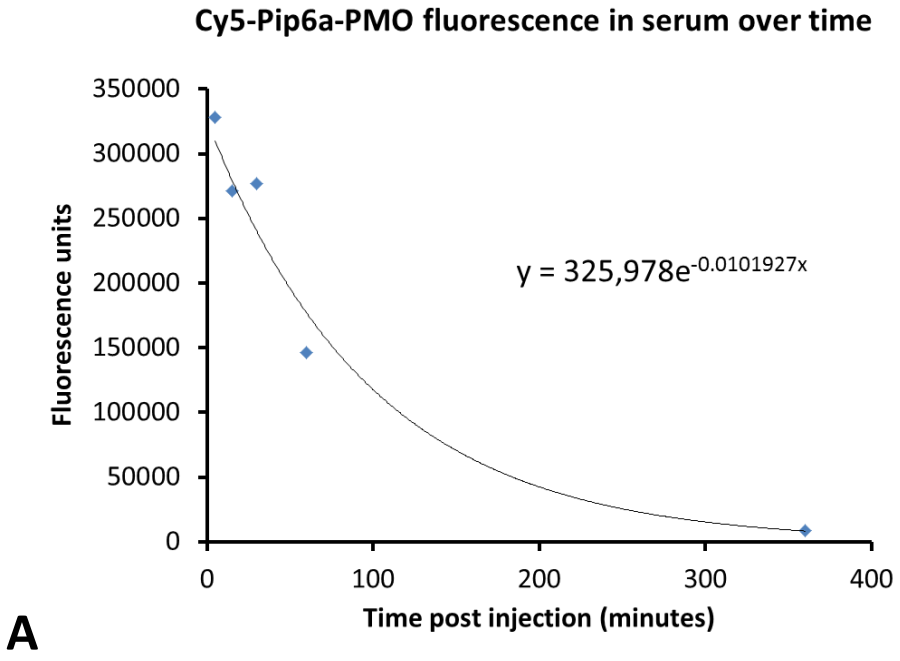

A

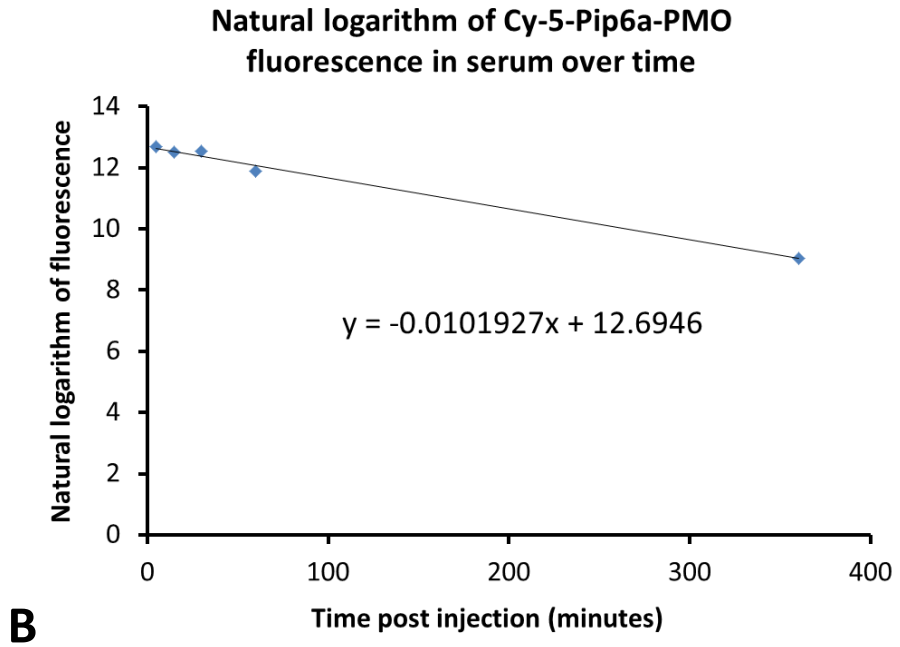

B

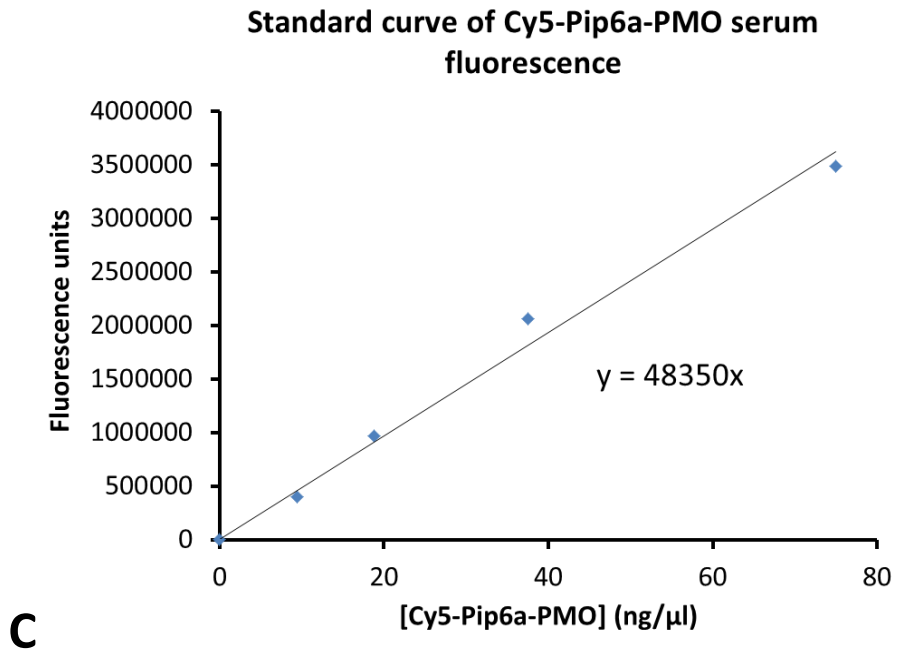

C

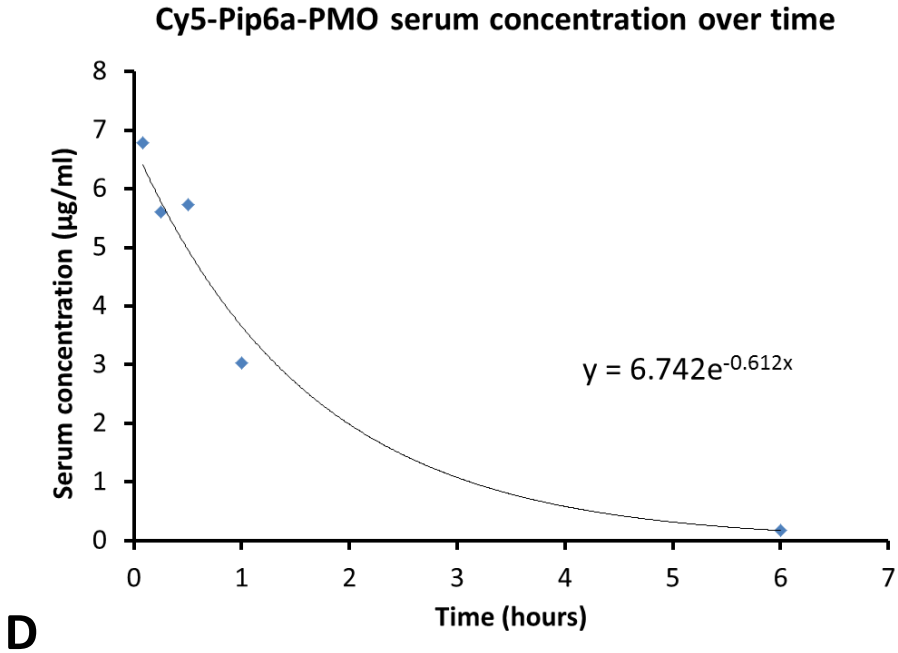

D

Figure 4.15. Serum clearance of Cy5-Pip6a-PMO. 6-week-old female *mdx* mice were injected intravenously with 10 mg/kg Cy5-Pip6a-PMO. **A.** Raw fluorescence values (corrected for background) of serum collected at 5, 15, 30, 60 and 360 minutes after injection. **B.** Natural logarithm values of fluorescence plotted against time. **C.** A standard

curve of fluorescence in serial dilutions of Cy5-Pip6a-PMO in *mdx* mouse serum. **D.** Serum concentration of Cy5-Pip6a-PMO over time.

4.2.14. Side effects of PPMOs

The majority of PPMOs tested *in vivo* were well tolerated up to a dose of 2 nmol/g (BrPepC7-PMO), 4 nmol/g (RVG-PMO, Angiopep-2-PMO, Tet1-PMO, ApoE-PMO) or 5 nmol/g (THR-PMO). However, a number of side effects were observed after intravenous administration of BrApoE-PMO (2 nmol/g) and Pip6a-PMO (1 nmol/g – 1.6 nmol/g). Cy5-Pip6a-PMO also elicited similar side effects at 1 nmol/g. These effects were apparent within several minutes of injection and included excessive salivation, general lethargy and alteration in gait, which became slow and somewhat unsteady. Some mice also exhibited unusual abdominal flexion movements. In some cases there was a degree of orbital secretion. In addition, injected mice appeared to have deeper, more laboured respiration after injection. Mice injected with Pip6a-PMO 1 nmol/g at weekly intervals had a respiratory rate of between 145-185 breaths per minute in the first hour after injection when measured by eye. In comparison, untreated *mdx* mice appeared to have a much higher respiratory rate, however it was not possible to directly measure respiratory rate in untreated animals because of its increased speed and because of the animals' increased activity level. These side effects were present for about one hour after injection after which time mice appeared to gradually improve in condition. One mouse died as a result of this toxicity following BrApoE-PMO administration. Mice that survived this acute period appeared to be completely recovered the next day. Mice that received

repeated injections of Pip6a appeared to respond in an identical way after each administration, with no obvious increase or decrease in severity of reaction.

4.3. Discussion

4.3.1. Summary of results

A total of eight different PPMOs were tested both *in vitro* and *in vivo*. In H2K *mdx* myoblast cultures, all PPMOs induced *Dmd* exon 23 skipping in a dose-dependent manner. When assayed in *mdx* mice by IV injection, most PPMOs (except for BrPepC7-PMO) induced some degree of exon skipping in skeletal muscle at the highest doses tested. The most active novel PPMO was branched ApoE-PMO, however this also proved to have a toxic effect at a dose of 2 nmol/g. Pip6a-PMO achieved the greatest degree of exon skipping at 1 nmol/g.

Exon skipping in the brain was not detectable by nested RT-PCR in any mice injected with IV PPMO. However, mice injected ICV with naked PMO or with Pip6a-PMO did show detectable brain exon skipping to varying degrees using this method, although no dystrophin protein restoration could be detected. Using a qRT-PCR assay specific for skipped product, it was possible to detect low levels of exon skipping in most of the brains from mice that received IV PPMO. Quantification by ddPCR indicated that Pip6a-PMO and BrApoE-PMO achieved the greatest degree of brain exon skipping, although the overall levels were still extremely low.

A repeat-dose study of Pip6a-PMO with nine doses of 1 nmol/g from P1 to 10 weeks resulted in a trend towards normalisation of activity in response to scruff-testing in *mdx* mice. Grip strength in these mice also appeared to be increased but best and average values were greater than those seen in wild-type control mice. The degree of exon 23

skipping in these brains was not significantly different from mice treated with a single dose of Pip6a-PMO. In addition, no restoration of dystrophin protein could be detected in these brains, although sensitivity of the Western blot assay used was probably low. Haematological and serum clinical chemistry values were comparable to wild-type values 2 weeks after the final injection and notably there was normalisation of ALT, AST and CK.

Biodistribution studies of Cy5-labelled Pip6a-PMO found that tissue distribution after 24 hours was improved over naked PMO. Fluorescent microscopy and *in situ* hydbridisation detection of PMO showed accumulation of Pip6a-PMO within the choroid plexus. Analysis of serum Cy5 fluorescence indicated that $t^{½}$ of this PPMO was around 68 minutes, with an estimated volume of distribution of 26 ml and a clearance of 269 µl/min.

4.3.2. Do PPMOs cross the BBB?

The lack of detectable exon skipping in brain using nested RT-PCR initially suggested a complete lack of BBB penetration by all PPMOs tested. However, employing a PCR approach specifically amplifying only skipped product yielded positive results in PPMO-treated brain tissue samples. This confirms a relative lack of sensitivity of the nested PCR approach in detecting low-abundance transcripts. Nevertheless, quantification of skipped transcript by ddPCR found the levels of skipping in brain to be very low indeed in IV-treated mice, with none of the PPMOs achieving more than 0.06% Δ23 skipped transcript. In comparison, the skipping efficiency obtained in brain after ICV injection of

PMO or Pip6a-PMO was around one hundred times greater, although the doses and harvesting timeframes were not directly comparable.

The reason for the disappointingly low efficacy of the putative brain-targeting peptides in delivering PMO to brain is not clear. It is possible that conjugation of the large PMO molecule to the peptides creates conformational changes that prevent their normal binding to native receptors. It may also be that the folding of these peptides synthesised *in vitro* does not mimic natural folding or post-translational modifications required for proper receptor binding *in vivo*. Another possibility is that the brain-targeting properties of these peptides are in fact not as pronounced as originally reported in the literature.

A common difficulty in demonstrating the delivery of a drug across the BBB lies in distinguishing between the specific neuronal drug effect and simple brain localisation of a drug, which may not represent true brain delivery at all but rather reflect accumulation of drug in non-neuronal cell types such as endothelium. The biodistribution study described above attempted to investigate this using the Cy5 fluorophore tag. While fluorescent imaging of whole brain suggested brain accumulation of Pip6a-PMO, direct microscopy did not reveal widespread uptake by brain tissue but instead showed isolated localisation of PPMO to choroid plexus. This discrepancy could be a reflection of both generalised intravascular binding of Pip6a-PMO and the inability to completely clear the brain vasculature of plasma by intracardial perfusion. It may of course be that fluorescent microscopy was simply not sensitive enough to detect low levels of Cy5 fluorescence that may have been present within the brain parenchyma. Perhaps more importantly, the 90-minute time point at which fluorescent microscopy was performed may not have allowed adequate time for PPMO to traverse the BBB. The high signal seen within choroid plexus

most likely represents trapping of PPMO within the perivascular space between the fenestrated endothelium and the basolateral face of the choroid plexus epithelium.

Disappointingly, repeated IV dosing of mice over a 10-week period with Pip6a-PMO did not result in significantly higher levels of brain skipping than a single IV injection. If the skipping observed in brain were the result of limited transfer of PPMO from blood to brain parenchyma, one might expect that repeated dosing would have resulted in a cumulative effect over time, as seen with muscle. The absence of this effect may indicate that such transfer did not occur. The skipped transcript may instead have arisen solely in brain capillary endothelium, since endothelial cells have been shown to express dystrophin (Loufrani et al., 2001). Alternatively, it may be that skipped transcript does not persist for an extended period in brain. In this case, PPMO transfer to brain may have occurred but levels of skipped transcript may have fallen over the 2-week intervening period between final treatment and harvesting so as to appear similar to that seen after single IV injection.

Interestingly, the behavioural activity measurements of Pip6a-PMO repeat-treated *mdx* mice appeared to normalise towards wild-type levels, possibly indicating restoration of brain dystrophin function. However, the lack of dystrophin protein expression (albeit on a suboptimal Western blot) makes this less likely to have been the case. Indeed, the experience of having received repeated IV injections is likely to have significantly modified the behaviour of these mice, while the control *mdx* and wild-type mice against which they were compared did not receive any sham injections. This same effect is likely to account for the apparent increase in grip strength observed in this repeat-treated group above and beyond that of untreated wild-type controls.

4.3.3. What is the mechanism of PPMO uptake?

The mechanism of *in vivo* PPMO uptake remains to be confirmed. Six out of the eight PPMOs tested in this study were designed to utilise receptor-mediated endocytosis at the brain capillary endothelium. Given the very limited exon skipping effects seen in brain, it is unclear whether any such transcytosis mechanism was achieved. Interestingly, the most highly active PPMOs, ApoE-PMO, BrApoE-PMO and Pip6a-PMO all shared a high degree of cationic charge, suggesting that this feature was important in determining their activity. *In vitro* studies of Pip6a-PMO have previously suggested that caveolae-mediated endocytosis is the predominant mechanism of uptake in muscle cells, while cardiomyocyte uptake may be more reliant on clathrin-mediated endocytosis (Lehto et al., 2014). In addition, cationic cell-penetrating peptides (CPPs) have previously been shown to be taken up by class A scavenger receptor-mediated endocytosis (Ezzat et al., 2012). Such receptors have been shown to be internalised by both caveolae- and clathrin-dependent pathways (Zhu et al., 2011). It may therefore be that scavenger receptors are involved in the uptake of cationic PPMOs.

Given the increased permeability of the BBB in neonatal mice as compared to adults (see Chapter 3), P1 *mdx* mice that were treated with Pip6a-PMO might have been expected to show increased exon skipping compared to older mice, both within the brain and elsewhere. This was not the case. Rather, less skipping was seen both peripherally and in brain. The reason for this is most likely a technical one relating to the difficulty of performing IV injections in P1 mice. It is highly likely that a proportion of the PPMO injected in these pups was in fact delivered subcutaneously rather than intravenously. It

is known that IV administration of PPMOs is more efficient than subcutaneous or intraperitoneal administration and this could therefore explain the decreased and variable effect seen (Jearawiriyapaisarn et al., 2008).

This benefit of IV treatment holds true even though elimination of compound from the body is likely to be much faster following IV administration. This therefore argues for the existence of a threshold plasma concentration at which uptake of compound is optimal and below which minimal uptake into tissues is achieved. This has important implications for the dosing of PPMOs. Given the relatively short circulatory half-life of Pip6a-PMO (around 70 minutes) and the apparently narrow therapeutic range indicated by the side effects observed in treated mice, bolus IV injections are likely to be an inefficient way of dosing. A more effective regimen would be to administer a loading dose, followed by repeated maintenance doses at regular intervals based on the rate of drug elimination. However, such frequent IV dosing would be impractical. A suitable alternative could therefore consist of an IV loading dose followed by an intravenous infusion of compound at a rate equal to its elimination.

4.3.4. Toxicity considerations

An important characteristic of any drug is its toxicity profile. No drug with an unacceptable level of toxicity is likely to make it into clinical trials. It is therefore important to consider what toxicity issues may exist for PPMOs. Whilst it is difficult to extrapolate directly to humans from mice, it is clear that at least some of the PPMOs used in this study had some toxic effects. In particular, BrApoE-PMO, Pip6a-PMO and Cy5-

Pip6a-PMO were noted to have some side effects in treated *mdx* mice. It is known that naked PMO has very little toxicity and that it can be administered to mice in very high doses (such as 3 g/kg) without detrimental effects (Wu et al., 2010). It therefore appears to be a property of the peptides or of their conjugation that generated toxicity. Notably, the side effects were only seen with those PPMOs that had the strongest exon skipping activity and which had the most cationic peptides. This may therefore suggest a link between cationic charge, PPMO activity and toxicity.

The experiments carried out here have not directly addressed the cause of this toxicity, however a number of observations are nevertheless apparent. The side effects observed were not only of rapid onset following PPMO administration, but were also consistently repeatable, most notably in the mice treated over a 10 week period with Pip6a-PMO. Furthermore, these same mice had very favourable biochemical and haematological profiles at time of harvesting, suggesting an absence of any long-term organ damage. This fact, combined with the observation that mice generally appeared to recover over a predictable time course of 1-2 hours (roughly consistent with drug elimination rate) suggests that these side effects were in fact a physiological response rather than an indication of end organ damage. A possible mechanism may be that such cationic peptides cause generalised parasympathetic stimulation, which could explain excess salivation as well as deep and slowed respiration. This could also potentially cause gut hypermotility, eliciting abdominal discomfort in treated mice.

4.3.5. Conclusion

The experiments outlined in this chapter have sought to investigate the ability of intravenously administered PPMOs to induce exon skipping within the brain. From these experiments, it can be concluded that targeting receptor-mediated transcytosis pathways in order to cross the BBB through peptide conjugation of PMO is not a highly effective method for ASO brain delivery. Although low levels of skipped *Dmd* transcript were detected in brain following IV PPMO treatment, the cellular source of these transcripts remains to be determined.

Pip6a-PMO was found to be the most active of the PPMOs tested. Further experiments on Pip6a-PMO sought to investigate its biodistribution and pharmacokinetics and to study the effects of its repeated dosing over time. In this regard, Pip6a-PMO achieved better biodistribution than naked PMO, although it was still cleared from the circulation relatively rapidly. Pip6a-PMO does not appear to be toxic at the level of blood analysis, however the compound does induce side effects that are likely to be dose-dependent pharmacological effects on physiology. It is likely that these side effects will be controllable through judicious dosing regimens and also if necessary by application of concurrent pharmacotherapy.

The BBB is clearly a very effective barrier to brain drug delivery. The low level of vesicular transcytosis seen in brain capillaries suggests that to achieve high levels of delivery across the BBB via this route may not in fact be feasible. Indeed, even in considering the most effective PPMO in this study, Pip6a-PMO, it cannot be said with certainty that any neuronal delivery was achieved since it was not possible to directly visualise fluorescent

compound within the brain parenchyma. However, having said this, the localisation of Pip6a-PMO to the choroid plexus is a potentially important finding. Given the unique features of the blood-CSF barrier and the apparent avidity of at least one PPMO for this structure, it may be that targeting the transport systems of the choroid plexus epithelium will ultimately prove a more fruitful route to achieving brain delivery of ASOs.

Chapter 5:

Investigation of *C9ORF72* molecular genetics and the applicability of ASO therapies

5.1. Introduction

As previously mentioned in chapter 1 (section 1.4.3), the pathogenic mechanisms responsible for c9FTD/ALS remain to be clarified. However, one of the principal mechanisms under consideration is that of haploinsufficiency. The *C9ORF72* hexanucleotide repeat expansion lies toward the 5' end of the gene in a region that can be considered both the promoter of transcript 1b and also the first intron of transcripts 1a and Δ1a. The expansion itself is flanked by two CpG islands, the upstream one of which has been shown to be methylated in expansion carriers (Xi et al., 2013) Given what is known about DNA methylation in other repeat expansion disorders such as fragile X syndrome and myotonic dystrophy, one might reasonably expect a similar relationship of increased methylation and decreased expression to hold true for c9FTD/ALS (Sutcliffe et al., 1992; Korade-Mirnics et al., 1999; López Castel et al., 2011). In support of this, reduced *C9ORF72* expression has been noted in brain samples from affected patients (DeJesus-Hernandez et al., 2011; Gijselinck et al., 2012).

If haploinsufficiency is indeed important for c9FTD/ALS pathogenesis, a standard ASO-mediated knockdown approach is unlikely to be therapeutically helpful. However, the

C9ORF72 locus is known to generate both sense and antisense transcripts (Gendron et al., 2013; Mori et al., 2013a). The function of the antisense transcript is unknown but it may act as a regulatory non-coding RNA that downregulates the sense transcript and may mediate epigenetic modifications that lead to transcriptional gene silencing. Such natural antisense transcripts (NATs) provide an attractive alternative target for ASO knockdown, which can in turn lead to target gene upregulation, thereby potentially ameliorating haploinsufficiency (Modarresi et al., 2012).

In trying to understand c9FTD/ALS, an important starting point is to look for a relationship between *C9ORF72* gene expression, CpG island DNA methylation and repeat expansion size. If a clear relationship can be demonstrated then this may point towards the mechanism of pathogenesis. In this chapter, such a relationship has been sought through the analysis of human fibroblasts from individuals both with and without the *C9ORF72* expansion. In addition, comparative methylation studies have been performed in motor neuron cell lines derived from two of these fibroblast cultures. To help investigate the natural role of the gene, expression of the mouse orthologue of *C9ORF72* has been assayed in mouse brains of different ages. In light of reports of a *C9ORF72* antisense transcript that could have regulatory function, human fibroblasts have been used to study the effects of oligonucleotide-based NAT knockdown on this gene.

5.2. Results

5.2.1. Expansion size in fibroblast cell lines

Eight primary fibroblast lines were obtained, four from *C9ORF72* expansion-positive patients and four from commercial sources. Of the four commercial lines, three were from healthy controls and the other was from a patient with a *C9ORF72* expansion who had Parkinson's disease (PD) and not ALS or FTD (Table 5.1). This PD cell line was obtained as it was the only readily available commercial fibroblast line with a confirmed *C9ORF72* expansion. Southern blotting using a $(GGGGCC)_5$ probe identified expansions in the four c9ALS/FTD patient lines ranging from around 600 to 1200 repeats (Figure 5.1). Repeat number was estimated by interpolating a plot (made in Microsoft Excel) of $\log_{10}$ band size versus distance travelled on the blot, subtracting 199 from the estimated base-pair number to account for the wild-type allele as performed by Beck et al. (2013). The fibroblast line from a PD patient did not show any detectable expansion on Southern blotting, however an abnormal expansion of at least 30 repeats was confirmed using repeat-primed PCR (Figure 5.2).

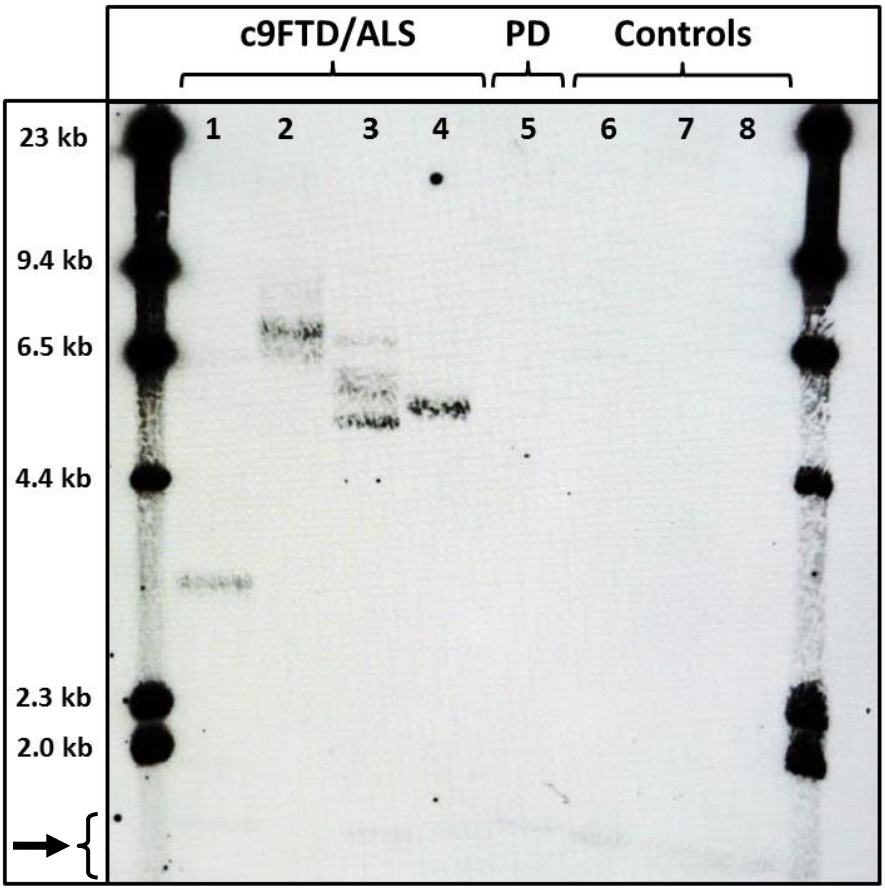

Figure 5.1. Southern blotting of patient fibroblast DNA identifies large *C9ORF72* repeat expansions in fibroblast lines from Pt 1 to Pt 4. Several discrete bands are discernable, particularly in Pt 2 and Pt 3, suggesting a degree of repeat instability during cell culture. Note that the faint bands near the base of the blot (arrowed region) are not believed to be the normal-length allele but rather represent unrelated genomic DNA regions that bind the $(GGGGCC)_5$ probe (Beck et al., 2013).

Fibroblast cell line	Patient gender	Patient age (years)	Clinical phenotype	*C9ORF72* repeat no.
Pt 1	M	58	FTD > ALS	520
Pt 2	F	48	ALS/FTD	1250, **1390**
Pt 3	M	71	Bulbar ALS	**970**, 1090-1180, 1310
Pt 4	F	58	ALS/FTD	1010
Pt 5	F	75	PD	>30
Pt 6	F	33	Healthy	2
Pt 7	F	50	Healthy	7
Pt 8	M	61	Healthy	3

Table 5.1. Details of fibroblast cell lines, the patients from which they were obtained and the fibroblast *C9ORF72* repeat number as determined by Southern blotting (Pt 1-4) or repeat-primed PCR (Pt 5-8). For Southern blotting, where more than one band was present, the most prominent band is highlighted in bold type. PD, Parkinson's disease.

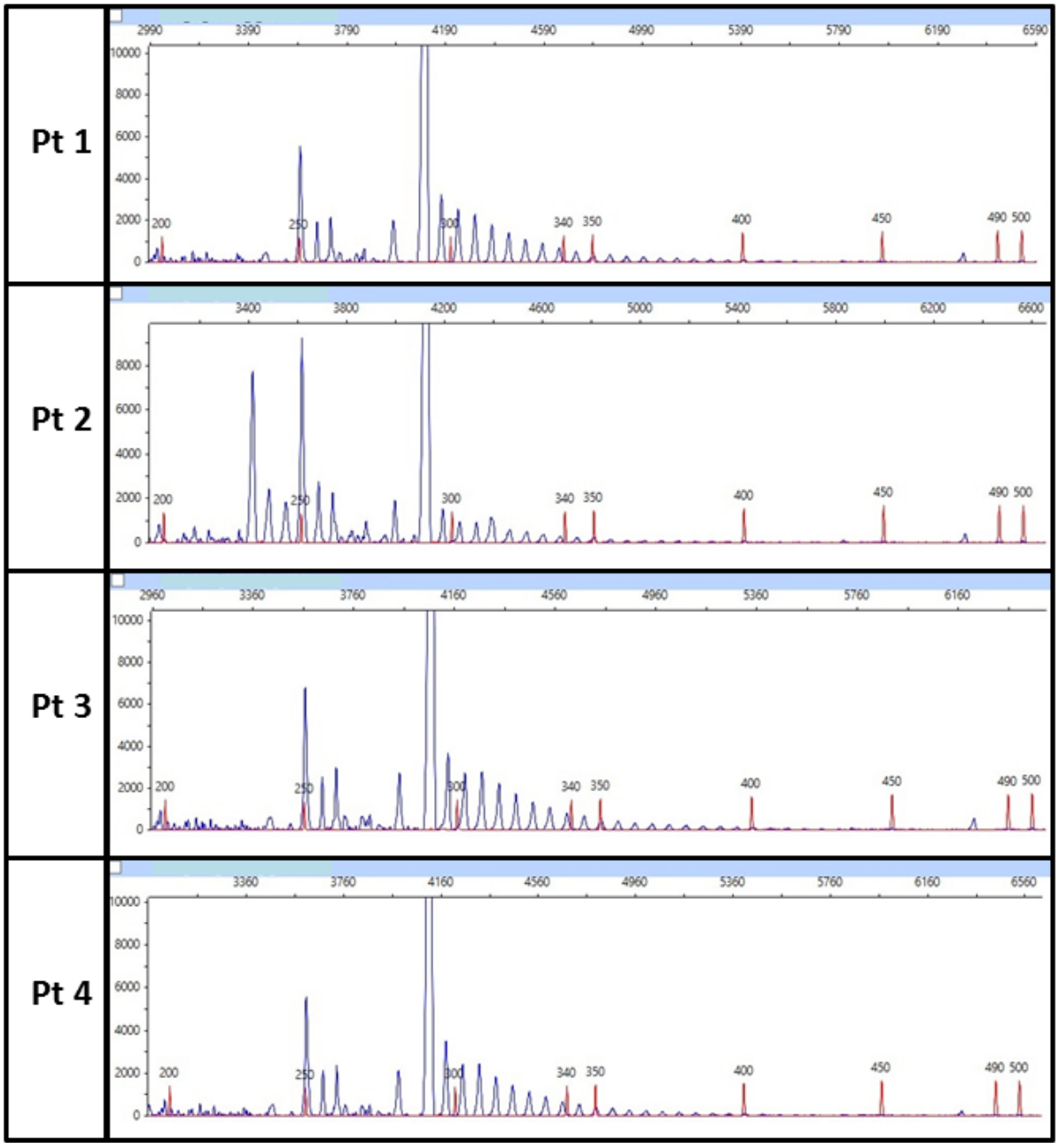
Pt 1
Pt 2
Pt 3
Pt 4

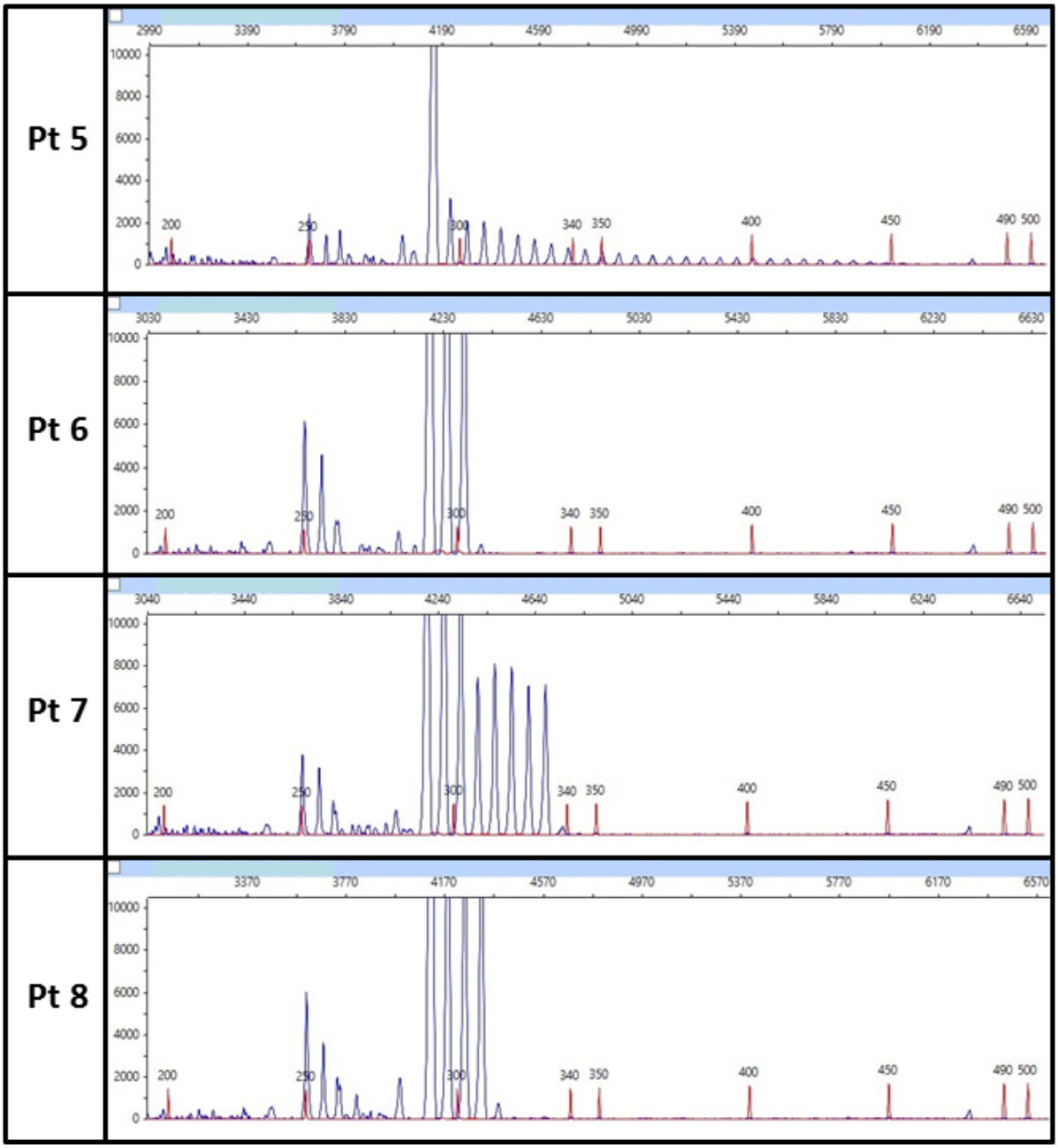

Figure 5.2. Repeat-primed PCR analysis of patient fibroblast DNA detects *C9ORF72* expansions in Pt 1-5 but not in Pt 6-8. Each peak within the visible blue 'saw-tooth' pattern represents one hexanucleotide repeat. The efficiency of the PCR decreases with increasing length of the repeat-containing amplicon and so above a certain threshold the product can no longer be detected. The upper limit of detection in this instance is around 30 repeats. ROX-labelled size markers are visible as red peaks.

5.2.2. *C9ORF72* CpG island methylation in fibroblasts

In order to assess the DNA methylation state of the CpG island just upstream of the *C9ORF72* repeat, a methyl-DNA immunoprecipitation method was used. Methylated genomic DNA fragments produced by restriction enzyme digestion with EcoRI and ScaI were pulled down using MBD2-Fc protein A beads. Relative enrichment for the upstream CpG island compared to input digested DNA was detected using a qPCR assay specific for the CpG island fragment. This analysis revealed that this CpG island exists in a highly variable state of methylation across different patient cell lines. While no significant difference in methylation was found between control fibroblasts from Pt 6-8, methylation was dramatically increased in Pt 1 (90.4 fold increase over controls) with significant increases of 15.7 and 5.3 fold also present in Pt 2 and Pt 3 respectively (Figure 5.3). Surprisingly, there was no increase in methylation in Pt 4 despite this cell line harbouring a large expansion of around 1010 repeats. No increased methylation was detected in Pt 5 with a short/intermediate expansion.

A.

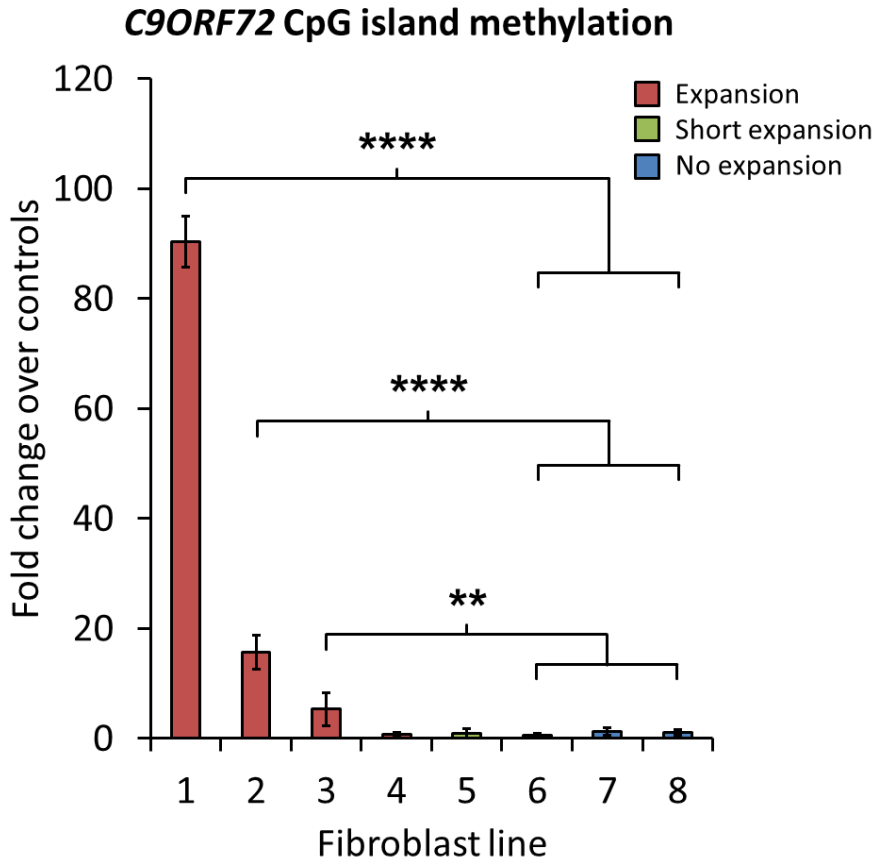

B.

Fibroblast cell line	Relative CpG island methylation	SD
Pt 1	90.4	4.63
Pt 2	15.7	3.09
Pt 3	5.30	2.96
Pt 4	0.732	0.418
Pt 5	0.880	0.834
Pt 6	0.656	0.297
Pt 7	1.31	0.705
Pt 8	1.04	0.498

Figure 5.3. Methylation analysis of the upstream CpG island of *C9ORF72* in patient fibroblasts. Fibroblast lines from Pt 1-4 have large hexanucleotide repeat expansions, Pt 5 has a short expansion and Pt 6-8 are controls and have no expansion. Three separate

methyl-DNA immunoprecipitations were performed per DNA sample (*n* = 3). **A.** qPCR analysis of pulled-down digested DNA compared to the non-pulled-down fraction (digested genomic DNA) shows marked differences in DNA fragment abundance (and hence in DNA methylation) of the upstream CpG island of *C9ORF72*. Compared to control cell lines Pt 6-8, Pt 1 has a 90.4-fold increase in methylated DNA at this region, while Pt 2 has 15.7 times more and Pt 3 5.3-fold more. Error bars represent standard deviation. **p<0.01, ****p<0.0001, based on single factor ANOVA with Bonferroni correction and post hoc t-test assuming equal variance. **B.** Data table for figure. SD, standard deviation.

In order to confirm this hypermethylation finding and to investigate it further, methylation-specific PCR (MS-PCR) was carried out on bisulphite-treated genomic DNA using a fluorescently-labelled common reverse primer and a mixture of two overlapping forward primers designed to generate products of different length depending on the methylation state of CpG dinucleotides within their sequences (Figure 5.4). When such PCR products are analysed by capillary gel electrophoresis, the presence of two peaks represents the presence of two differentially methylated DNA templates, for example from two differentially methylated alleles. A similar technique has been used previously to analyse the methylation state of various imprinted genomic loci in patient blood samples (Mackay et al., 2008). Using MS-PCR, it was possible to confirm the presence of methylated CpG dinucleotides in Pt 1 since both methylated and unmethylated template products were seen (two peaks). However, only single peaks amplified from unmethylated template were detectable in the other fibroblast lines (Figure 5.4). Please note that this analysis only provides information about the CpG dinucleotides contained within the forward primer binding sites.

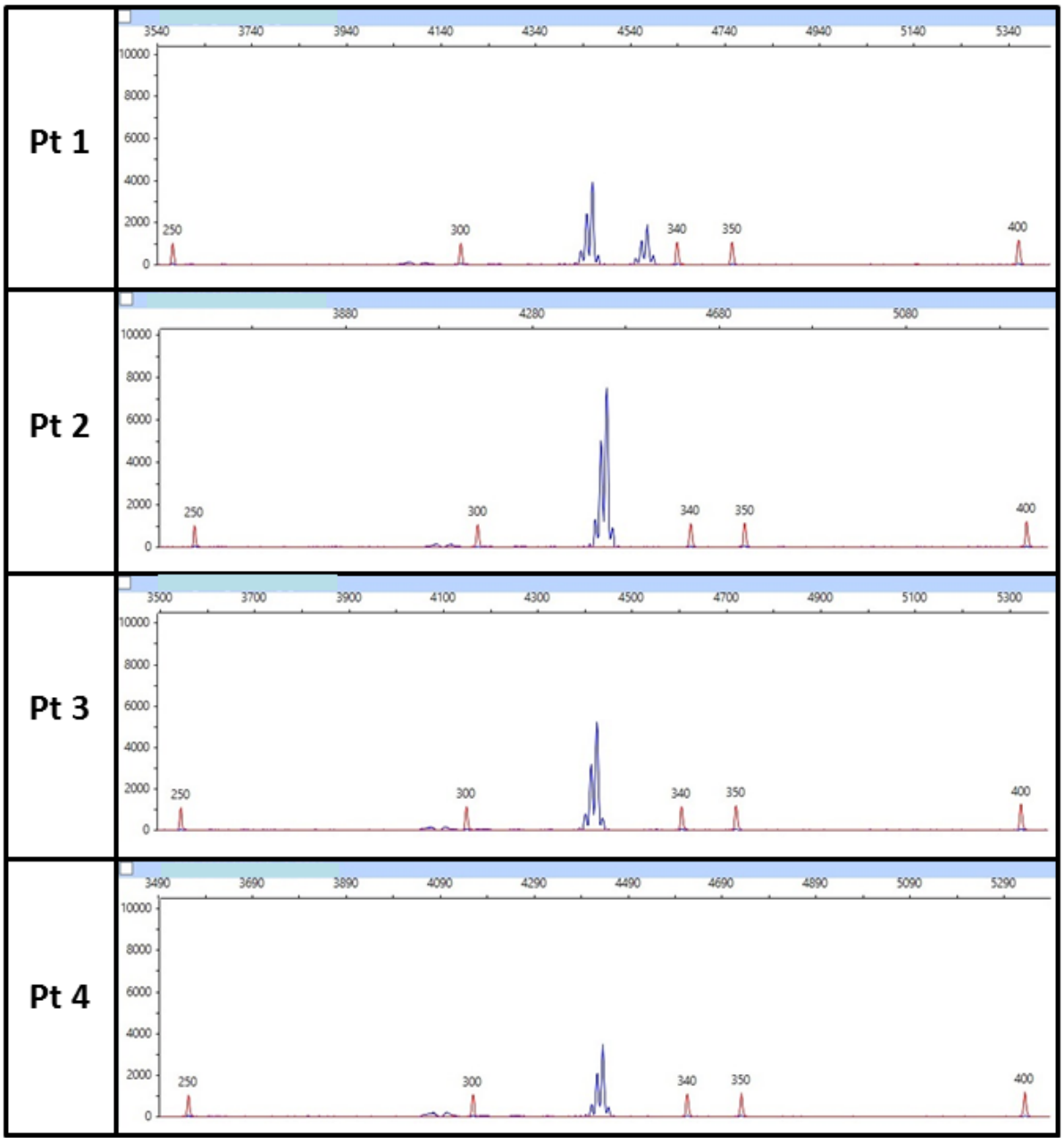
Pt 1
3540
3740
3940
4140
4340
4540
4740
4940
5140
5340
10000
8000
6000
4000
2000
0
250
300
340
350
400
Pt 2
3880
4280
4680
5080
10000
8000
6000
4000
2000
0
250
300
340
350
400
Pt 3
3500
3700
3900
4100
4300
4500
4700
4900
5100
5300
10000
8000
6000
4000
2000
0
250
300
340
350
400
Pt 4
3490
3690
3890
4090
4290
4490
4690
4890
5090
5290
10000
8000
6000
4000
2000
0
250
300
340
350
400

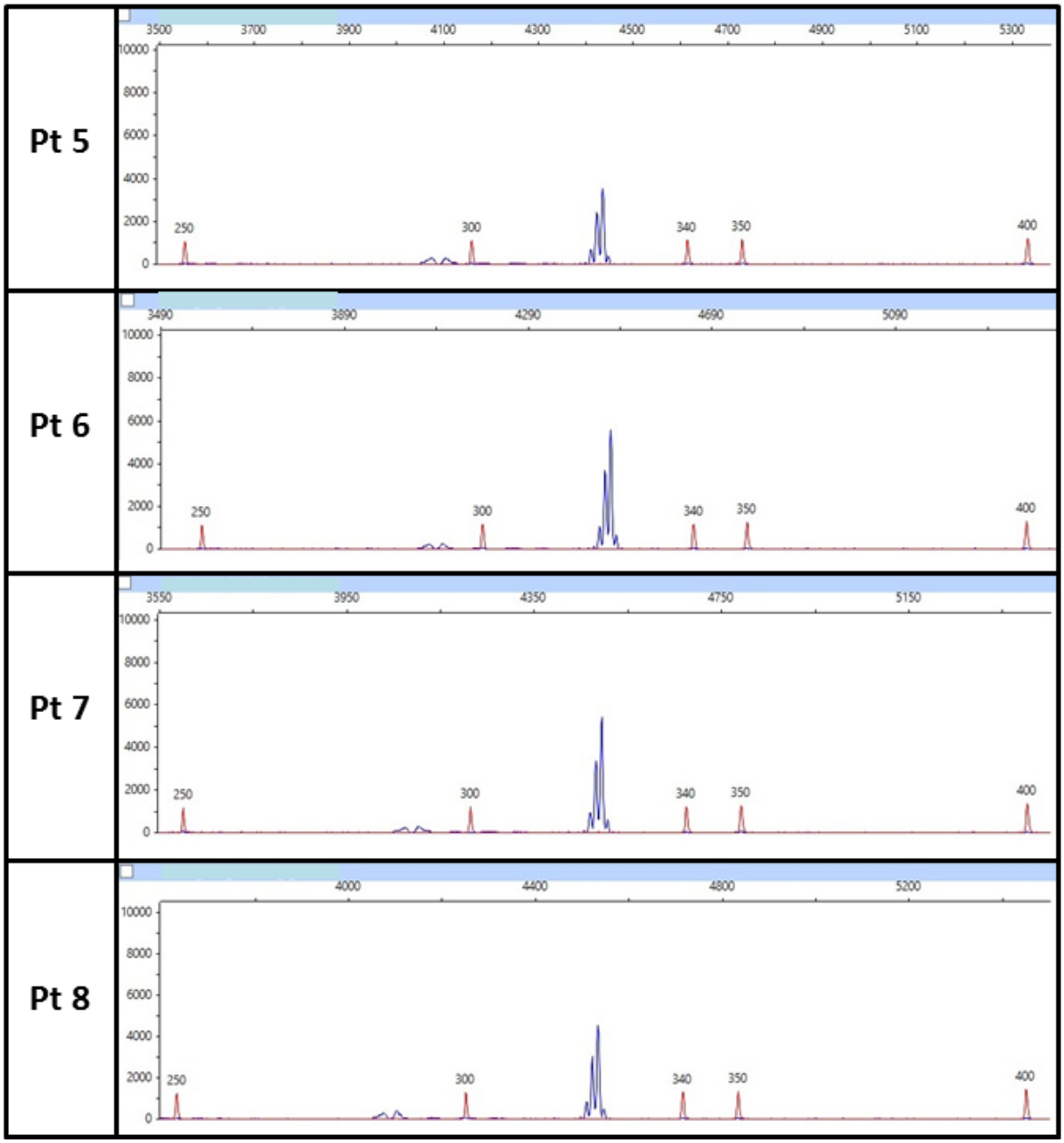

Figure 5.4. Methylation-specific PCR analysis performed on sodium bisulphite-treated DNA from patient fibroblasts. Two overlapping forward PCR primers are used. These differentially bind to bisulphite-treated DNA depending on its CpG methylation state (i.e. one primer assumes C>U bisulphite conversion and the other does not). Here the methylated-specific primer generates a product of 330 bp while the unmethylated-specific primer generates a 319 bp product. Only Pt 1 demonstrates the presence of two

distinct peaks, indicating that only Pt 1 has differentially methylated CpG dinucleotides at this primer binding site. Note that the apparent sizes of these peaks are slightly larger than expected based on the ROX sizing ladder visible in red on the traces. The reason for this is not clear.

5.2.3. Comparative *C9ORF72* methylation in iPS motor neurons

In order to investigate whether the methylation changes seen in fibroblasts perisisted in neuronal cell types, DNA from induced pluripotent stem cell (iPS) motor neurons was obtained for analysis. Two patient fibroblast lines and an additional control line were reprogrammed first to iPS cells at the Oxford Stem Cell Institute (Dr Sally Cowley) and then differentiated to iPS motor neurons (iPS MNs) at the Nuffield Department of Clinical Neuroscience (Dr Ruxandra Mutihac). Genomic DNA from these iPS motor neuron lines was kindly provided by Dr Ruxandra Mutihac. These lines (two derived from Pt 1, two from Pt 2 and one from control fibroblasts) were assayed for CpG island methylation by methyl-DNA immunoprecipitation. The patient-derived iPS MNs all showed increased DNA methylation compared to control. However, unlike the fibroblast lines where methylation of Pt 1 was greater than Pt 2, the opposite appears to be true for the iPS MN lines (Figure 5.5). Southern blotting of DNA extracted from these cell lines revealed a fairly similar modal repeat size compared to the original fibroblast lines from which they were derived. However, during the course of the de-differentiation and re-differentiation process, some repeat instability appears to have occurred, leading to several bands of different size becoming apparent in the iPS MNs.

A.

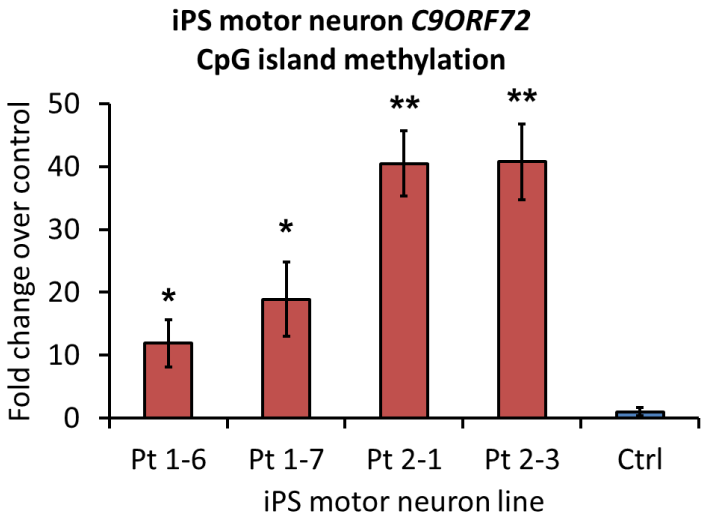
iPS motor neuron C9ORF72
CpG island methylation
Fold change over control
50
40
30
20
10
0
*
*
**
**
Pt 1-6
Pt 1-7
Pt 2-1
Pt 2-3
Ctrl
iPS motor neuron line

B.

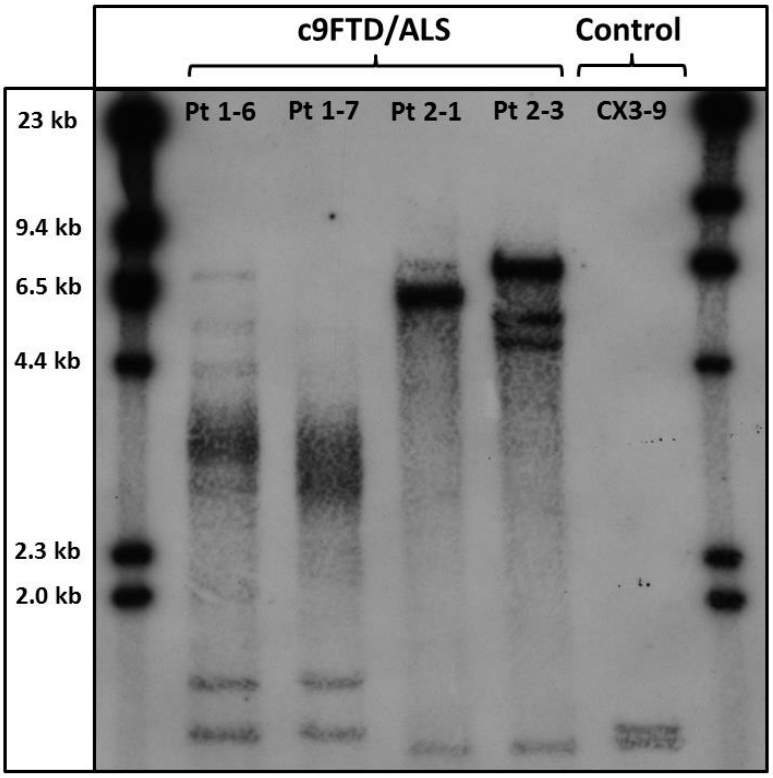
c9FTD/ALS
Control
Pt 1-6
Pt 1-7
Pt 2-1
Pt 2-3
CX3-9
23 kb
9.4 kb
6.5 kb
4.4 kb
2.3 kb
2.0 kb

C.

iPS MN line	iPS MN *C9ORF72* repeat no.	Fibroblast *C9ORF72* repeat no.
Pt 1-6	460, **510-690**, 840, 1030, 1320	520
Pt 1-7	420-640	520
Pt 2-1	1210	1250, **1390**
Pt 2-3	940, 1080, **1380**	1250, **1390**

Figure 5.5. Analysis of fibroblast-derived iPS motor neurons (iPS MN). A. *C9ORF72* CpG island DNA methylation in iPS motor neurons determined by methyl-DNA immuoprecipitation. Lines Pt1-6 and Pt1-7 were derived from Pt 1 fibroblasts and Pt2-1 and Pt2-3 were derived from Pt 2 fibroblasts. CX3-9 was derived from fibroblasts of a healthy control. Contrary to the fibroblast result (see Figure 5.3), in these iPS motor neurons lines from Pt 2 have greater DNA methylation than those from Pt 1, although both still have significantly more methylation than the control. Asterisks denote comparison of each bar to control: * $p<0.05$, ** $p<0.01$, based on single factor ANOVA with Bonferroni correction and post hoc t-test. Error bars represent standard deviation. **B.** Southern blotting of iPS motor neuron DNA reveals some variability in expansion size between lines. **C.** Estimated *C9ORF72* repeat number. Where multiple bands are present, bold type indicates the most prominent band.

5.2.4. *C9ORF72* expression in fibroblasts

Expression analysis was carried out by qRT-PCR on RNA extracted from patient fibroblast lines. As with the results of CpG island methylation, total *C9ORF72* expression varied considerably across the different cell lines (Figure 5.6). Pt 1 showed marked increase of expression over the control average (2.4-fold) and Pt 2 showed a milder yet still significant increase (1.3-fold). However, despite having similarly large repeat expansions, neither Pt 3 nor Pt 4 showed significant change in total *C9ORF72* expression and neither did Pt 5 with a short expansion. Using an assay specific for *C9ORF72* transcript 1b, increased expression was still seen in Pt 1 (1.7-fold) but not in Pt 2. Pt 3 and Pt 5 in fact showed decreased relative expression (0.61 and 0.67-fold expression respectively).

A.

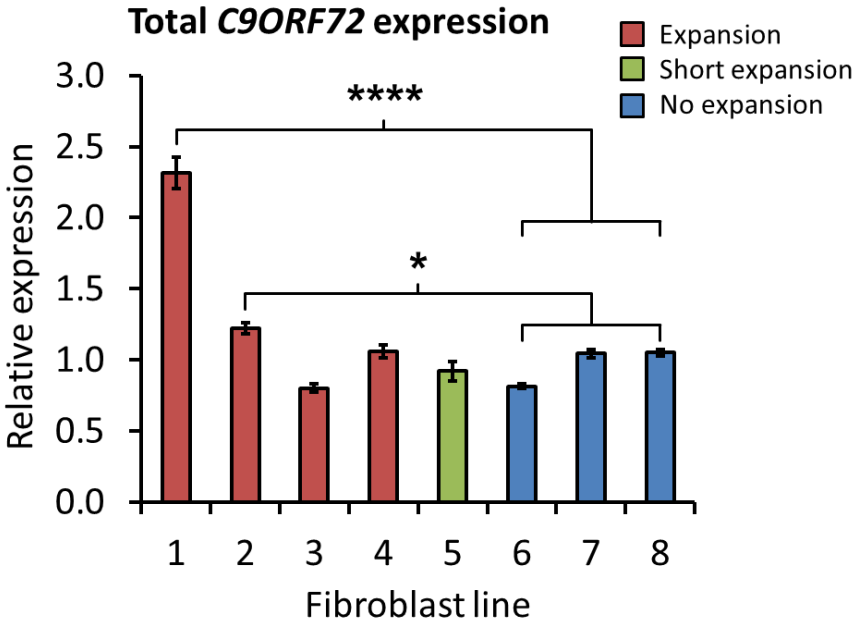

B.

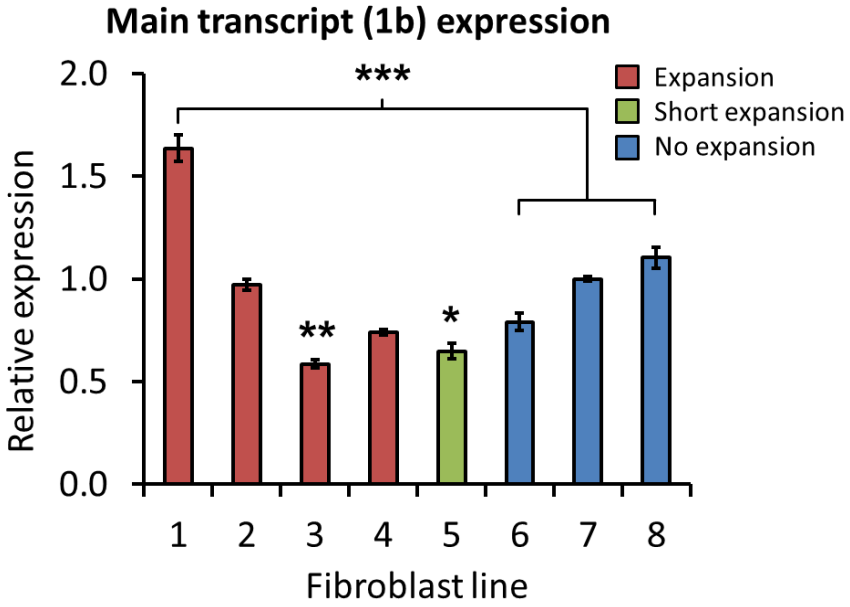

C.

Fibroblast cell line	*C9ORF72* total expression	SD	*C9ORF72* 1b expression	SD
Pt 1	2.311	0.0404	1.635	0.0635
Pt 2	1.222	0.0302	0.971	0.0276
Pt 3	0.802	0.0381	0.586	0.0191
Pt 4	1.057	0.0720	0.742	0.0131
Pt 5	0.921	0.0871	0.648	0.0362
Pt 6	0.814	0.0237	0.790	0.0422
Pt 7	1.042	0.0027	1.000	0.0092
Pt 8	1.051	0.0317	1.103	0.0493

D.

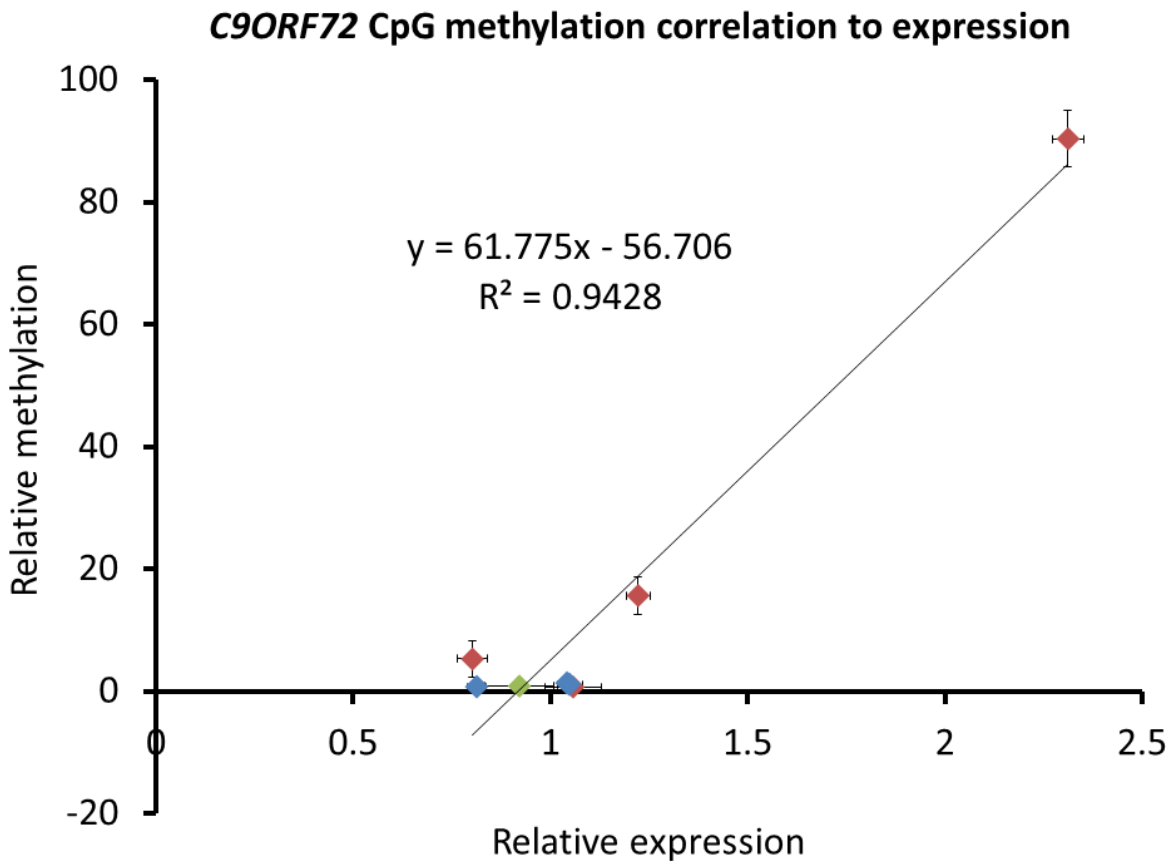

Figure 5.6. Expression of *C9ORF72* in patient fibroblasts. **A.** Total *C9ORF72* expression (all three transcripts) as measured by qRT-PCR shows significant increase over controls in Pt 1 (relative expression 2.31 versus 0.97 for control average) and Pt 2 (relative expression 1.22). **B.** Expression of transcript 1b only shows a broadly similar pattern to that of total *C9ORF72* with increased relative expression in Pt 1 (1.64 versus 0.96 control average) but not in Pt 2 and in fact there is significant decreased expression in Pt 3 (0.59) and Pt 5 (0.65). **C.** Data table for expression. SD, standard deviation. Fibroblasts were prepared in triplicate wells. Expression values have been normalised to *ACTB* and *GAPDH* using the geometric mean. Error bars represent standard deviation. *n* = 3, * p<0.05, **

p<0.01, *** p<0.001, **** p<0.0001, based on single factor ANOVA with Bonferroni correction and post hoc t-test assuming equal variance. **D.** Plot of *C9ORF72* expression against CpG island DNA methylation for the eight fibroblast lines. A positive Pearson product-moment correlation coefficient (r) of 0.971 is shown by the best-fit line and its equation, calculated in Microsoft Excel (p=0.00006).

Assays were also designed to quantify expression of *C9ORF72* transcripts 1a and Δ1a. However, these transcripts appear to be expressed at very low levels and could not be reliably quantified by qRT-PCR. In light of this low copy number abundance, a further attempt was made to detect these transcripts using digital droplet PCR (ddPCR). This technique uses the same qRT-PCR assays to look for fluorescent signal but in addition it is able to accurately quantify absolute copy numbers of template in a given 20 µl reaction by encapsulating each individual PCR in many thousands of oil-enclosed droplets. One droplet will on average contain either just one copy of the template cDNA or else no copies. In this way, each droplet will either be positive for a PCR product (it fluoresces) or else negative (no fluorescence). The numbers of positives and negatives can be counted by a droplet reader, providing an absolute copy number quantification. A similar method has been used previously to detect Δ1a *C9ORF72* transcripts in patient brain samples (Belzil et al., 2013). Using this technique it was possible to obtain limited quantitation data for these transcripts, although their low abundance was at the limit of detection. Normalising to total *C9ORF72* expression revealed that both Δ1a and 1a contribute only up to around 1% and 2.4% of total gene expression respectively (Figure 5.7).

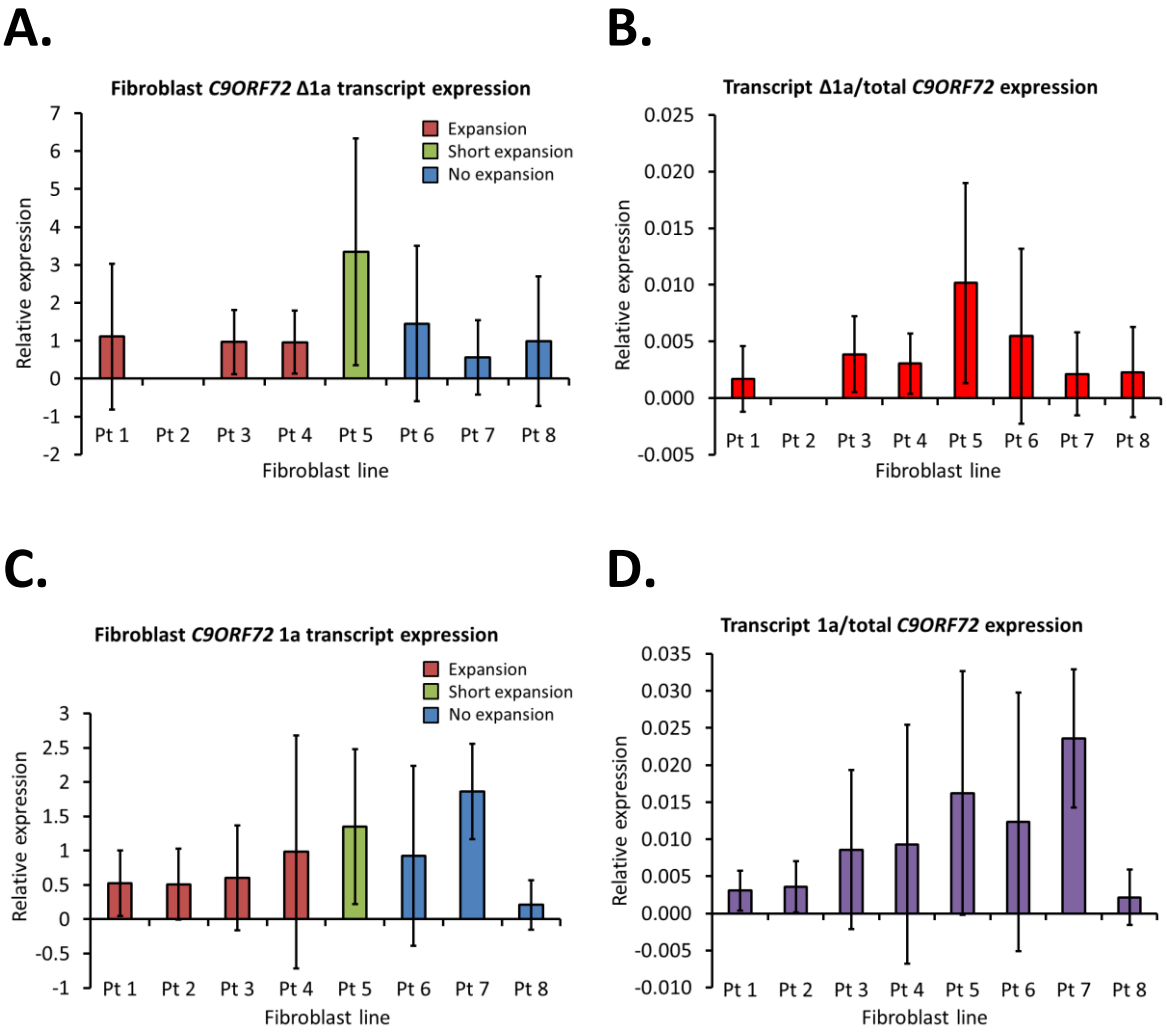

Figure 5.7. Expression of minor *C9ORF72* transcripts Δ1a and 1a determined by ddPCR. Note that both transcripts are at the limit of detection for this technology. **A.** Transcript Δ1a is present at very low levels in fibroblasts and could not be detected at all in Pt 2. Expression has been normalised to the mean value obtained from control lines. **B.** Δ1a contributes very little to total *C9ORF72* expression, with the highest level found in Pt 5 where around 1% of transcript is Δ1a. **C.** Transcript 1a is also expressed only at very low levels. **D.** Normalisation to total *C9ORF72* expression shows that its contribution is similarly small, the highest level (2.4%) being found in Pt 7. Expression values in A and C are normalised to *ACTB* and *GAPDH*. Assays were performed on cDNA obtained from 3

separate RNA samples per line (*n* = 3). However, one cDNA sample appeared to fail for Pt 6 and so here *n* = 2. Error bars represent standard deviation.

5.2.5. Expression of the mouse *C9ORF72* orthologue at different ages

Since human brain material was not directly available for study, wild-type mice were used to investigate the expression of the endogenous mouse *C9ORF72* orthologue in brain over time. The mouse orthologue of *C9ORF72* is known as *3110043O21Rik*. Expression of this gene in mouse cerebrum was analysed across a range of ages in wild-type C57BL/10 mice by qRT-PCR (Figure 5.8). Brain expression of this gene was found to be fairly uniform in mice aged from 4 weeks up to 1 year. However, there was higher expression seen in younger ages with 1.76-fold more expression at P1 compared to 13 weeks, 1.30-fold at P7 and 1.24-fold at P14. A sharp decline in expression was seen to occur in the first week of life, followed by a more gradual decline up until 4 weeks of age.

A.

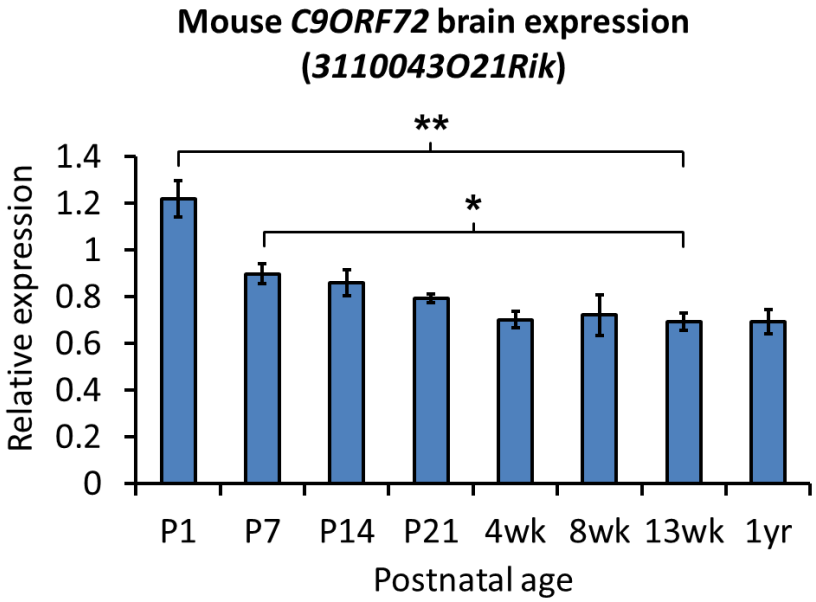

B.

Figure 5.8. Relative brain expression of the mouse *C9ORF72* orthologue *3110043O21Rik* at different ages. mRNA expression levels as measured by qRT-PCR have been normalised to two highly stable reference genes *Csnk2a2* and *Fbxw2*. Relative expression level is with respect to the value obtained for cDNA pooled across all age groups. **A.** Significantly increased expression is seen at P1 (relative value 1.22) and P7 (0.89) compared to 13 weeks of age (0.69). n = 3, * $p<0.05$, ** $p<0.01$, based on single factor ANOVA with Bonferroni correction and post hoc t-test. Error bars represent standard deviation. **B.** The same data is displayed against age of mouse in days.

5.2.6. LNA gapmer knockdown of *C9ORF72* natural antisense transcript

Previously reported studies have assessed the effect of ASO knockdown of *C9ORF72* transcripts containing the hexanucleotide repeat expansion (Donnelly et al., 2013; Lagier-Tourenne et al., 2013; Sareen et al., 2013). The ASOs used in these studies all used chemistries that induced RNase H-mediated cleavage of target RNA and treated cells

demonstrated a reduction in nuclear RNA foci. However, no previous studies have targeted the antisense transcript of *C9ORF72* with ASOs. In order to assess the function of the antisense transcript of *C9ORF72*, LNA gapmers were designed to knock down the NAT at either side of the repeat expansion. This experiment was performed by Dr Miguel Varela, University of Oxford. It should be noted that the transcriptional start site of the NAT and the extent of its transcription are both unknown at present. Nevertheless, two gapmers were chosen, each complementary to the antisense transcript (i.e. the same sequence as sense *C9ORF72* transcript) but gapmer 1 (NAT5) targeted the region 5' (with respect to the sense strand) of the repeat expansion, while gapmer 2 (NAT3) targeted the region 3' of the repeat (Figure 5.9).

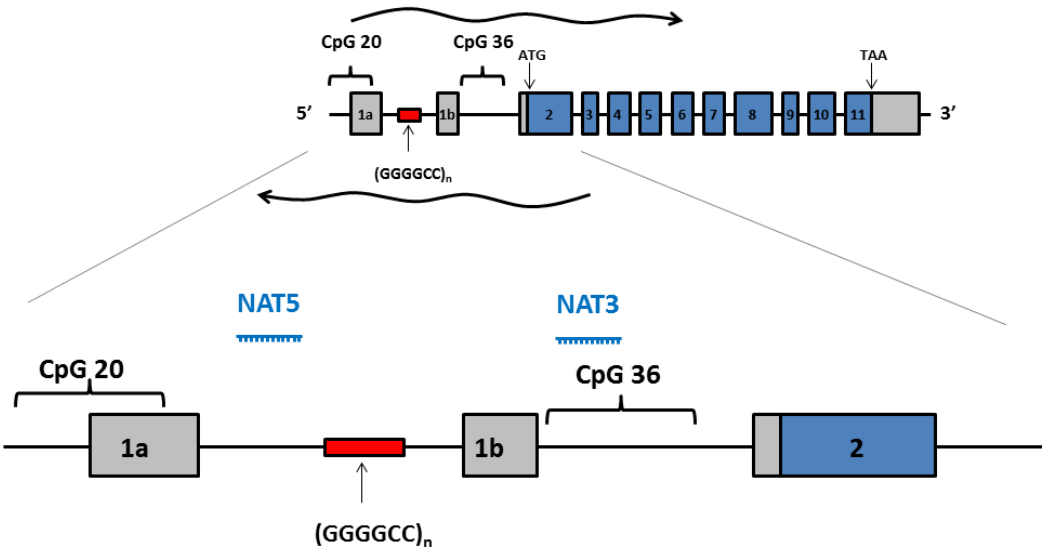

Figure 5.9. Diagram illustrating the positions of the two NAT-targeting LNA gapmers used. NAT5 targets the sequence 5' of the repeat with respect to the sense strand, while NAT3 targets the 3' sequence. Note that the start site of the NAT and its extent are unknown. Note also that of course with respect to the putative NAT itself, NAT5 in fact targets the sequence 3' of the repeat while NAT3 targets the 5' end.

Patient fibroblasts were reverse-transfected with 100 nM gapmer and RNA was collected after 48 hours. Compared to scrambled control (SCR), in most cases the NAT5 LNA gapmer targeting the *C9ORF72* NAT at the (sense strand) 5' side of the hexanucleotide repeat resulted in increased expression of *C9ORF72* total mRNA expression (Figure 5.10). Interestingly, the largest degree of upregulation was seen in Pt 5 (13.8-fold), a fibroblast line with an intermediate-sized repeat expansion. Considerable upregulation was also seen in Pt 3 (8.8-fold increase) and Pt 4 (7.7-fold), both with large repeat expansions, however this was only statistically significant in Pt 4. Control lines Pt 6 and Pt 7 also showed significant increases with NAT5 of 1.6 and 10.5-fold respectively. The only statistically significant change in expression with NAT3 was in Pt 6 where there was in fact a decrease in expression with only 0.59-fold expression compared to SCR control.

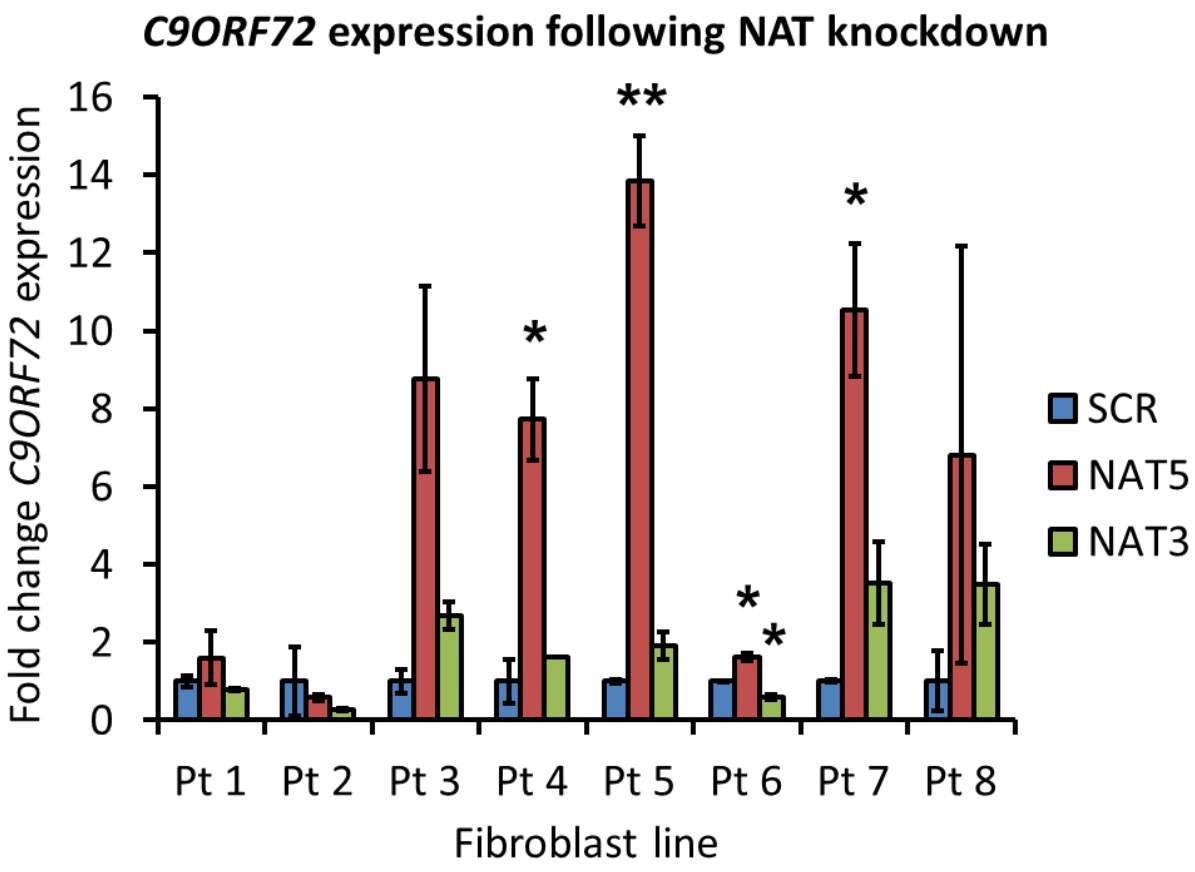

Figure 5.10. Effect of NAT knockdown on *C9ORF72* expression. LNA gapmers targeting NAT sequence upstream (with respect to the sense strand) of the GGGGCC repeat (NAT5), 3' of the repeat (NAT3) and scrambled sequence (SCR) were applied to patient fibroblast lines and *C9ORF72* expression assayed by qRT-PCR after 48 hours. Fold change in *C9ORF72* expression compared to scrambled control has been calculated using the ΔΔCt method with normalisation to *ACTB*. *n* = 2 and error bars represent standard deviation. Asterisks denote significant difference compared to scrambled control: * $p<0.05$, ** $p<0.01$, based on single factor ANOVA with Bonferroni correction and post hoc t-test.

5.3. Discussion

5.3.1. Summary of results

In this study, 8 fibroblast cell lines were analysed for their *C9ORF72* expansion size. The 4 cell lines from c9FTD/ALS patients carried expansions of between 520 and 1390 repeats. A further cell line from an individual with PD carried a shorter expansion of over 30 repeats. When the DNA methylation state of the upstream CpG island of *C9ORF72* was analysed in these fibroblasts, 3 out of 4 of the c9FTD/ALS cell lines had significant hypermethylation of this region, however the fourth showed no such increase and neither did the cell line with >30 repeats. An increase in methylation was maintained in iPS MN lines derived from 2 of the c9FTD/ALS fibroblast lines, though the degree of increased methylation differed between fibroblasts and iPS MN lines. Surprisingly, fibroblast *C9ORF72* expression analysis by qRT-PCR found a significant positive correlation between CpG island methylation state and total *C9ORF72* expression across these cell lines. Transcript-specific analysis revealed that *C9ORF72* expression almost entirely comprised transcript 1b, with transcripts Δ1a and 1a only contributing up to 1% and 2.4% respectively. Human brain material was not readily available, however analysing expression of the mouse *C9ORF72* orthologue revealed that brain expression was relatively stable in adult mice but was around 76% higher at birth. Knocking down the *C9ORF72* natural antisense transcript 5' to the repeat in fibroblasts resulted in significant upregulation in 4 out of 8 cell lines.

5.3.2. Using fibroblasts to study c9FTD/ALS

The c9FTD/ALS fibroblasts used in this study (Pt 1 – Pt 4) were obtained from patients with typical disease phenotypes. Unfortunately no comparative blood or brain samples from these patients were available for analysis. However, published studies have shown that there can be considerable discrepancy in hexanucleotide repeat number between different tissues (van Blitterswijk et al., 2013). Fibroblast cultures in particular have been shown to have consistently smaller and more discrete expansions than seen in matched blood samples. It is therefore not possible to infer the degree to which the repeat numbers found in Pt 1 – Pt 4 reflect the sizes of the expansions in brain or spinal cord of these patients. Nevertheless, the use of fibroblasts provides some potential benefits in studying *C9ORF72* expansions. Aside from their ease of culture and ability to be transfected, perhaps the most obvious of these is the benefit of having a uniform cell-type in which to study gene behaviour. This cannot be readily achieved when studying neural tissue as many different cell types will be present, each potentially expressing *C9ORF72* in different ways. Similarly, iPS-derived motor neuron cultures are never 100% pure but rather comprise a mixture of other neuronal and glial cell types. Indeed, only around 30-45% of cells in such cultures have been shown to stain positive for motor neuron markers (Donnelly et al., 2013; Sareen et al., 2013). The use of fibroblasts therefore allows study of the hexanucleotide repeat's cellular effects in relative isolation. In particular, should it turn out that a tissue-independent effect on gene expression or DNA methylation results from the nature of the repeat sequence itself, it should be possible to demonstrate this in fibroblasts.

A reasonable hypothesis might be to expect larger repeat sizes to be associated with increased CpG island methylation and decreased *C9ORF72* expression. Such a relationship has previously been demonstrated in other repeat-associated disorders such as Friedreich's ataxia, fragile X syndrome and myotonic dystrophy (Evans-Galea et al., 2012; Castaldo et al., 2008; Sutcliffe et al., 1992; Korade-Mirnics et al., 1999; López Castel et al., 2011). However, this is not the pattern seen in the c9FTD/ALS fibroblasts tested in this study. Rather, whilst increased CpG island methylation was indeed only seen in fibroblasts harbouring the GGGGCC expansion, the degree of this increase was very variable and in fact one such cell line (Pt 4) did not have any increased methylation above controls despite having some 1010 repeats. Furthermore, although CpG island DNA methylation is commonly associated with downregulation of gene expression, the c9FTD/ALS fibroblasts appear to show exactly the opposite trend with more highly methylated cell lines expressing higher levels of *C9ORF72*. Based on these results, one could conclude that the presence of the repeat expansion appears to be associated with increased CpG island methylation but that the length of the expansion itself is not directly proportional to the degree of methylation.

Why should there be such variation between patient cell lines? Why is the relationship not a straightforward one? This lack of clarity may simply belie our incomplete understanding of epigenetic regulatory mechanisms. It has become increasingly clear in recent years that DNA methylation is not just a simple on/off switch for gene regulation (Jones, 2012). Rather, it is a heavily nuanced system whose effects depend on the precise positioning of the methylated region with respect to the transcripts of interest. While it is generally true that DNA methylation of CpG islands located at transcriptional start sites

(TSSs) tends to repress initiation of transcription (Weber et al., 2007; De Smet et al., 1999), this relationship is by no means universal, particularly in the case of complex genes with multiple CpG islands, alternative promoters and embedded antisense transcripts (Illingworth and Bird, 2009).

One particularly relevant and recent study has looked at primary fibroblast cultures from 62 unrelated individuals, relating genome-wide expression to CpG methylation (Wagner et al., 2014). Interestingly, the authors found a correlation between gene expression and highly variable CpG methylation states in the same genomic region for 587 genes. About one quarter of these genes showed correlation of expression to CpG sites within 1.5 kilobases of their TSSs. This did not just represent examples of negative correlation since in about one third of these cases (perhaps around 8% of the original 587 genes) there was in fact a positive correlation of increased CpG methylation with increased expression. Somewhat surprisingly, the regions found to have such positive correlation were also found to strongly overlap with known regions of H3K27 trimethylation, a histone mark that has been reported in c9FTD/ALS (Belzil et al., 2013). Notably, the four *HOX* gene clusters were over-represented in the genes showing methylation-expression correlations, with some such as *PAX8* showing a positive correlation of expression with methylated CpG sites at their TSS but a negative correlation to methylated sites within the gene body. In the case of *PAX8* this is postulated to be related to the regulation of an antisense transcript that lies within the gene. Such analysis may well have relevance to understanding *C9ORF72* and may help shed some light on the fibroblast data presented here. For example, it may be that *C9ORF72* plays an important developmental role and may somehow be involved in the pathways related to certain *HOX* genes. If this is the

case, it may help explain the increased levels of mouse *C9ORF72* orthologue seen expressed in the brain at young ages.

5.3.3. The relevance of different *C9ORF72* transcripts

What of the minor *C9ORF72* transcripts 1a and Δ1a? If nothing else, it appears that their levels of expression are extremely low, at least in terms of mature mRNA. This raises the possibility that their primary function is not actually to generate mRNA for protein translation. Instead, it could be that both these transcripts act as non-coding RNAs (ncRNAs). This possibility is suggested not only by their low levels of mRNA expression but also by the fact that they lie directly across what is effectively the promoter region of the main *C9ORF72* transcript 1b. As such, they could therefore be thought of as promoter-associated transcripts, which are ncRNAs known to regulate gene expression (Varela et al., 2013). Furthermore, the fact that these transcripts overlap both CpG island regions of *C9ORF72* and thus also include the hexanucleotide repeat region has potentially important implications for the proposed pathogenic mechanisms of c9FTD/ALS. In particular, is it reasonable to support an RNA toxicity model based on transcription of the repeat sequence when transcription levels of these same repeat-containing isoforms appears to be so low? Of course it may be that such toxicity can slowly accrue from low-level transcription over the many years it takes to develop c9FTD/ALS. Alternatively it may be that actual transcription of this region is much higher than can be detected by simply looking at the spliced mRNA products.

What is the function of the *C9ORF72* antisense transcript? While evidence for the existence of such transcripts has previously been published, it should be noted that the present study has not directly identified or characterised the NAT but has rather inferred its presence and characteristics by the effects of its knockdown. Furthermore, these data must be treated with caution owing to the low n number of 2 for each knockdown experiment. However, notwithstanding these technical limitations, the results of NAT knockdown appear to support the idea that the antisense transcript downregulates *C9ORF72*. The two cell lines where this effect was most apparent were Pt 5 and Pt 7. Neither of these lines had significant changes in CpG island methylation or total *C9ORF72* expression. However, looking back to Figure 5.7 there is a suggestion that these are the same two lines that had more expression of minor *C9ORF72* transcript 1a. While this hints at a tantalising link between sense and antisense promoter-associated transcripts in regulating *C9ORF72*, the strength of the data is not really sufficient to make any firm conclusions about this. The fact that NAT knockdown had a larger effect when targeted to the 5' end of the repeat rather than the 3' end would suggest that NAT transcription may in fact commence at the repeat itself or else in the immediate vicinity. The location of the NAT3 target region lies within the CpG island downstream of the repeat and just downstream of exon 1b. It could be that this downstream CpG island is therefore in fact acting as a regulatory element for NAT transcription and its position may therefore denote the NAT promoter region. Of course, these inferences assume that both NAT5 and NAT3 gapmers were similarly effective at knocking down their respective target sequences. To be more certain of this would require direct quantification of NAT knockdown and indeed a more comprehensive characterisation of this transcript, which has not yet been achieved.

5.3.4. The function of *C9ORF72* and the effects of the GGGGCC expansion

This study has not attempted to answer the question of the function of the *C9ORF72* gene product. The heavily conserved nature of the gene through evolution points towards an important function, however its omission from notable groups of organisms such as insects and plants perhaps suggests that it is not critical to multicellular life *per se* but that its role may have some redundancy or overlap with other related genes. This idea could fit with its putative role as a Rab-GTPase GEF protein involved in vesicular trafficking, since a great many Rab proteins are known to exist in humans as well as an increasing number of related GEFs (Hutagalung and Novick, 2011; Zhang et al., 2012). It may therefore be possible for other vesicular trafficking pathways to partially compensate for any aberrant function of the *C9ORF72* pathway.

How does the GGGGCC repeat lead to disease? While this question remains to be conclusively answered, a number of further points are worthy of note. Much has been made of the apparent similarity of c9FTD/ALS to other repeat-expansion diseases, in particular myotonic dystrophy. In type 1 myotonic dystrophy (DM1), non-coding CTG repeats in the *DMPK* gene are transcribed within the gene's 3'UTR and form RNA foci within affected cells. These foci sequester splicing factors, depleting them from the cell and resulting in widespread errors in splicing (Ranum and Cooper, 2006). Perhaps the attraction of equating the mechanism of c9FTD/ALS with that of DM1 is because it provides a ready-made road map of how to investigate and potentially treat the disease. Multiple studies have sought to identify the cellular factors presumed to be sequestered

by the *C9ORF72* expansion. However, despite this effort, all these attempts to date have for the most part found different candidate binding partners such as Pur α, nucleolin, ADARB2, hnRNP A1, SRSF1 and hnRNP A2/B1 (Xu et al., 2013; Haeusler et al., 2014; Donnelly et al., 2013; Sareen et al., 2013; DeJesus-Hernandez et al., 2011). This may therefore point towards another mechanism being to blame.

RAN translation is a potentially attractive option. However, in order for such translation to happen, the repeat-containing transcripts must exit the nucleus to the cytoplasm so as to encounter ribosomes. This runs somewhat contrary to the RNA foci hypothesis since the formation of such foci is predicated on the idea that the expanded repeat RNA becomes trapped within the nucleus. Furthermore, the human genome is a very repetitive place with many loci containing highly repetitive DNA sequences. Indeed, a simple BLASTN query of $(GGGGCC)_5$ will quickly demonstrate that this motif is present at multiple locations throughout the genome and also exists in multiple annotated mRNA transcripts (not including *C9ORF72*). Given the widespread nature of repetitive DNA, this perhaps makes it seem less likely that RAN translation should be confined solely to the *C9ORF72* repeat so as to cause disease.

Could loss of function provide the answer? Once again there is some evidence for this, not only from the reports of decreased expression and methylation, but also in sequence similarities to other loss-of-function repeat disorders. In particular, it is striking that the GGGGCC sequence of *C9ORF72* bears so much resemblance to the CGG repeat sequence of *FMR1* responsible for fragile X syndrome. Both repeats are located at the 5' end of their respective genes. Both repeats have also been shown to form G-quadruplex structures (Fratta et al., 2012; Reddy et al., 2013; Kettani et al., 1995). Intriguingly, a rare

folate-sensitive fragile chromosome site is known to exist at 9p21 but as yet this has never been molecularly characterised (Sutherland, 2003). It may just be possible that this fragile site represents the *C9ORF72* expansion. Furthermore, a zebrafish model of c9FTD/ALS, using morpholino-induced knockdown of the zebrafish *C9ORF72* orthologue, demonstrated motor neuron axonal degeneration, suggesting a role for loss of function in this disease (Ciura et al., 2013). Despite these arguments, there are caveats against the loss-of-function hypothesis. One is the lack of any c9FTD/ALS patients with a straightforward loss-of-function nonsense or frameshift mutation in *C9ORF72*. Another is that at least one patient homozygous for *C9ORF72* expansions has been reported but this patient still expressed the gene in brain tissue, albeit at a reduced level (Fratta et al., 2013).

5.3.5. Conclusion

The work described in this chapter has sought to understand something of the molecular genetics of *C9ORF72*, how this could relate to c9FTD/ALS and whether oligonucleotide therapies might be applicable to this disease. From the experimental data reported here, it can be said that there is no straightforward linear relationship between DNA methylation at the upstream CpG island of *C9ORF72* and the size of the repeat expansion, although the presence of a repeat expansion makes methylation more likely. Similarly there does not appear to be a link between expansion size and *C9ORF72* gene expression in patient fibroblasts. However, there is a positive correlation between CpG island methylation and *C9ORF72* gene expression. Targeted oligonucleotide knockdown of the antisense transcript of *C9ORF72* shows promise of being able to upregulate expression of

the sense transcript. Confirmation of this will require further experiments. However, should loss of *C9ORF72* function through transcriptional silencing prove to be the principal cause of c9FTD/ALS, targeted NAT knockdown could potentially provide a useful therapeutic approach.

Chapter 6:

Summary discussion and conclusion

6.1. Summary and extension

This thesis has focussed on three different but inter-relating themes:the blood-brain barrier, one of the great challenges to developing neurological therapies; Duchenne muscular dystrophy, a primary disorder of muscle; and amyotrophic lateral sclerosis, a primary motor neurone disease. Running through these three themes and linking them together has been a fourth: oligonucleotide therapeutics. Having surveyed and investigated these four areas over the preceding chapters, what key findings have arisen from this work, what further work could be done in the future and what can ultimately be said about each one of these topics? In this final conclusion section, a few final thoughts come to mind.

6.2. The blood-brain barrier in *mdx* mice

The experiments of chapter 3 found no gross structural abnormalities of the BBB in adult *mdx* mice. Gene expression analysis of pertinent BBB-associated genes also failed to show consistent major expression differences in the brains of *mdx* mice from birth to one year of age. Finally, functional analysis of the BBB by fluorescent tracer uptake showed a substantial and dramatic decrease in brain tracer accumulation in both wild-type and *mdx* mice in the first 3 weeks of life. On the whole there was little functional difference in the degree of tracer uptake between wild-type and *mdx* mice. It therefore seems likely that

the BBB is neither severely defective in its structure nor functionally impaired in *mdx* mice.

Further work could be done to try to confirm these findings. One possibility would be to perform systematic structural analysis of the NVU by fluorescent and electron microscopy at other ages across development. This could be particularly informative if done across the first 3 weeks of life, especially if the choroid plexus and BCFSB were also to be examined. The present study of gene expression was limited to RNA analysis but this could further be analysed at the protein level by performing Western blotting for BBB proteins in brain samples. Furthermore, performing detailed dissections of brain tissue could allow expression analysis to be done in different brain regions, where BBB development may potentially behave differently. Finally, one of the more intriguing findings in this study was the unusual patterns of tracer uptake seen in brain sections. This may represent CSF tracer accumulation and it would be of interest to investigate fluorescent tracer uptake into CSF by direct sampling and analysis of this fluid.

This thesis, as well as the work of countless other investigators, has demonstrated the effectiveness of the blood-brain barrier as a physiological system. Despite the efforts of many groups over many years, it remains very hard indeed to transport a large molecule drug from the blood into the brain. The experiments of chapter 4 suggest that low-level transfer of PMO to brain may be possible through the use of peptide conjugation, however it remains unclear whether the activity seen in brain represents true neuronal delivery of compound across the BBB. Indeed, if an answer to the BBB problem does in fact exist, it has not yet been clearly solved or explained. These shortcomings likely belie

our relative lack of understanding about how the BBB truly functions *in vivo*. One major contributor to this failing is the absence of a truly representative *in vitro* model. This is consequent to the neurovascular unit's complexity as a multicellular barrier system. All too often the BBB is described in the literature in an overly simplified manner, for example by the equating of transendothelial electrical resistance (TEER) with BBB permeability, or by the description of the neonatal mouse BBB as being simply 'open'. The BBB will not be crossed until it is first understood. The key to this will most probably lie in studying the integrative cell biology of the neurovascular unit and the endogenous mechanisms of molecular cargo trafficking within the brain.

A potential alternative route of CNS delivery has been suggested by the experiments in chapters 3 and 4 of this thesis: delivery across the blood-CSF barrier. This may be achievable by targeting the choroid plexus, which has a number of features that make it perhaps a more suitable target than the endothelial barrier of the BBB present throughout the rest of the brain. To start with, the choroid plexus receives, weight for weight, nearly ten times more blood flow than the cerebral cortex (Szmydynger-Chodobska et al., 1994). Choroid plexus endothelium is highly fenestrated and lacks tight junctions and this allows free access of plasma constituents to the basolateral surface of choroid plexus epithelium (Hurley et al., 1981). This specialised epithelium is highly metabolic since it is responsible for CSF secretion. Indeed, choroid plexus is estimated to contribute up to 75% of the water content transferred from plasma into the CNS (Johanson et al., 2011). Additionally, it contains a unique set of receptors and transporters not present on brain capillary endothelium and these make attractive targets for drug transport. Examples of such transport includes folate, vitamin C,

prolactin, insulin-like growth factor 1 and leptin (Spector and Johanson, 2006; Spector, 2006; Walsh et al., 1987; Carro et al., 2005; Dietrich et al., 2008). In the case of folate, evidence exists that transport into the brain is mediated via exosome release from the choroid plexus and it may be that this pathway can be utilised for therapeutic drug delivery (Grapp et al., 2013). In any case it is clear that further study of these transport systems is warranted.

6.3. Treating *mdx* mice with peptide-conjugated antisense oligonucleotides

In chapter 4 it was demonstrated that exon skipping could be detected in the brains of mice treated with intravenous PPMOs. This is an important and intriguing finding, since although intravenous tcDNA has been shown to induce exon skipping in the brain, it has not previously been demonstrated for this kind of ASO chemistry (Goyenvalle et al., 2015). However, the levels of skipped transcript in the brain, even after repeated intravenous treatment with the best-performing PPMO (Pip6a-PMO), were very low (around 0.044%). It is unclear whether such low levels of activity would be enough to significantly alter the cognitive deficit in DMD and it is likely that a more efficient delivery system will be needed if the cognitive features of DMD and other neurogenetic diseases are to be treated intravenously. Nevertheless, this work provides a valuable starting point on which to base further work.

If PPMOs are to be trialled in a clinical setting, the most vital issue to resolve will be the significant toxic side effects observed immediately following their systemic administration. As previously mentioned in section 4.3.4, it is quite possible that this toxicity represents a pharmacological effect on the autonomic nervous system, since the effects seem temporary and tend to resolve over a similar time period to the plasma half-life of PPMO. In addition, no signs of end-organ damage are apparent, even after repeated dosing over 10 weeks. If parasympathetic overstimulation is indeed the cause of *in vivo* PPMO side effects, this would be cause for optimism, since it would then be likely that concomitant pharmacological therapy could ameliorate and hopefully abolish such side effects. Such experiments would therefore be highly informative and desirable for the field of therapeutic PPMO research.

A further important topic for future research will be to more completely ascertain whether the exon skipping seen in the brain originates from neuronal cells or from other sources such as glia, endothelium or vessel-associated smooth muscle. This may prove quite challenging, especially as the levels of skipped transcript in brain are so low. However, one possible approach may be to perform ultrastructural analysis of brain tissue by electron microscopy after the intravenous administration of gold-labelled PPMOs. In this way, it may be possible to directly visualise PPMOs within the cells of interest. It may be, for example, that PPMOs can access the brain via the choroid plexus rather than via the BBB and so any such analysis should also include choroid plexus tissue. Furthermore, it would be possible to analyse the CSF of mice treated with fluorescently-labelled PPMOs to see whether accumulation within this fluid occurs.

In terms of future PPMO design, the possibilities for the conjugation of new and different peptides remain very broad. The receptor-mediated approach utilised in this study did not yield as effective results as was hoped. However, it may be that some modification of this approach would be more successful. A better understanding of *in vivo* BBB transcytosis mechanisms would help inform such work. In addition, consideration of the choroid plexus epithelium as an alternative target to the BBB may prove a more fruitful avenue of research.

6.4. Investigation of *C9ORF72* molecular genetics and the applicability of ASO therapies

Chapter 5 showed that in fibroblasts there was no consistent correlation between *C9ORF72* expansion size, DNA methylation and gene expression. However, there was an unexpected positive correlation between the degree of DNA methylation and *C9ORF72* gene expression in these cell lines. Examining this gene's expression in mice, the mouse orthologue of *C9ORF72* appeared to be upregulated in the neonatal period, suggesting a role in brain development. Since haploinsufficiency is a possible pathogenic mechanism in c9FTD/ALS, an ASO-mediated therapeutic approach was sought for upregulation of the gene. By using LNA gapmers to target the natural antisense transcript (NAT) of *C9ORF72*, gene upregulation was seen in several fibroblast lines.

C9ORF72 and c9FTD/ALS is currently a topic of considerable research interest and it is likely that a much fuller understanding of this gene and of its role in disease will become

clear in the next few years. However, for now there are several key aspects that remain unclear and that therefore warrant further research. One such aspect is to better characterise the DNA methylation state across the whole gene locus, not only at the upstream CpG island but also at the downstream CpG island and at the repeat itself. This will be important to clarify, as it seems plausible that these separate CpG islands may regulate different *C9ORF72* transcripts, perhaps including the NAT. Experiments examining this in detail and linking these findings to the differential expression of various *C9ORF72* transcripts would therefore be highly desirable in helping to understand this gene. In addition, a much more comprehensive study of the *C9ORF72* NAT will be essential in order to understand its function. Experiments to determine its transcriptional start site, its length and its differential expression in relation to the *C9ORF72* sense transcripts in various tissues will all aid in deciphering the molecular biology of this locus. In line with this, a more detailed NAT knockdown study would better determine whether this approach can indeed upregulate *C9ORF72* in a therapeutically relevant way. To examine whether such NAT knockdown leads to long-term epigenetic changes in gene expression would also be of great interest.

ALS continues to perplex us as a disease. Whilst our understanding of neurodegenerative diseases appears to increase on an almost daily basis, great uncertainty still exists as to the precise cause of neuronal death in the majority of such disorders. Again we are limited in our ability to model these diseases of old age either in a dish or in short-lived animals such as mice. From a clinician's perspective, it is indeed curious to consider how disorders such as spinal muscular atrophy, spinobulbar muscular atrophy, hereditary

spastic paraplegia and ALS can all have such diverse aetiologies and yet all preferentially affect motor neurones, albeit with different onsets and patterns.

Much remains to be understood about *C9ORF72* and how the hexanucleotide expansion at its 5' end causes disease. What is perhaps most clear is that c9FTD/ALS does not behave like a straightforward expansion-related disease. From what is known about other expansion diseases, it may have been expected that repeat number would correlate inversely with age of onset, i.e. the higher the repeat number, the younger the onset. However, studies have so far not found any such correlation in expansion-positive ALS patients and indeed in FTD patients the opposite correlation appears to hold: the higher the repeat number in frontal cortex, the older the disease onset (van Blitterswijk et al., 2013; Dols-Icardo et al., 2014). Similarly, there appears to be variability in onset within affected families and although claims of disease anticipation have been made, these studies have so far been small and remain to be confirmed on larger cohorts (Chiò et al., 2012; Benussi et al., 2014). A number of disease-modifying genes may be at work, such as *TMEM106B*, however the mechanism by which they may have their effects remain to be determined (van Blitterswijk et al., 2014). Certainly the penetrance of c9FTD/ALS does not appear to be complete, particularly as the expansion has been implicated in a significant proportion of apparently 'sporadic' cases. This uncertainty is a particular issue when it comes to the genetic counselling of unaffected family members seeking predictive testing for this late-onset disease. It can only be hoped that further work will help to clarify the situation and potentially offer the hope of a therapy for this devastating illness, perhaps in the form of oligonucleotides.

6.5. The future of oligonucleotide therapeutics

Oligonucleotide therapies show great promise in the potential treatment of many genetic disorders. They are immensely versatile due to their dynamic chemistries, wonderfully targetable owing to their reliance on sequence specificity, and furthermore they can potentially be designed so as to be fully personalised and tailored to an individual's specific mutation. Indeed in many ways they perfectly embody what it means to have personalised medicine. With the rapidly increasing availability of genomic sequence data for individual patients, one may perhaps envisage a future in which a patient's disorder can be diagnosed, an appropriate therapeutic oligonucleotide designed and synthesised, and a personalised treatment supplied to the patient in relatively short order. While this vision remains for now a fantasy, it is not outwith the realms of possibility. In order to get to such a point, not only will the cost of such compounds have to reduce and the efficacy of delivery increase, but a lot more experience will also be needed in the use of oligonucleotides as clinical drugs.

One particularly limiting factor for personalised oligonucleotide development comes in the form of the established drug regulatory legislation. The current process means that each novel compound requires full triple-phase clinical trial evidence in order to be approved and medically licensed. While this tends to ensure safety and efficacy, for rare diseases the scale of the clinical trials required is a problematic issue that can impede progress in drug development. Oligonucleotide development for DMD is a case in point, with patients suffering from rarer though potentially skippable mutations being at risk of feeling left out from the current exon-skipping trials. However, negotiations are currently

underway with bodies such as the FDA and EMA with a view to modifying the latter stages of the development pipeline for exon skipping oligonucleotides in order to streamline and facilitate treatment of rarer mutations. While such negotiations are cause for optimism, they also place a considerable burden of responsibility on those conducting these trials, since both industry and regulators will be watching to see the outcome of any modified trial process for DMD patients. It is likely that these results will inform their decisions on future oligonucleotide therapies.

Despite the promise of personalised medicine, we deceive ourselves if we claim that oligonucleotide drugs will solve all medical problems. The more that is understood about disease, the more apparent it becomes that every disease is a complex and multifaceted disorder. This holds true even for monogenic disorders, the majority of which have so far confounded our best efforts in terms of developing a cure. Given that we are only now just starting to fathom the possibility of curative treatments for a small number of these monogenic disorders, how much more daunting will it be to seek to understand and to cure the many complex polygenic disorders affecting modern medicine and society? Only time can tell us the answer to this. However, so long as there remains the will and effort to do it, there is reason enough for optimism in this endeavour. What is certain is that, notwithstanding our current limitations in knowledge and technology, we are better placed and better armed than ever before to tackle the problem of genetic disease in all its forms.

One area that may prove particularly suited to the versatility and specificity of oligonucleotide drugs is cancer therapy. Cancer is of course a somatic form of genetic disease and a tumour is a continually evolving system which has the potential to respond

to and thus evade the selective pressures (i.e. chemotherapies) applied to it. The increasing ability to sequence and genotype tumours will provide a wealth of genomic data that will likely yield abundant molecular targets for oligonucleotide therapies. Unlike conventional drugs, oligonucleotides are uniquely suited to dealing with the challenge of tumour evolution since their design and choice of sequence-specific target can effectively 'evolve' alongside an individual cancer.

What future then for oligonucleotide therapeutics? For the moment it seems likely that the scope of oligonucleotide applications will continue to expand. The relative ease with which such compounds can be generated and tested, both *in vitro* and preclinically *in vivo*, is likely to ensure a continued pipeline of drug development for the foreseeable future. In addition, pharmaceutical companies might be expected to favour the oligonucleotide model because of its general reliance on repeated dosing, which necessitates long-term treatment and thus requires continued production and supply of therapeutic compound. In the longer term, oligonucleotide therapies may in some cases be superseded by other forms of gene therapy which yield effective gene replacement or repair and thus offer the prospect of single-treatment cures. However, this is unlikely to be possible in all cases and so there will always likely be a role for oligonucleotides within the physician's therapeutic armoury.

6.6. Final thoughts

A quote from Sir William Gowers, the pre-eminent neurologist of the nineteenth century, seems an apt note on which to finish. In his lecture about 'pseudo-hypertrophic muscular

paralysis' (later known as DMD), delivered in 1879 at Queen Square, London, he states the following:

"The disease is one of the most interesting, and at the same time most sad, of all those with which we have to deal: interesting on account of its peculiar features and mysterious nature; sad on account of our powerlessness to influence its course, except in a very slight degree…

" These facts do not render its study a matter of the less importance. Because we can do little by our treatment, it is not the less necessary to be able to recognise the disease when it occurs, and to know the little, and to know how little, we can do. Moreover, regarding every disease now incurable we may entertain the hope – faint it may be with respect to some, stronger in the case of others – that our powerlessness may not be permanent, and that we, or those who come after us, may be able to speak of it in very different terms."

- Sir William R. Gowers, 1879

Over 135 years later, Gowers' words still speak vividly to us of this disease. Our hope remains the same as his, that our powerlessness may not be permanent. From where we stand today, it appears that we may be on the brink of turning that hope into reality, and of being able to speak of Duchenne muscular dystrophy, and perhaps other neuromuscular disorders, in very different terms.

7. References

Aartsma-Rus, A, Fokkema, I, Verschuuren, J, Ginjaar, I, van Deutekom, J, van Ommen, G-J, den Dunnen, JT. 2009. Theoretic applicability of antisense-mediated exon skipping for Duchenne muscular dystrophy mutations. Hum. Mutat. 30: 293–299.

Abbott, NJ, Patabendige, A a K, Dolman, DEM, Yusof, SR, Begley, DJ. 2010. Structure and function of the blood-brain barrier. Neurobiol. Dis. 37: 13–25.

Alhonen-Hongisto, L, Jänne, J. 1980. Polyamine depletion induces enhanced synthesis and accumulation of cadaverine in cultured Ehrlich ascites carcinoma cells. Biochem. Biophys. Res. Commun. 93: 1005–1013.

Allen, DG, Whitehead, NP. 2011. Duchenne muscular dystrophy--what causes the increased membrane permeability in skeletal muscle? Int. J. Biochem. Cell Biol. 43: 290–294.

Almeida, S, Gascon, E, Tran, H, Chou, HJ, Gendron, TF, Degroot, S, Tapper, AR, Sellier, C, Charlet-Berguerand, N, Karydas, A, Seeley, WW, Boxer, AL, Petrucelli, L, Miller, BL, Gao, F-B. 2013. Modeling key pathological features of frontotemporal dementia with C9ORF72 repeat expansion in iPSC-derived human neurons. Acta Neuropathol. 126: 385–399.

Al-Sarraj, S, King, A, Troakes, C, Smith, B, Maekawa, S, Bodi, I, Rogelj, B, Al-Chalabi, A, Hortobágyi, T, Shaw, CE. 2011. p62 positive, TDP-43 negative, neuronal cytoplasmic and intranuclear inclusions in the cerebellum and hippocampus define the pathology of C9orf72-linked FTLD and MND/ALS. Acta Neuropathol. 122: 691–702.

Alvarez, JI, Dodelet-devillers, A, Kebir, H, Ifergan, I, Fabre, PJ, Terouz, S, Sabbagh, M, Wosik, K, Bourbonnière, L, Bernard, M, Horssen, J Van, Vries, HE De, Charron, F, Prat, A. 2011. The Hedgehog pathway promotes blood-brain barrier integrity and CNS immune quiescence. Science 334: 1727–1731.

Alvarez-Erviti, L, Seow, Y, Yin, H, Betts, C, Lakhal, S, Wood, MJA. 2011. Delivery of siRNA to the mouse brain by systemic injection of targeted exosomes. Nat. Biotechnol. 29: 341–345.

Amantana, A, Iversen, PL. 2005. Pharmacokinetics and biodistribution of phosphorodiamidate morpholino antisense oligomers. Curr. Opin. Pharmacol. 5: 550–555.

Amantana, A, Moulton, HM, Cate, ML, Reddy, MT, Whitehead, T, Hassinger, JN, Youngblood, DS, Iversen, PL. 2007. Pharmacokinetics, biodistribution, stability and toxicity of a cell-penetrating peptide-morpholino oligomer conjugate. Bioconjug. Chem. 18: 1325–1331.

Amato, AA, Russell, JA eds. 2008. Neuromuscular Disorders. New York; London: McGraw-Hill Medical.

Anderson, JL, Head, SI, Morley, JW. 2004. Long-term depression is reduced in cerebellar Purkinje cells of dystrophin-deficient mdx mice. Brain Res. 1019: 289–292.

Anderson, JL, Head, SI, Rae, C, Morley, JW. 2002. Brain function in Duchenne muscular dystrophy. Brain 125: 4–13.

Anderson, JL, Morley, JW, Head, SI. 2010. Enhanced homosynaptic LTD in cerebellar Purkinje cells of the dystrophic MDX mouse. Muscle Nerve 41: 329–334.

Andersson, A-C, Henningsson, S, Rosengren, E. 1978. Increased formation of diamines and polyamines in the pregnant rat. J. Physiol. 285: 311–324.

Angelini, C. 2007. The role of corticosteroids in muscular dystrophy: a critical appraisal. Muscle Nerve 36: 424–435.

Aoki, Y, Nagata, T, Yokota, T, Nakamura, A, Wood, MJ a, Partridge, T, Takeda, S. 2013. Highly efficient in vivo delivery of PMO into regenerating myotubes and rescue in laminin-α2 chain-null congenital muscular dystrophy mice. Hum. Mol. Genet. 22: 4914–4928.

Aoki, Y, Yokota, T, Nagata, T, Nakamura, A, Tanihata, J, Saito, T, Duguez, SMR, Nagaraju, K, Hoffman, EP, Partridge, T, Takeda, S. 2012. Bodywide skipping of exons 45-55 in dystrophic mdx52 mice by systemic antisense delivery. Proc. Natl. Acad. Sci. 109: 13763–13768.

Argaw, AT, Asp, L, Zhang, J, Navrazhina, K, Pham, T, Mariani, JN, Mahase, S, Dutta, DJ, Seto, J, Kramer, EG, Ferrara, N, Sofroniew, M V, John, GR. 2012. Astrocyte-derived VEGF-A drives blood-brain barrier disruption in CNS inflammatory disease. J. Clin. Invest. 122: 2454–2468.

Armulik, A, Genové, G, Betsholtz, C. 2011. Pericytes: developmental, physiological, and pathological perspectives, problems, and promises. Dev. Cell 21: 193–215.

Armulik, A, Genové, G, Mäe, M, Nisancioglu, MH, Wallgard, E, Niaudet, C, He, L, Norlin, J, Lindblom, P, Strittmatter, K, Johansson, BR, Betsholtz, C. 2010. Pericytes regulate the blood-brain barrier. Nature 468: 557–561.

Ash, PE a, Bieniek, KF, Gendron, TF, Caulfield, T, Lin, W-L, Dejesus-Hernandez, M, van Blitterswijk, MM, Jansen-West, K, Paul, JW, Rademakers, R, Boylan, KB, Dickson, DW, Petrucelli, L. 2013. Unconventional translation of C9ORF72 GGGGCC expansion generates insoluble polypeptides specific to c9FTD/ALS. Neuron 77: 639–646.

Bachrach, E, Li, S, Perez, AL, Schienda, J, Liadaki, K, Volinski, J, Flint, A, Chamberlain, J, Kunkel, LM. 2004. Systemic delivery of human microdystrophin to regenerating

mouse dystrophic muscle by muscle progenitor cells. Proc. Natl. Acad. Sci. U. S. A. 101: 3581–3586.

Bakker, E, Veenema, H, den Dunnen, JT, van Broeckhoven, C, Grootscholten, PM, Bonten, EJ, van Ommen, GJ, Pearson, PL. 1989. Germinal mosaicism increases the recurrence risk for “new” Duchenne muscular dystrophy mutations. J. Med. Genet. 26: 553–559.

Ballabh, P, Braun, A, Nedergaard, M. 2004. The blood-brain barrier: an overview: structure, regulation, and clinical implications. Neurobiol. Dis. 16: 1–13.

Bang, M-L, Centner, T, Fornoff, F, Geach, a. J, Gotthardt, M, McNabb, M, Witt, CC, Labeit, D, Gregorio, CC, Granzier, H, Labeit, S. 2001. The Complete Gene Sequence of Titin, Expression of an Unusual 700-kDa Titin Isoform, and Its Interaction With Obscurin Identify a Novel Z-Line to I-Band Linking System. Circ. Res. 89: 1065–1072.

Bar, S, Barnea, E, Levy, Z, Neuman, S, Yaffe, D, Nudel, U. 1990. A novel product of the Duchenne muscular dystrophy gene which greatly differs from the known isoforms in its structure and tissue distribution. Biochem. J. 272: 557–560.

Barnhart, MI, Lusher, JM. 1979. Structural physiology of the human spleen. Am. J. Pediatr. Hematol. Oncol. 1: 311–330.

Barton-Davis, ER, Cordier, L, Shoturma, DI, Leland, SE, Sweeney, HL. 1999. Aminoglycoside antibiotics restore dystrophin function to skeletal muscles of mdx mice. J. Clin. Invest. 104: 375–381.

Basso, M, Massignan, T, Samengo, G, Cheroni, C, De Biasi, S, Salmona, M, Bendotti, C, Bonetto, V. 2006. Insoluble mutant SOD1 is partly oligoubiquitinated in amyotrophic lateral sclerosis mice. J. Biol. Chem. 281: 33325–33335.

Beck, J, Poulter, M, Hensman, D, Rohrer, JD, Mahoney, CJ, Adamson, G, Campbell, T, Uphill, J, Borg, A, Fratta, P, Orrell, RW, Malaspina, A, Rowe, J, Brown, J, Hodges, J, Sidle, K, Polke, JM, Houlden, H, Schott, JM, Fox, NC, Rossor, MN, Tabrizi, SJ, Isaacs, AM, Hardy, J, Warren, JD, Collinge, J, Mead, S. 2013. Large C9orf72 hexanucleotide repeat expansions are seen in multiple neurodegenerative syndromes and are more frequent than expected in the UK population. Am. J. Hum. Genet. 92: 345–353.

Belzil, V V, Bauer, PO, Prudencio, M, Gendron, TF, Stetler, CT, Yan, IK, Pregent, L, Daughrity, L, Baker, MC, Rademakers, R, Boylan, K, Patel, TC, Dickson, DW, Petrucelli, L. 2013. Reduced C9orf72 gene expression in c9FTD/ALS is caused by histone trimethylation, an epigenetic event detectable in blood. Acta Neuropathol. 126: 895–905.

Benarroch, EE. 2011. Circumventricular organs: receptive and homeostatic functions and clinical implications. Neurology 77: 1198–1204.

Benchaouir, R, Meregalli, M, Farini, A, D'Antona, G, Belicchi, M, Goyenvalle, A, Battistelli, M, Bresolin, N, Bottinelli, R, Garcia, L, Torrente, Y. 2007. Restoration of human dystrophin following transplantation of exon-skipping-engineered DMD patient stem cells into dystrophic mice. Cell Stem Cell 1: 646–657.

Bennett, CF, Swayze, EE. 2010. RNA targeting therapeutics: molecular mechanisms of antisense oligonucleotides as a therapeutic platform. Annu. Rev. Pharmacol. Toxicol. 50: 259–293.

Benussi, L, Rossi, G, Glionna, M, Tonoli, E, Piccoli, E, Fostinelli, S, Paterlini, A, Flocco, R, Albani, D, Pantieri, R, Cereda, C, Forloni, G, Tagliavini, F, Binetti, G, Ghidoni, R. 2014. C9ORF72 hexanucleotide repeat number in frontotemporal lobar degeneration: a genotype-phenotype correlation study. J. Alzheimers. Dis. 38: 799–808.

Ben-Zvi, A, Lacoste, B, Kur, E, Andreone, BJ, Mayshar, Y, Yan, H, Gu, C. 2014. Mfsd2a is critical for the formation and function of the blood-brain barrier. Nature 509: 507–511.

Béroud, C, Tuffery-Giraud, S, Matsuo, M, Hamroun, D, Humbertclaude, V, Monnier, N, Moizard, M-P, Voelckel, M-A, Calemard, LM, Boisseau, P, Blayau, M, Philippe, C, Cossée, M, Pagès, M, Rivier, F, Danos, O, Garcia, L, Claustres, M. 2007. Multiexon skipping leading to an artificial DMD protein lacking amino acids from exons 45 through 55 could rescue up to 63% of patients with Duchenne muscular dystrophy. Hum. Mutat. 28: 196–202.

Betts, C, Saleh, AF, Arzumanov, AA, Hammond, SM, Godfrey, C, Coursindel, T, Gait, MJ, Wood, MJA. 2012. Pip6-PMO, A New Generation of Peptide-oligonucleotide Conjugates With Improved Cardiac Exon Skipping Activity for DMD Treatment. Mol. Ther. — Nucleic Acids 1: e38.

Bladen, CL, Salgado, D, Monges, S, Foncuberta, ME, Kekou, K, Kosma, K, Dawkins, H, Lamont, L, Roy, AJ, Chamova, T, Guergueltcheva, V, Chan, S, Korngut, L, Campbell, C, Dai, Y, Wang, J, Barišić, N, Brabec, P, Lahdetie, J, Walter, MC, Schreiber-Katz, O, Karcagi, V, Garami, M, Viswanathan, V, Bayat, F, Buccella, F, Kimura, E, Koeks, Z, van den Bergen, JC, Rodrigues, M, Roxburgh, R, Lusakowska, A, Kostera-Pruszczyk, A, Zimowski, J, Santos, R, Neagu, E, Artemieva, S, Rasic, VM, Vojinovic, D, Posada, M, Bloetzer, C, Jeannet, P-Y, Joncourt, F, Díaz-Manera, J, Gallardo, E, Karaduman, a. A, Topaloğlu, H, El Sherif, R, Stringer, A, Shatillo, A V., Martin, AS, Peay, HL, Bellgard, MI, Kirschner, J, Flanigan, KM, Straub, V, Bushby, K, Verschuuren, J, Aartsma-Rus, A, Beroud, C, Lochmüller, H. 2015. The TREAT-NMD DMD Global Database: Analysis of More than 7,000 Duchenne Muscular Dystrophy Mutations. Hum. Mutat. 36: 395–402.

Blake, DJ, Hawkes, R, Benson, MA, Beesley, PW. 1999. Different Dystrophin-like Complexes Are Expressed in Neurons and Glia. J. Cell Biol. 147: 645–657.

Van Blitterswijk, M, DeJesus-Hernandez, M, Niemantsverdriet, E, Murray, ME, Heckman, MG, Diehl, NN, Brown, PH, Baker, MC, Finch, N a, Bauer, PO, Serrano, G, Beach, TG, Josephs, K a, Knopman, DS, Petersen, RC, Boeve, BF, Graff-Radford, NR, Boylan, KB, Petrucelli, L, Dickson, DW, Rademakers, R. 2013. Association between repeat sizes and clinical and pathological characteristics in carriers of C9ORF72 repeat expansions (Xpansize-72): a cross-sectional cohort study. Lancet Neurol. 12: 978–988.

Van Blitterswijk, M, Mullen, B, Nicholson, AM, Bieniek, KF, Heckman, MG, Baker, MC, DeJesus-Hernandez, M, Finch, N a, Brown, PH, Murray, ME, Hsiung, G-YR, Stewart, H, Karydas, AM, Finger, E, Kertesz, A, Bigio, EH, Weintraub, S, Mesulam, M, Hatanpaa, KJ, White, CL, Strong, MJ, Beach, TG, Wszolek, ZK, Lippa, C, Caselli, R, Petrucelli, L, Josephs, K a, Parisi, JE, Knopman, DS, Petersen, RC, Mackenzie, IR, Seeley, WW, Grinberg, LT, Miller, BL, Boylan, KB, Graff-Radford, NR, Boeve, BF, Dickson, DW, Rademakers, R. 2014. TMEM106B protects C9ORF72 expansion carriers against frontotemporal dementia. Acta Neuropathol. 127: 397–406.

Boyce, FM, Beggs, AH, Feener, C, Kunkel, LM. 1991. Dystrophin is transcribed in brain from a distant upstream promoter. Proc. Natl. Acad. Sci. U. S. A. 88: 1276–1280.

Braasch, DA, Corey, DR. 2001. Locked nucleic acid (LNA): fine-tuning the recognition of DNA and RNA. Chem. Biol. 8: 1–7.

Brady, ST, Tai, L. 2012. Cell biology of the nervous system. In: Brady, ST, Siegel, GJ, Albers, RW, Price, DL, editors. Basic neurochemistry: principles of molecular, cellular, and medical neurobiology, 8the. Oxford: Elsevier Academic Press, p 3–25.

Brenman, JE, Chao, DS, Xia, H, Aldape, K, Bredt, DS. 1995. Nitric oxide synthase complexed with dystrophin and absent from skeletal muscle sarcolemma in Duchenne muscular dystrophy. Cell 82: 743–752.

Bulfield, G, Siller, WG, Wight, P a, Moore, KJ. 1984. X chromosome-linked muscular dystrophy (mdx) in the mouse. Proc. Natl. Acad. Sci. U. S. A. 81: 1189–1192.

Burghes, A, Logan, C, Hu, X, Belfall, B, Worton, R, Ray, P. 1987. A cDNA clone from the Duchenne/Becker muscular dystrophy gene. Nature 328: 434–437.

Bushby, K, Finkel, R, Birnkrant, DJ, Case, LE, Clemens, PR, Cripe, L, Kaul, A, Kinnett, K, McDonald, C, Pandya, S, Poysky, J, Shapiro, F, Tomezsko, J, Constantin, C. 2010a. Diagnosis and management of Duchenne muscular dystrophy, part 1: diagnosis, and pharmacological and psychosocial management. Lancet Neurol. 9: 77–93.

Bushby, K, Finkel, R, Birnkrant, DJ, Case, LE, Clemens, PR, Cripe, L, Kaul, A, Kinnett, K, McDonald, C, Pandya, S, Poysky, J, Shapiro, F, Tomezsko, J, Constantin, C. 2010b. Diagnosis and management of Duchenne muscular dystrophy, part 2: implementation of multidisciplinary care. Lancet Neurol. 9: 177–189.

Bushby, K, Gardner-Medwin, D. 1993. The clinical, genetic and dystrophin characteristics of Becker muscular dystrophy. J. Neurol. 240: 98–104.

Bushby, KM. 1992. Genetic and clinical correlations of Xp21 muscular dystrophy. J. Inherit. Metab. Dis. 15: 551–564.

Buvoli, M, Buvoli, A, Leinwand, L a. 2007. Interplay between exonic splicing enhancers, mRNA processing, and mRNA surveillance in the dystrophic Mdx mouse. PLoS One 2: e427.

Byers, TJ, Lidov, HGW, Kunkel, LM. 1993. An alternative dystrophin transcript specific to peripheral nerve. Nat. Genet. 4: 77–81.

Carro, E, Spuch, C, Trejo, JL, Antequera, D, Torres-Aleman, I. 2005. Choroid plexus megalin is involved in neuroprotection by serum insulin-like growth factor I. J. Neurosci. 25: 10884–10893.

Castaldo, I, Pinelli, M, Monticelli, a, Acquaviva, F, Giacchetti, M, Filla, a, Sacchetti, S, Keller, S, Avvedimento, VE, Chiariotti, L, Cocozza, S. 2008. DNA methylation in intron 1 of the frataxin gene is related to GAA repeat length and age of onset in Friedreich ataxia patients. J. Med. Genet. 45: 808–812.

Cerletti, M, Jurga, S, Witczak, CA, Hirshman, MF, Jennifer, L, Goodyear, LJ, Wagers, AJ. 2008. Highly efficient, functional engraftment of skeletal muscle stem cells in dystrophic muscles. Cell 134: 37–47.

Chamova, T, Guergueltcheva, V, Raycheva, M, Todorov, T, Genova, J, Bichev, S, Bojinova, V, Mitev, V, Tournev, I, Todorova, a. 2013. Association between loss of dp140 and cognitive impairment in duchenne and becker dystrophies. Balkan J. Med. Genet. 16: 21–30.

Chen, Y, Liu, L. 2012. Modern methods for delivery of drugs across the blood-brain barrier. Adv. Drug Deliv. Rev. 64: 640–665.

Chiò, A, Borghero, G, Restagno, G, Mora, G, Drepper, C, Traynor, BJ, Sendtner, M, Brunetti, M, Ossola, I, Calvo, A, Pugliatti, M, Sotgiu, MA, Murru, MR, Marrosu, MG, Marrosu, F, Marinou, K, Mandrioli, J, Sola, P, Caponnetto, C, Mancardi, G, Mandich, P, La Bella, V, Spataro, R, Conte, A, Monsurrò, MR, Tedeschi, G, Pisano, F, Bartolomei, I, Salvi, F, Lauria Pinter, G, Simone, I, Logroscino, G, Gambardella, A, Quattrone, A, Lunetta, C, Volanti, P, Zollino, M, Penco, S, Battistini, S, Renton, AE, Majounie, E, Abramzon, Y, Conforti, FL, Giannini, F, Corbo, M, Sabatelli, M. 2012. Clinical characteristics of patients with familial amyotrophic lateral sclerosis carrying the pathogenic GGGGCC hexanucleotide repeat expansion of C9ORF72. Brain 135: 784–793.

Chiò, A, Calvo, A, Moglia, C, Mazzini, L, Mora, G. 2011. Phenotypic heterogeneity of amyotrophic lateral sclerosis: a population based study. J. Neurol. Neurosurg. Psychiatry 82: 740–746.

Ciura, S, Lattante, S, Le Ber, I, Latouche, M, Tostivint, H, Brice, A, Kabashi, E. 2013. Loss of function of C9orf72 causes motor deficits in a zebrafish model of amyotrophic lateral sclerosis. Ann. Neurol. 74: 180–187.

Coomber, BL, Stewart, PA. 1985. Morphometric Analysis of CNS Microvascular Endothelium. Microvasc. Res. 30: 99–115.

Cotton, S, Voudouris, N, Greenwood, K. 2005. Association between intellectual functioning and age in children and young adults with Duchenne muscular dystrophy: further results from a meta-analysis. Dev. Med. Child Neurol. 47: 257–265.

Cotton, S, Voudouris, NJ, Greenwood, KM. 2001. Intelligence and Duchenne muscular dystrophy: Full-Scale, Verbal, and Performance intelligence quotients. Dev. Med. Child Neurol. 43: 497–501.

D'Angelo, MG, Lorusso, ML, Civati, F, Comi, G Pietro, Magri, F, Del Bo, R, Guglieri, M, Molteni, M, Turconi, AC, Bresolin, N. 2011. Neurocognitive profiles in Duchenne muscular dystrophy and gene mutation site. Pediatr. Neurol. 45: 292–299.

D'Souza, VN, Nguyen, TM, Morris, GE, Karges, W, Pillers, D a, Ray, PN. 1995. A novel dystrophin isoform is required for normal retinal electrophysiology. Hum. Mol. Genet. 4: 837–842.

Daneman, R, Prat, A. 2015. The Blood-Brain Barrier. Cold Spring Harb. Perspect. Biol. 7: 1–24.

Daneman, R, Zhou, L, Kebede, A a, Barres, B a. 2010. Pericytes are required for blood-brain barrier integrity during embryogenesis. Nature 468: 562–566.

Daoud, F, Angeard, N, Demerre, B, Martie, I, Benyaou, R, Leturcq, F, Cossée, M, Deburgrave, N, Saillour, Y, Tuffery, S, Urtizberea, A, Toutain, A, Echenne, B, Frischman, M, Mayer, M, Desguerre, I, Estournet, B, Réveillère, C, Penisson-Besnier, Cuisset, JM, Kaplan, JC, Héron, D, Rivier, F, Chelly, J. 2009. Analysis of Dp71 contribution in the severity of mental retardation through comparison of Duchenne and Becker patients differing by mutation consequences on Dp71 expression. Hum. Mol. Genet. 18: 3779–3794.

Davies, KE, Nowak, KJ. 2006. Molecular mechanisms of muscular dystrophies: old and new players. Nat. Rev. Mol. Cell Biol. 7: 762–773.

Davies, KE, Pearson, PL, Harper, PS, Murray, JM, O'Brien, T, Sarfarazi, M, Williamson, R. 1983. Linkage analysis of two cloned DNA sequences flanking the Duchenne

muscular dystrophy locus on the short arm of the human X chromosome. Nucleic Acids Res. 11: 2303–2312.

Deconinck, N, Dan, B. 2007. Pathophysiology of duchenne muscular dystrophy: current hypotheses. Pediatr. Neurol. 36: 1–7.

DeJesus-Hernandez, M, Mackenzie, IR, Boeve, BF, Boxer, AL, Baker, M, Rutherford, NJ, Nicholson, AM, Finch, N a, Flynn, H, Adamson, J, Kouri, N, Wojtas, A, Sengdy, P, Hsiung, G-YR, Karydas, A, Seeley, WW, Josephs, K a, Coppola, G, Geschwind, DH, Wszolek, ZK, Feldman, H, Knopman, DS, Petersen, RC, Miller, BL, Dickson, DW, Boylan, KB, Graff-Radford, NR, Rademakers, R. 2011. Expanded GGGGCC hexanucleotide repeat in noncoding region of C9ORF72 causes chromosome 9p-linked FTD and ALS. Neuron 72: 245–256.

Deleavey, GF, Damha, MJ. 2012. Designing chemically modified oligonucleotides for targeted gene silencing. Chem. Biol. 19: 937–954.

Demeule, M, Currie, J-C, Bertrand, Y, Ché, C, Nguyen, T, Régina, A, Gabathuler, R, Castaigne, J-P, Béliveau, R. 2008a. Involvement of the low-density lipoprotein receptor-related protein in the transcytosis of the brain delivery vector angiopep-2. J. Neurochem. 106: 1534–1544.

Demeule, M, Régina, A, Ché, C, Poirier, J, Nguyen, T, Gabathuler, R, Castaigne, J-P, Béliveau, R. 2008b. Identification and design of peptides as a new drug delivery system for the brain. J. Pharmacol. Exp. Ther. 324: 1064–1072.

Desguerre, I, Christov, C, Mayer, M, Zeller, R, Becane, H-M, Bastuji-Garin, S, Leturcq, F, Chiron, C, Chelly, J, Gherardi, RK. 2009. Clinical heterogeneity of duchenne muscular dystrophy (DMD): definition of sub-phenotypes and predictive criteria by long-term follow-up. PLoS One 4: e4347.

Dezawa, M, Ishikawa, H, Itokazu, Y, Yoshihara, T, Hoshino, M, Takeda, S, Ide, C, Nabeshima, Y. 2005. Bone marrow stromal cells generate muscle cells and repair muscle degeneration. Science (80-.). 309: 314–318.

Dias, N, Stein, CA. 2002. Antisense Oligonucleotides : Basic Concepts and Mechanisms. Mol. Cancer Ther. 1: 347–355.

Dietrich, MO, Spuch, C, Antequera, D, Rodal, I, de Yébenes, JG, Molina, JA, Bermejo, F, Carro, E. 2008. Megalin mediates the transport of leptin across the blood-CSF barrier. Neurobiol. Aging 29: 902–912.

Dols-Icardo, O, García-Redondo, A, Rojas-García, R, Sánchez-Valle, R, Noguera, A, Gómez-Tortosa, E, Pastor, P, Hernández, I, Esteban-Pérez, J, Suárez-Calvet, M, Antón-Aguirre, S, Amer, G, Ortega-Cubero, S, Blesa, R, Fortea, J, Alcolea, D, Capdevila, A, Antonell, A, Lladó, A, Muñoz-Blanco, JL, Mora, JS, Galán-Dávila, L, Rodríguez De Rivera, FJ, Lleó, A, Clarimón, J. 2014. Characterization of the repeat expansion size in

C9orf72 in amyotrophic lateral sclerosis and frontotemporal dementia. Hum. Mol. Genet. 23: 749–754.

Donnelly, CJ, Zhang, P-W, Pham, JT, Heusler, AR, Mistry, N a, Vidensky, S, Daley, EL, Poth, EM, Hoover, B, Fines, DM, Maragakis, N, Tienari, PJ, Petrucelli, L, Traynor, BJ, Wang, J, Rigo, F, Bennett, CF, Blackshaw, S, Sattler, R, Rothstein, JD. 2013. RNA Toxicity from the ALS/FTD C9ORF72 Expansion Is Mitigated by Antisense Intervention. Neuron 80: 415–428.

Doorenweerd, N, Straathof, CS, Dumas, EM, Spitali, P, Ginjaar, IB, Wokke, BH, Schrans, DG, van den Bergen, JC, van Zwet, EW, Webb, A, van Buchem, M a., Verschuuren, JJ, Hendriksen, JG, Niks, EH, Kan, HE. 2014. Reduced cerebral gray matter and altered white matter in boys with Duchenne muscular dystrophy. Ann. Neurol. 76: 403–411.

Douglas, AGL, Wood, MJ a. 2013. Splicing therapy for neuromuscular disease. Mol. Cell. Neurosci. 56: 169–185.

Dubowitz, V, Crome, L. 1969. The central nervous system in Duchenne muscular dystrophy. Brain 92: 805–808.

Duchenne, G. 1868. Recherches sur la paralysie musculaire pseudo-hypertrophique, ou paralysie myo-sclérosique. Arch. Génerales Médicine 6: 5–25, 179–209, 305–321, 421–443, 552–588.

Den Dunnen, JT, Grootscholten, PM, Bakker, E, Blonden, L a, Ginjaar, HB, Wapenaar, MC, van Paassen, HM, van Broeckhoven, C, Pearson, PL, van Ommen, GJ. 1989. Topography of the Duchenne muscular dystrophy (DMD) gene: FIGE and cDNA analysis of 194 cases reveals 115 deletions and 13 duplications. Am. J. Hum. Genet. 45: 835–847.

Dupont, E, Prochiantz, A, Joliot, A. 2011. Penetratin story: an overview. Methods Mol. Biol. 683: 21–29.

Eagle, M, Baudouin, S V, Chandler, C, Giddings, DR, Bullock, R, Bushby, K. 2002. Survival in Duchenne muscular dystrophy: improvements in life expectancy since 1967 and the impact of home nocturnal ventilation. Neuromuscul. Disord. 12: 926–929.

Eckstein, F. 2002. Developments in RNA chemistry, a personal view. Biochimie 84: 841–848.

Edwards, JH. 1986. The population genetics of Duchenne: natural and artificial selection in Duchenne muscular dystrophy. J. Med. Genet. 23: 521–530.

Emery, AEH. 2002. The muscular dystrophies. Lancet 359: 687–695.

Emery, AEH, Muntoni, F, Quinlivan, R. 2015. Duchenne muscular dystrophy, 4th edition. Oxford: Oxford University Press.

Ervasti, JM. 2007. Dystrophin, its interactions with other proteins, and implications for muscular dystrophy. Biochim. Biophys. Acta 1772: 108–117.

Van Essen, AJ, Abbs, S, Bakker, E, Boileau, C, Ciaustres, M, Ferrari, M, Ferlini, A, Galluzzi, G, Grimm, T, Grubben, C, Jeanpierre, M, Kiiiiri, H, Liechti-gailati, S, Melis, MA, Ommen, GB Van, Poncin, JE, Scheffer, H, Schwartz, M, Speer, A, Stuhrmann, M, Verellen-dumoulin, C, Wilcox, DE, Kate, LP. 1992. Parental origin and germline mosaicism of deletions and duplications of the dystrophin gene : a European study. Hum. Genet. 59: 249–257.

Evans-Galea, M V, Carrodus, N, Rowley, SM, Corben, L a, Tai, G, Saffery, R, Galati, JC, Wong, NC, Craig, JM, Lynch, DR, Regner, SR, Brocht, AFD, Perlman, SL, Bushara, KO, Gomez, CM, Wilmot, GR, Li, L, Varley, E, Delatycki, MB, Sarsero, JP. 2012. FXN methylation predicts expression and clinical outcome in Friedreich ataxia. Ann. Neurol. 71: 487–497.

Ezzat, K, Helmfors, H, Tudoran, O, Juks, C, Lindberg, S, Padari, K, El-Andaloussi, S, Pooga, M, Langel, U. 2012. Scavenger receptor-mediated uptake of cell-penetrating peptide nanocomplexes with oligonucleotides. FASEB J. 26: 1172–1180.

Fanning, a. S, Jameson, BJ, Jesaitis, L a., Anderson, JM. 1998. The Tight Junction Protein ZO-1 Establishes a Link between the Transmembrane Protein Occludin and the Actin Cytoskeleton. J. Biol. Chem. 273: 29745–29753.

Farg, M a, Sundaramoorthy, V, Sultana, JM, Yang, S, Atkinson, R a K, Levina, V, Halloran, M a, Gleeson, P a, Blair, IP, Soo, KY, King, AE, Atkin, JD. 2014. C9ORF72, implicated in amytrophic lateral sclerosis and frontotemporal dementia, regulates endosomal trafficking. Hum. Mol. Genet. 23: 3579–3595.

Fernandes, SA, Douglas, AGL, Varela, MA, Wood, MJA, Aoki, Y. 2013. Oligonucleotide-Based Therapy for FTD/ALS Caused by the C9orf72 Repeat Expansion: A Perspective. J. Nucleic Acids 2013: 1–11.

Flanigan, KM, Voit, T, Rosales, XQ, Servais, L, Kraus, JE, Wardell, C, Morgan, A, Dorricott, S, Nakielny, J, Quarcoo, N, Liefaard, L, Drury, T, Campion, G, Wright, P. 2014. Pharmacokinetics and safety of single doses of drisapersen in non-ambulant subjects with Duchenne muscular dystrophy: results of a double-blind randomized clinical trial. Neuromuscul. Disord. 24: 16–24.

Foster, H, Sharp, PS, Athanasopoulos, T, Trollet, C, Graham, IR, Foster, K, Wells, DJ, Dickson, G. 2008. Codon and mRNA sequence optimization of microdystrophin transgenes improves expression and physiological outcome in dystrophic mdx mice following AAV2/8 gene transfer. Mol. Ther. 16: 1825–1832.

Fratta, P, Mizielinska, S, Nicoll, AJ, Zloh, M, Fisher, EMC, Parkinson, G, Isaacs, AM. 2012. C9orf72 hexanucleotide repeat associated with amyotrophic lateral sclerosis and frontotemporal dementia forms RNA G-quadruplexes. Sci. Rep. 2: 1016.

Fratta, P, Poulter, M, Lashley, T, Rohrer, JD, Polke, JM, Beck, J, Ryan, N, Hensman, D, Mizielinska, S, Waite, AJ, Lai, M-C, Gendron, TF, Petrucelli, L, Fisher, EMC, Revesz, T, Warren, JD, Collinge, J, Isaacs, AM, Mead, S. 2013. Homozygosity for the C9orf72 GGGGCC repeat expansion in frontotemporal dementia. Acta Neuropathol. 126: 401–409.

Furuse, M. 2010. Molecular basis of the core structure of tight junctions. Cold Spring Harb. Perspect. Biol. 2: a002907.

Gendron, TF, Bieniek, KF, Zhang, Y-J, Jansen-West, K, Ash, PE a, Caulfield, T, Daughrity, L, Dunmore, JH, Castanedes-Casey, M, Chew, J, Cosio, DM, van Blitterswijk, M, Lee, WC, Rademakers, R, Boylan, KB, Dickson, DW, Petrucelli, L. 2013. Antisense transcripts of the expanded C9ORF72 hexanucleotide repeat form nuclear RNA foci and undergo repeat-associated non-ATG translation in c9FTD/ALS. Acta Neuropathol. 126: 829–844.

Gerhardt, H, Wolburg, H, Redies, C. 2000. N-Cadherin Mediates Pericytic-Endothelial Interaction During Brain Angiogenesis in the Chicken. Dev. Dyn. an Off. Publ. Am. Assoc. Anat. 218: 472–479.

Gijselinck, I, Van Langenhove, T, van der Zee, J, Sleegers, K, Philtjens, S, Kleinberger, G, Janssens, J, Bettens, K, Van Cauwenberghe, C, Pereson, S, Engelborghs, S, Sieben, A, De Jonghe, P, Vandenberghe, R, Santens, P, De Bleecker, J, Maes, G, Bäumer, V, Dillen, L, Joris, G, Cuijt, I, Corsmit, E, Elinck, E, Van Dongen, J, Vermeulen, S, Van den Broeck, M, Vaerenberg, C, Mattheijssens, M, Peeters, K, Robberecht, W, Cras, P, Martin, J-J, De Deyn, PP, Cruts, M, Van Broeckhoven, C. 2012. A C9orf72 promoter repeat expansion in a Flanders-Belgian cohort with disorders of the frontotemporal lobar degeneration-amyotrophic lateral sclerosis spectrum: a gene identification study. Lancet Neurol. 11: 54–65.

Goldspink, G. 1999. Changes in muscle mass and phenotype and the expression of autocrine and systemic growth factors by muscle in response to stretch and overload. J. Anat. 194: 323–334.

Gowers, WR. 1879. Clinical lecture on pseudo-hypertrophic muscular paralysis. Lancet 2: 1–2, 37–39, 73–75, 113–116.

Goyenvalle, A, Griffith, G, Babbs, A, Andaloussi, S El, Ezzat, K, Avril, A, Dugovic, B, Chaussenot, R, Ferry, A, Voit, T, Amthor, H, Bühr, C, Schürch, S, Wood, MJ a, Davies, KE, Vaillend, C, Leumann, C, Garcia, L. 2015. Functional correction in mouse models of muscular dystrophy using exon-skipping tricyclo-DNA oligomers. Nat. Med. 21: 270–275.

Grapp, M, Wrede, A, Schweizer, M, Hüwel, S, Galla, H-J, Snaidero, N, Simons, M, Bückers, J, Low, PS, Urlaub, H, Gärtner, J, Steinfeld, R. 2013. Choroid plexus transcytosis and exosome shuttling deliver folate into brain parenchyma. Nat. Commun. 4: 2123.

Haas, M, Vlcek, V, Balabanov, P, Salmonson, T, Bakchine, S, Markey, G, Weise, M, Schlosser-Weber, G, Brohmann, H, Yerro, CP, Mendizabal, MR, Stoyanova-Beninska, V, Hillege, HL. 2015. European Medicines Agency review of ataluren for the treatment of ambulant patients aged 5 years and older with Duchenne muscular dystrophy resulting from a nonsense mutation in the dystrophin gene. Neuromuscul. Disord. 25: 5–13.

Haenggi, T, Soontornmalai, a, Schaub, MC, Fritschy, J-M. 2004. The role of utrophin and Dp71 for assembly of different dystrophin-associated protein complexes (DPCs) in the choroid plexus and microvasculature of the brain. Neuroscience 129: 403–413.

Haeusler, AR, Donnelly, CJ, Periz, G, Simko, EAJ, Shaw, PG, Kim, M, Maragakis, NJ, Troncoso, JC, Pandey, A, Sattler, R, Rothstein, JD, Wang, J. 2014. C9orf72 nucleotide repeat structures initiate molecular cascades of disease. Nature 507: 195–200.

Hauser, PS, Narayanaswami, V, Ryan, RO. 2011. Apolipoprotein E: from lipid transport to neurobiology. Prog. Lipid Res. 50: 62–74.

Hawel, L, Tjandrawinata, RR, Fukumoto, GH, Byus, C V. 1994. Biosynthesis and selective export of 1,5-diaminopentane (cadaverine) in mycoplasma-free cultured mammalian cells. J. Biol. Chem. 269: 7412–7418.

Heemskerk, H, de Winter, C, van Kuik, P, Heuvelmans, N, Sabatelli, P, Rimessi, P, Braghetta, P, van Ommen, G-JB, de Kimpe, S, Ferlini, A, Aartsma-Rus, A, van Deutekom, JCT. 2010. Preclinical PK and PD studies on 2'-O-methyl-phosphorothioate RNA antisense oligonucleotides in the mdx mouse model. Mol. Ther. 18: 1210–1217.

Heier, CR, Damsker, JM, Yu, Q, Dillingham, BC, Huynh, T, Van der Meulen, JH, Sali, A, Miller, BK, Phadke, A, Scheffer, L, Quinn, J, Tatem, K, Jordan, S, Dadgar, S, Rodriguez, OC, Albanese, C, Calhoun, M, Gordish-Dressman, H, Jaiswal, JK, Connor, EM, Mccall, JM, Hoffman, EP, Reeves, EKM, Nagaraju, K. 2013. VBP15, a novel anti-inflammatory and membrane-stabilizer, improves muscular dystrophy without side effects. EMBO Mol. Med. 5: 1569–1585.

Helderman-van den Enden, A, de Jong, R, den Dunnen, J, Houwing-Duistermaat, J, Kneppers, A, Ginjaar, H, Breuning, M, Bakker, E. 2009. Recurrence risk due to germ line mosaicism: Duchenne and Becker muscular dystrophy. Clin. Genet. 75: 465–472.

Helliwell, TR, Man, NT, Morris, GE, Davies, KE. 1992. The dystrophin-related protein, utrophin, is expressed on the sarcolemma of regenerating human skeletal muscle fibres in dystrophies and inflammatory myopathies. Neuromuscul. Disord. 2: 177–184.

Hoffman, EP, Brown, RH, Kunkel, LM. 1987. Dystrophin: the protein product of the Duchenne muscular dystrophy locus. Cell 51: 919–928.

Hoogerwaard, EM, van der Wouw, P a., Wilde, A a. M, Bakker, E, Ippel, PF, Oosterwijk, JC, Majoor-Krakauer, DF, van Essen, AJ, Leschot, NJ, de Visser, M. 1999. Cardiac involvement in carriers of Duchenne and Becker muscular dystrophy. Neuromuscul. Disord. 9: 347–351.

Hua, Y, Sahashi, K, Hung, G, Rigo, F, Passini, MA, Bennett, CF, Krainer, AR. 2010. Antisense correction of SMN2 splicing in the CNS rescues necrosis in a type III SMA mouse model. 1634–1644.

Hua, Y, Sahashi, K, Rigo, F, Hung, G, Horev, G, Bennett, CF, Krainer, AR. 2011. Peripheral SMN restoration is essential for long-term rescue of a severe spinal muscular atrophy mouse model. Nature 478: 123–126.

Hurley, J V, Anderson, RM, Sexton, PT. 1981. The fate of plasma protein which escapes from blood vessels of the choroid plexus of the rat - an electron microscope study. J. Pathol. 134: 57–70.

Hutagalung, AH, Novick, PJ. 2011. Role of Rab GTPases in Membrane Traffic and Cell Physiology. 119–149.

Illingworth, RS, Bird, AP. 2009. CpG islands--'a rough guide'. FEBS Lett. 583: 1713–1720.

Ittig, D, Luisier, S, Weiler, J, Schümperli, D, Leumann, CJ. 2010. Improving gene silencing of siRNAs via tricyclo-DNA modification. Artif. DNA. PNA XNA 1: 9–16.

Ivanova, GD, Arzumanov, A, Abes, R, Yin, H, Wood, MJ a, Lebleu, B, Gait, MJ. 2008. Improved cell-penetrating peptide-PNA conjugates for splicing redirection in HeLa cells and exon skipping in mdx mouse muscle. Nucleic Acids Res. 36: 6418–6428.

Jacobs, PA, Hunt, PA, Mayer, M, Bart, RD. 1981. Duchenne Muscular Dystrophy (DMD) in a Female with an X/Autosome Translocation: Further Evidence That the DMD Locus Is at Xp21. Am. J. Hum. Genet. 33: 513–518.

Janssen, I, Heymsfield, SB, Wang, Z, Ross, R. 2000. Skeletal muscle mass and distribution in 468 men and women aged 18 − 88 yr. J. Appl. Physiol. 89: 81–88.

Jearawiriyapaisarn, N, Moulton, HM, Buckley, B, Roberts, J, Sazani, P, Fucharoen, S, Iversen, PL, Kole, R. 2008. Sustained dystrophin expression induced by peptide-conjugated morpholino oligomers in the muscles of mdx mice. Mol. Ther. 16: 1624–1629.

Johanson, C, Stopa, E, McMillan, P, Roth, D, Funk, J, Krinke, G. 2011. The distributional nexus of choroid plexus to cerebrospinal fluid, ependyma and brain: toxicologic/pathologic phenomena, periventricular destabilization, and lesion spread. Toxicol. Pathol. 39: 186–212.

Johnston, C a, Stanton, BR, Turner, MR, Gray, R, Blunt, AH-M, Butt, D, Ampong, M-A, Shaw, CE, Leigh, PN, Al-Chalabi, A. 2006. Amyotrophic lateral sclerosis in an urban setting: a population based study of inner city London. J. Neurol. 253: 1642–1643.

Jones, P a. 2012. Functions of DNA methylation: islands, start sites, gene bodies and beyond. Nat. Rev. Genet. 13: 484–492.

Kettani, A, Kumar, RA, Patel, DJ. 1995. Solution Structure of a DNA Quadruplex Containing the Fragile X Syndrome Triplet Repeat. 638–656.

Khirani, S, Ramirez, A, Aubertin, G, Boulé, M, Chemouny, C, Forin, V, Fauroux, B. 2014. Respiratory muscle decline in duchenne muscular dystrophy. Pediatr. Pulmonol. 49: 473–481.

Khurana, TS, Watkins, SC, Chafey, P, Chelly, J, Tomé, FMS, Fardeau, M, Kaplan, J-C, Kunkel, LM. 1991. Immunolocalization and developmental expression of dystrophin related protein in skeletal muscle. Neuromuscul. Disord. 1: 185–194.

Kiernan, MC, Vucic, S, Cheah, BC, Turner, MR, Eisen, A, Hardiman, O, Burrell, JR, Zoing, MC. 2011. Amyotrophic lateral sclerosis. Lancet 377: 942–955.

Kim, TW, Wu, K, Xu, JL, Black, IB. 1992. Detection of dystrophin in the postsynaptic density of rat brain and deficiency in a mouse model of Duchenne muscular dystrophy. Proc. Natl. Acad. Sci. U. S. A. 89: 11642–11644.

Knuesel, I, Mastrocola, M, Zuellig, RA, Bornhauser, B, Schaub, MC, Fritschy, J. 1999. Short communication: altered synaptic clustering of GABAA receptors in mice lacking dystrophin (mdx mice). Eur. J. Neurosci. 11: 4457–4462.

Koenig, M, Hoffman, EP, Bertelson, CJ, Monaco, a P, Feener, C, Kunkel, LM. 1987. Complete cloning of the Duchenne muscular dystrophy (DMD) cDNA and preliminary genomic organization of the DMD gene in normal and affected individuals. Cell 50: 509–517.

Konieczny, P, Swiderski, K, Chamberlain, JS. 2013. Gene and cell-mediated therapies for muscular dystrophy. Muscle Nerve 47: 649–663.

Koo, T, Okada, T, Foster, H, Takeda, S, Dickson, G. 2011. Long-term functional adeno-associated virus- microdystrophin expression in the dystrophic CXMDj dog. J. Gene Med. 13: 497–506.

Koo, T, Wood, MJ. 2013. Clinical trials using antisense oligonucleotides in duchenne muscular dystrophy. Hum. Gene Ther. 24: 479–488.

Korade-Mirnics, Z, Tarleton, J, Servidei, S, Casey, RR, Gennarelli, M, Pegoraro, E, Angelini, C, Hoffman, EP. 1999. Myotonic dystrophy: tissue-specific effect of somatic CTG

expansions on allele-specific DMAHP/SIX5 expression. Hum. Mol. Genet. 8: 1017–1023.

Kumar, P, Wu, H, McBride, JL, Jung, K-E, Kim, MH, Davidson, BL, Lee, SK, Shankar, P, Manjunath, N. 2007. Transvascular delivery of small interfering RNA to the central nervous system. Nature 448: 39–43.

Kwon, EJ, Lasiene, J, Jacobson, BE, Park, I-K, Horner, PJ, Pun, SH. 2010. Targeted nonviral delivery vehicles to neural progenitor cells in the mouse subventricular zone. Biomaterials 31: 2417–2424.

Labeit, S, Kolmerer, B. 1995. Titins : Giant Proteins in Charge of Muscle Ultrastructure and Elasticity features such as different passive tensions. Science (80-.). 270: 293–296.

Lagier-Tourenne, C, Baughn, M, Rigo, F, Sun, S, Liu, P, Li, H-R, Jiang, J, Watt, AT, Chun, S, Katz, M, Qiu, J, Sun, Y, Ling, S-C, Zhu, Q, Polymenidou, M, Drenner, K, Artates, JW, McAlonis-Downes, M, Markmiller, S, Hutt, KR, Pizzo, DP, Cady, J, Harms, MB, Baloh, RH, Vandenberg, SR, Yeo, GW, Fu, X-D, Bennett, CF, Cleveland, DW, Ravits, J. 2013. Targeted degradation of sense and antisense C9orf72 RNA foci as therapy for ALS and frontotemporal degeneration. Proc. Natl. Acad. Sci. U. S. A. 110: E4530–E4539.

Lehto, T, Castillo Alvarez, A, Gauck, S, Gait, MJ, Coursindel, T, Wood, MJ a, Lebleu, B, Boisguerin, P. 2014. Cellular trafficking determines the exon skipping activity of Pip6a-PMO in mdx skeletal and cardiac muscle cells. Nucleic Acids Res. 42: 3207–3217.

Lentz, TL. 1990. Rabies Virus Binding to an Acetylcholine Receptor. J. Mol. Recognit. 3: 82–88.

Lentz, TL, Hawrot, E, Paul, T. 1987. Synthetic Peptides Corresponding to Sequences of Snake Venom Neurotoxins and Rabies Virus Glycoprotein Bind to the Nicotinic Acetylcholine Receptor. Proteins 2: 298–307.

Levine, TP, Daniels, RD, Gatta, AT, Wong, LH, Hayes, MJ. 2013. The product of C9orf72, a gene strongly implicated in neurodegeneration, is structurally related to DENN Rab-GEFs. Bioinformatics 29: 499–503.

Li, J, Zhang, Q, Pang, Z, Wang, Y, Liu, Q, Guo, L, Jiang, X. 2012. Identification of peptide sequences that target to the brain using in vivo phage display. Amino Acids 42: 2373–2381.

Lidov, H, Byers, T, Watkins, S, Kunkel, L. 1990. Localization of dystrophin to postsynaptic regions of central nervous system cortical neurons. Nature 348: 725–728.

Lidov, HG, Selig, S, Kunkel, LM. 1995. Dp140: a novel 140 kDa CNS transcript from the dystrophin locus. Hum. Mol. Genet. 4: 329–335.

Lim, J-H, Kim, D-Y, Bang, MS. 2004. Effects of exercise and steroid on skeletal muscle apoptosis in the mdx mouse. Muscle Nerve 30: 456–462.

Lindenbaum, R, Clarke, G, Patel, C, Moncrieff, M, Hughes, JT. 1979. Muscular dystrophy in an X;1 translocation female suggests that Duchenne locus is on X chromosome short arm. J. Med. Genet. 16: 389–392.

Liu, JK, Teng, Q, Garrity-Moses, M, Federici, T, Tanase, D, Imperiale, MJ, Boulis, NM. 2005. A novel peptide defined through phage display for therapeutic protein and vector neuronal targeting. Neurobiol. Dis. 19: 407–418.

Logroscino, G, Traynor, BJ, Hardiman, O, Chiò, A, Mitchell, D, Swingler, RJ, Millul, A, Benn, E, Beghi, E. 2010. Incidence of amyotrophic lateral sclerosis in Europe. J. Neurol. Neurosurg. Psychiatry 81: 385–390.

Longatti, A, Lamb, C a, Razi, M, Yoshimura, S, Barr, F a, Tooze, S a. 2012. TBC1D14 regulates autophagosome formation via Rab11- and ULK1-positive recycling endosomes. J. Cell Biol. 197: 659–675.

López Castel, A, Nakamori, M, Tomé, S, Chitayat, D, Gourdon, G, Thornton, C a, Pearson, CE. 2011. Expanded CTG repeat demarcates a boundary for abnormal CpG methylation in myotonic dystrophy patient tissues. Hum. Mol. Genet. 20: 1–15.

Loufrani, L, Matrougui, K, Gorny, D, Duriez, M, Blanc, I, Levy, BI, Henrion, D. 2001. Flow (Shear Stress)-Induced Endothelium-Dependent Dilation Is Altered in Mice Lacking the Gene Encoding for Dystrophin. Circulation 103: 864–870.

Lu, QL, Wu, B. 2012. Systemic delivery of antisense oligomer in animal models and its implications for treating DMD. Methods Mol. Biol. 867: 393–405.

Lundin, P, Johansson, H, Guterstam, P, Holm, T, Hansen, M, Langel, U, EL Andaloussi, S. 2008. Distinct uptake routes of cell-penetrating peptide conjugates. Bioconjug. Chem. 19: 2535–2542.

Mackay, DJG, Callaway, JL a, Marks, SM, White, HE, Acerini, CL, Boonen, SE, Dayanikli, P, Firth, H V, Goodship, J a, Haemers, AP, Hahnemann, JMD, Kordonouri, O, Masoud, AF, Oestergaard, E, Storr, J, Ellard, S, Hattersley, AT, Robinson, DO, Temple, IK. 2008. Hypomethylation of multiple imprinted loci in individuals with transient neonatal diabetes is associated with mutations in ZFP57. Nat. Genet. 40: 949–951.

Majounie, E, Renton, AE, Mok, K, Dopper, EGP, Waite, A, Rollinson, S, Chiò, A, Restagno, G, Nicolaou, N, Simon-Sanchez, J, van Swieten, JC, Abramzon, Y, Johnson, JO, Sendtner, M, Pamphlett, R, Orrell, RW, Mead, S, Sidle, KC, Houlden, H, Rohrer, JD, Morrison, KE, Pall, H, Talbot, K, Ansorge, O, Hernandez, DG, Arepalli, S, Sabatelli, M, Mora, G, Corbo, M, Giannini, F, Calvo, A, Englund, E, Borghero, G, Floris, GL, Remes, AM, Laaksovirta, H, McCluskey, L, Trojanowski, JQ, Van Deerlin, VM, Schellenberg, GD, Nalls, M a, Drory, VE, Lu, C-S, Yeh, T-H, Ishiura, H, Takahashi, Y, Tsuji, S, Le Ber, I,

Brice, A, Drepper, C, Williams, N, Kirby, J, Shaw, P, Hardy, J, Tienari, PJ, Heutink, P, Morris, HR, Pickering-Brown, S, Traynor, BJ. 2012. Frequency of the C9orf72 hexanucleotide repeat expansion in patients with amyotrophic lateral sclerosis and frontotemporal dementia: a cross-sectional study. Lancet Neurol. 11: 323–330.

Malik, R, Roy, I. 2011. Making sense of therapeutics using antisense technology. Expert Opin. Drug Discov. 6: 507–526.

Margus, H, Padari, K, Pooga, M. 2012. Cell-penetrating peptides as versatile vehicles for oligonucleotide delivery. Mol. Ther. 20: 525–533.

Mendell, JR, Kissel, JT, Amato, a a, King, W, Signore, L, Prior, TW, Sahenk, Z, Benson, S, McAndrew, PE, Rice, R. 1995. Myoblast transfer in the treatment of Duchenne's muscular dystrophy. N. Engl. J. Med. 333: 832–838.

Mendell, JR, Rodino-Klapac, LR, Sahenk, Z, Roush, K, Bird, L, Lowes, LP, Alfano, L, Gomez, AM, Lewis, S, Kota, J, Malik, V, Shontz, K, Walker, CM, Flanigan, KM, Corridore, M, Kean, JR, Allen, HD, Shilling, C, Melia, KR, Sazani, P, Saoud, JB, Kaye, EM. 2013. Eteplirsen for the treatment of Duchenne muscular dystrophy. Ann. Neurol. 74: 637–647.

Meryon, E. 1852. On granular and fatty degeneration of the voluntary muscles. Med. Chir. Trans. 35: 73–84.

Millecamps, S, Boillée, S, Le Ber, I, Seilhean, D, Teyssou, E, Giraudeau, M, Moigneu, C, Vandenberghe, N, Danel-Brunaud, V, Corcia, P, Pradat, P-F, Le Forestier, N, Lacomblez, L, Bruneteau, G, Camu, W, Brice, A, Cazeneuve, C, Leguern, E, Meininger, V, Salachas, F. 2012. Phenotype difference between ALS patients with expanded repeats in C9ORF72 and patients with mutations in other ALS-related genes. J. Med. Genet. 49: 258–263.

Miller, RG, Sharma, KR, Pvlath, GK, Gussoni, E, Mynhier, M, Lnctot, AM, Greco, CM, Steinman, L, Blau, HM. 1997. Myoblast implantation in Duchenne muscular dystrophy: the San Francisco study. Muscle Nerve 20: 469–478.

Miranda, R, Sébrié, C, Degrouard, J, Gillet, B, Jaillard, D, Laroche, S, Vaillend, C. 2009. Reorganization of inhibitory synapses and increased PSD length of perforated excitatory synapses in hippocampal area CA1 of dystrophin-deficient mdx mice. Cereb. Cortex 19: 876–888.

Modarresi, F, Faghihi, MA, Lopez-Toledano, M a, Fatemi, RP, Magistri, M, Brothers, SP, van der Brug, MP, Wahlestedt, C. 2012. Inhibition of natural antisense transcripts in vivo results in gene-specific transcriptional upregulation. Nat. Biotechnol. 30: 453–459.

Moens, P, Baatsen, PHWW, Maréchal, G. 1993. Increased susceptibility of EDL muscles from mdx mice to damage induced by contractions with stretch. J. Muscle Res. Cell Motil. 451: 446–451.

Monaco, A, Neve, R, Colletti-Feener, C. 1986. Isolation of candidate cDNAs for portions of the Duchenne muscular dystrophy gene. Nature 323: 646–650.

Monaco, AP, Bertelson, CJ, Liechti-Gallati, S, Moser, H, Kunkel, LM. 1988. An explanation for the phenotypic differences between patients bearing partial deletions of the DMD locus. Genomics 2: 90–95.

Mori, K, Arzberger, T, Grässer, F a, Gijselinck, I, May, S, Rentzsch, K, Weng, S-M, Schludi, MH, van der Zee, J, Cruts, M, Van Broeckhoven, C, Kremmer, E, Kretzschmar, H a, Haass, C, Edbauer, D. 2013a. Bidirectional transcripts of the expanded C9orf72 hexanucleotide repeat are translated into aggregating dipeptide repeat proteins. Acta Neuropathol. 126: 881-893.

Mori, K, Weng, S-M, Arzberger, T, May, S, Rentzsch, K, Kremmer, E, Schmid, B, Kretzschmar, H a, Cruts, M, Van Broeckhoven, C, Haass, C, Edbauer, D. 2013b. The C9orf72 GGGGCC repeat is translated into aggregating dipeptide-repeat proteins in FTLD/ALS. Science 339: 1335–1338.

Morita, K, Sasaki, H, Furuse, M, Tsukita, S. 1999. Endothelial claudin: claudin-5/TMVCF constitutes tight junction strands in endothelial cells. J. Cell Biol. 147: 185–194.

Moulton, HM, Nelson, MH, Hatlevig, SA, Reddy, MT, Iversen, PL. 2004. Cellular Uptake of Antisense Morpholino Oligomers Conjugated to Arginine-Rich Peptides. Bioconjug. Chem. 15: 290–299.

Moxley, RT, Pandya, S, Ciafaloni, E, Fox, DJ, Campbell, K. 2010. Change in natural history of Duchenne muscular dystrophy with long-term corticosteroid treatment: implications for management. J. Child Neurol. 25: 1116–1129.

Muntoni, F, Mateddu, A, Serra, G. 1991. Passive avoidance behaviour deficit in the mdx mouse. Neuromuscul. Disord. 1: 121–123.

Muntoni, F, Torelli, S, Ferlini, A. 2003. Dystrophin and mutations: one gene, several proteins, multiple phenotypes. Lancet Neurol. 2: 731–740.

Murray, J, Davies, K, Harper, P, Meredith, L, Mueller, C, Williamson, R. 1982. Linkage relationship of a cloned DNA sequence on the short arm of the X chromosome to Duchenne muscular dystrophy. Nature 300: 69–71.

Nico, B, Frigeri, A, Nicchia, GP, Corsi, P, Ribatti, D, Quondamatteo, F, Herken, R, Girolamo, F, Marzullo, A, Svelto, M, Roncali, L. 2003. Severe alterations of endothelial and glial cells in the blood-brain barrier of dystrophic mdx mice. Glia 42: 235–251.

Nico, B, Paola Nicchia, G, Frigeri, a, Corsi, P, Mangieri, D, Ribatti, D, Svelto, M, Roncali, L. 2004. Altered blood-brain barrier development in dystrophic MDX mice. Neuroscience 125: 921–935.

Nico, B, Tamma, R, Annese, T, Mangieri, D, De Luca, A, Corsi, P, Benagiano, V, Longo, V, Crivellato, E, Salmaggi, A, Ribatti, D. 2010. Glial dystrophin-associated proteins, laminin and agrin, are downregulated in the brain of mdx mouse. Lab. Invest. 90: 1645–1660.

Nielsen, PE. 2010. Peptide nucleic acids (PNA) in chemical biology and drug discovery. Chem. Biodivers. 7: 786–804.

Nielsen, S, Nagelhus, E a, Amiry-Moghaddam, M, Bourque, C, Agre, P, Ottersen, OP. 1997. Specialized membrane domains for water transport in glial cells: high-resolution immunogold cytochemistry of aquaporin-4 in rat brain. J. Neurosci. 17: 171–180.

Niewoehner, J, Bohrmann, B, Collin, L, Urich, E, Sade, H, Maier, P, Rueger, P, Stracke, JO, Lau, W, Tissot, AC, Loetscher, H, Ghosh, A, Freskgård, P-O. 2014. Increased brain penetration and potency of a therapeutic antibody using a monovalent molecular shuttle. Neuron 81: 49–60.

Nishida, Y, Arakawa, S, Fujitani, K, Yamaguchi, H, Mizuta, T, Kanaseki, T, Komatsu, M, Otsu, K, Tsujimoto, Y, Shimizu, S. 2009. Discovery of Atg5/Atg7-independent alternative macroautophagy. Nature 461: 654–658.

Nitta, T, Hata, M, Gotoh, S, Seo, Y, Sasaki, H, Hashimoto, N, Furuse, M, Tsukita, S. 2003. Size-selective loosening of the blood-brain barrier in claudin-5-deficient mice. J. Cell Biol. 161: 653–660.

Noy, A, Luque, FJ, Orozco, M. 2008. Theoretical Analysis of Antisense Duplexes : Determinants of the RNase H Susceptibility when complementary strands of DNA and RNA bind following. J. Am. Chem. Soc. 130: 3486–3496.

Oshima, J, Magner, DB, Lee, J a, Breman, AM, Schmitt, ES, White, LD, Crowe, C a, Merrill, M, Jayakar, P, Rajadhyaksha, A, Eng, CM, del Gaudio, D. 2009. Regional genomic instability predisposes to complex dystrophin gene rearrangements. Hum. Genet. 126: 411–423.

De Paepe, B, De Bleecker, JL. 2013. Cytokines and chemokines as regulators of skeletal muscle inflammation: presenting the case of Duchenne muscular dystrophy. Mediators Inflamm. 2013: 540370.

Palmer, E, Wilhelm, JM, Sherman, F. 1979. Phenotypic suppression of nonsense mutants in yeast by aminoglycoside antibiotics. Nature 277: 148–150.

Partridge, T a. 2013. The mdx mouse model as a surrogate for Duchenne muscular dystrophy. FEBS J. 280: 4177–4186.

Pastoret, C, Sebille, A. 1995. mdx mice show progressive weakness and muscle deterioration with age. J. Neurol. Sci. 129: 97–105.

Pearson, a M, Rich, a, Krieger, M. 1993. Polynucleotide binding to macrophage scavenger receptors depends on the formation of base-quartet-stabilized four-stranded helices. J. Biol. Chem. 268: 3546–3554.

Ploquin, A, Büning, H, Salvetti, A. 2014. Adeno-associated virus (AAV) vectors. In: Scherman, D, editor. Advanced textbook on gene transfer, gene therapy and genetic pharmacology. London: Imperial College Press, p 151–164.

Politano, L, Nigro, G, Nigro, V, Piluso, G, Papparella, S, Paciello, O, Comi, LI. 2003. Gentamicin administration in Duchenne patients with premature stop codon. Preliminary results. Acta Myol. 22: 15–21.

Porter, JD, Khanna, S, Kaminski, HJ, Rao, JS, Merriam, AP, Richmonds, CR, Leahy, P, Li, J, Guo, W, Andrade, FH. 2002. A chronic inflammatory response dominates the skeletal muscle molecular signature in dystrophin-deficient mdx mice. 11: 263–272.

Prades, R, Guerrero, S, Araya, E, Molina, C, Salas, E, Zurita, E, Selva, J, Egea, G, López-Iglesias, C, Teixidó, M, Kogan, MJ, Giralt, E. 2012. Delivery of gold nanoparticles to the brain by conjugation with a peptide that recognizes the transferrin receptor. Biomaterials 33: 7194–7205.

Punitha, AD, Srivastava, AK. 2013. CNS drug targeting: have we travelled in right path? J. Drug Target. 21: 787–800.

Rae, C, Scott, RB, Thompson, CH, Dixon, RM, Dumughn, I, Kemp, GJ, Male, A, Pike, M, Styles, P, Radda, GK. 1998. Brain biochemistry in Duchenne muscular dystrophy : A 1 H magnetic resonance and neuropsychological study. J. Neurol. Sci. 160: 148–157.

Ranum, LPW, Cooper, T a. 2006. RNA-mediated neuromuscular disorders. Annu. Rev. Neurosci. 29: 259–277.

Re, F, Cambianica, I, Zona, C, Sesana, S, Gregori, M, Rigolio, R, La Ferla, B, Nicotra, F, Forloni, G, Cagnotto, A, Salmona, M, Masserini, M, Sancini, G. 2011. Functionalization of liposomes with ApoE-derived peptides at different density affects cellular uptake and drug transport across a blood-brain barrier model. Nanomedicine 7: 551–559.

Reddy, K, Zamiri, B, Stanley, SYR, Macgregor, RB, Pearson, CE. 2013. The disease-associated r(GGGGCC)n repeat from the C9orf72 gene forms tract length-dependent uni- and multimolecular RNA G-quadruplex structures. J. Biol. Chem. 288: 9860–9866.

Reese, TS, Karnovsky, MJ. 1967. Fine structural localization of a blood-brain barrier to exogenous peroxidase. J. Cell Biol. 34: 207–217.

Reiner, a, Veenman, CL, Medina, L, Jiao, Y, Del Mar, N, Honig, MG. 2000. Pathway tracing using biotinylated dextran amines. J. Neurosci. Methods 103: 23–37.

Renneberg, D, Bouliong, E, Reber, U, Schümperli, D, Leumann, CJ, Bern, DU, Bern, C-. 2002. Antisense properties of tricyclo-DNA. Nucleic Acids Res. 30: 2751–2757.

Renton, AE, Chiò, A, Traynor, BJ. 2014. State of play in amyotrophic lateral sclerosis genetics. Nat. Neurosci. 17: 17–23.

Renton, AE, Majounie, E, Waite, A, Simón-Sánchez, J, Rollinson, S, Gibbs, JR, Schymick, JC, Laaksovirta, H, van Swieten, JC, Myllykangas, L, Kalimo, H, Paetau, A, Abramzon, Y, Remes, AM, Kaganovich, A, Scholz, SW, Duckworth, J, Ding, J, Harmer, DW, Hernandez, DG, Johnson, JO, Mok, K, Ryten, M, Trabzuni, D, Guerreiro, RJ, Orrell, RW, Neal, J, Murray, A, Pearson, J, Jansen, IE, Sondervan, D, Seelaar, H, Blake, D, Young, K, Halliwell, N, Callister, JB, Toulson, G, Richardson, A, Gerhard, A, Snowden, J, Mann, D, Neary, D, Nalls, M a, Peuralinna, T, Jansson, L, Isoviita, V-M, Kaivorinne, A-L, Hölttä-Vuori, M, Ikonen, E, Sulkava, R, Benatar, M, Wuu, J, Chiò, A, Restagno, G, Borghero, G, Sabatelli, M, Heckerman, D, Rogaeva, E, Zinman, L, Rothstein, JD, Sendtner, M, Drepper, C, Eichler, EE, Alkan, C, Abdullaev, Z, Pack, SD, Dutra, A, Pak, E, Hardy, J, Singleton, A, Williams, NM, Heutink, P, Pickering-Brown, S, Morris, HR, Tienari, PJ, Traynor, BJ. 2011. A hexanucleotide repeat expansion in C9ORF72 is the cause of chromosome 9p21-linked ALS-FTD. Neuron 72: 257–268.

Reynolds, ES. 1963. The use of lead citrate at high pH as an electron-opaque stain in electron microscopy. J. Cell Biol. 17: 208–212.

Rifai, Z, Lorenson, M, Griggs, C, Moxley, T. 1995. Effect of prednisone on protein in Duchenne dystrophy metabolism. Am. J. Physiol. 268: E67–E74.

Robberecht, W, Philips, T. 2013. The changing scene of amyotrophic lateral sclerosis. Nat. Rev. Neurosci. 14: 248–264.

Roberts, R, Coffey, A, Bobrow, M, Bentley, D. 1993. Exon structure of the human dystrophin gene. Genomics 16: 536–538.

Rosen, DR, Siddique, T, Patterson, D, Figlewicz, DA, Sapp, P, Hentati, A, Donaldson, D, Goto, J, O'Regan, JP, Deng, HX, Rahmani, Z, Krizus, A, McKenna-Yasek, D, Cayabyab, A, Gaston, SM, Berger, R, Tanzi, RE, Halperin, JJ, Herzfeldt, B, van den Bergh, R, Hung, W-Y, Bird, T, Deng, G, Mulder, DW, Smyth, C, Laing, NG, Soriano, E, Pericak-Vance, MA, Haines, J, Rouleau, GA, Gusella, JS, Horvitz, HR, Brown, RH. 1993. Mutations in Cu/Zn superoxide dismutase gene are associated with familial amyotrophic lateral sclerosis. Nature 362: 59–62.

Rosenberg, G a. 2012. Neurological diseases in relation to the blood-brain barrier. J. Cereb. Blood Flow Metab. 32: 1139–1151.

Ross, MH, Pawlina, W. 2011. Histology: a text and atlas: with correlated cell and molecular biology, 6th edition. Philadelphia, PA; London: Lippincott Willaims & Wilkins.

Rydström, A, Deshayes, S, Konate, K, Crombez, L, Padari, K, Boukhaddaoui, H, Aldrian, G, Pooga, M, Divita, G. 2011. Direct translocation as major cellular uptake for CADY self-assembling peptide-based nanoparticles. PLoS One 6: e25924.

Saleh, AF, Arzumanov, AA, Gait, MJ. 2012. Overview of Alternative Oligonucleotide Chemistries for Exon Skipping. Methods Mol. Biol. 867: 365–378.

Saleh, M-C, van Rij, RP, Hekele, A, Gillis, A, Foley, E, O'Farrell, PH, Andino, R. 2006. The endocytic pathway mediates cell entry of dsRNA to induce RNAi silencing. Nat. Cell Biol. 8: 793–802.

Salzman, SK, Stepita-Klauco, M. 1981. Cadaverine in the rat brain: regional distribution and acylation of [14C]cadaverine in vivo and uptake in vitro. J. Neurochem. 37: 1308–1315.

Sander, M, Chavoshan, B, Harris, S a, Iannaccone, ST, Stull, JT, Thomas, GD, Victor, RG. 2000. Functional muscle ischemia in neuronal nitric oxide synthase-deficient skeletal muscle of children with Duchenne muscular dystrophy. Proc. Natl. Acad. Sci. U. S. A. 97: 13818–13823.

Sandri, M, Podhorska-Okolow, M, Geromel, V, Rizzi, C, Arslan, P, Franceschi, C, Carraro, U. 1997. Exercise induces myonuclear ubiquitination and apoptosis in dystrophin-deficient muscle of mice. J. Neuropathol. Exp. Neurol. 56: 45–57.

Sareen, D, O'Rourke, JG, Meera, P, Muhammad, a KMG, Grant, S, Simpkinson, M, Bell, S, Carmona, S, Ornelas, L, Sahabian, A, Gendron, T, Petrucelli, L, Baughn, M, Ravits, J, Harms, MB, Rigo, F, Bennett, CF, Otis, TS, Svendsen, CN, Baloh, RH. 2013. Targeting RNA foci in iPSC-derived motor neurons from ALS patients with a C9ORF72 repeat expansion. Sci. Transl. Med. 5: 208ra149.

Sarin, H. 2010. Physiologic upper limits of pore size of different blood capillary types and another perspective on the dual pore theory of microvascular permeability. J. Angiogenes. Res. 2: 14.

Sbriccoli, A, Santarelli, M, Carretta, D. 1995. Architectural changes of the cortico-spinal system in the dystrophin defective mdx mouse. Neurosci. Lett. 200: 53–56.

Segal, SS. 2012. Special circulations. In: Boron, WF, Boulpaep, EL, editors. Medical physiology: a cellular and molecular approach, 2nde. Philadelphia: Saunders Elsevier, p 577–592.

Sekiguchi, M, Zushida, K, Yoshida, M, Maekawa, M, Kamichi, S, Yoshida, M, Sahara, Y, Yuasa, S, Takeda, S, Wada, K. 2009. A deficit of brain dystrophin impairs specific

amygdala GABAergic transmission and enhances defensive behaviour in mice. Brain 132: 124–135.

Septien, L, Gras, P, Borsotti, JP, Giroud, M, Nivelon, JL, Dumas, R. 1991. Mental development in Duchenne muscular dystrophy. Correlation of data of the brain scanner. Pediatrie 46: 817–819.

Sesay, AK, Errington, ML, Levita, L, Bliss, T V. 1996. Spatial learning and hippocampal long-term potentiation are not impaired in mdx mice. Neurosci. Lett. 211: 207–210.

Shabanpoor, F, Gait, MJ. 2013. Development of a general methodology for labelling peptide-morpholino oligonucleotide conjugates using alkyne-azide click chemistry. Chem. Commun. (Camb). 49: 10260–10262.

Shore, VG, Shore, B. 1973. Heterogeneity of Human Plasma Very Low Density Lipoproteins. Separation of Species Differing in Protein Components. Biochemistry 12: 502–507.

Sicinski, P, Geng, Y, Ryder-cook, AS, Barnard, EA, Darlison, MG, Barnard, PJ, Geng, YAN, Darlison, MG, Barnardt, PJ. 1989. The Molecular Basis of Muscular Dystrophy in the mdx Mouse : A Point Mutation. Science (80-.). 244: 1578–1580.

Simón-Sánchez, J, Dopper, EGP, Cohn-Hokke, PE, Hukema, RK, Nicolaou, N, Seelaar, H, de Graaf, JR a, de Koning, I, van Schoor, NM, Deeg, DJH, Smits, M, Raaphorst, J, van den Berg, LH, Schelhaas, HJ, De Die-Smulders, CEM, Majoor-Krakauer, D, Rozemuller, AJM, Willemsen, R, Pijnenburg, Y a L, Heutink, P, van Swieten, JC. 2012. The clinical and pathological phenotype of C9ORF72 hexanucleotide repeat expansions. Brain 135: 723–735.

Singh, A, Ursic, D, Davies, J. 1979. Phenotypic suppression and misreading in Saccharomyces cerevisiae. Nature 277: 146–148.

Sisó, S, Jeffrey, M, González, L. 2010. Sensory circumventricular organs in health and disease. Acta Neuropathol. 120: 689–705.

Sklar, RM, Brown, RHJ. 1991. Methylprednisolone increases dystrophin levels by inhibiting myotube death during myogenesis of normal human muscle in vitro. J. Neurol. Sci. 101: 73–81.

De Smet, C, Lurquin, C, Lethé, B, Smet, CDE, Lethe, B, Boon, T. 1999. DNA Methylation Is the Primary DNA methylation is the primary silencing mechanism for a set of germ line- and tumor-specific genes with a CpG-rich promoter Genes with a CpG-Rich Promoter. Mollecular Cell. Biol. 19: 7327–7335.

Spector, R. 2006. Nucleoside and Vitamin Homeostasis in the Mammalian Central Nervous System. Ann. N. Y. Acad. Sci. 481: 221–230.

Spector, R, Johanson, C. 2006. Micronutrient and urate transport in choroid plexus and kidney: implications for drug therapy. Pharm. Res. 23: 2515–2524.

Stein, C a, Hansen, JB, Lai, J, Wu, S, Voskresenskiy, A, Høg, A, Worm, J, Hedtjärn, M, Souleimanian, N, Miller, P, Soifer, HS, Castanotto, D, Benimetskaya, L, Ørum, H, Koch, T. 2010. Efficient gene silencing by delivery of locked nucleic acid antisense oligonucleotides, unassisted by transfection reagents. Nucleic Acids Res. 38: e3.

Stepita-Klauco, M, Dolezalova, H. 1974. Cadaverine in the brain of axenic mice. Nature 252: 158–159.

Sutcliffe, JS, Nelson, DL, Zhang, F, Pieretti, M, Caskey, CT, Saxe, D, Warren, ST. 1992. DNA methylation represses FMR-1 transcription in fragile X syndrome. Hum. Mol. Genet. 1: 397–400.

Sutherland, GR. 2003. Rare fragile sites. Cytogenet. Genome Res. 100: 77–84.

Suzuki, N, Maroof, AM, Merkle, FT, Koszka, K, Intoh, A, Armstrong, I, Moccia, R, Davis-Dusenbery, BN, Eggan, K. 2013. The mouse C9ORF72 ortholog is enriched in neurons known to degenerate in ALS and FTD. Nat. Neurosci. 16: 1725–1727.

Swinnen, B, Robberecht, W. 2014. The phenotypic variability of amyotrophic lateral sclerosis. Nat. Rev. Neurol. 10: 661–670.

Szmydynger-Chodobska, J, Chodobski, A, Johanson, CE. 1994. Postnatal developmental changes in blood flow to choroid plexuses and cerebral cortex of the rat. Am. J. Physiol. Regul. Integr. Comp. Physiol. 266: R1488–R1492.

Tadayoni, R, Rendon, A, Soria-Jasso, LE, Cisneros, B. 2012. Dystrophin Dp71: the smallest but multifunctional product of the Duchenne muscular dystrophy gene. Mol. Neurobiol. 45: 43–60.

Tait, MJ, Saadoun, S, Bell, BA, Papadopoulos, MC. 2008. Water movements in the brain: role of aquaporins. Trends Neurosci. 31: 37–43.

Takemitsu, M, Ishiura, S, Koga, R, Kamakura, K, Arahata, K, Nonaka, I, Sugita, H. 1991. Dystrophin-related protein in the fetal and denervated skeletal muscles of normal and mdx mice. Biochem. Biophys. Res. Commun. 180: 1179–1186.

Tamma, R, Annese, T, Capogrosso, RF, Cozzoli, A, Benagiano, V, Sblendorio, V, Ruggieri, S, Crivellato, E, Specchia, G, Ribatti, D, De Luca, A, Nico, B. 2013. Effects of prednisolone on the dystrophin-associated proteins in the blood-brain barrier and skeletal muscle of dystrophic mdx mice. Lab. Invest. 93: 592–610.

Tanabe, Y, Esaki, K, Nomura, T. 1986. Skeletal muscle pathology in X chromosome-linked muscular dystrophy (mdx) mouse. Acta Neuropathol. 69: 91–95.

Tedesco, FS, Hoshiya, H, D'Antona, G, Gerli, MFM, Messina, G, Antonini, S, Tonlorenzi, R, Benedetti, S, Berghella, L, Torrente, Y, Kazuki, Y, Bottinelli, R, Oshimura, M, Cossu, G. 2011. Stem cell-mediated transfer of a human artificial chromosome ameliorates muscular dystrophy. Sci. Transl. Med. 3: 96ra78.

Tidball, JG, Spencer, MJ. 2000. Calpains and muscular dystrophies. Int. J. Biochem. Cell Biol. 32: 1–5.

Tinsley, J, Deconinck, N, Fisher, R, Kahn, D, Phelps, S, Gillis, J-M, Davies, K. 1998. Expression of full-length utrophin prevents muscular dystrophy in mdx mice. Nat. Med. 4: 1441–1444.

Tinsley, JM, Blake, DJ, Roche, A, Fairbrother, U, Riss, J, Blyth, BC, Knight, AE, Kendrick-Jones, J, Suthers, GK, Love, DR, Edwards, YH, Davies, KE. 1992. Primary structure of dystrophin-related protein. Nature 360: 591–593.

Tinsley, JM, Fairclough, RJ, Storer, R, Wilkes, FJ, Potter, AC, Squire, SE, Powell, DS, Cozzoli, A, Capogrosso, RF, Lambert, A, Wilson, FX, Wren, SP, De Luca, A, Davies, KE. 2011. Daily treatment with SMTC1100, a novel small molecule utrophin upregulator, dramatically reduces the dystrophic symptoms in the mdx mouse. PLoS One 6: e19189.

Todd, PK, Oh, SY, Krans, A, He, F, Sellier, C, Frazer, M, Renoux, AJ, Chen, K, Scaglione, KM, Basrur, V, Elenitoba-Johnson, K, Vonsattel, JP, Louis, ED, Sutton, M a, Taylor, JP, Mills, RE, Charlet-Berguerand, N, Paulson, HL. 2013. CGG repeat-associated translation mediates neurodegeneration in fragile X tremor ataxia syndrome. Neuron 78: 440–455.

Torres, AG, Threlfall, RN, Gait, MJ. 2011. Potent and sustained cellular inhibitioon of miR-122 by lysine-derivatized peptide nucleic acids (PNS) and phosphorothioate locked nucleic acid (LNA)/2'-O-methyl (OMe) mixmer anti-miRs in the absence of transfection agents. Artif. DNA. PNA XNA 2: 71–78.

Tozawa, T, Itoh, K, Yaoi, T, Tando, S, Umekage, M, Dai, H, Hosoi, H, Fushiki, S. 2012. The shortest isoform of dystrophin (Dp40) interacts with a group of presynaptic proteins to form a presumptive novel complex in the mouse brain. Mol. Neurobiol. 45: 287–297.

Turner, MR, Hardiman, O, Benatar, M, Brooks, BR, Chio, A, de Carvalho, M, Ince, PG, Lin, C, Miller, RG, Mitsumoto, H, Nicholson, G, Ravits, J, Shaw, PJ, Swash, M, Talbot, K, Traynor, BJ, Van den Berg, LH, Veldink, JH, Vucic, S, Kiernan, MC. 2013. Controversies and priorities in amyotrophic lateral sclerosis. Lancet Neurol. 12: 310–322.

Turner, MR, Scaber, J, Goodfellow, J a, Lord, ME, Marsden, R, Talbot, K. 2010. The diagnostic pathway and prognosis in bulbar-onset amyotrophic lateral sclerosis. J. Neurol. Sci. 294: 81–85.

Uchino, M, Teramoto, H, Naoe, H, Miike, T, Yoshioka, K, Ando, M. 1994a. Dystrophin and dystrophin-related protein in the central nervous system of normal controls and Duchenne muscular dystrophy. Acta Neuropathol. 87: 129–134.

Uchino, M, Yoshioka, K, Miike, T, Tokunaga, M, Teramoto, H, Ando, M. 1994b. Dystrophin and dystrophin-related protein in the brains of normal and mdx mice. Muscle Nerve 17: 533–538.

Vaillend, C, Billard, J-M, Laroche, S. 2004. Impaired long-term spatial and recognition memory and enhanced CA1 hippocampal LTP in the dystrophin-deficient Dmd(mdx) mouse. Neurobiol. Dis. 17: 10–20.

Vaillend, C, Rendon, a, Misslin, R, Ungerer, a. 1995. Influence of dystrophin-gene mutation on mdx mouse behavior. I. Retention deficits at long delays in spontaneous alternation and bar-pressing tasks. Behav. Genet. 25: 569–579.

Vandebrouck, C, Martin, D, Colson-Van Schoor, M, Debaix, H, Gailly, P. 2002. Involvement of TRPC in the abnormal calcium influx observed in dystrophic (mdx) mouse skeletal muscle fibers. J. Cell Biol. 158: 1089–1096.

Vandesompele, J, De Preter, K, Pattyn, F, Poppe, B, Van Roy, N, De Paepe, A, Speleman, F. 2002. Accurate normalization of real-time quantitative RT-PCR data by geometric averaging of multiple internal control genes. Genome Biol. 3: RESEARCH0034.

Varela, M a, Roberts, TC, Andaloussi, S El, Wood, MJ. 2012. Natural Antisense Makes Sense for Gene-specific Activation in Brain. Mol. Ther. Nucleic Acids 1: e24.

Varela, M a, Roberts, TC, Wood, MJ a. 2013. Epigenetics and ncRNAs in brain function and disease: mechanisms and prospects for therapy. Neurotherapeutics 10: 621–631.

Viggiano, E, Picillo, E, Cirillo, a, Politano, L. 2013. Comparison of X-chromosome inactivation in Duchenne muscle/myocardium-manifesting carriers, non-manifesting carriers and related daughters. Clin. Genet. 84: 265–270.

Voit, T, Topaloglu, H, Straub, V, Muntoni, F, Deconinck, N, Campion, G, De Kimpe, SJ, Eagle, M, Guglieri, M, Hood, S, Liefaard, L, Lourbakos, A, Morgan, A, Nakielny, J, Quarcoo, N, Ricotti, V, Rolfe, K, Servais, L, Wardell, C, Wilson, R, Wright, P, Kraus, JE. 2014. Safety and efficacy of drisapersen for the treatment of Duchenne muscular dystrophy (DEMAND II): an exploratory, randomised, placebo-controlled phase 2 study. Lancet. Neurol. 13: 987–996.

Wagner, JR, Busche, S, Ge, B, Kwan, T, Pastinen, T, Blanchette, M. 2014. The relationship between DNA methylation, genetic and expression inter-individual variation in untransformed human fibroblasts. Genome Biol. 15: R37.

Wagner, KR, Hamed, S, Hadley, DW, Gropman, AL, Burstein, AH, Escolar, DM, Hoffman, EP, Fischbeck, KH. 2001. Gentamicin treatment of Duchenne and Becker muscular dystrophy due to nonsense mutations. Ann. Neurol. 49: 706–711.

Wahlestedt, C, Salmi, P, Good, L, Kela, J, Johnsson, T, Ho, T, Broberger, C, Porreca, F, Lai, J, Ren, K, Ossipov, M, Koshkin, A, Jakobsen, N, Skouv, J, Oerum, H, Jacobsen, MH, Wengel, J. 2000. Potent and nontoxic antisense oligonucleotides containing locked nucleic acids. Proc. Natl. Acad. Sci. U. S. A. 97: 5633–5638.

Walsh, RJ, Slaby, FJ, Posner, BI. 1987. A receptor-mediated mechanism for the transport of prolactin from blood to cerebrospinal fluid. Endocrinology 120: 1846–1850.

Weber, M, Hellmann, I, Stadler, MB, Ramos, L, Pääbo, S, Rebhan, M, Schübeler, D. 2007. Distribution, silencing potential and evolutionary impact of promoter DNA methylation in the human genome. Nat. Genet. 39: 457–466.

Welch, EM, Barton, ER, Zhuo, J, Tomizawa, Y, Friesen, WJ, Trifillis, P, Paushkin, S, Patel, M, Trotta, CR, Hwang, S, Wilde, RG, Karp, G, Takasugi, J, Chen, G, Jones, S, Ren, H, Moon, Y-C, Corson, D, Turpoff, A a, Campbell, J a, Conn, MM, Khan, A, Almstead, NG, Hedrick, J, Mollin, A, Risher, N, Weetall, M, Yeh, S, Branstrom, A a, Colacino, JM, Babiak, J, Ju, WD, Hirawat, S, Northcutt, VJ, Miller, LL, Spatrick, P, He, F, Kawana, M, Feng, H, Jacobson, A, Peltz, SW, Sweeney, HL. 2007. PTC124 targets genetic disorders caused by nonsense mutations. Nature 447: 87–91.

Van Westering, T, Betts, C, Wood, M. 2015. Current Understanding of Molecular Pathology and Treatment of Cardiomyopathy in Duchenne Muscular Dystrophy. Molecules 20: 8823–8855.

White, RB, Biérinx, A-S, Gnocchi, VF, Zammit, PS. 2010. Dynamics of muscle fibre growth during postnatal mouse development. BMC Dev. Biol. 10: 21.

Williamson, LC, Bateman, KE, Clifford, JCM, Neale, E a. 1999. Neuronal Sensitivity to Tetanus Toxin Requires Gangliosides. J. Biol. Chem. 274: 25173–25180.

Wilton, SD, Fall, AM, Harding, PL, McClorey, G, Coleman, C, Fletcher, S. 2007. Antisense oligonucleotide-induced exon skipping across the human dystrophin gene transcript. Mol. Ther. 15: 1288–1296.

Wisse, E, Braet, F, De Zanger, R, Jans, D, Crabbe, E, Vermoesen, A. 1996. Structure and Function of Sinusoidal Lining Cells in the Liver. Toxicol. Pathol. 24: 100–111.

Wolburg, H, Lippoldt, A. 2002. Tight junctions of the blood-brain barrier: development, composition and regulation. Vascul. Pharmacol. 38: 323–337.

Wu, B, Lu, P, Benrashid, E, Malik, S, Ashar, J, Doran, TJ, Lu, QL. 2010. Dose-dependent restoration of dystrophin expression in cardiac muscle of dystrophic mice by systemically delivered morpholino. Gene Ther. 17: 132–140.

Wu, B, Moulton, HM, Iversen, PL, Jiang, J, Li, J, Li, J, Spurney, CF, Sali, A, Guerron, AD, Nagaraju, K, Doran, T, Lu, P, Xiao, X, Lu, QL. 2008. Effective rescue of dystrophin improves cardiac function in dystrophin-deficient mice by a modified morpholino oligomer. Proc. Natl. Acad. Sci. U. S. A. 105: 14814–14819.

Xi, Z, Zinman, L, Moreno, D, Schymick, J, Liang, Y, Sato, C, Zheng, Y, Ghani, M, Dib, S, Keith, J, Robertson, J, Rogaeva, E. 2013. Hypermethylation of the CpG Island Near the G4C2 Repeat in ALS with a C9orf72 Expansion. Am. J. Hum. Genet. 92: 981–989.

Xu, Z, Poidevin, M, Li, X, Li, Y, Shu, L, Nelson, DL, Li, H, Hales, CM, Gearing, M, Wingo, TS, Jin, P. 2013. Expanded GGGGCC repeat RNA associated with amyotrophic lateral sclerosis and frontotemporal dementia causes neurodegeneration. Proc. Natl. Acad. Sci. U. S. A. 110: 7778–7783.

Yin, H, Moulton, HM, Betts, C, Seow, Y, Boutilier, J, Iverson, PL, Wood, MJ a. 2009. A fusion peptide directs enhanced systemic dystrophin exon skipping and functional restoration in dystrophin-deficient mdx mice. Hum. Mol. Genet. 18: 4405–4414.

Yin, H, Saleh, AF, Betts, C, Camelliti, P, Seow, Y, Ashraf, S, Arzumanov, A, Hammond, S, Merritt, T, Gait, MJ, Wood, MJ. 2011. Pip5 transduction peptides direct high efficiency oligonucleotide-mediated dystrophin exon skipping in heart and phenotypic correction in mdx mice. Mol. Ther. 19: 1295–1303.

Yoshioka, M, Okuno, T, Honda, Y, Nakano, Y. 1980. Central nervous system involvement in progressive muscular dystrophy. Arch. Dis. Child. 55: 589–594.

Zatz, M, Vianna-Morgante, AM, Campos, P, Diament, A. 1981. Translocation (X;6) in a female with Duchenne muscular dystrophy: implications for the localisation of the DMD locus. J. Med. Genet. 18: 442–447.

Zhang, D, Iyer, LM, He, F, Aravind, L. 2012. Discovery of Novel DENN Proteins: Implications for the Evolution of Eukaryotic Intracellular Membrane Structures and Human Disease. Front. Genet. 3: 283.

Zhu, X-D, Zhuang, Y, Ben, J-J, Qian, L-L, Huang, H-P, Bai, H, Sha, J-H, He, Z-G, Chen, Q. 2011. Caveolae-dependent endocytosis is required for class A macrophage scavenger receptor-mediated apoptosis in macrophages. J. Biol. Chem. 286: 8231–8239.

Zlokovic, B V. 2008. The blood-brain barrier in health and chronic neurodegenerative disorders. Neuron 57: 178–201.

Zoppino, FCM, Militello, RD, Slavin, I, Alvarez, C, Colombo, MI. 2010. Autophagosome formation depends on the small GTPase Rab1 and functional ER exit sites. Traffic 11: 1246–1261.

Zu, T, Gibbens, B, Doty, NS, Gomes-pereira, M, Huguet, A, Stone, MD. 2011. Non-ATG – initiated translation directed by microsatellite expansions. Proc Natl Acad Sci U S A 108: 260–265.

Zubrzycka-Gaarn, EE, Bulman, DE, Karpati, G, Burghes, AH, Belfall, B, Klamut, HJ, Talbot, J, Hodges, RS, Ray, PN, Worton, RG. 1988. The Duchenne muscular dystrophy gene product is localized in sarcolemma of human skeletal muscle. Nature 333: 466–469.